Numerical and Experimental Investigations of Thermal Debinding Process in Powder Injection Molding

Khoong Ling Eng

School of Mechanical & Aerospace Engineering

A thesis submitted to the Nanyang Technological University
in fulfillment of the requirement for the degree of
Doctor of Philosophy

2006

ABSTRACT

Powder injection molding (PIM) is an important net-shape manufacturing process and has received much attention. This process is capable of producing complicated metal and ceramic products in mass volume with low production cost. PIM involves mixing, molding, debinding, and sintering processes. Debinding process is one of the most critical steps. This process consumes a major part of the processing time. And yet, attempts to speed up this process often results in failure of PIM components, like distortion, contamination, and cracking. Among various types of debinding methods, thermal debinding is a common methodology to remove binders from PIM components. During thermal debinding, binders are heated thermally, melted into liquid, and evaporate into vapor. The overall removal of binder involves evaporation, thermal degradation of polymer, transports of liquid and gas phases, and heat transfer in a PIM compact. A successful theoretical modeling and a comprehensive experimental observation provide the potential for optimization of the debinding process to shorten the processing time without causing defects on the PIM products.

In current PIM industry, a two-step debinding is used. In the early stage of debinding process, low molecular weight (LMW) components in the binder system like wax and stearic acid are removed. The final stage of debinding process is the removal of high molecular weight (HMW) components, namely polymers at higher temperatures by thermal debinding process. In this thesis, a theoretical model was developed to describe the thermal debinding of two-component binder system from a PIM compact. The PIM compact consists of carbonyl iron as metal powder and polypropylene (PP)

and stearic acid (SA) as a two-component binder system. This model describes physical phenomena that involve simultaneous heat and mass transfers and phase changes in a porous medium (PIM compact) during the thermal debinding. Two limiting cases, which are the thermal debinding of the HMW component and the LMW component, were deduced from the theoretical model and solved numerically, respectively. The experiment works were conducted to investigate the binder distributions during the thermal debinding process and to validate the numerical models. The result comparisons of the numerical results with the experimental data are in good agreement.

Based on the numerical results, the physical trends, the phase changes, the mass transfers, and the binder removal mechanisms were studied. The mass transfers during the early stage are mainly due to the liquid phase transport. Both of the liquid and gas phase transports contribute to the mass transfers during the final stage. The results indicate that the early stage of thermal debinding is dominated by a surface controlled reaction and the final stage is dominated by volumetric reactions.

ACKNOWLEDGEMENT

I am deeply indebted to my supervisors A/P Chai Chee Kiong, John and Prof Lam Yee Cheong for their guidance and encouragement in all of the time of the research and the thesis writing.

Secondly, I would like to thank to Prof Tam Kam Chiu and A/P Ma Jan for their support on the experimental works. I also would like to thank Dr. Jiang Long and Dr. Ying Sheng Jie for their englightening discussions.

I am grateful to all the technicians and students in Thermal and Fluids Research Lab, Material Labs A and B, Ceramics Processing Lab, Ceramics Lab, and Metals Processing Lab for their kind help extended to me

Last but not least, I would like to thank my family for their understanding and support.

CONTENTS

LIST OF FIGURES

LIST OF TABLES

NOMENCLATURE

SYMBOLS	*DESCRIPTIONS*	*UNITS*
A_{l-m}	Interfacial area of the liquid-solid interface	m^2
A_{l-g}	Interfacial area of the liquid-gas interface	m^2
a	Activity of species liquid phase in solution	
C_o	Specific rate constant	$1/s$
C_p	Heat capacity	$J/mol\ K$
$(\rho C_p)_{eff}$	Effective volumetric heat capacity	$J/mol\ K$
D	Diffusion coefficient	m^2/s
D_{01}	Pre-exponential factor for binary diffusion in Eq. (B-12)	m^2/s
D_0	Pre-exponential factor for binary diffusion in Eq. (B-13)	m^2/s
D_l	Binary diffusion coefficient of solution	m^2/s
D_g	Diffusion coefficient of the binary gas system	m^2/s
D_{geff}	Effective gas diffusion coefficient in porous medium	m^2/s
d	Powder diameter	μm
E_{coh}	Cohesive energy of polymer	J/mol
E_{dg}	Activation energy of thermal degradation	J/mol
E_{dif}	Activation energy of binary diffusion	J/mol
E_μ	Action energy for viscous flow of polymer	J/mol
f_e	Length ratio in Eq. (3-8)	

H	Mean meniscus curvature	
H_{μ}	Molar viscosity-temperature function	$gJ^{1/3}mol^{-4/3}$
ΔH_{vap}	Enthalpy of evaporation	J/mol
h	Number of conducted experiment or measurement	
h_m	Convective mass transfer coefficient	m/s
J	Flux	kg/m^2
$J(S_j)$	Leverett reduced function	
K	Intrinsic permeability	m^2
$K_{rl,j}$	Relative permeability of species liquid phase	
K_{rg}	Relative permeability of gas phase	
K_{stiff}	Molar stiffness function of polymer	$g^{0.25}\,cm^{1.5}/mol^{0.75}$
k	Thermal conductivity	$W/m\,K$
k_{eff}	Effective thermal conductivity	$W/m\,K$
L	Total length of the PIM compact	m
l	Distance in z-axis in Eq. (5-29)	m
M	Molecular weight	kg/mol or g/mol
M_{cr}	Critical average molecular weight of Newtonian viscosity of polymer	g/mol
M_w	Average molecular weight	g/mol
$\dot{m}_d$	Thermal degradation rate of polymer	$kg/m^3\,s$
$\dot{m}_v$	Evaporation rate of liquid phase to vapor phase	$kg/m^3\,s$

N	Total number of conducted experiment or measurement	
$\vec{n}$	Unit normal vector directed from interface or boundary surface	
P	Pressure	Pa
P_c	Capillary pressure	Pa
P_{cri}	Critical pressure	Bar
P_s	Molar parachor	$(cm^3/mol)(dyn/cm)^{1/4}$
p_g	Vapor pressure	Pa
p_g^o	Vapor pressure over pure liquid phase	Pa
q_B	Boundary flux	kg/m^2
R	Universal gas constant	$J/mol\ k$
r	Reaction order	
S	Source term	
S_C	Constant of source term in Eq. (3-5)	
S_l	Liquid saturation	
$S_{l,ir}$	Irreducible liquid saturation	
S_g	Gas saturation	
$S_{g,ir}$	Irreducible gas saturation	
S_P	Coefficient of source term in Eq. (3-5)	
T	Local temperature	K
T_b	Normal boiling temperature	K
T_{cri}	Critical temperature	K

T_g	Glass transition temperature	K
T^*	Dimensionless Temperature	
t	Time	s
V	Volume of phase	m^3
V_b	Molar volume at boiling temperature	cm^3/mol
V_{cri}	Critical volume	cm^3/mol
$V(0)$	Specific volume at 0 K	m^3/kg
V_l	Molar volume	cm^3/mol
$\vec{v}$	Convective velocity	m/s
v_∞	Average free stream velocity	m/s
W	Mass fraction	
$\vec{w}_n$	Speed of displacement of interface	m/s
x, y, z	Coordinates	
X_{RB}	Measured residual binder of the sample	
x_k	Coordinate normal to the boundary of interest	
δx	x-direction distance between two adjacent grid points	m
δX_{RB}, δY_{BP}, δY_{GP}	Standard error for best estimates of X_{RB}, Y_{BP}, and Y_{GP}	
Y_{BP}	Measured binder content of the brown part	
Y_{GP}	Measured binder content of the green part	
Δy, δy	Similar to Δx, δx	m
Z_{AB}	Mixing coefficient for gas diffusion coefficient	

Δz , δz	Similar to Δx , δx	m

GREEK LETTERS

α	Characteristic length	$\AA$
β	Phase	
Γ	Diffusion coefficients for the combined governing equations (Eqs. (2-31), (2-41), (2-47), (2-57), and (2-27))	kg/m^2s, $kg/m^2s\ K$, $kg/m^2s\ Pa$
γ_a and γ_c	Parameters for the effective thermal conductivity	
Δt	Time step	s
Δx	x-direction width of the control volume	m
δ	Solubility parameter	$(J/cm^3)^{0.5}$
ε	Porosity	
η	Overlap factor for free volume	
μ	Viscosity	$Pa\ s$
ξ	Ratio of critical molar volume of hopping units of monomer and polymer	
Π_D	Dimensionless diffusion collision integral	
ρ	Density	kg/m^3
σ	Surface tension	N/m
Φ	Independent variable	
ϕ	Volume fraction	
Θ	Underrelaxation factor	
θ_l	Ratio of volume fraction of species liquid phase over the total liquid phase	
K_{stiff}	Molar stiffness function	$g^{0.25}cm^{1.5}/mol^{0.75}$

κ_{11} and κ_{12}	Free volume parameters	
κ_{21} and κ_{22}	William-Landel-Ferry (WLF) constants	
Λ	Molar fraction of the pure gas components	
χ	Interaction parameter	
ψ	Mobility of phase	$m^2/Pa\ s$
Ω	Coefficients of transient terms in combined governing equations (Eqs. (2-31), (2-41), (2-47), (2-57), and (2-27))	
ω	Thermal expansion coefficient	

SUBSCRIPT

E	Neighbor point in the positive x direction
e	Control-volume face between P and E
f	Volatile fragments
g	Gas phase
h	Number of experiment conducted
i	Inert gas
j	Species of LMW component, HMW component or volatile fragments
l	Liquid phase
m	Solid phase
N	Neighbor point in the positive y direction
n	Control-volume face between P and N
nb	General neighbor grid point
P	Central grid point under consideration
p	HMW component

S	Neighbor point in the negative y direction
s	Control-volume face between P and S
sa	LMW component
W	Neighbor point in the negative x direction
w	Control-volume face between P and W

SUBSCRIPT

N	Number of iteration

MATHEMATICAL SYMBOLS

$\frac{d}{dt}$	Total time derivative
$\frac{\partial}{\partial t}$	Partial time derivative
$\langle \Phi_\beta \rangle$	Phase average of a variable Φ_β
$\langle \Phi_\beta \rangle^\beta$	Intrinsic phase average of a variable Φ_β

CHAPTER 1

INTRODUCTION

1.1 Background

Powder injection molding (PIM) is a manufacturing process that produces metal and ceramic parts using modified technology of plastic injection molding process. It can be classified into metal injection molding (MIM) and ceramic injection molding (CIM). PIM process involves combining organic binders with inorganic powder to form feedstock. The feedstock is then molded into product with desired shape. After shaped, the binders are extracted and the powder is sintered to near-theoretical densities, in which the final product is made.

PIM technology is attractive due to low production costs in mass production with high yields. This technology has advantage of material flexibility for allowing metals and ceramics molded in various complex shapes and tight tolerances. This technology always produces products that need minimum treatment or fining processes. Thus, minimum machining cost is needed for PIM process.

In the history of PIM technology, CIM was developed in the 1920s to produce ceramic spark plug bodies. By late 1950s, many carbide and ceramic components were shaped using binders like wax, epoxy or cellulose binder in small volume. The PIM process was commercialized in the 1980s when it is used to produce ceramic heat engine components (German, 1990). Since 1980s, the world market for PIM grows rapidly and it achieved thirty-two percent growth over the past 10 years (Yoshikawa and Ohmori, 2001). The applications of the PIM technology include but are not limited to

electronics, aerospace, medical, and automotive industries. Final products include but are not limited to micromotors, actuators, sensors, heat exchangers, filters, microvalves and pumps, medical instruments, biomedical implants, and engine components.

However, there are still some limitations in PIM process. The dimensional accuracy of the PIM products is limited to $\pm 10 \mu m$ (Yoshikawa and Ohmori, 2001). The component size is another limitation since large components require more powder and large molding and sintering machines. The binder removal is also difficult for big component. Normally, the largest dimension suitable for PIM is 10 mm with a total volume of 100 mm^3 (German and Bose, 1997). Besides, the cost of powder is a barrier for many applications. Smaller powder particles are more expensive.

More importantly, the thermal treatment technology like thermal debinding and sintering are the key problems in PIM process. The large shrinkage accompanying the sintering process is one of the critical issues in manufacturing final products with desired shape and dimensions. The debinding process is a time-consuming step and attempts to speed up this process prior to sintering process always results in defects. Therefore, the debinding process, namely binder removal, is one of the most critical steps in PIM process.

1.1.1 Powder Injection Molding

Figure 1.1 shows a schematic of the steps for PIM process. First step of PIM is mixing of selected powder and binders. The powder is metal or ceramic powder. Normally multi-component binder system, which consists of high molecular weight (HMW) component and low molecular weight (LMW) component, is used. The LMW components are substances with simple molecules such as wax and stearic acid. The HMW components are polymers such as polypropylene and polyethylene. Binders are needed to hold the powder particles together and to lubricate the particles sliding during molding (German, 1990). After mixing, the feedstocks are produced. The feedstocks are then formed into pellets.

The next step is molding process to make the PIM green parts. The palletized feedstocks are transferred to a molding machine. In the molding machine, the feedstocks are hot rammed under pressure into a tool cavity to form a desired shape. Subsequently, the molded parts is cooled and solidified to preserve the molded shape.

After molding, the binders have served the purposes. The binders are then removed from the PIM green parts by debinding process. The PIM brown parts are produced at the end of the debinding process.

The final step is sintering process, which bonds the powder particles together. Sintering is often conducted in a protective atmosphere or vacuum at peak temperature that creates rapid elimination of the pores in the parts. As a result, the parts shrink to the final dimension.

1.1.2 Debinding Process

Debinding techniques can be categorized as solvent and thermal processes (German and Bose, 1997). The solvent processes remove the binders by chemical approaches. The thermal processes remove the binders by means of heating.

The solvent debinding process includes solvent immersion, supercritical extraction, solvent vapor condensation, and catalytic depolymerization. In solvent immersion method, the green parts are immersed in a solvent to dissolve the binders. Open pores are then created inside the green parts for subsequent binder removal via heating process. In supercritical extraction, a solvent is heated and pressurized above the critical point and used to dissolve the binders. This method can minimize the formation of defects in the parts. However precise temperature and pressure controls are required and the binder removal rate is slow. For solvent vapor condensation, the green parts are placed in a heated solvent vapor. The binders are then absorbed by condensation. For catalytic depolymerization, the green parts are heated in atmosphere. The catalyst is added to depolymerize and remove the binders. By this method, the debinding process can be accelerated with excellent shape retention and high automation. The disadvantages of solvent debinding methods like solvent immersion, solvent vapor condensation, and catalytic depolymerization, are environmental concerns and solvent hazard. Moreover, the debound parts are required to be dried before sintering.

Thermal debinding is an alternate to solvent debinding. Four thermal debinding approaches are used in PIM process. These are diffusion-controlled, permeation-controlled, wicking, and oxidation. In diffusion-controlled method, the green parts are heated slowly in a low-pressure system. The binders inside the green parts change

phase from solid phase to liquid phase then vapor phase. A carrier gas is used to remove the vapor binders. In permeation-controlled method, the green parts are heated slowly with carrier gas flows above the green parts to cause a progressive degradation of binders. For wicking method, binders are removed by heating the green parts in a packed powder bed or on a porous substrate to absorb the molten binders. In oxidation method, the green parts are heated in air to remove the binders and oxidize the powder to strengthen the parts.

Thermal debinding is the most common method for removing the binders from the green parts for both CIM and MIM (Trunec and Cihlar, 2002). However, the binders must be removed slowly, carefully, and completely to preserve the quality of the final products (Tsai, 1991). Therefore, thermal debinding process is an expensive and critical process in PIM. Understanding the physical mechanisms involve in thermal debinding process is essential. As such, the process can be optimized to shorten the debinding time and reduce the operation cost.

1.2 Literature Review

Over nearly two decades, the thermal debinding process of PIM green parts or compacts has received considerable attention. There are a number of modeling and experimental investigations on this process. However, the binder removal mechanisms of thermal debinding process remain not fully understood. In this section, the modeling works are reviewed. The considered physical phenomena and the shortcomings of the models are discussed. The experimental observations and their discussions are also reviewed.

1.2.1 Modeling Works

Literature on modeling works is discussed by grouping into four categories. The grouping is based on the physical phenomena considered in the models. These are the receding of liquid-gas interface, the diffusion of degraded products in liquid polymer, the transport of liquid or gas phases, and the transports of liquid and gas phases.

German (1987) modeled the isothermal debinding of a single component binder system by assuming a liquid-gas interface recedes into the PIM compact (see Fig. 1.2). Three mechanisms namely, vapor diffusion, vapor permeation, and wicking, were considered respectively. The vapor diffusion (Knudsen diffusion) was considered for the debinding of compact with small pore sizes at low gas pressures. In this case, the gas motion was determined by the collisions between the gas molecules and pore walls. The vapor permeation was considered for the debinding of compact with larger pore sizes at higher gas pressures. In this case, the laminar flow of a viscous gas phase through the pores was described using Darcy's law. In both mentioned cases, the kinetics of thermal degradation of binders was not considered. The wicking is the

binder removal that controlled by capillary driven liquid flow. The model of these three mechanisms overestimated the debinding time.

Calver and Cima (1990) modeled the removal of polymeric binder from a ceramic compact. The model considered the degradation of polymer to monomer, the diffusion of monomer in liquid polymer, and the vaporization. The model assumed that a liquid-gas interface recedes uniformly into the compact during binder removal. The model was used to optimize the debinding process. The model also overestimated the debinding time.

Langer and Lehnert (1998) described the thermal debinding process based on the mathematical theory of drying process. A semi-empiric model was developed to optimize the debinding process. The model assumed that a drying front (liquid-gas interface) moves back from the surface to the compact.

There are models that mainly considered the diffusion of degraded products in liquid polymer. Evans et al. (1991) modeled the binder removal of a ceramic compact in a shape of infinite cylinder. The model considered the degradation of polymer to monomer and the diffusion of the monomer in a solution of polymer and monomer. However, only the early stage of degradation was considered and the binder loss from the compact was neglected. The model was used to predict the incidence of boiling (vapor pressure of monomer greater than atmospheric pressure) which results in the formation of internal defects. The critical heating rate, which is the fastest heating rate that the binder removal can be conducted without creating defects, was estimated. The model underestimated the critical heating rate.

Matar et al. (1993) modified the model of Evan et al. (1991) by considering the evolution of porosity in two hypothetical configurations. These are the receding of a shrinking core (liquid-gas interface) and the formation of distributed porosity. For the case of shrinking core, liquid polymer recedes into the compact and forms new internal plane surface. The diffusion of monomer in the liquid polymer inside the shrinking core was considered. In the case of distributed porosity, a uniform distribution of porosity is developed due to the redistribution of liquid polymer throughout the porous body. The diffusions of monomer in the liquid polymer and in the open pores were considered. Matar et al. (1995) further extended the shrinking core model to include gas phase transport in the pores of the compact. Song et al. (1996) modified the shrinking core model by considering the contributions of diffusion and viscous flows to the gas phase transport. Matar et al. (1996) extended the shrinking core model by considering different compact geometries. These are a sphere, an infinite plate, and an infinite cylinder.

Based on the model of Evan et al. (1991), Shaw and Edirisinghe (1995a) modeled the binder removal from a one-dimensional flat ceramic compact. The model considered the creation of porosity simultaneously at the surface and in the core of the ceramic compact. The shrinkage of compacts during the binder removal was considered. However, the gas flow in the pores of ceramic compact was neglected.

Oliveira et al. (1999) considered the degradation of polymer to volatile products and the diffusion of the volatile products in modeling the binder removal. Based on a

criterion for the onset of bubble formation (same as Evan et al., 1991), the model was used to optimize the thermal debinding process.

Based on the shrinking core model, Shi et al. (2002) and Shi and Guo (2003) modeled the removal of fiber from a ceramic powder compact. This work considered the degradation of polymer into monomer, the diffusion of monomer in liquid polymer, and the gas phase transport in the pores. Shi and Guo (2004) extended the model by considering the shrinkage of compact during thermal debinding process.

Some models either considered the transports of liquid or gas phases. Barone and Ulicny (1990) modeled the early stage of thermal debinding for an injection molded ceramic compact in one-dimensional. The model took account of the thermal degradation of polymeric binder. However, the thermal debinding process was assumed to be dominated by the capillary driven liquid phase transport and the gas phase transport was neglected. The model was used to evaluate the hydraulic pressures in the compact during the thermal expansion of liquid binder before significant binder removal occurred. In estimating the hydraulic pressures, the evaporative losses were neglected and fully saturated condition was assumed. The predicted results reported that the liquid phase distribution of LMW component over the compacts is quite uniform. These results were reported in agreement qualitatively with the observations of Barone et al. (1988).

Lewis et al. (1996) used Monte-Carlo method to model the isothermal removal of LMW component. The model considered the diffusion of volatile species in the liquid binder and the capillary driven binder redistribution.

Maximenko et al. (1998) conducted the numerical simulation on thermal debinding process using finite element method. The diffusion of LMW component and the liquid flow of binder were considered in the model. The internal stress distribution over the compact was investigated.

Tsai (1991) modeled the binder removal of a one-dimensional cylinder powder compact. The model was based on the gas phase transport in a porous medium, the pyrolysis of binder, and the elasticity theory. The model was used to analyze the buildup of gas pressure and stresses in the compact during binder removal. The effects of sample size, specific surface area, and pressurized atmosphere were discussed.

West and Lombardo (1998) developed a mathematical model to describe the removal of polymeric binder from an injection-molded ceramic compact. The heat conduction within the ceramic green part, the mass transfer by convective flow of gas phases, and the Arrhenius dependence degradation rate were considered. The influences of the thermal and transport properties on the binder distribution and on the pressure buildup within the compact were examined. The results indicated that the binder is removed homogenously when the small temperature gradients exist across the body. However, the binder is removed as a receding planar front when large temperature gradients are present.

Feng et al. (2002) modeled the binder removal from a ceramic compact by considering the permeation of gas phase in a solid porous structure. The stresses and the internal pressure buildup were analyzed. Lombardo and Feng (2002) further developed the

model by taking account of the thermal degradation of polymeric binder. The effects of the sizes of the ceramic compacts, the degradation rate, and the permeability of the porous structure on the pressure buildup were discussed. Feng and Lombardo (2003a) extended the model by taking account of anisotropic permeability. The three-dimensional stress distribution of ceramic compacts during thermal debinding process was investigated. Feng and Lombardo (2003b) presented an analytical expression to predict the heating profile to minimize the debinding time. The factors of the ceramic compact sizes, the isotropic permeability, the binder volume fraction, and the threshold pressure were considered in the analytical solution.

There are few models considered both of the liquid and gas phase transports. Stangle and Aksay (1990) modeled thermal debinding process in one-dimensional. The model considered the capillary-driven liquid phase transport, the diffusive and convective gas phase transport, and the phase changes by chemical reaction and evaporation in porous media. The internal stresses that generated in the ceramic body were analyzed. The predicted results were reported in agreement with the TGA experimental results. However, the model focused on the thermal debinding of LMW component.

Lam et al. (2000) modeled thermal debinding process and analyzed the physical mechanisms involve in this process. The considered mechanisms are the liquid flow, the gas flow, and the vapor diffusion in liquid phase and gas phase. The results revealed that a distinct liquid-gas interface that recedes into the PIM compact as removal progresses does not exist. The binder distribution in the compact is a function of distance from the outer surface of the compact and debinding time. Ying et al. (2001) extended the numerical work of Lam et al. (2000) into two-dimensional. After

that, Ying et al. (2002a) extended the model to investigate the deformation of compacts during the thermal debinding process. Lam et al. (2002) compared the numerical results with experimental data on the thermal debinding of polymeric binder from PIM compact.

Ying et al. (2002b) further developed the model to analyze the deformation and the stress generation during thermal debinding. The strain and stresses that induced from the polymeric binder content change, the gas pressure, and the temperature change were analyzed. Ying et al. (2004a) investigated the liquid-bond strength in the PIM compact during thermal debinding. The results revealed that the liquid-bond strength that induced during the softening of polymeric binder is significant in formation of defect. Ying et al. (2004b) studied the effects of mass transport on the equivalent stress. The results indicated that the inducing of equivalent stress is mainly due to the non-uniform distribution of binder distribution in PIM compact.

1.2.2 Experimental Works

In investigating the thermal debinding process, the experimental techniques are included but not limited to thermal analysis, mercury porosimetry analysis, and direct observation. The common thermal analysis techniques applied are thermogravimetric analysis (TGA), thermomechanical analysis (TMA), and differential thermal analysis (DTA). Thermogravimteric analysis is used to measure the weight loss of a sample (binder content) and to analyze the degradation behavior of binders. TMA is used to measure the dimensional change of the PIM compact during or/and after binder removal. DTA is useful in studying thermally sensitive events that occur during binder removal. The endothermic (sublimation and vaporization) and exothermic (chemical

reaction, decomposition, and oxidation) process can be differentiated using DTA. Mercury porosimetry is used to measure the pore size distribution of the PIM compact. For direction observations on the microstructure of the compact after binder removal, the optical microscope and the scanning electron microscopy (SEM) are used.

In what follows, the experimental observations of the thermal debinding are reviewed. These are the binder distributions, the porosity development, the kinetics of binder removal, and the shrinkage.

Barone et al. (1988) investigated the binder distributions of a multi-component binder system in ceramic compacts after binder removal. The results reported that the binders distribute uniformly indicating a nearly uniform volumetric reaction occurs throughout the compact. There was no indication of a frontal progression of the reaction zone (liquid-gas interface).

Sproson and Messing (1988) investigated the isothermal removal of a multi-component binder system from ceramic compacts. The results implied that the LMW components are removed at low temperatures by diffusion. At higher temperatures, the molten HMW components migrate outwards and are then removed by decomposition at the surface of the compacts. The presence of binder enrichment at the surface was observed. This work suggested that the binder migration could be due to the capillary driven and pressure driven forces. However, the relative importances of these driving forces were not investigated.

Cima et al. (1989) also studied the isothermal removal of a multi-component binder system from ceramic compacts. The binder distributions and the pore growth after binder removal were observed. The capillary forces were found dominating the binder distributions in the sample. However, the dominant of the capillary forces depends on the physical properties of molten binder (surface tension and viscosity) and the removal rate of volatile products. The mass transfer could be controlled by the vapor phase transport if the porosity has developed throughout the compacts. Lewis and Cima (1990) conducted direct observations on the binder distributions during binder removal. The distributions of binder in a two-dimensional microstructure model were observed using Hot-stage/optical microscopy. The observations indicated that the mass transport process (capillary-controlled or diffusion-controlled) and the development of pore structure depend on the properties of binder system. The binder distributions could be controlled by diffusion if the binder viscosity or the binder removal rate is high as compared to the capillary redistribution.

Shaw et al. (1993) investigated the binder degradation and the binder redistribution during the binder removal of ceramic compacts. The work focused on the removal of wax (LMW component) during initial stage. The results indicated that the wax migrates from the core to the surface regions during the initial stages of binder removal. An enrichment of wax at the surface region was observed.

Trunec and Cihlar (2002) studied the thermal removal of LMW component of a multi-component binder system from ceramic compacts. The results indicated that the decisive process of thermal debinding of LMW is evaporation. The binder redistributes during evaporation and the distribution is nearly uniform. The binder loss is

accompanied with the shrinkage of body. The shrinkage stops when the movements of ceramic particles are blocked. The open pores then begin to develop in the surface region of the compacts and move quickly to the center of the compacts. With high binder removal rate, the binder could distribute non-uniformly and this led to the formation of defects.

Some works investigated the porosity development in the compacts after binder removal. Shaw et al. (1992) investigated the formation of porosity during binder removal. The results showed that the removal of LMW components is important in generating open pores inside the injection-molded compacts during the early stage of thermal debinding. The open pores are essential for the removal of HMW components at later stage.

Hwang and Tsou (1992) studied the binder removal mechanisms during the thermal debinding process of a multicomponent binder system. Based on the mercury porosimetry analysis and SEM observations, three stages of debinding mechanisms were proposed. The first stage of debinding is the uniform development of fine pore due to the decomposition of LMW component. These fine pores provide paths for decomposed gas to escape to the surrounding. The intermediate stage indicated that less viscous binders are forced to the surface by internal gas pressure. The binders redistribute due to capillary driven force. This redistribution gives a structure of powder agglomerates and large interparticle voids. The debinding rate increases at this stage due to more binder-vapor interface and more large pores. The final stage showed that less than 20% of binders are trapped and remain in compact, which hold the particles with capillary force.

Some of the works studied the kinetics of debinding. Angermann et al. (1992) studied the removal mechanism of LMW component from stainless steel powder compacts. The TGA results showed that the debinding rate is dominated by the diffusion of LMW component in the polymeric binder. Angermann and Van Der Biest (1993) also reported that the debinding rate is controlled by the diffusion of LMW component in the polymeric binder to the inner surfaces of pores. However, this is only valid if the intermolecular interaction between the binders is similar.

Hrdina et al. (1998) studied the removal of polymeric binder that undergoes a two-stage thermal degradation from ceramic compacts in an inert atmospheric. The investigation focused on the removal of the degraded products of polymeric binder at early stage. The results showed no porosity developed and only shrinkage occurred during this stage. The degraded products diffuse through the liquid polymer filled pores to the surface of compacts and then evaporates. The formation of cracks was attributed to the concentrations of degraded products exceeding a critical value that results in bubbling.

Liu and Tseng (1999) studied the binder removal of wax-based binder from ceramic compacts. The results showed that the weight-loss behavior is strongly affected by the solid content and the specimen thickness. The binder migration/diffusion from the interior to the surface region of the compacts was found significantly restricting the binder removal. The activation energies of the thermal degradation and the evaporation of the binder during thermolysis were evaluated. The results implied that evaporation is a dominant mechanism for the removal of LMW component.

The dimensional change of the compact (expansion and shrinkage) during or after the binder removal was studied. Sundback et al. (1989) investigated the part distortion of compacts by detecting the dimensional changes using TMA. The results suggested that the major part distortion occurs before and during the periods of major weight loss. The maximum dimensional change is around 1 %.

Shaw and Edirisinghe (1995b) studied the shrinkage and the particle packing during binder removal from ceramic compacts. The shrinkage due to the packing of ceramic particles in the compacts during initial stage binder removal was estimated. The estimation considered the shrinkage due to the changes in the thermal expansion coefficient and the crystalline melting of the organic binder. The maximum measured shrinkage after binder removal is 4 vol%.

Lu and Lannutti (2000) examined the combined effects of binder removal and density gradients of the compacts on dimensional tolerance. The results reported that non-uniform binder distribution during compaction molding provides density gradients in the compacts. These local differences in density lead to binder redistribution and differential shrinkage during binder removal. The binder migration/removal could result in dimensional changes. The reported maximum dimensional change is less than 1 %.

1.3 Remarks On the Existing Works

From the literature review, it is shown that there exist many modeling and experimental works investigating the thermal debinding process. The modeling works are conducted to understand the binder removal mechanisms and to optimize the thermal debinding process. Though, there are several researchers intend to model thermal debinding process by considering various mass transport mechanisms, yet, it remains not fully understood.

Some modelings of thermal debinding process (German, 1987, Calvert and Cima, 1990, Langer and Lehnert, 1998, Matar et al., 1995, Song et al., 1996, Matar et al., 1996, Shi et al., 2002, Shi and Guo, 2003 and 2004) assumed a receding liquid front in their models. These are in disagreement with the experimental observations of Barone et al. (1988) that suggested no such moving front (liquid-gas interface) during the binder removal process. The numerical results of Lam et al. (2000) and Ying et al. (2001, 2002a) also indicated that the assumption of moving front did not reflect the physical reality of the thermal debinding process.

Some modeling works (Evans et al., 1991, Shaw and Edirisinghe, 1995a, Matar et al., 1996) only based on the diffusion of degraded product in liquid polymer. Tsai (1991), West and Lombardo (1998), Feng et al. (2002), Lombardo and Feng (2002), and Feng and Lombardo (2003a) only considered gas flow. Barone et al. (1990) only considered liquid flow. The modeling works of Lewis et al. (1996) and Maximenko and Van Der Biest (1998) focused on the thermal debinding of LMW component. Evans et al. (1991) and Oliveira et al. (1999) modeled the thermal debinding of HMW component. However, only the early stage of thermal degradation of HMW component was

considered. The above-mentioned models are not complete in modeling the thermal debinding process in a PIM compact.

Lam et al. (2000), Ying et al. (2001), and Ying et al. (2002a) modeled the thermal debinding process and analyzed the binder removal mechanisms. However, the model focused on the thermal debinding of HMW component from a PIM compact. The models did not account for highly viscous liquid polymer and assumed that the degraded product evaporates instantly after the thermal degradation of HMW component.

Most of the reviewed experimental investigations mainly focused on the early stage of thermal debinding (Cima et al., 1989, Shaw et al., 1993, Trunec and Cihlar, 2002, Shaw et al., 1992, Angermann et al., 1992, Angermann and Van Der Biest, 1993, Hrdina et al., 1998, Liu and Tseng, 1999). Based on the experimental observations, the binder removal mechanisms were discussed. During thermal debinding, the LMW component evaporates and is first removed at low temperatures (Sproson and Messing, 1988, Liu and Tseng, 1999, Trunec and Cihlar, 2002). The removal of LMW component creates open pores for subsequent removal of the HMW component at higher temperatures (Shaw et al., 1992, Hwang and Tsou, 1992). The binder migrates and diffuses outwards to the outer surfaces of the compacts during thermal debinding. The binder migration/diffusion could be due to the capillary driven action (Sproson and Messing, 1988, Trunec and Cihlar, 2002, Hwang and Tsou, 1992) and the pressure driven action (Sproson and Messing, 1988, Cima et al., 1989, Hwang and Tsou, 1992). Some works suggested that the diffusion of LMW component (Angermann et al.,

1992, Angermann and Van Der Biest, 1993) or degraded products (Hrdina et al. 1998) dominates the binder removal during the early stage of thermal debinding.

Hitherto, there is no theoretical model that describes and analyzes the binder removal mechanisms (as suggested in the above-mentioned experimental investigations) in detail. There is also no model that describes the complete process of thermal debinding of two-component binder system. The complete process involves the early and the final stages. The LMW component is removed during the early stage, while the removal of HMW component occurs at the final stage. As such, the thermal debinding of two-component binder system is modeled and the binder removal mechanisms are analyzed in this thesis.

1.4 Objective and Scope

The objective of this thesis is to investigate the thermal debinding process numerically and experimentally to understand the mechanisms involve during thermal debinding of a PIM compact. Numerical modeling are conducted to simulate the thermal debinding process and followed by experimental works to validate the model. The scope of this thesis involves:

1. A theoretical model is developed to describe the thermal debinding of two-component binder system from a PIM compact.
2. Two limiting cases are deduced from the model and are solved numerically to simulate the thermal debinding of the HMW and the LMW components, respectively. The physical phenomena during thermal debinding process are studied.

3. Experimental investigations are conducted on the binder distributions of PIM compacts for HMW component and LMW component after thermal debinding, respectively. The experimental data are used to validate the numerical models.
4. The validated numerical models are integrated to simulate the thermal debinding of two-component binder system from a PIM compact.

1.5 Contributions

These are the three main contributions in this thesis:

1. A novel model was developed to describe the thermal debinding of two-component binder system from a PIM compact. To capture the physical phenomena of thermal debinding process, the model takes into account of the thermal degradation of liquid HMW component into liquid volatile fragments, the evaporation of liquid LMW component and liquid volatile fragments, the capillary driven liquid phase transport, the binary diffusion in solutions, the convection and diffusion of gas phases, and the heat transfer in a porous medium (PIM compact).
2. Two limiting cases were deduced from the model and were solved numerically to simulate the thermal debinding of HMW component and LMW component, respectively. The numerical models were validated with obtained experimental data.
3. The numerical models were integrated to simulate the thermal debinding of two-component binder system. The binder removal, the phase changes, the buildups of pressures, the binder distributions, the mass transfers, and the binder removal mechanisms were analyzed and understood. This numerical model provides a fundamental platform for the analysis and the optimization of the thermal debinding process.

1.6 Outline of the Dissertation

There are six chapters in this report. The PIM process and the thermal debinding process are introduced in Chapter 1. The review of the modeling and experimental works in thermal debinding process are presented and remarked in Chapter 1 as well. In Chapter 2, the theoretical model on the thermal debinding of two-component binder system is presented. In Chapter 3, the numerical method is presented. The experimental methods are described in Chapter 4. The experimental results, the result comparisons of experimental data with numerical results and the result discussions are presented in Chapter 5. Finally, the conclusions and the recommendations for the future works are discussed in Chapter 6.

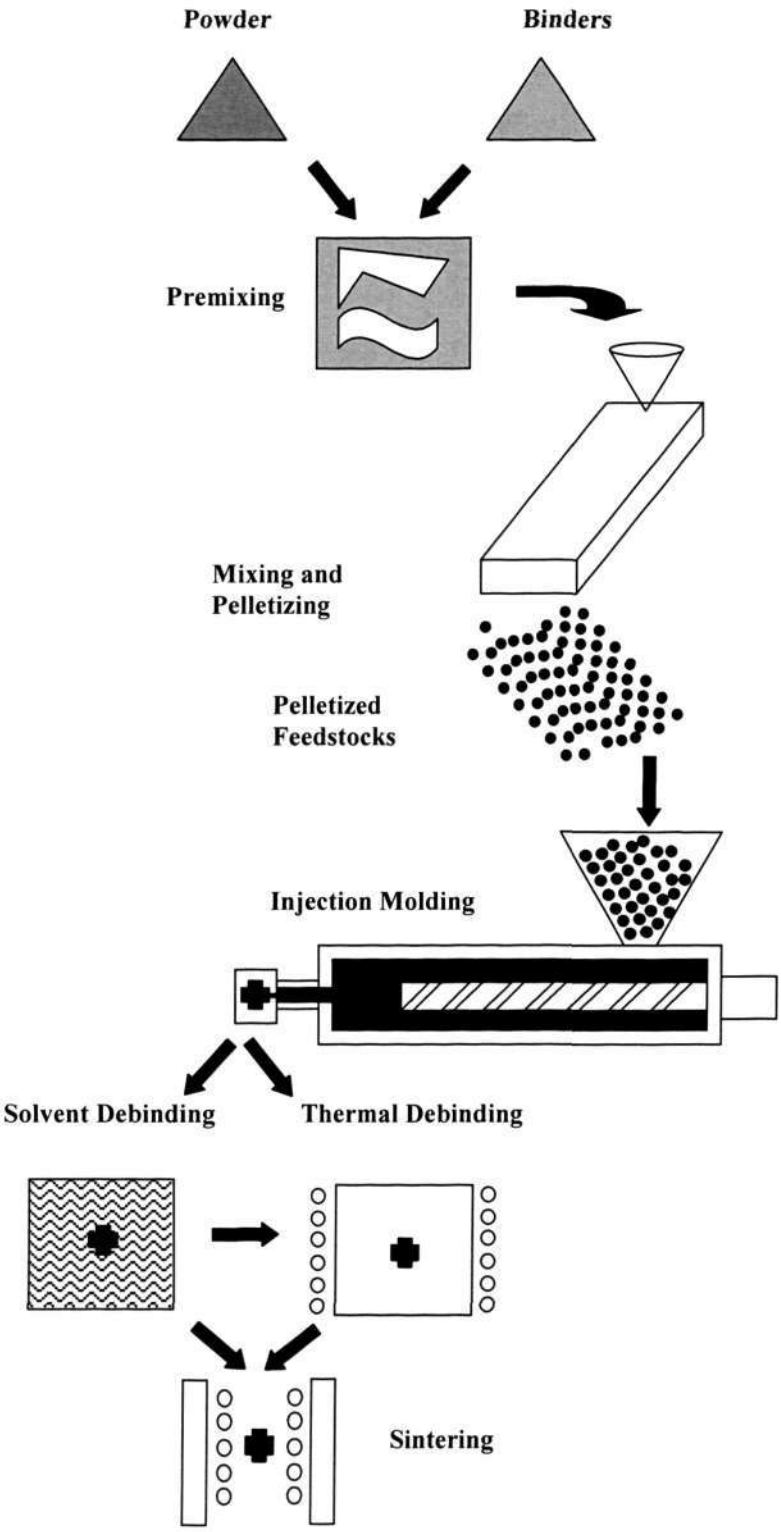

Figure 1.1 Powder injection molding process

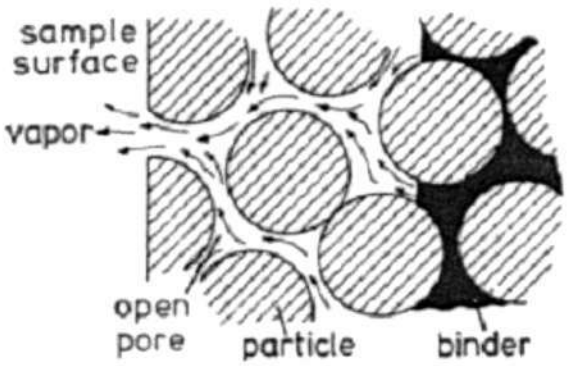

Figure 1.2 Liquid-gas interface (German, 1987)

CHAPTER 2

THEORETICAL MODEL

In this chapter, the physical phenomena of thermal debinding are discussed in section 2.1. In section 2.2, the theoretical model for the thermal debinding of two-component binder system from a PIM compact is described. The constitutive equations, the transport equations, and the material properties are presented in Appendices.

2.1 Physical Phenomena

A PIM compact consists of metal powder and a binder system (see Fig. 2.1). In industrial practice, multi-component binder system is used. This binder system consists of LMW components, for example, paraffin wax and stearic acid (SA), and HMW components, for example, polypropylene (PP) and poly(alpha-methylstyrene). Thermal debinding is a process of removing the binder system from the PIM compact. During this process, a PIM compact is heated in a debinding furnace. The metal powder remains as solid porous structure in the PIM compact. The LMW components and the HMW components change phase from solid phase to liquid phase then vapor phase. The vapor phase is then removed from the compact. The main differences between them are the phase-change temperatures. The phase-change temperatures for the HMW components are higher than the LMW components (see Fig. 2.2).

In this thesis, a mathematical model is formulated for the thermal debinding process within the temperature range between T_0 and T_5 (Fig. 2.2). The process can be classified into 5 regions according to the phase changes of these two components.

Region 1 ($T_0 < T < T_1$): The solid LMW and the solid HMW components are heated in the furnace.

Region 2 ($T_1 < T < T_2$): When the debinding temperature reaches the melting point of the LMW components, these components melt into liquid phase. The HMW components remain as solid phase. The liquid LMW components migrate to the outer surfaces of PIM compact due to the gradients of temperature, concentration, and total gas pressure.

Region 3 ($T_2 < T < T_3$): The liquid LMW components evaporate into vapor phase. The vapor LMW components diffuse outwards and being removed at the outer surfaces by convective mass transfer.

Region 4 ($T_3 < T < T_4$): At this temperature range, the HMW components undergo the glass transition, which is the onset of the molecule movement. When the HMW components are heated further, these components melt into viscous liquid phase at the melting temperature (see Fig. 2.3(a)). The liquid HMW components migrate towards the outer surfaces. After both of the components are melted, the liquid phases can be treated as a solution of these two components. Therefore, the binary diffusion occurs between the liquid LMW components and the liquid HMW components. When vapor LMW components are removed, more pores are formed inside the PIM compact. The vapor LMW components will diffuse through the initial pores, which consists of the vapor LMW components and the inert gas that fills inside the furnace. Normally, the removal of the LMW components is almost complete ($T = T_4$) before the HMW components are being removed.

Region 5 ($T_4 < T < T_5$): After the degradation temperature has been reached, the liquid HMW components degrade into the liquid monomers or liquid volatile fragments. The HMW components, namely polymers, can be categorized into two types based on their thermal degradation behavior. These are (1) polymers that degrade via chain depolymerization and yield almost 100 % monomers, for example, poly(alpha-methylstyrene), and (2) polymers that degrade by means of random chain scission to volatile fragments with almost 0 % of monomer yield, for example, polypropylene. In this thesis, the latter case is considered. At this moment, the liquid HMW components and the liquid volatile fragments can be treated as a solution (see Fig. 2.3(b)). These two liquid phases migrate due to temperature, concentration, and pressure gradients. At the same time, the liquid HMW components will continue to degrade into the liquid volatile fragments. The liquid volatile fragments will either evaporate to form vapor phase or diffuse through the solution before evaporating into vapor phase. Then, the vapor volatile fragments will diffuse through the binary gas phase that consists of the vapor volatile fragments and the inert gas inside the pores of PIM compact. The vapor volatile fragments are removed at the surfaces of the PIM compact by convective mass transfer.

The thermal debinding process can be divided into two stages, namely, the early stage and the final stage. Figure 2.4 shows these two stages of thermal debinding. During the early stage of thermal debinding, the LMW components are removed. It involves the phase changes of the binders within the temperature range T_0 and T_4 (Fig. 2.2). The HMW components are removed at the final stage of thermal debinding. This stage involves the phase changes of the binders from the temperature T_4 to T_5.

In this thesis, the LMW and HMW components are chosen to be SA and PP, respectively. The distinct different in the removal temperature of these two components allows the separate theoretical study and experimental investigation of the early stage and the final stage of thermal debinding process as shown in Figs. 2.2 and 2.4.

2.2 Modeling of Thermal Debinding

Thermal debinding is a complex physicochemical process that involves simultaneous heat and mass transfers of multiphase flow in porous media. In order to simplify the model, some assumptions are made in section 2.2.1. The basic governing equations for the thermal debinding process are shown in section 2.2.2. These basic governing equations are written at microscopic level. At this level, the geometries of the interfaces that bound the phases are too complicated to be described and modeled. Therefore, the governing equations at macroscopic level are obtained using a volume averaging method discussed in section 2.2.3. At this level, the measurable, continuous, and differentiable quantities can be determined and the boundary-value problems can be stated and solved (Jacob, 1989). The formulation of the model is completed in section 2.2.3.2. These volume averaging governing equations are convection-diffusion equations. In section 2.2.3.3, these governing equations are further combined into diffusion equations. It is because diffusion equations are easier and more stable to be solved numerically.

To capture the physical phenomena of thermal debinding, the theoretical model accounts for (1) the liquid phase transport due to capillary driven action and binary

diffusion in the solutions, (2) the thermal degradation of polymer to volatile fragments, (3) the evaporations of the liquid LMW component and the liquid volatile fragments, (4) the gas phase transport by convection and diffusion, and (5) the heat transfer within the PIM compact.

2.2.1 Assumptions of the Model

In this theoretical model, the following assumptions are made:

i) The metal powder porous media is considered rigid. As a result, the shrinkage of the PIM compact during thermal debinding is not considered.

ii) There is no chemical reaction between metallic powder porous media and inert gas phase.

iii) The three-phase system is considered in local thermodynamic equilibrium. Therefore the local temperature of the solid phase, the liquid phase, and the gas phase is the same.

iv) The total gas phase is considered as a mixture of ideal gases.

v) The solutions are in phase equilibrium.

vi) The polymer degrades to identical volatile fragments throughout the thermal debinding process.

2.2.2 Basic Governing Equations

The thermal debinding process is governed by the conservation of mass, the conservation of momentum, and the conservation of the energy.

The conservation of mass is

$$\frac{\partial \rho}{\partial t} + \nabla \cdot (\rho \vec{v}) = \nabla \cdot [\rho D \nabla (\frac{\rho}{\rho_{total}})] + \dot{m}_d \qquad (2\text{-}1)$$

The conservation of momentum is

$$0 = -\nabla P + \mu \nabla^2 \vec{v} \tag{2-2}$$

The conservation of energy is

$$(\rho C_p)(\frac{\partial T}{\partial t} + \vec{v} \cdot \nabla T) = \nabla \cdot (k \nabla T) - \Delta H_{vap} \dot{m}_v \tag{2-3}$$

where ρ is the density, $\vec{v}$ is the convective velocity, D is the diffusion coefficient, $\dot{m}_d$ is the polymer degradation rate, μ is the viscosity, P is the pressure, T is the local temperature, C_p is the heat capacity, k is the thermal conductivity, ΔH_{vap} is the enthalpy of evaporation, and $\dot{m}_v$ is the evaporation rate. These basic governing equations are volume averaged in the next section.

2.2.3 Volume Averaging Governing Equations

2.2.3.1 Volume Averaging Method

The volume averaging method is used to obtain the macroscopic governing equations to describe the thermal debinding process. This method is commonly used in modeling the transport phenomena in porous media (Whitaker, 1977, Jacob, 1989, Kaviany, 1991). The PIM compact is considered as a porous medium that is composed of representative elementary volumes (REV). The representative elementary volume where solid, liquid, and gas phases coexist is shown in Fig. 2.5. This is the smallest differential volume that results in statistically meaningful local average properties (Kaviany, 1991). The macroscopic governing equations are assumed to be valid over the REV.

Unless otherwise specified, the following notations are adopted in the presentation of the governing equations. The subscripts *l* stands for the liquid phase, *g* represents the gas phase, *m* is the solid phase, *sa* is the LMW component, *p* is the HMW component, *f* is the volatile fragments and *i* is the inert gas. The total volume of a REV in the PIM compact is

$$V_{total} = V_m + V_l + V_g \tag{2-4}$$

The volume fractions of the liquid, gas and solid phases, the porosity, the liquid saturation, and the gas saturation can be expressed as

$$\phi_l = \frac{V_l}{V_{total}} \tag{2-5}$$

$$\phi_g = \frac{V_g}{V_{total}} \tag{2-6}$$

$$\varepsilon = \phi_g + \phi_l = 1 - \phi_m \tag{2-7}$$

$$S_l = \frac{\phi_l}{\varepsilon} \tag{2-8}$$

$$S_g = 1 - S_l \tag{2-9}$$

The general tools of the volume averaging method are presented. The phase average is the volume averaging of any quantity Φ for the phase β is defined as

$$\langle \Phi_\beta \rangle = \frac{1}{V} \int_V \Phi_\beta dV \tag{2-10}$$

The intrinsic phase average is the volume averaging of that quantity over the volume occupied by the phase β only, which is

$$\langle \Phi_\beta \rangle^\beta = \frac{1}{V_\beta} \int_V \Phi_\beta dV \tag{2-11}$$

The two averages are related by

$$\langle \Phi_\beta \rangle = \phi_\beta \langle \Phi_\beta \rangle^\beta \tag{2-12}$$

The spatial averaging theorem is

$$\frac{1}{V}\int_V \nabla\Phi_\beta dV = \langle\nabla\Phi_\beta\rangle = \nabla\langle\Phi_\beta\rangle + \frac{1}{V}\int_{A_{l-m}} \vec{n}_{l-m}\Phi_\beta dA + \frac{1}{V}\int_{A_{l-g}} \vec{n}_{l-g}\Phi_\beta dA \tag{2-13}$$

where A_{l-m} and A_{l-g} are the interfacial areas of the liquid-solid interface and the liquid-gas interface, respectively; $\vec{n}_{l-m}$ and $\vec{n}_{l-g}$ represent the unit normal vector directed from the liquid phase towards the solid phase and the gas phase, respectively. The general transport theorem is

$$\begin{aligned}\frac{1}{V}\int_V \frac{\partial\Phi_\beta}{\partial t}dV = \langle\frac{\partial\Phi_\beta}{\partial t}\rangle = \frac{d}{dt}(\frac{1}{V}\int_V \Phi_\beta dV) - \frac{1}{V}\int_{A_{l-m}} \Phi_\beta \vec{w}_n\cdot\vec{n}_{l-m}dA \\ -\frac{1}{V}\int_{A_{l-g}} \Phi_\beta \vec{w}_n\cdot\vec{n}_{l-g}dA\end{aligned} \tag{2-14}$$

where $\vec{w}_n\cdot\vec{n}_{l-m}$ and $\vec{w}_n\cdot\vec{n}_{l-g}$ represent the speeds of displacement for the liquid-solid interface and the liquid-gas interface, respectively.

2.2.3.2 Governing Equations

Based on the basic governing equations in section 2.2.2, the volume averaging equations for the conservation of mass, the conservation of momentum, and the conservation of energy are obtained.

The continuity equations are

$$\varepsilon\frac{\partial\langle\rho_{l,sa}\rangle^{l,sa}S_{l,sa}}{\partial t} + \nabla\cdot(\langle\rho_{l,sa}\rangle^{l,sa}\langle\vec{v}_{l,sa}\rangle) = \nabla\cdot(\langle\rho_{l,sa}\rangle^{l,sa}D_{l,p-sa}\nabla(\theta_{l,sa})) - \langle\dot{m}_{v,sa}\rangle \tag{2-15}$$

$$\varepsilon\frac{\partial\langle\rho_{l,p}\rangle^{l,p}S_{l,p}}{\partial t} + \nabla\cdot(\langle\rho_{l,p}\rangle^{l,p}\langle\vec{v}_{l,p}\rangle) = \nabla\cdot(\langle\rho_{l,p}\rangle^{l,p}D_{l,p-j}\nabla(1-\theta_{l,j})) - \langle\dot{m}_d\rangle \tag{2-16}$$

$$\varepsilon\frac{\partial\langle\rho_{l,f}\rangle^{l,f}S_{l,f}}{\partial t} + \nabla\cdot(\langle\rho_{l,f}\rangle^{l,f}\langle\vec{v}_{l,f}\rangle) = \nabla\cdot(\langle\rho_{l,f}\rangle^{l,f}D_{l,p-f}\nabla(\theta_{l,f})) + \langle\dot{m}_d\rangle - \langle\dot{m}_{v,f}\rangle \tag{2-17}$$

$$\varepsilon \frac{\partial}{\partial t}(S_g \langle \rho_{g,sa} \rangle^g) + \nabla \cdot (\langle \rho_{g,sa} \rangle^g \langle \vec{v}_g \rangle) = \nabla \cdot (\langle \rho_g \rangle^g D_{geff,i-sa} \nabla (\frac{\langle \rho_{g,sa} \rangle^g}{\langle \rho_g \rangle^g})) + \langle \dot{m}_{v,sa} \rangle \quad (2\text{-}18)$$

$$\varepsilon \frac{\partial}{\partial t}(S_g \langle \rho_{g,f} \rangle^g) + \nabla \cdot (\langle \rho_{g,f} \rangle^g \langle \vec{v}_g \rangle) = \nabla \cdot (\langle \rho_g \rangle^g D_{geff,i-f} \nabla (\frac{\langle \rho_{g,f} \rangle^g}{\langle \rho_g \rangle^g})) + \langle \dot{m}_{v,f} \rangle \quad (2\text{-}19)$$

$$\varepsilon \frac{\partial}{\partial t}(S_g \langle \rho_{g,i} \rangle^g) + \nabla \cdot (\langle \rho_{g,i} \rangle^g \langle \vec{v}_g \rangle) = \nabla \cdot (\langle \rho_g \rangle^g D_{geff,i-j} \nabla (\frac{\langle \rho_{g,i} \rangle^g}{\langle \rho_g \rangle^g})) \quad (2\text{-}20)$$

where,

$$\theta_{l,sa} = \frac{S_{l,sa}}{S_{l,p} + S_{l,sa}} \quad (2\text{-}21)$$

$$\theta_{l,f} = \frac{S_{l,f}}{S_{l,p} + S_{l,f}} \quad (2\text{-}22)$$

In Eqs. (2-15) to (2-22), the subscript j indicates the species of LMW component, HMW component or volatile fragments, $\langle \rho_l \rangle^l$ and $\langle \rho_g \rangle^g$ are the volume averaged densities of the liquid and gas phases, $\langle v_l \rangle$ and $\langle \vec{v}_g \rangle$ are the volume averaged convective velocities of the liquid and gas phases, $\langle \dot{m}_v \rangle$ is the volume averaged evaporation rate of the species liquid phase, θ_l is the ratio of volume fraction of the species liquid phase over the solution, $\langle \dot{m}_d \rangle$ is the volume averaged thermal degradation rate, D_l is the binary diffusion coefficient of the solution, and D_{geff} is the effective diffusion coefficient of the total gas phase in porous media.

The momentum equations are

$$\langle \vec{v}_{l,j} \rangle = -\psi_{l,j} \nabla (\langle P_{l,j} \rangle^{l,j}) \quad (2\text{-}23)$$

$$\langle \vec{v}_g \rangle = -\psi_g \nabla (\langle P_{g,t} \rangle^g) \quad (2\text{-}24)$$

where the mobilities of liquid and gas phases are

$$\psi_{l,j} = \frac{KK_{rl,j}}{\mu_{l,j}} \tag{2-25}$$

$$\psi_{g} = \frac{KK_{rg}}{\mu_{g}} \tag{2-26}$$

In Eqs. (2-23) to (2-26), $\langle P_{l,j} \rangle^{l,j}$ is the volume averaged pressure of species liquid phase, $\langle P_{g,t} \rangle^{g}$ is the volume averaged total gas pressure, K is the intrinsic permeability, $K_{rl,j}$ is the relative permeability of species liquid phase, K_{rg} is the relative permeability of total gas phase, $\mu_{l,j}$ is the viscosity of the species liquid phase, and μ_g is the viscosity of the total gas phase.

The energy equation is

$$\begin{aligned}(\rho C_p)_{eff} \frac{\partial \langle T \rangle}{\partial t} + (\varepsilon S_{l,sa} \langle \rho_{l,sa} \rangle^{l,sa} (C_{p,l})_{sa} \langle \vec{v}_{l,sa} \rangle + \varepsilon S_{l,p} \langle \rho_{l,p} \rangle^{l,p} (C_{p,l})_p \langle \vec{v}_{l,p} \rangle \\ + \varepsilon S_{l,f} \langle \rho_{l,f} \rangle^{l,f} (C_{p,l})_f \langle \vec{v}_{l,f} \rangle + \varepsilon S_g \langle \rho_g \rangle^{g} C_{p,g} \langle \vec{v}_g \rangle) \cdot \nabla \langle T \rangle = \nabla \cdot (k_{eff} \nabla \langle T \rangle) \\ - \Delta H_{vap,sa} \langle \dot{m}_{v,sa} \rangle - \Delta H_{vap,f} \langle \dot{m}_{v,f} \rangle\end{aligned} \tag{2-27}$$

where the effective volumetric heat capacity is

$$\begin{aligned}(\rho C_p)_{eff} = (1-\varepsilon)\rho_s C_{p,s} + \varepsilon [S_{l,sa} \langle \rho_{l,sa} \rangle^{l,sa} (C_{p,l})_{sa} + S_{l,p} \langle \rho_{l,p} \rangle^{l,p} (C_{p,l})_p \\ + S_{l,f} \langle \rho_{l,f} \rangle^{l,f} (C_{p,l})_f] + \varepsilon S_g [\langle \rho_{g,sa} \rangle^{g} (C_{p,g})_{sa} + \langle \rho_{g,f} \rangle^{g} (C_{p,g})_f + \langle \rho_{g,i} \rangle^{g} (C_{p,g})_i]\end{aligned} \tag{2-28}$$

In Eqs. (2-27) and (2-28), k_{eff} is the effective thermal conductivity and $\langle T \rangle$ is the volume averaged local temperature.

Remarks:

This completes the formulation of the theoretical model for the thermal debinding process. For the early stage of thermal debinding, which includes the temperature

range between T_0 and T_4 (Fig. 2.2), the equations solved are (1) the liquid LMW component: Eqs. (2-15) and (2-18), (2) the liquid HMW component: Eq. (2-16), (3) the liquid volatile fragments: Eqs. (2-17) and (2-19), (4) the convective velocities: Eqs. (2-23) and (2-24), and (5) the local temperature: Eq. (2-27). Equations (2-15) and (2-18) and Eqs. (2-17) and (2-19) are combined to solve the liquid LMW component and liquid volatile fragments, respectively. The evaporation terms are not shown explicitly. These terms are needed to calculate the latent heat source terms in the energy equation (Eq. 2-27). Using Eqs. (2-18) and (2-19), these terms are calculated after all parameters have been obtained.

For the final stage of thermal debinding, which includes the temperature range between T_4 and T_5, the equations solved are (1) the liquid HMW component: Eq. (2-16), (2) the liquid volatile fragments: Eqs. (2-17) and (2-19), (3) the convective velocities: Eqs. (2-23) and (2-24), (4) the local temperature: Eq. (2-27).

On top of these equations, the following constitutive equations are used. The capillary pressure is related to the liquid phase pressure and the total gas pressure via

$$\langle P_{c,j} \rangle = \langle P_{g,t} \rangle^{g} - \langle P_{l,j} \rangle^{l,j} \tag{2-29}$$

The total gas pressure is the sum of the partial pressures of the species gas phase,

$$\langle P_{g,t} \rangle^{g} = \frac{\langle \rho_{g,sa} \rangle^{g} R\langle T \rangle}{M_{sa}} + \frac{\langle \rho_{g,f} \rangle^{g} R\langle T \rangle}{M_{f}} + \frac{\langle \rho_{g,i} \rangle^{g} R\langle T \rangle}{M_{i}} \tag{2-30}$$

where M is the molecular weight of the species gas phase and R is the universal gas constant. Eqs. (2-15)-(2-20) are the convection-diffusion equations. In the subsequent section, these equations are combined into diffusion equations, which are more stable to be solved numerically.

2.2.3.3 *Combined Governing Equations*

Five characteristic variables are selected to investigate the binder removal via thermal debinding process. These are the liquid saturation of LMW component $S_{l,sa}$, the liquid saturation of HMW component $S_{l,p}$, the liquid saturation of volatile fragments $S_{l,f}$, the total gas pressure $\langle P_{g,t}\rangle^g$, and the local temperature $\langle T\rangle$.

A) Liquid saturation of LMW component

Substituting Eqs. (2-23) to (2-24) and (2-29) to (2-30) into Eqs. (2-15) and (2-18), the combined continuity equation for the liquid LMW component is obtained as

$$\Omega_{sa}\frac{\partial S_{l,sa}}{\partial t}=\nabla\cdot(\Gamma_{sa}\nabla S_{l,sa})+\nabla\cdot(\Gamma_{sa}^{sp}\nabla S_{l,p})+\nabla\cdot(\Gamma_{sa}^{T}\nabla\langle T\rangle)+\nabla\cdot(\Gamma_{sa}^{P}\nabla\langle P_{g,t}\rangle^g)$$
$$+\nabla\cdot(\Gamma_{sa}^{pv}\nabla\langle p_{g,sa}\rangle^g)+\Omega_{sa}^{T}\frac{\partial\langle T\rangle}{\partial t}+\Omega_{sa}^{pv}\frac{\partial\langle p_{g,sa}\rangle^g}{\partial t} \tag{2-31}$$

where,

$$\Omega_{sa}=\varepsilon\langle\rho_{l,sa}\rangle^{l,sa}-\frac{\varepsilon M_{sa}\langle p_{g,sa}\rangle^g}{R\langle T\rangle} \tag{2-32}$$

$$\Omega_{sa}^{T}=\frac{\varepsilon M_{sa}(1-S_l)\langle p_{g,sa}\rangle^g}{R\langle T\rangle^2} \tag{2-33}$$

$$\Omega_{sa}^{pv}=-\frac{\varepsilon M_{sa}(1-S_l)}{R\langle T\rangle} \tag{2-34}$$

$$\Gamma_{sa}=-\langle\rho_{l,sa}\rangle^{l,sa}\psi_{l,sa}\frac{\partial\langle P_{c,sa}\rangle}{\partial S_{l,sa}}+\langle\rho_{l,sa}\rangle^{l,sa}D_{l,p-sa}\left(\frac{1-\theta_{l,sa}}{S_{l,sa}+S_{l,p}}\right) \tag{2-35}$$

$$\Gamma_{sa}^{sp}=-\langle\rho_{l,sa}\rangle^{l,sa}D_{l,p-sa}\left(\frac{\theta_{l,sa}}{S_{l,sa}+S_{l,p}}\right) \tag{2-36}$$

$$\Gamma_{sa}^{T}=-\langle\rho_{l,sa}\rangle^{l,sa}\psi_{l,sa}\frac{\partial\langle P_{c,sa}\rangle}{\partial\langle T\rangle} \tag{2-37}$$

$$\Gamma_{sa}^{P} = \langle \rho_{l,sa} \rangle^{l,sa} \psi_{l,sa} + \frac{M_{sa} \langle p_{g,sa} \rangle^{l,sa}}{R\langle T \rangle} \psi_g - \frac{D_{geff,i-sa} M_{sa}}{R\langle T \rangle} \left(\frac{\langle p_{g,sa} \rangle^{g}}{\langle P_{g,t} \rangle^{g}} \right) \tag{2-38}$$

$$\Gamma_{sa}^{pv} = \frac{D_{geff,i-sa} M_{sa}}{R\langle T \rangle} \tag{2-39}$$

$$S_l = S_{l,p} + S_{l,sa} + S_{l,f} \tag{2-40}$$

The left side of Eq. (2-31) is the changing rate of liquid saturation of LMW component with time over the REV. The first term of the right side is the transport of the liquid LMW component due to the capillary driven action and the binary diffusion in the solution of LMW component and HMW component. The second term of the right side is the binary diffusion in the solution due to the liquid saturation gradient of HMW component. The third term of the right side represents the Marangoni effect, which is the transport of the liquid LMW component due to the surface tension gradient. The fourth and the fifth terms of the right side represent the mass transfers due to the pressure driven action. The sixth and seventh terms of the right side are due to the changing rate of density of the vapor LMW component with time.

B) Liquid saturation of HMW component

Substituting Eqs. (2-23) and (2-29) into Eq.(2-16), the combined continuity equation for the liquid HMW component can be obtained as

$$\begin{aligned} \Omega_{sp} \frac{\partial S_{l,p}}{\partial t} &= \nabla \cdot (\Gamma_{sp} \nabla S_{l,p}) + \nabla \cdot (\Gamma_{sp}^{sj} \nabla S_{l,j}) + \nabla \cdot (\Gamma_{sp}^{T} \nabla \langle T \rangle) \\ &+ \nabla \cdot (\Gamma_{sp}^{P} \nabla \langle P_{g,t} \rangle^{g}) - \langle \dot{m}_d \rangle \end{aligned} \tag{2-41}$$

where,

$$\Omega_{sp} = \varepsilon \langle \rho_{l,p} \rangle^{l,p} \tag{2-42}$$

$$\Gamma_{sp} = -\langle \rho_{l,p} \rangle^{l,p} \psi_{l,p} \frac{\partial \langle P_{c,p} \rangle}{\partial S_{l,p}} + \langle \rho_{l,p} \rangle^{l,p} D_{l,p-j} \left(\frac{\theta_{l,j}}{S_{l,p} + S_{l,j}} \right) \tag{2-43}$$

$$\Gamma_{sp}^{sj} = -\frac{\langle \rho_{l,p} \rangle^{l,p} D_{l,p-j}(1-\theta_{l,j})}{(S_{l,p}+S_{l,j})^2} \tag{2-44}$$

$$\Gamma_{sp}^{T} = -\langle \rho_{l,p} \rangle^{l,p} \psi_{l,p} \frac{\partial \langle P_{c,p} \rangle}{\partial \langle T \rangle} \tag{2-45}$$

$$\Gamma_{sp}^{P} = \langle \rho_{l,p} \rangle^{l,p} \psi_{l,p} \tag{2-46}$$

The meanings of the terms in Eq. (2-41) are the same as those in Eq. (2-31).

C) Liquid saturation of volatile fragments

Combining Eqs. (2-23) to (2-24) and (2-29) to (2-30) into Eqs. (2-17) and (2-19), the combined continuity equation for the liquid volatile fragments can be obtained as

$$\begin{aligned} \Omega_{sf} \frac{\partial S_{l,f}}{\partial t} &= \nabla \cdot (\Gamma_{sf} \nabla S_{l,f}) + \nabla \cdot (\Gamma_{sf}^{sp} \nabla S_{l,p}) + \nabla \cdot (\Gamma_{sf}^{T} \nabla \langle T \rangle) + \nabla \cdot (\Gamma_{sf}^{P} \nabla \langle P_{g,t} \rangle^{g}) \\ &+ \nabla \cdot (\Gamma_{sf}^{pv} \nabla \langle p_{g,f} \rangle^{g}) + \Omega_{sf}^{sp} \frac{\partial S_{l,p}}{\partial t} + \Omega_{sf}^{T} \frac{\partial \langle T \rangle}{\partial t} + \Omega_{sf}^{pv} \frac{\partial \langle p_{g,f} \rangle^{g}}{\partial t} + \langle \dot{m}_{d} \rangle \end{aligned} \tag{2-47}$$

where,

$$\Omega_{sf} = \varepsilon \langle \rho_{l,f} \rangle^{l,f} - \frac{\varepsilon M_f \langle p_{g,f} \rangle^{g}}{R \langle T \rangle} \tag{2-48}$$

$$\Omega_{sf}^{sp} = \frac{\varepsilon M_f \langle p_{g,f} \rangle^{g}}{R \langle T \rangle} \tag{2-49}$$

$$\Omega_{sf}^{T} = \frac{\varepsilon M_f (1-S_l) \langle p_{g,f} \rangle^{g}}{R (\langle T \rangle)^2} \tag{2-50}$$

$$\Omega_{sf}^{f} = -\frac{\varepsilon M_f (1-S_l)}{R \langle T \rangle} \tag{2-51}$$

$$\Gamma_{sf} = -\langle \rho_{l,f} \rangle^{l,f} \psi_{l,f} \frac{\partial \langle P_{c,f} \rangle}{\partial S_{l,f}} + \langle \rho_{l,f} \rangle^{l,f} D_{l,p-f} \left(\frac{1-\theta_{l,f}}{S_{l,p}+S_{l,f}} \right) \tag{2-52}$$

$$\Gamma_{sf}^{sp} = -\frac{\langle \rho_{l,f} \rangle^{l,f} D_{l,p-f} \theta_{l,f}}{(S_{l,p}+S_{l,f})^2} \tag{2-53}$$

$$\Gamma_{sf}^{T} = -\langle \rho_{l,f} \rangle^{l,f} \psi_{l,f} \frac{\partial \langle P_{c,f} \rangle}{\partial \langle T \rangle} \tag{2-54}$$

$$\Gamma_{sf}^{P} = \langle \rho_{l,f} \rangle^{l,f} \psi_{l,f} + \frac{M_f \langle p_{g,f} \rangle^{g}}{R\langle T \rangle} \psi_g - \frac{D_{geff,i-f} M_f}{R\langle T \rangle} \left(\frac{\langle p_{g,f} \rangle^{g}}{\langle P_{g,t} \rangle^{g}} \right) \tag{2-55}$$

$$\Gamma_{sf}^{pv} = \frac{D_{geff,i-f} M_f \langle p_{g,f} \rangle^{g}}{R\langle T \rangle} \tag{2-56}$$

Again, the meanings of the terms in Eq. (2-47) are the same as those in Eq. (2-31).

D) Total gas pressure of gas phase

Substituting Eqs. (2-24) and (2-30) into Eq. (2-20), the combined continuity equation for the total gas pressure can be obtained as

$$\begin{aligned} \Omega_P \frac{\partial \langle P_{g,t} \rangle^{g}}{\partial t} &= \nabla \cdot (\Gamma_P \nabla \langle P_{g,t} \rangle^{g}) + \nabla \cdot (\Gamma_P^{sa} \nabla \langle p_{g,sa} \rangle^{g}) + \nabla \cdot (\Gamma_P^{f} \nabla \langle p_{g,f} \rangle^{g}) \\ &+ \Omega_P^{S} \frac{\partial S_l}{\partial t} + \Omega_P^{T} \frac{\partial \langle T \rangle}{\partial t} + \Omega_P^{f} \frac{\partial \langle p_{g,f} \rangle^{g}}{\partial t} + \Omega_P^{sa} \frac{\partial \langle p_{g,sa} \rangle^{g}}{\partial t} \end{aligned} \tag{2-57}$$

where,

$$\Omega_P = \frac{\varepsilon M_i (1 - S_l)}{R\langle T \rangle} \tag{2-58}$$

$$\Omega_P^{S} = \frac{\varepsilon M_i \langle p_{g,i} \rangle^{g}}{R\langle T \rangle} \tag{2-59}$$

$$\Omega_P^{T} = \frac{\varepsilon M_i (1 - S_l) \langle p_{g,i} \rangle^{g}}{R(\langle T \rangle)^2} \tag{2-60}$$

$$\Omega_P^{sa} = \frac{\varepsilon M_i (1 - S_l)}{R\langle T \rangle} \tag{2-61}$$

$$\Omega_P^{f} = \frac{\varepsilon M_i (1 - S_l)}{R\langle T \rangle} \tag{2-62}$$

$$\Gamma_P = \frac{M_i \langle p_{g,i} \rangle^{g}}{R\langle T \rangle} \psi_g + \frac{D_{geff,i-f} M_i}{R\langle T \rangle} \left(\frac{\langle p_{g,f} \rangle^{g}}{\langle P_{g,t} \rangle^{g}} \right) \tag{2-63}$$

$$\Gamma_P^{sa} = -\frac{D_{geff,i-j} M_i}{R\langle T \rangle} \tag{2-64}$$

$$\Gamma_P^{f} = -\frac{D_{geff,i-j} M_i}{R\langle T \rangle} \tag{2-65}$$

$$\langle p_{g,i} \rangle^g = \langle P_{g,t} \rangle^g - \langle p_{g,sa} \rangle^g - \langle p_{g,f} \rangle^g \tag{2-66}$$

The meanings of the terms are the same as those in Eq. (2-31).

E) Total energy equation

The total energy equation is given by Eqs. (2-27).

Remarks:

For the early stage of thermal debinding, which includes the temperature range between T_0 and T_4, Eqs. (2-31), (2-41), (2-47), (2-57), and (2-27) are solved. For the final stage of thermal debinding, which includes the temperature range between T_4 and T_5, Eqs. (2-41), (2-47), (2-57), and (2-27) are solved.

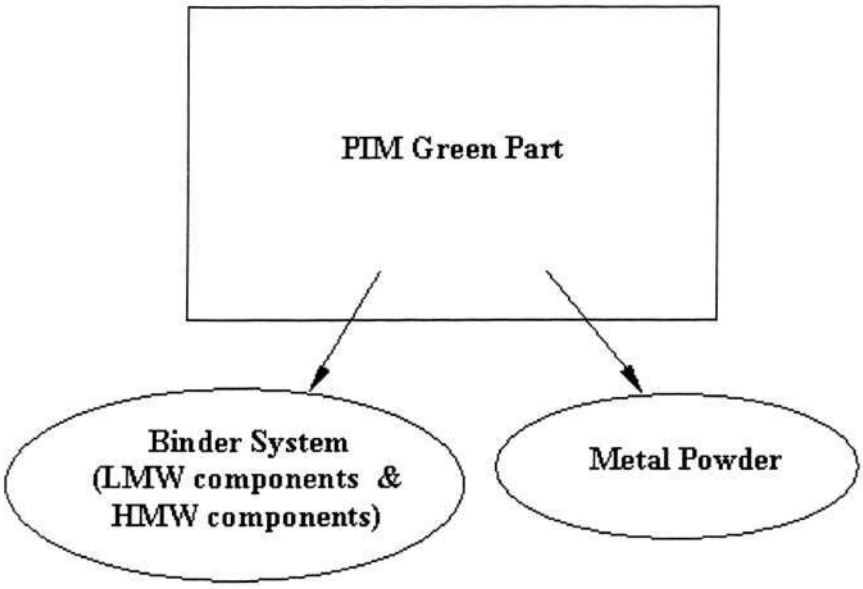

Figure 2.1 PIM compact

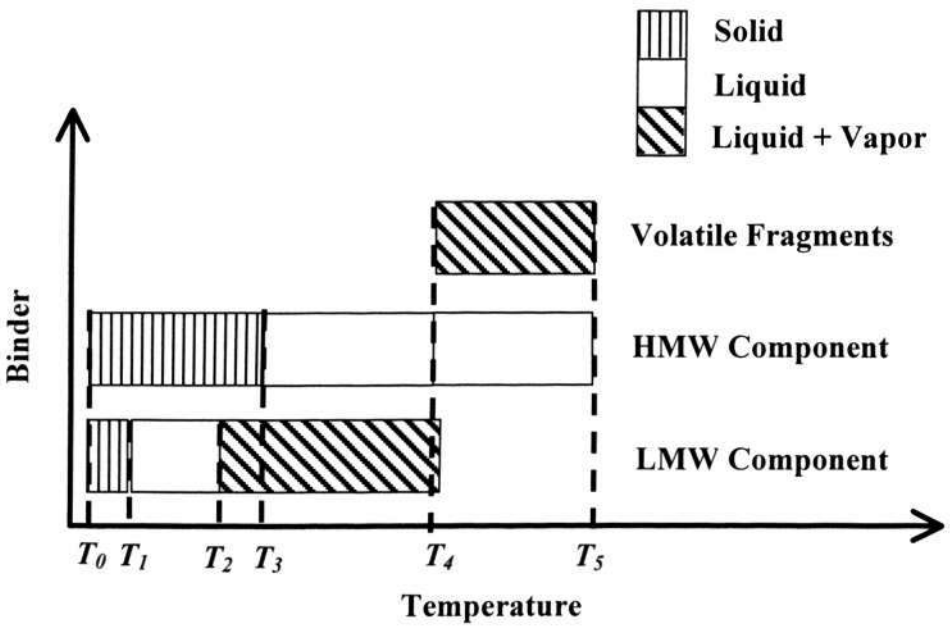

Figure 2.2 Phase changes of binders during thermal debinding

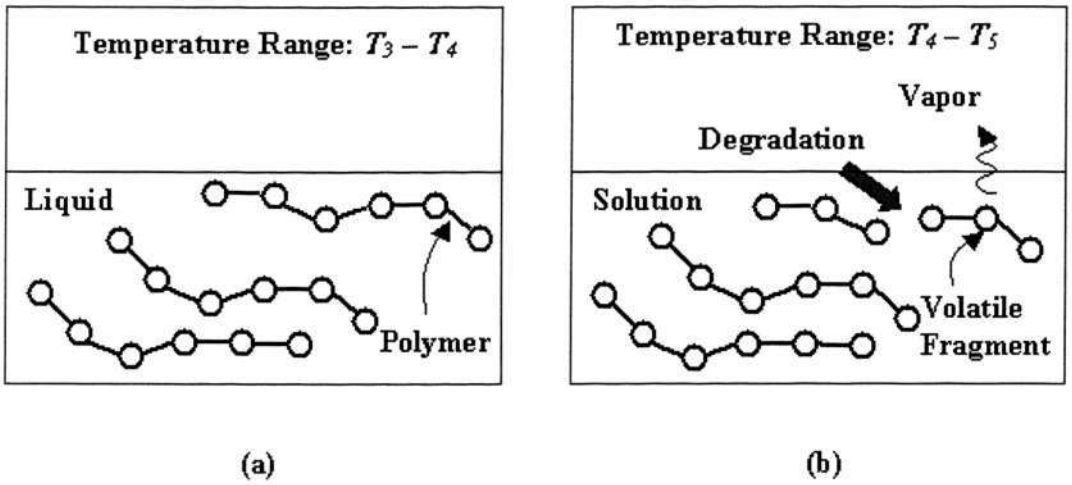

Figures 2.3 Liquid Polymer at (a) Temperature Range: $T_3 - T_4$ and (b) Temperature Range: $T_4 - T_5$

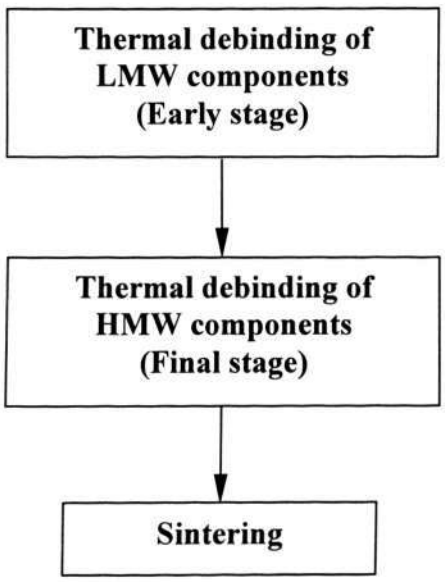

Figure 2.4 Thermal debinding of multi-component binder system

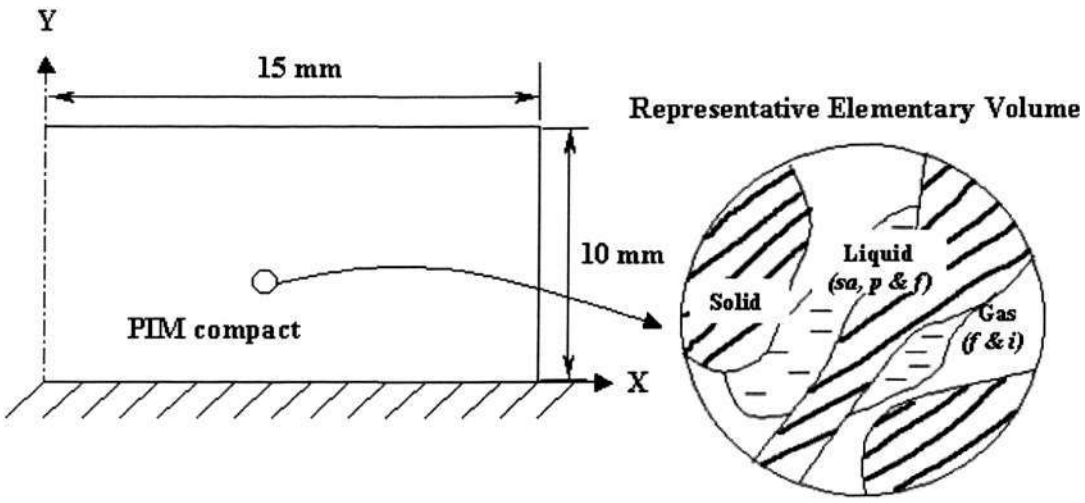

Figure 2.5 Computation domain and representative elementary volume

CHAPTER 3

NUMERICAL METHOD

In this chapter, the numerical method used in the simulation is described. In section 3.1, the general form of the governing equations is presented. The Finite Volume Method is described in section 3.2. The discretization of the Partial Differential Equations is discussed in section 3.3. In section 3.4, the underrelaxation for nonlinear problems is presented. The boundary conditions are discussed in section 3.5.

3.1 Governing Equations

As presented in section 2.2.3.3, the governing equations of the thermal debinding process are derived as unsteady diffusion equations. These equations are the liquid saturation of LMW component (Eq. 2-31), the liquid saturation of HMW component (Eq. 2-41), the liquid saturation of volatile fragments (Eq. 2-47), the total gas pressure (Eq. 2-57), and the energy equation (Eq. 2-27). The general form of the governing equations (differential equations) can be written as

$$\underbrace{\frac{\partial(\rho\Phi)}{\partial t}}_{Transient} = \underbrace{\frac{\partial}{\partial x_i}\left(\Gamma \frac{\partial \Phi}{\partial x_i}\right)}_{Diffusion} + \underbrace{\underset{\sim}{S}}_{Source} \tag{3-1}$$

where ρ, Φ, Γ and S are the density, the dependent variable, the diffusion coefficient, and the source term, respectively. These governing equations are solved using Finite Volume Method (Patankar, 1980) which is discussed briefly in the following sections.

3.2 Finite Volume Method

Finite Volume Method is also called as control volume method. In Finite Volume Method, the domain is divided into a number of control volumes. The control volume

is surrounding by grid points. The grid points are located in the center of control volume. The governing equation is integrated over each control volume to derive a discretization equation with values of Φ. This discretization equation expresses the conservation principle for Φ for the finite control volume.

Typical two-dimensional cartesian control volume are presented in Fig. 3.1. The control volume interface is subdivided into four plane faces for two-dimensional problem, which are denoted by lower case letters with corresponding to their direction (*e*, *w*, *n*, and *s*) with respect to the central grid point *P*. The neighbor grid points are denoted by upper case letters *E*, *W*, *N*, and *S*.

3.3 Discretization

The discretization equation is an algebraic equation that involves the unknown values of Φ at the grid points. For a diffusion equation, the total flux (diffusive flux) through a control volume interface is

$$J_i = \Gamma \frac{\partial \Phi}{\partial x_i} \tag{3-2}$$

The two-dimensional form of Eq. (3-1) can be written as

$$\rho C_p \frac{\partial \Phi}{\partial t} = \frac{\partial J_i}{\partial x_i} + S \tag{3-3}$$

Using fully implicit scheme, the integration of Eq. (3-3) over a control volume (Fig. 3.1) is

$$\rho C_p (\Phi_P - \Phi_P{}^0)\Delta x \Delta y = (J_e - J_w)\Delta y \Delta t + (J_n - J_s)\Delta x \Delta t + S \Delta x \Delta y \Delta t \tag{3-4}$$

where Φ_P and $\Phi_P{}^0$ are the valuables that going to be solved at present time step and previous time step, and J_e, J_w, J_n, and J_s are the integrated total flux through control volume interfaces. The linearization of the source terms in Eq. (3-3) can be done as

$$S = S_C + S_P \Phi_P \tag{3-5}$$

where S_C is the constant and S_P is the coefficient. In this simulation, linear interpolation scheme is implemented; the value at control volume interface center is assumed to be linear interpolation of two grid points (Fig. 3.2). The assumption of linear profile between grid points P and E can provide a simple approximation of the gradient,

$$\left(\frac{\partial \Phi}{\partial x}\right)_e \approx \frac{\Phi_E - \Phi_P}{(\delta x)_e} \tag{3-6}$$

To obtain the interface diffusion coefficient Γ_e, the flux at the interface is considered as

$$J_e = \frac{\Gamma_e (\Phi_P - \Phi_E)}{(\delta x)_e} \tag{3-7}$$

The linear interpolation in the interface e can be expressed as

$$\Gamma_e = f_e \Gamma_P + (1 - f_e)\Gamma_E \tag{3-8}$$

where length ratio f_e is

$$f_e = \frac{(\delta x)_{e+}}{(\delta x)_e} \tag{3-9}$$

Considering the diffusion coefficients of the grid points P and E, Eq. (3-7) can be written as

$$J_e = \frac{\Phi_P - \Phi_E}{\frac{(\delta x)_{e-}}{\Gamma_P} + \frac{(\delta x)_{e+}}{\Gamma_E}} \tag{3-10}$$

Using Eqs. (3-7), (3-9), and (3-10), the effective diffusion coefficient at the interface can be obtained,

$$\Gamma_e = \left(\frac{1-f_e}{\Gamma_P} + \frac{f_e}{\Gamma_E}\right)^{-1} \tag{3-11}$$

The interface e placed in the middle between P and E gives value of $f_e = 0.5$. As such, Eq. (3-11) becomes

$$\Gamma_e = \frac{2\Gamma_P \Gamma_E}{\Gamma_P + \Gamma_E} \tag{3-12}$$

Equation (3-12) shows Γ_e as the harmonic mean of Γ_P and Γ_E. The similar analysis (Eqs. 3-6 to 3-12) can be done for grid points W, N, and S. The discretizition equation (3-4) can be written as a general form of

$$a_P \Phi_P = a_E \Phi_E + a_W \Phi_W + a_N \Phi_N + a_S \Phi_S + b \tag{3-13}$$

where

$$a_E = \frac{\Gamma_e \Delta y}{(\delta x)_e} \tag{3-14}$$

$$a_W = \frac{\Gamma_w \Delta y}{(\delta x)_w} \tag{3-15}$$

$$a_N = \frac{\Gamma_n \Delta x}{(\delta x)_n} \tag{3-16}$$

$$a_S = \frac{\Gamma_s \Delta x}{(\delta x)_s} \tag{3-17}$$

$$a_P^0 = \frac{\rho c_p \Delta x \Delta y}{\Delta t} \tag{3-18}$$

$$a_P = a_E + a_W + a_N + a_S - S_P \Delta x \Delta y \Delta z \tag{3-19}$$

$$b = S_C \Delta x \Delta y + a_P^0 \Phi_P^0 \tag{3-20}$$

where $\Delta x, \Delta y, \Delta z$ are the distances between control volume interfaces, and $\delta x, \delta y, \delta z$ are the distances between grid points.

3.4 Underrelaxation For Nonlinear Problems

The governing equations (Eqs. 2-27, 2-31, 2-41, 2-47, and 2-57) involve a number of coefficients that are the functions of the variables. As a result, the derived discretization equations are highly nonlinear equations. These nonlinear equations can be solved using an iterative method. The coefficients in the discretized equations are calculated by substituting the guessing or estimating variable values (initial values). New variable values are calculated by solving the linearized algebraic equations. The coefficients are recalculated using the new values to solve the discretized equations again. This process is repeated until the convergent results are obtained.

During the iteration process, a divergent solution might be obtained. To avoid divergence, the underrelaxation method is used to slow down the changes of solution from iteration to iteration. On the *N*th iteration, the algebraic equation for general variable Φ_P can be written

$$a_P \Phi_P^N = \sum a_{nb} \Phi_{nb}^N + b \tag{3-21}$$

$$\Phi_P^N = \frac{\sum a_{nb} \Phi_{nb}^N + b}{a_P} \tag{3-22}$$

where subscript *nb* is the neighbor point. An underrelaxation method can be written

$$\Phi_P^N = \Phi_P^{N-1} + \Theta(\Phi_P^N - \Phi_P^{N-1}) \tag{3-23}$$

where Θ is the underrelaxation factor ($0 < \Theta \leq 1$). Substituting Eq (3-22) into Eq. (3-23) gives

$$\frac{a_P}{\Theta}\Phi_P^N = \sum a_{nb}\Phi_{nb}^N + b + (1-\Theta)\frac{a_P}{\Theta}\Phi_P^{N-1} \tag{3-24}$$

The optimum underrelaxation factor Θ is problem dependent. Underrelaxation can be used in other terms in the equations, such as viscosity, density, boundary fluxes, and etc.

3.5 Boundary Conditions

Boundary conditions are needed to solve the algebraic equations. The boundary values can be given as (1) given boundary values, (2) given boundary fluxes, and (3) boundary fluxes expressed as the function of variables and coefficients.

If the boundary values are given, the equations can be solved directly. For boundary fluxes, the boundary conditions can be added into the source terms. The appropriate coefficients of the discretized equations are set to zero to disconnect the boundary side with the internal grid points. The boundary fluxes are modified and introduced into source terms S_C and S_P. For example, if the flux is given (see Fig. 3.3 (a)), the extra source term is

$$S_{extra} = \frac{q_B(area)}{volume} \tag{3-25}$$

where $S_{C,extra} = S_{extra}$ and $S_{P,extra} = 0$.

If the diffusion coefficient Γ is given or can be calculated (see Fig. 3.3(b)), the extra source term is

$$q_B = \frac{\phi_B - \phi_P}{\delta/\Gamma} \tag{3-26}$$

$$S_{extra} = \frac{q_B(area)}{volume} = \frac{\phi_B}{\delta/\Gamma}\frac{(area)}{(volume)} + (\frac{-1}{\delta/\Gamma})\frac{(area)}{(volume)}\phi_P \qquad (3\text{-}27)$$

where $S_{C,extra} = \frac{\phi_B}{\delta/\Gamma}\frac{(area)}{(volume)}$ and $S_{P,extra} = \frac{-1}{\delta/\Gamma}\frac{(area)}{(volume)}$.

3.6 Convergence Criteria

The solution is deemed converged with the difference in the values of a given variable between two successive iterations is less than a prescribed tolerance. The convergence criteria for all grid points are tabulated in Table 3.1.

Table 3.1 Convergence criteria

Valuables	Convergence Criteria
Temperature	1.0×10^{-6}
Liquid saturation of polymeric binder	1.0×10^{-5}
Liquid saturation of volatile fragment	1.0×10^{-9}
Liquid saturation of stearic acid	1.0×10^{-7}
Total gas pressure	1.0×10^{-3} & 1.0×10^{-1}

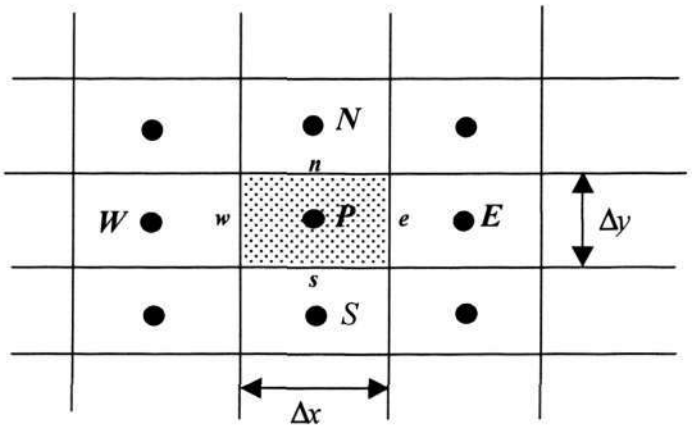

Figure 3.1 Typical control volume and notation used for two-dimensional grid in Cartesian coordinate system

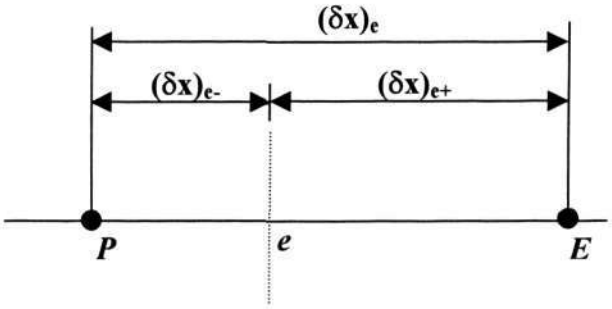

Figure 3.2 Distances related with the interface *e*

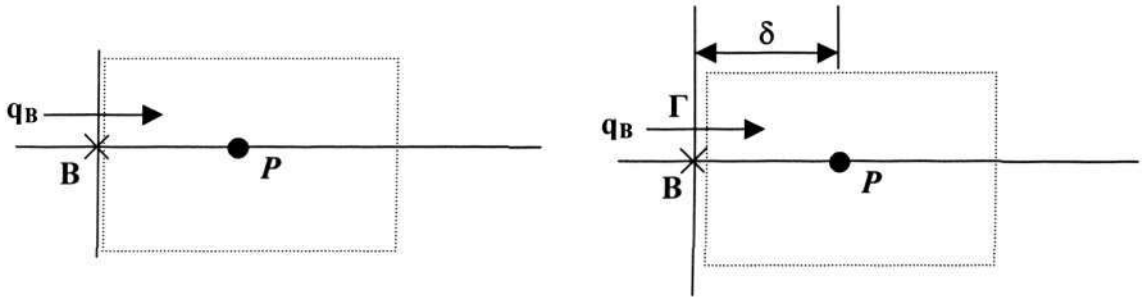

(a) (b)

Figure 3.3 Flux boundary conditions

CHAPTER 4

EXPERIMENTAL METHODS

Experiments were carried out to investigate the binder distributions during the thermal debinding process of the HMW component and the LMW component. In this Chapter, the materials and the experimental approaches are presented in sections 4.1 and 4.2 respectively. TGA behaviours of the materials and homogeneity of the green parts are presented in sections 4.3 and 4.4 respectively. In section 4.5, an error analysis of the experimental results is described.

4.1 Materials

Carbonyl iron was chosen as the metal powder. It is ideal for PIM process due to its small particle size and nearly spherical shape (Lin and German, 1989). Firstly, the thermal debinding of HMW component was investigated, in which PP was used as the polymeric binder. It was chosen due to its popular usage in commercial binder (German, 1990). In investigating the thermal debinding of LMW component, SA was used as the LMW component in a two-component binder system, which consists of PP and SA. However, only the removal of the SA was studied. SA is often employed in commercial binders as a powder wetting agent to improve the molding properties of feedstock (Angermann and Van Der Biest, 1993). This binder system was selected due to its distinct differences in the degradation temperatures of SA and PP. This allows the separate investigation of their content inside the PIM compacts. The materials used are listed in Table 4.1.

Table 4.1 Materials used in this work

Materials	Manufacturer
Carbonyl iron	BASF
Polypropylene (PP)	HMC Polymer
Stearic acid (SA)	MERCK

4.2 Experimental Approaches

Sample preparation involved mixing, compression molding, thermal debinding of the green parts, and sectioning of the brown parts. The brown parts were the debound green parts after thermal debinding. Through thermogravimetric analysis (TGA), the homogeneity of the green parts and the residual binder contents inside the brown parts were evaluated.

4.2.1 Mixing

Carbonyl iron metal powder and the binders were mixed to produce the feedstocks. A Haake Rheocord 90 Torque Mixer (Fig. 4.1) was used for the mixing.

To investigate the thermal debinding of the HMW component, green parts with a single component binder system were produced. Carbonyl iron metal powder and PP were mixed with a volume fraction ratio of 0.6: 0.3. Thus, there was 10 vol% of porosity inside the green parts. The mixing temperature was 200 °C with a motor speed of 40 rpm. PP was first melted in the mixing chamber. Subsequently, the metal

powder was put into the chamber in small quantity each time for more homogeneous mixing.

To investigate the thermal debinding of LMW component, green parts with a two-component binder system were produced. Carbonyl iron metal powder, PP, and SA were mixed with a volume fraction ratio of 0.60: 0.24: 0.16, respectively. The mixing temperature was 175 °C with a motor speed of 40 rpm. To minimize vaporization of SA, PP was first melted in the mixer. Subsequently, the carbonyl iron metal powder and SA were added into the mixer alternately in small quantity.

The mixing process was conducted until the motor torque stabilized (about 15-30 minutes) in order to produce a homogenous feedstock. After this, the feedstock was taken out in the molten state for immediate compression molding.

4.2.2 Compression Molding

During the mixing process, the mold and the punch (Fig. 4.2) were preheated to 230 °C in a furnace. After mixing, the molten feedstock was instantly transferred to the mold and covered with the punch. The mold and punch were then pressed with a hot press machine (Fig. 4.3) for 5 minutes. The purpose of compression molding the feedstocks in molten form was to shorten the processing period. This would minimise the binder lost due to the degradation of PP and the vaporization of SA. After this, PIM green parts with dimension $10 \times 30 \times 100$ mm^3 were produced for subsequent thermal debinding. The compression molding parameters for producing the PIM green parts are shown in Table 4.2.

Table 4.2 Parameters of compression molding

Binder System	Preheat temperature of mold and punch (°C)	Molding temperature (°C)	Molding Pressure (KPa)
Single Component	230	200	700
Two-Component	200	175	700

4.2.3 Thermal Debinding

A Lenton UAF 15/27 high temperature general-purpose chamber furnace (Fig. 4.4) was used to heat the green parts and to remove the binders from them.

For the thermal debinding of HMW component, a heating rate of 1°C/min was applied. For each run of the thermal debinding process, a PIM green part was heated from room temperature to the desired temperature. Nitrogen gas was supplied into the furnace at a constant flow rate (4 litre/min) to carry away the vapor of the binder from the furnace. After the desired temperature was reached, the furnace was cooled down at a rate of 10 °C/min. Before the PIM green part was taken out for measurements of its residual binder content, it was cooled for around 1-2 hours under a constant supply of nitrogen gas. This step was to remove the vapor inside the furnace and for ease of sample handling. A thermocouple was inserted into the furnace at a distance of 1-2 cm above the green part to measure the debinding temperature (see Fig. 4.5). This measured temperature is an approximation of the surface temperature of the green part. The bottom portion of the green part was wrapped with an adhesive aluminium foil with height about 0.5 mm and fitted into a cavity of aluminium plate with 0.3 mm deepness as shown in Fig. 4.6. This step was to minimize the binder loss from the bottom of the green part, such that it resembled closely an impermeable wall boundary condition.

This is to ensure that the simulated boundary conditions matched well with the experimental boundary conditions.

Almost similar procedures as that stated above were applied for investigating the thermal debinding of LMW component. However, there were some differences. Instead of using a constant heating rate, a multi-segment heating rate as shown in Table 4.3 was used. Furthermore, the green part was put in an aluminium container for supporting purpose as depicted in Fig. 4.7. Except for the top surface, the other five outer surfaces of a green part were approximated as impermeable walls by wrapping adhesive aluminium foils over them. As such, there was only mass transfer across the top surface of the green part during the thermal debinding of LMW component. In this thesis, green parts with 10 mm thickness were used. This thickness is considered large for a conventional PIM process. Normally, samples with thickness of 1-5 mm were used (Angermann et al., 1992, Shaw et al., 1993, Liu and Tseng, 1997, Li et al., 2003). However, this thickness was considered necessary in order to provide the required resolution for the investigation of the binder distributions inside the PIM green parts. With this relative large thickness, the original shape of the green parts were difficult to be maintained after both of the LMW and HMW components were melted. As a result, an aluminium container was used to support the PIM green parts.

Table 4.3 Heating schedule for thermal debinding of LMW component

No	Temperature range (K)	Heating ramp (K/min)	Holding time (min)
1	300-473	2	60
2	473-493	1	20
3	493-503	1	20
4	503-513	1	20
5	513-523	1	20
6	523-533	1	20
7	533-543	1	20
8	543	-	90

4.2.4 Sample Cutting

Brown parts were sectioned into 5 equal parts with the aid of a diamond blade cutter (see Fig. 4.8). In sectioning the brown parts, water instead of a chemical coolant was used as the coolant to avoid chemical contamination of the brown parts, which could have an effect on the determination of the binder distributions. The brown part sections were then placed inside a vacuum oven overnight to remove moisture, which might cause the brown parts to be rusty. For two-dimensional analysis, the shaded brown section, which is the center section (Fig. 4.8), was selected for the investigation on the binder distributions of the brown parts. It was cut into 20 samples corresponding to their identified locations as shown in Fig. 4.9. The sample cutting was accomplished with cutters and wood carving tools. Care was exercised in cutting the brown part sections to obtain samples with precisely identified location. Following this, the samples were analyzed with the TGA equipment to measure their residual binder content in order to obtain the binder distributions of the brown part sections.

4.2.5 Thermogravimetric Analysis (TGA)

Thermogravimetric Analysis (TGA) is a thermal analysis technique to measure changes in the weight of a sample as a function of temperature and/or time. The Hi-Res Modulated TGA 2950 Thermogravimetric Analyzer (Fig. 4.10) was employed. The homogeneity of the green parts and the binder distributions in the brown parts could be determined by TGA. Before these analyses, the TGA machine was evaluated with the individual materials and the PIM feedstocks in order to study their TGA behaviours.

4.3 TGA Behaviour of the Materials

4.3.1 Individual Materials Before Mixing

A heating rate of 30 °C/min and a nitrogen flow rate of 80 ml/min were used. For PP, the temperature range for the TGA test was 35-550 °C. As depicted in Fig. 4.11, PP starts to degrade around 350 °C and degrades totally after 500 °C. For the temperature range of 35-350 °C, SA starts vaporizing around 180 °C and is thoroughly removed at around 300 °C (see Fig. 4.12).

For carbonyl iron metal powder, weight gains were observed after 200 °C during TGA testing for the temperature range of 35-550 °C (see Fig. 4.13). The weight gain of carbonyl iron was probably due to imperfect sealing of the TGA instrument which allowed a slight oxidation of the sample (Chung et al., 1989). In this study, every first TGA test was conducted on an empty sample pan with higher nitrogen flow rate (120 ml/min). In addition, the samples were purged about 5 minutes before every TGA test. These precautionary steps were to purge away any entrapped oxygen inside the TGA

equipment to minimize oxidation and to maintain consistency of the test results. Table 4.4 shows the weight gain of the metal powder after these precautionary steps were taken. As shown in Table 4.4, the average weight gain is 0.20 wt% and the weight gains of the metal powder are consistent during the TGA analysis.

Table 4.4 Weight gain of carbonyl iron metal powder

Sample	Weight gain (wt %)
1	0.1914
2	0.1999
3	0.2059
Average	0.1991

4.3.2 Feedstocks

The TGA behaviours of the PIM feedstocks with a single component binder system and two-component binder system were studied.

Based on the volume ratio of the materials, the PIM green parts with a single component binder system were estimated to contain 5.50 wt % of PP. Three batches of feedstock were tested with TGA (see Fig. 4.14) and the average binder content was approximately 5.40 wt % as shown in Table 4.5. This is fairly close to the theoretical estimation. The deviation is less than 2 %.

Table 4.5 Single component: Binder content of the feedstocks

Test	Sample 1 (wt%)	Sample 2 (wt%)	Sample 3 (wt%)
(a)	5.402	5.359	5.385
(b)	5.464	5.490	5.365
(c)	5.433	5.398	5.366
Average	5.433	5.416	5.372

Isothermal heating at 300 °C for 10 minutes was used to remove all the SA before the PP started degrading during the TGA testing of the two-component binder system (see Fig. 4.15). As such, the weight loss regions could be distinguished between the PP and the SA. Based on the composition, the PIM green parts with two-component binder system were estimated containing 4.34 wt % of PP and 2.70 wt % of SA, respectively. Table 4.6 shows that the average binder content was approximately 4.40 wt% of PP and 2.45 wt % of SA. The lower SA content of the samples was possibly due to its vaporization during mixing and compression molding. Taking account of this inevitable binder loss, homogeneous feedstocks with a two-component binder system were produced.

Table 4.6 Two Component: Binder content of the feedstocks

Test	Sample 1 (wt%)		Sample 2 (wt%)		Sample 3 (wt%)	
(a)	2.394	4.322	2.498	4.355	2.520	4.404
(b)	2.387	4.430	2.462	4.389	2.455	4.469
(c)	2.397	4.381	2.486	4.388	2.469	4.436
Average	2.393	4.378	2.482	4.377	2.481	4.436

4.4 Homogeneity Test of the PIM Green Part

4.4.1 Single component binder system

The homogeneity of a PIM green part is essential to ensure that its binder distribution is uniform before the thermal debinding process. In this section, three PIM green parts were investigated on their homogeneity. For each PIM green part, 10 samples were taken out randomly and TGA analysis was carried out to measure their binder content.

The mean of the binder content of the green part $\overline{Y}_{GP}$ and the standard deviation of the mean (SDOM) $\delta\overline{Y}_{GP}$ were calculated (see Table 4.7) as

$$\overline{Y}_{GP} = \frac{\sum_{h=1}^{N} Y_{GP,h}}{N} \tag{4-1}$$

$$\delta\overline{Y}_{GP} = \sqrt{\frac{\frac{1}{N-1}\sum_{h=1}^{N}(Y_{GP,h} - \overline{Y}_{GP})^2}{N}} \tag{4-2}$$

In Eqs. (4-1) and (4-2), h denotes number of measurement conducted and N represents the total number of measurement conducted. The mean and SDOM of these three

green parts were used to estimate the weighted average $Y_{GP,avg}$ and its uncertainty $\delta Y_{GP,avg}$ (Taylor, 1997). These are

$$Y_{GP,avg} = \frac{\sum \frac{\overline{Y}_{GP,h}}{(\delta \overline{Y}_{GP,h})^2}}{\sum \frac{1}{(\delta \overline{Y}_{GP,h})^2}} \tag{4-3}$$

$$\delta Y_{GP,avg} = \frac{1}{\sqrt{\sum \frac{1}{(\delta \overline{Y}_{GP,h})^2}}} \tag{4-4}$$

In calculating the weighted average and its uncertainty (Eqs. (4-3) to (4-4)), $h = 3$ since three green parts were considered. This weighted average was considered as a best estimate of the binder content for the PIM green parts. Based on Table 4.7, the best estimate of the binder content was 5.430 ± 0.010 wt %. With this small uncertainty, the prepared green parts were considered homogeneous. However, the results in Table 4.7 show deviations in binder content for each green part. To maintain the consistency of the binder content, each batch of the feedstocks was mixed to produce only one green part. The average binder content for each batch was used for the corresponding PIM green part as its initial binder content.

Table 4.7 Single component: Binder content of the PIM green parts

Test	Sample 1 (wt %)	Sample 2 (wt %)	Sample 3 (wt %)
(a)	5.437	5.349	5.393
(b)	5.433	5.403	5.352
(c)	5.483	5.413	5.107
(d)	5.492	5.477	5.341
(e)	5.467	5.447	5.226
(f)	5.367	5.466	5.438
(g)	5.456	5.457	5.376
(h)	5.493	5.480	5.322
(i)	5.41	5.482	5.177
(j)	5.373	5.414	5.359
Mean, $\overline{Y}_{GP,i}$	5.441	5.439	5.309
SDOM, $\delta\overline{Y}_{GP,i}$	0.015	0.014	0.033

4.4.2 Two-component binder system

The homogeneity test was conducted on the PIM green parts with two-component binder system before thermal debinding process. The mean, the standard deviation of the mean (SDOM), the weighted average, and its uncertainty were calculated using Eqs. (4-1) to (4-4).

Based on Table 4.8, the best estimate of the binder content for the prepared green part was estimated to be 2.540 ± 0.010 wt % and 4.380 ± 0.010 wt % for the SA and the PP, respectively. The homogeneous green parts with two-component binder system were prepared similarly to the single component system.

Table 4.8 Two-component: Binder content of the PIM green parts

Test	Sample 1 (wt %)		Sample 2 (wt %)		Sample 3 (wt %)	
	SA	PP	SA	PP	SA	PP
(a)	2.556	4.313	2.549	4.356	2.507	4.438
(b)	2.535	4.288	2.627	4.408	2.489	4.363
(c)	2.506	4.432	2.524	4.334	2.457	4.533
(d)	2.561	4.364	2.533	4.371	2.372	4.356
(e)	2.534	4.339	2.605	4.371	2.513	4.396
(f)	2.567	4.288	2.533	4.343	2.516	4.387
(g)	2.506	4.424	2.577	4.363	2.521	4.408
(h)	2.583	4.373	2.560	4.347	2.528	4.427
(i)	2.590	4.378	2.550	4.301	2.504	4.418
(j)	2.588	4.373	2.485	4.454	2.502	4.432
Mean, $\overline{Y}_{GP,i}$	2.553	4.357	2.554	4.365	2.491	4.416
SDOM, $\delta\overline{Y}_{GP,i}$	0.010	0.016	0.013	0.013	0.015	0.016

4.5 Error Analysis

Experimental error analysis was conducted by considering the system errors and the random errors (Taylor, 1997). Error analysis on the experimental results for the thermal debinding of HMW component will be discussed. Similar analysis was conducted on the thermal debinding of LMW component.

The system error induced by TGA equipment was $\leq \pm 0.10$ % according to the manual of TA Instrument. Based on the calculated best estimate of binder content for the PIM green parts with single binder system $Y_{GP,avg}$, which was 5.430 wt%, the system error could be estimated as

$$\delta Y_{GP,sys} = Y_{GP,avg} \times \frac{0.10}{100} \approx 0.005 \text{ wt \%} \quad (4\text{-}5)$$

The random errors were caused by the homogeneity of a green part and the repeatability of the debinding result of a brown part. For repeatability of the experimental result, the debinding of a green part was conducted three times for the same debinding temperature for the thermal debinding of HMW component and two times for the thermal debinidng of LMW component.

Since all the green parts in the present investigation were prepared with the same procedures, the uncertainty of the weighted average $\delta Y_{GP,avg}$, which was calculated as ± 0.010 wt %, was considered as the random error due to the homogeneity of the green parts $\delta Y_{GP,rand}$. Considering the system error introduced by TGA equipment $\delta Y_{GP,sys}$, the standard error due to the homogeneity of green part δY_{GP} was estimated as

$$\delta Y_{GP} = \sqrt{\delta Y_{GP,rand}{}^2 + \delta Y_{GP,sys}{}^2} \approx 0.010 \text{ wt \%} \quad (4\text{-}6)$$

The residual binder in weight ratio for each sample of the brown parts were estimated using

$$X_{RB,h} = \frac{Y_{BP,h}}{Y_{GP,h}} \quad (4\text{-}7)$$

In Eq. (4-7), h represents the number of experiment conducted for the same temperature (for example, $h = 1$ for the first time of the experiment, $h = 2$ for the second time of the experiment and etc); $Y_{BP,h}$ is the residual binder content of the brown parts and $Y_{GP,h}$ is the initial binder content of the PIM green parts for each batch of feedstocks. Taking account of error propagation, the standard error of the residual

binder for each sample $\delta X_{RB,h}$ is affected by the system error of the TGA equipment on the residual binder content of the brown parts $Y_{BP,h}$ and the standard error due to the homogeneity of green part δY_{GP}. It can be expressed as

$$\frac{\delta X_{RB,h}}{|X_{RB,h}|} = \frac{\delta Y_{BP,h}}{|Y_{BP,h}|} + \frac{\delta Y_{GP}}{|Y_{GP,h}|} \tag{4-8}$$

The best estimate of the residual binder δX_{RB} and its random error $\delta X_{RB,ran}$ were estimated using Eqs. (4-1) and (4-2). Considering error propagation, the overall standard error is

$$\delta X_{RB} = \delta X_{RB,ran} + \sum(\delta X_{RB,h}) \tag{4-9}$$

Where $\delta X_{RB,ran}$ is the random error for the best estimate of residual binder content and $\sum(\delta X_{RB,h})$ is the sum of the standard errors of residual binder for h times of experiment conducted at the same temperature.

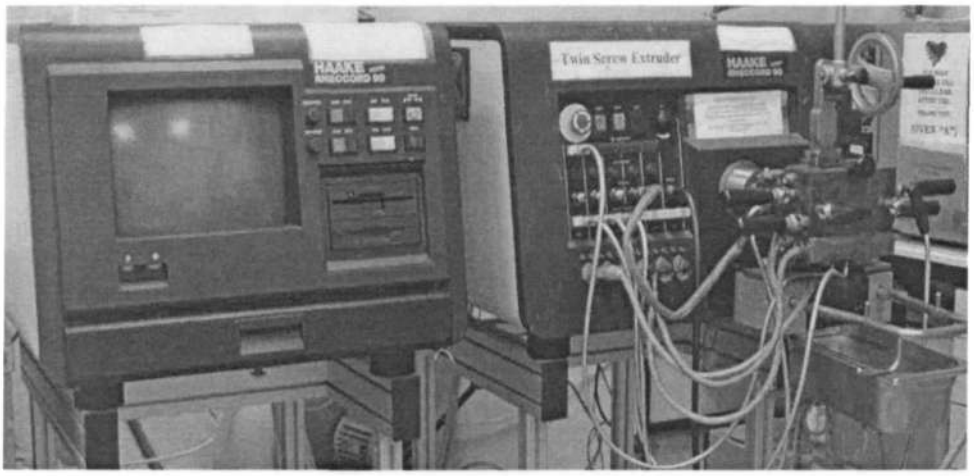

Figure 4.1 Haake Rheocord 90 Torque mixer

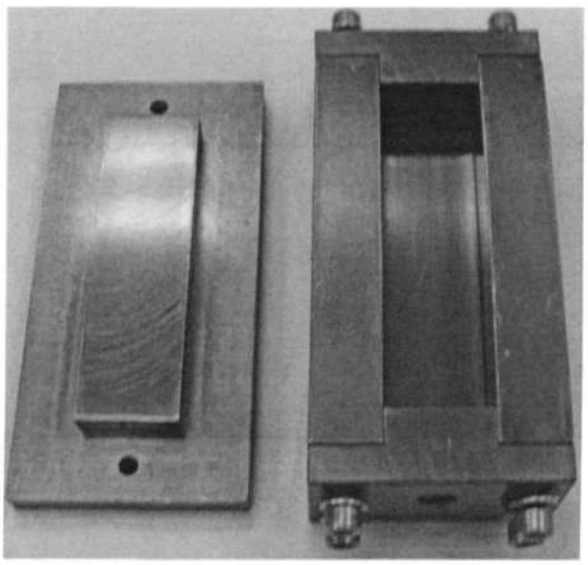

Figure 4.2 Punch and mold

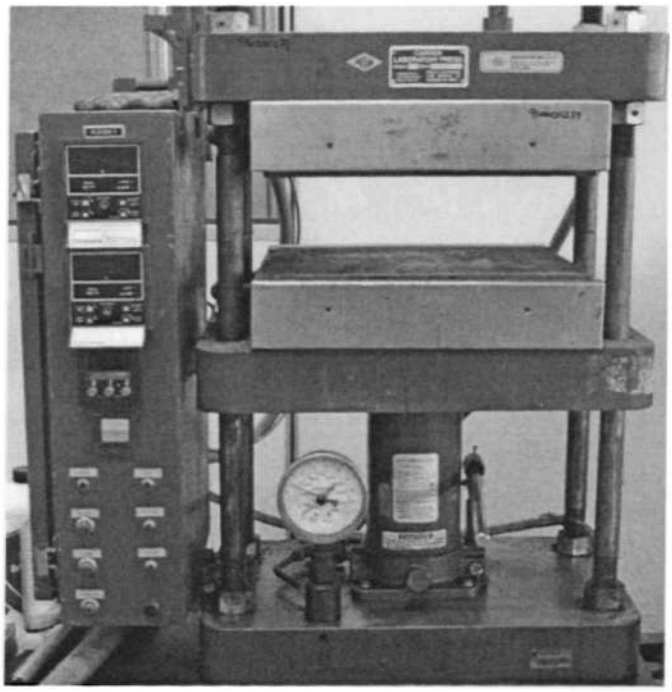

Figure 4.3 Hot press machine

Figure 4.4 Lenton general-purpose chamber furnace

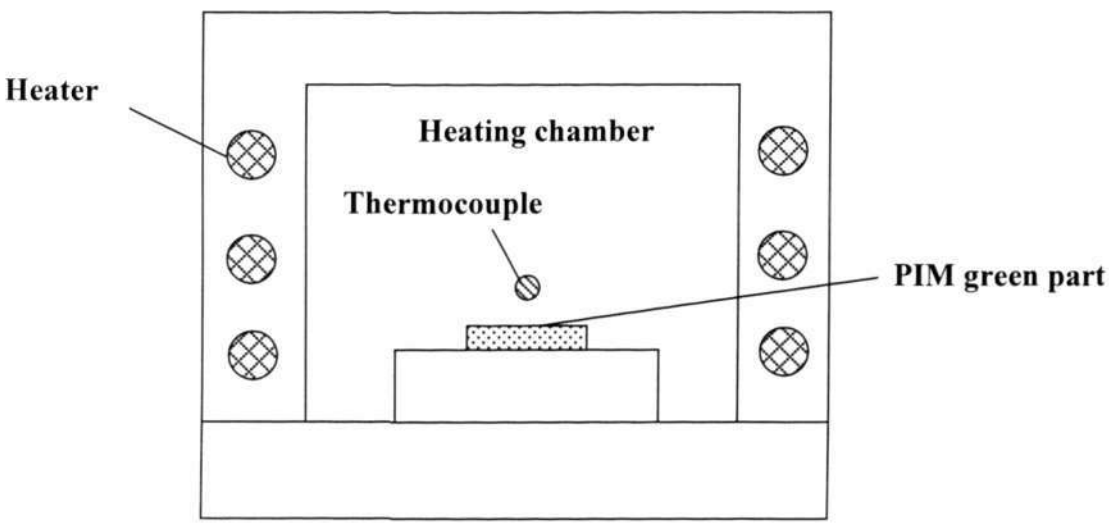

Figure 4.5 Green part in debinding furnace with thermocouple

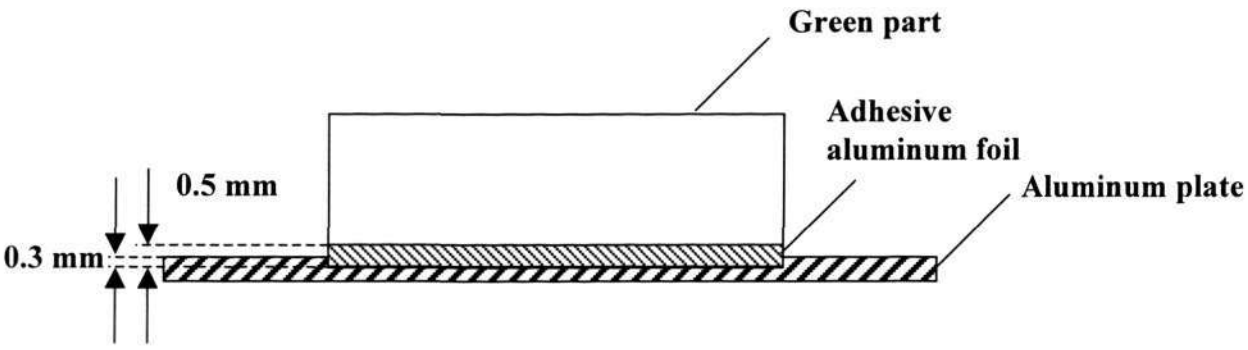

Figure 4.6 PIM green part in debinding furnace for HMW component

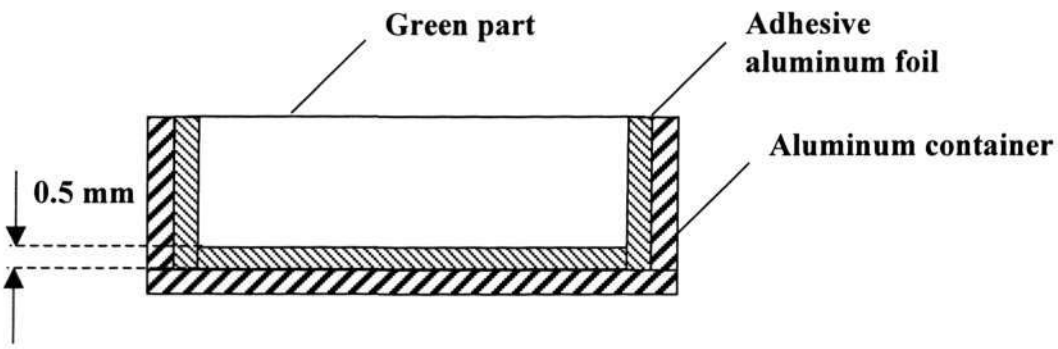

Figure 4.7 PIM green part in debinding furnace for LMW component

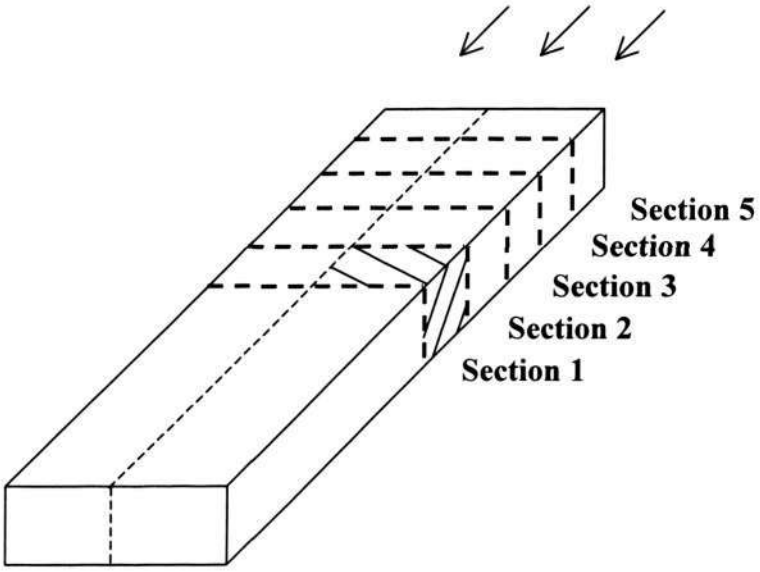

Figure 4.8 Sectioning of the brown part

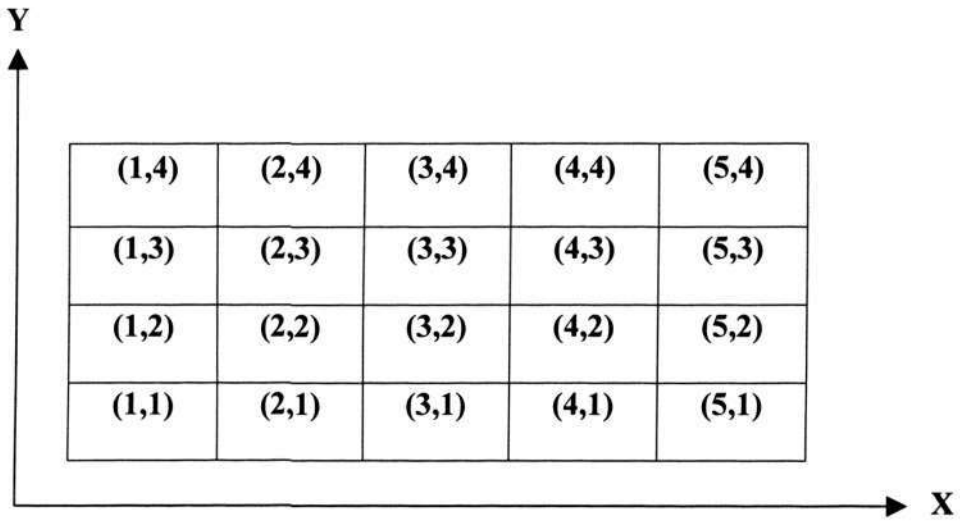

Figure 4.9 Identified locations of the 2D brown part section

Figure 4.10 Hi-Res Modulated TGA 2950 thermogravimetric analyzer

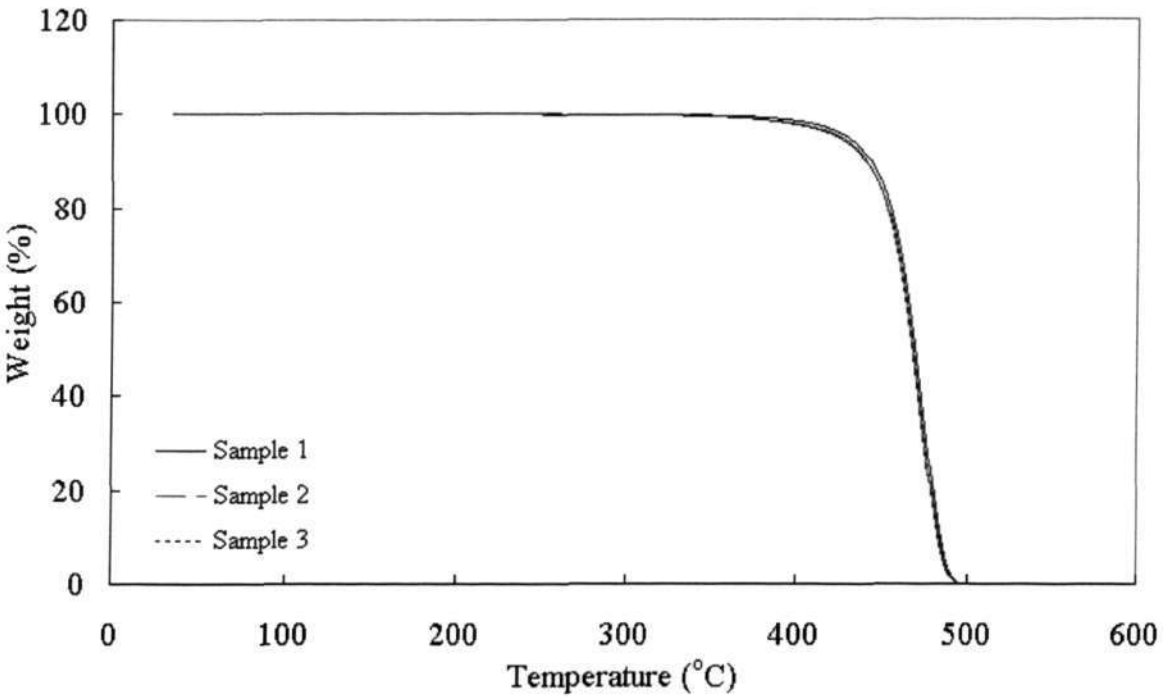

Figure 4.11 TGA curve of polypropylene

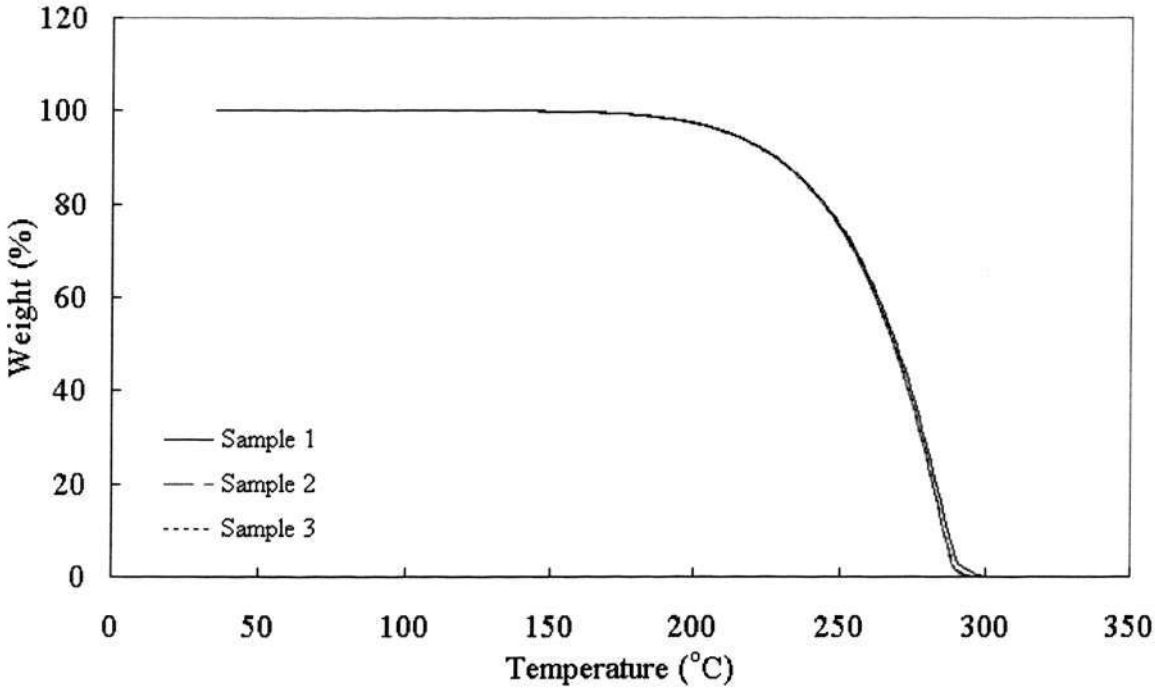

Figure 4.12 TGA curve of stearic acid

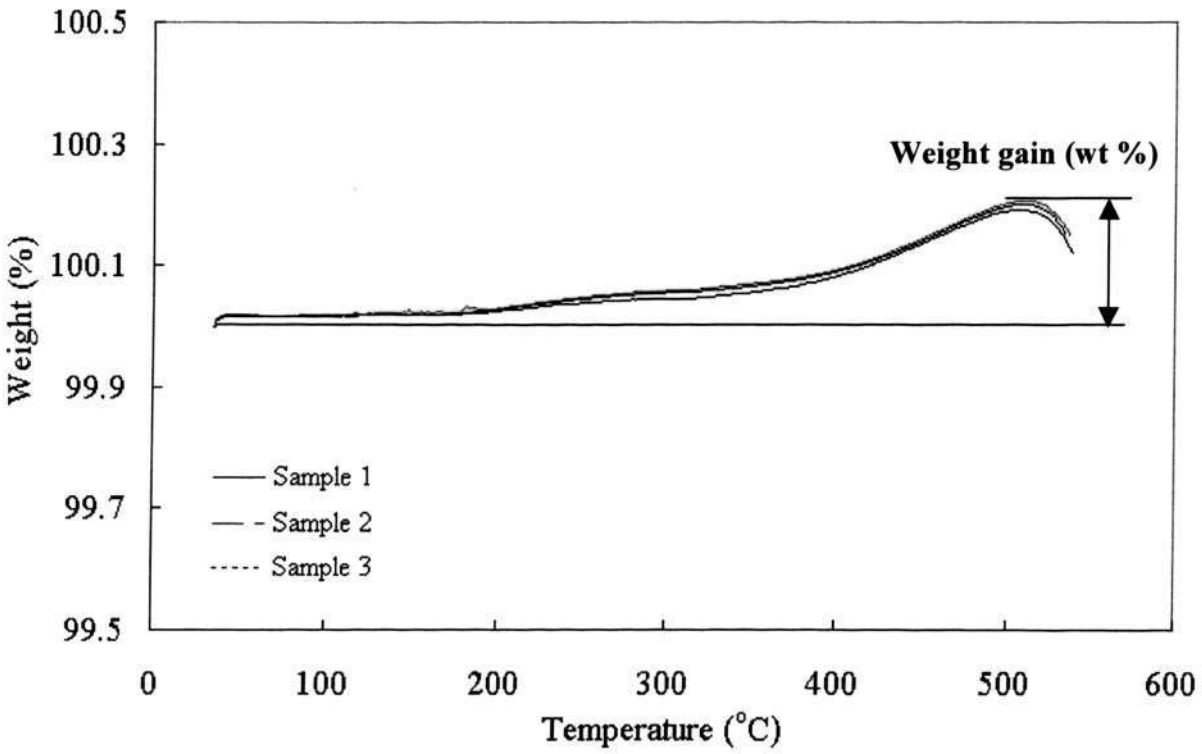

Figure 4.13 TGA curve of carbonyl iron metal powder

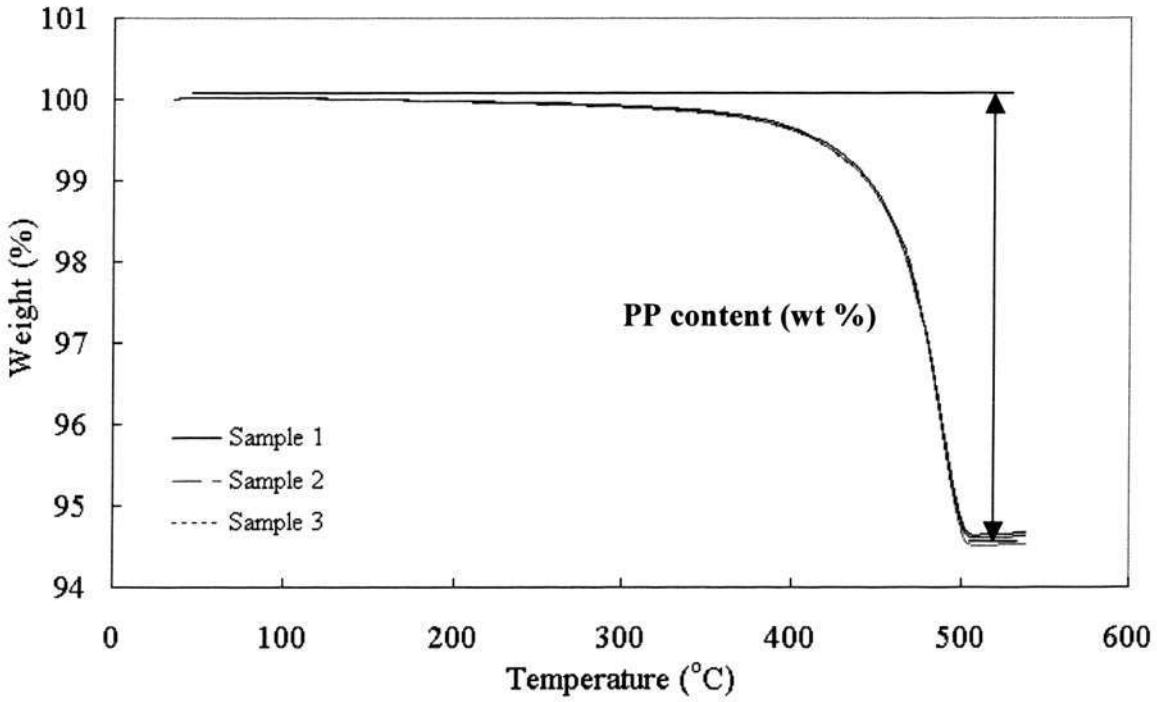

Figure 4.14 TGA curve of feedstock with single component binder system

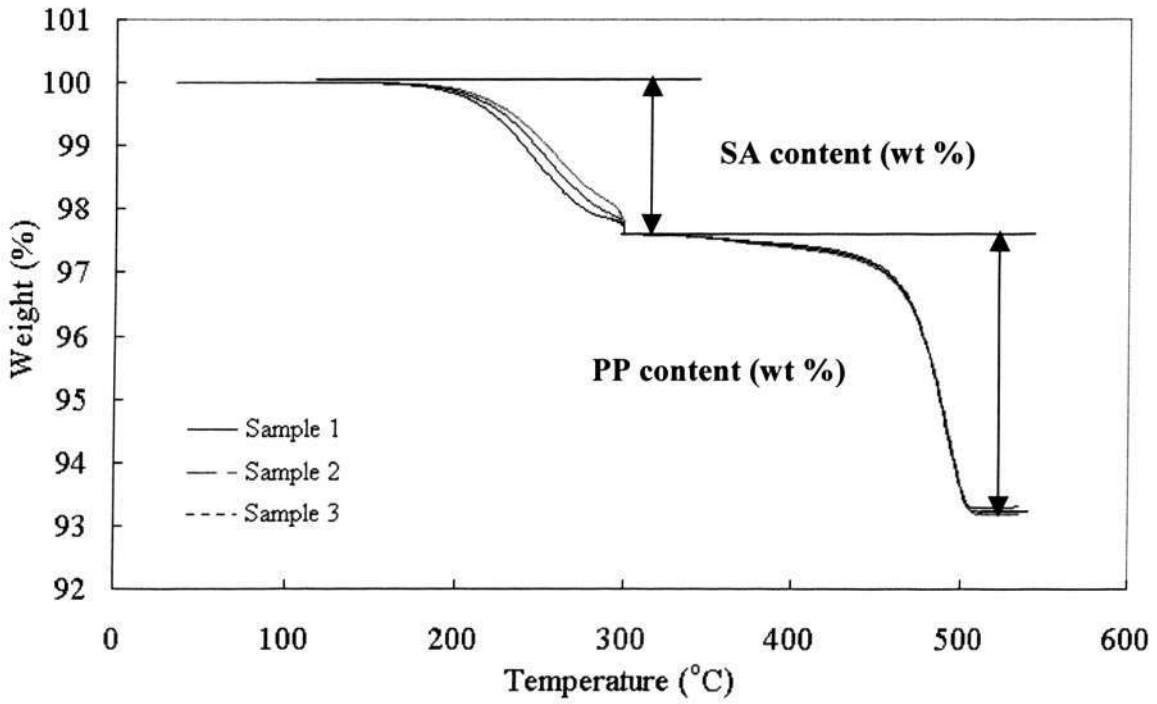

Figure 4.15 TGA curve of feedstock with two-component binder system

CHAPTER 5

RESULTS AND DISCUSSIONS

In this chapter, the experimental results are presented in section 5.1. In sections 5.2 and 5.3, two limiting cases of the mathematical model are solved numerically to simulate the binder distributions of a PIM compact during thermal debinding of the HMW component and the LMW component, respectively. The numerical results are compared with experimental data to validate the numerical models. Following this, the discussions of the numerical results are presented. In section 5.4, the numerical results on the thermal debinding of the two-component binder system are presented.

Residual binder, average residual binder, debinding rate, and thermal degradation rate will be used extensively in presenting the results. The residual binder is the ratio of the remaining binder mass to the initial binder mass of the compact. The average residual binder represents the average value of the residue binder over the compact. The debinding rate, which is the rate of change of the average residual binder with time, is calculated as

$$\text{Debinding rate} = \frac{\text{Change in average residual binder between 2 consecutive times}}{\text{Elapsed time between the same 2 consecutive times}} \quad (5\text{-}1)$$

The thermal degradation rate of the HMW component is a function of liquid saturation of HMW component $S_{l,p}$ and temperature $\langle T \rangle$ as given in Eq. (A-1). It is reproduced here for ease of reference.

$$\langle \dot{m}_d \rangle = \varepsilon \langle \rho_{l,p} \rangle^{l,p} \left(\frac{S_{l,p}}{S_{l,initial}}\right)^r C_o \exp\left(\frac{-E_{dg}}{R\langle T \rangle}\right) \quad (5\text{-}2)$$

where C_o is the rate constant, E_{dg} is the activation energy, and r is the reaction order.

5.1 Experimental Results

Two stages of experimental investigations were conducted. These are the investigations of the distributions of residual binder after the thermal debinding of HMW component and LMW component. For the investigation of the thermal debinding of the HMW component, PIM compacts with a single component binder system (PP) are used. The volume fractions for the metal powder, PP, and initial porosity are 0.6, 0.3, and 0.1 respectively. PIM compacts with two-component binder system (SA and PP) are used in investigating the thermal debinding of LMW component. The volume fractions for the metal powder, PP, and SA are 0.60, 0.24, and 0.16 respectively. However, only removal of the SA is studied. As mentioned in Chapter 4, the compacts were cooled before measurements were carried out. Therefore, there is a heating and a cooling period.

5.1.1 Thermal Debinding of the HMW Component

In investigating the thermal debinding of the HMW component, four debinding times, which are 26940 s, 28140 s, 29340 s, and 30540 s, are presented and analyzed. The corresponding debinding temperatures are 632 K, 653 K, 674 K, and 697 K, respectively.

Figures 5.1(a)-(d) show the distributions of residual binder at the center section (section 1 of Fig. 4.8) of the brown parts for the above-mentioned debinding times. The grid locations are shown in Fig. 4.9. Figures 5.2(a)-(h) show these distributions in X- and Y-directions (Fig. 4.9). The average values of the residual binder at these four

times are approximately 95 %, 88 %, 72 %, and 26 %, respectively. Though the compacts are subjected to a constant heating rate of 1 °C/min, the binder removal increases drastically as debinding temperature increases. During the temperature range of 674 K to 697 K or the last two debinding times, almost 50 % of the binder is removed. The TGA result (Fig. 5.3) shows that the HMW component starts degrading after 623 K and the degradation rate increases steeply after 668 K. These results imply that the binder removal is possibly controlled by the thermal degradation of HMW component.

The residual binder decreases towards the outer surfaces at the first two debinding times (see Figs. 5.1(a)-(b) and 5.2(a)-(d)). This is because the debinding temperatures are higher at the outer surfaces. As a result, the HMW component degrades and evaporates faster at the outer surfaces. At the third debinding time, although still exhibiting the same trends as the first two debinding times, the residual binder distributes more uniformly (see Figs. 5.1(c) and 5.2(e)-(f)). This implies that there is migration of binder from the internal region towards the outer surfaces. At the fourth debinding time, binder accumulation at the outer surfaces is observed as shown in Figs. 5.1(d) and 5.2(g)-(h). This implies that the migration rate of liquid binder towards the outer surfaces is faster than the removal rate of binder at the outer surface. This could be due to the decreased binder viscosity at higher temperatures that leads to faster outward migration rate as compared to the degradation rate of binder at the outer surfaces. Sproson and Messing (1988) also observed the binder enrichment at the outer surfaces during the binder removal in a powder-binder system.

Overall, the residual binder distributes quite uniformly at these four debinding times. There is no abrupt change in residual binder throughout the compacts. This implies that a moving front (liquid-gas interface) does not exist during the thermal debinding process. The liquid HMW component degrades into liquid volatile fragments throughout the whole compact when the degradation temperature is reached. The liquid volatile fragments then evaporate and escape uniformly from the PIM compacts via the pores. Barone et al. (1988) also reported that no moving front progresses in the compact during the binder removal indicating a nearly uniform volumetric reaction.

5.1.2 Thermal Debinding of LMW Component

For the investigation on thermal debinding of LMW component, four debinding times namely, 17250 s, 25290 s, 25275 s, and 29025 s are analyzed. The corresponding debinding temperatures are 455 K, 495 K, 505 K, and 519 K, respectively.

Figures 5.4(a)-(d) show the distributions of residual binder in the brown parts for the above-mentioned debinding times (see Fig. 4.9 for the grid locations). The average values of residual binder are approximately 96 %, 82 %, 66 %, and 61 %, respectively. Figures 5.5(a)-(h) show the distributions of residual binder in X- and Y-directions (Fig. 4.9). As mentioned in Chapter 4, the vertical surfaces of the compacts were covered with an aluminum plate (see Fig. 4.7). As a result, there is no mass transfer across these impermeable vertical surfaces. The residual binder remains higher near the vertical surfaces as shown in Figs. 5.5(a), (c), (e) and (g). The mass transfers across the top surface of the compacts. However, the residual binder increases in the Y-direction at the first debinding time (see Figs. 5.4(a) and 5.5(b)). This observation implies that the molten LMW component starts migrating towards the top surface and the surface

mass transfer rate is slow to remove the LMW component. Shaw et al. (1993) also reported the phenomenon of wax enrichment at the surfaces of a ceramic powder compact. At the second debinding time, the residual binder decreases in the Y-direction (see Figs. 5.4(b) and 5.5(d)). The average difference in residual binder between the internal region and the outer surface is 14 %. This implies that the surface mass transfer rate increases as debinding temperature increases. At the third debinding time (Figs. 5.4(c) and 5.5(f)), the average difference in residual binder between the internal region and the outer surface increases to 42 %. The surface mass transfer rate has increased significantly as compared to the outward migration of residual binder. As temperature continues to increase, the residual binder becomes more uniform (see Figs. 5.4(d) and 5.5(h)). At this time, the average difference in residual binder between the internal region and the outer surface reduces to 24 %. This could be due to the increase in outward migration rate of less viscous binder at higher temperatures.

These experimental observations show that the LMW component begins to be removed at the outer surface. Subsequently, the liquid LMW component migrates towards the outer surface and being removed. These imply that the thermal debinding of LMW component is probably dominated by a surface controlled reaction.

5.1.3 Concluding Remarks

The experimental results on the distributions of residual binder for the thermal debinding of HMW component and LMW component have been presented. The experimental observations show that the residual binder distributes almost uniformly throughout the compacts during the thermal debinding of HMW component. For the thermal debinding of LMW component, the residual binder is preferentially removed

at the outer surface. Binder accumulations at the outer surfaces are observed for the thermal debinding of both HMW component and LMW component. The binder accumulation is observed at the high temperatures ($T \geq 697$ K), which is the latter stage of the thermal debinding of HMW component. For the thermal debinding of LMW component, the binder accumulation is observed at the low temperatures ($T \leq 455$ K), which is the beginning stage.

5.2 Simulation on the Thermal Debinding of HMW Component

For this limiting case, the simulation focuses on the final stage of thermal debinding that covers the temperature range from T_4 to T_5 (see Fig. 2.2). In this section, the removal of the LMW component is not considered. The binder system contains HMW component only.

5.2.1 Computational Domain

The computational domain is shown in Fig. 5.6. OA is the symmetry axis and OB is an impermeable and adiabatic wall. AC and BC are the outer surfaces that exchange heat and mass with the surroundings.

5.2.2 Governing Equations

Four variables are solved. These are the liquid saturation of HMW component $S_{l,p}$ (Eq. 2-41), the liquid saturation of volatile fragments $S_{l,f}$ (Eq. 2-47), the total gas pressure $\langle P_{g,t}\rangle^g$ (Eq. 2-57), and the local temperature $\langle T\rangle$ (Eq. 2-27). As a result of neglecting the removal of LMW component, some modifications are made to the governing equations. As there are only liquid HMW component and liquid volatile fragments in the solution, Eq. (2-40) is rewritten as

$$S_l = S_{l,p} + S_{l,f} \tag{5-5}$$

Equation (2-44) is rewritten as

$$\Gamma_{sp}^{sf} = -\frac{\langle \rho_{l,p}\rangle^{l,p} D_{l,p-f}(1-\theta_{l,f})}{(S_{l,p}+S_{l,f})^2} \tag{5-6}$$

As there is no vapor LMW component in the total gas phase. Therefore, the second and the last terms on the right side of Eq. (2-57) vanish. Equation (2-66) is rewritten as

$$\langle p_{g,i}\rangle^{g} = \langle P_{g,t}\rangle^{g} - \langle p_{g,f}\rangle^{g} \tag{5-7}$$

Equation (2-27) is rewritten as

$$\begin{aligned}(\rho C_p)_{eff}\frac{\partial\langle T\rangle}{\partial t} + [\varepsilon S_{l,p}\langle\rho_{l,p}\rangle^{l,p}(C_{p,l})_p\langle\vec{v}_{l,p}\rangle + \varepsilon S_{l,f}\langle\rho_{l,f}\rangle^{l,f}(C_{p,l})_f\langle\vec{v}_{l,f}\rangle \\ + \varepsilon S_g\langle\rho_g\rangle^{g}C_{p,g}\langle\vec{v}_g\rangle]\cdot\nabla\langle T\rangle = \nabla\cdot(k_{eff}\nabla\langle T\rangle) - \Delta H_{vap,f}\langle\dot{m}_{v,f}\rangle\end{aligned} \tag{5-8}$$

where,

$$\begin{aligned}(\rho C_p)_{eff} = (1-\varepsilon)\rho_s C_{p,s} + \varepsilon[S_{l,p}\langle\rho_{l,p}\rangle^{l,p}(C_{p,l})_p + S_{l,f}\langle\rho_{l,f}\rangle^{l,f}(C_{p,l})_f] \\ + \varepsilon S_g[\langle\rho_{g,f}\rangle^{g}(C_{p,g})_f + \langle\rho_{g,i}\rangle^{g}(C_{p,g})_i]\end{aligned} \tag{5-9}$$

5.2.3 Initial and Boundary Conditions

The PIM compact is initially at room temperature (300 K). This is to ensure that there is no volatile fragment initially. The initial total gas pressure equals the atmospheric pressure (100 KPa). The initial liquid saturation of the HMW component is 0.75, which is 30 vol% of the whole compact. Initial pores of 10 vol% are assumed.

At OA (symmetry axis) and OB (impermeable and adiabatic wall), the symmetry boundary condition and the impermeable boundary condition are imposed. There is no flow or flux across the boundary. For a variable Φ, it can be expressed as

$$\nabla\Phi = 0 \tag{5-10}$$

In Eq. (5-10), the variables are the liquid saturations of HMW component and volatile fragments, the total gas pressure, and the temperature. At AC and BC (outer surfaces), the flux boundary condition is used for the liquid saturation of the HMW component. This is written as

$$(J_{l,p})_{surface} = 0 \tag{5-11}$$

where $(J_{l,p})_{surface}$ is the liquid phase mass flux of the HMW component at the outer surfaces. Equation (5-11) is expanded as

$$-\Gamma_{sp}\frac{\partial S_{l,p}}{\partial x_k}=\Gamma_{sp}^{sj}\frac{\partial S_{l,j}}{\partial x_k}+\Gamma_{sp}^{T}\frac{\partial\langle T\rangle}{\partial x_k}+\Gamma_{sp}^{P}\frac{\partial\langle P_{g,t}\rangle^{g}}{\partial x_k} \tag{5-12}$$

Equation (5-12) is the boundary condition for the liquid saturation of HMW component. In Eq. (5-12), x_k is the coordinate normal to the boundary of interest. Assuming that all the liquid volatile fragments evaporate and are removed instantly at the outer surfaces, the liquid saturation of volatile fragments at the outer surfaces is specified as

$$(S_{l,f})_{surface}=0 \tag{5-13}$$

The total gas pressure always remains at the atmospheric pressure at the outer surfaces,

$$(P_{g,t})_{surface}=P_{atm} \tag{5-14}$$

The temperature at the outer surfaces is prescribed based on the measured temperatures (see Fig. 5.7). This is

$$\begin{aligned}(T)_{surface}=&-2.537\times10^{-15}t^{6}+1.3870\times10^{-11}t^{5}-6.2181\times10^{-9}t^{4}\\&-3.7288\times10^{-6}t^{3}+3.2361\times10^{-3}t^{2}+2.1806\times10^{-1}t+299.02\end{aligned} \tag{5-15}$$

where t is the debinding time in seconds. To compare with the experimental data, the cooling period is included in the model. The temperature at the outer surfaces during the cooling period is calculated using

$$(T)_{surface}=T_{cool}+\frac{dT}{dt}(t_{cool}) \tag{5-16}$$

where T_{cool} is the initial temperature of the cooling period, t_{cool} is the cooling time in seconds, and $\frac{dT}{dt}$ is the measured cooling rate (-1.5 K/min).

5.2.4 Results and Discussions

Figure 5.8 shows the flow chart of the thermal debinding of HMW component. The liquid saturations ($S_{l,p}$, $S_{l,f}$, and S_l) are the volume fractions of the liquid phases inside the pores of the PIM compact. Once the degradation temperature is reached ($\langle T \rangle \geq T_4$; Fig. 2.2), liquid HMW component $S_{l,p}$ degrades into liquid volatile fragments $S_{l,f}$. The total liquid saturation S_l is the sum of the liquid saturations of the HMW component and the volatile fragments. The liquid volatile fragments then evaporate into vapor phase resulting in an increase in vapor pressure $\langle p_{g,f} \rangle^g$. The buildup of the vapor pressure causes the increase in the total gas pressure $\langle P_{g,t} \rangle^g$.

Grid independence study was performed using 6x4, 18x12 and 36x24 control volumes. The maximum binder liquid saturation difference between 18x12 and 36x24 is less than 4 % over the whole debinding period. Thus, 18x12 control volumes are used. The time step of 15 s is sufficient to achieve time independence.

5.2.4.1 Comparisons with Experimental Results

Six regions of the brown part (Fig. 4.9) are used to check the accuracy of the numerical method. The six regions consist of 3 internal regions, which are (1,2), (2,3), and (3,1), and 3 outer regions, which are (1,4), (4,4), and (5,2). The results at four debinding times, which are 26940 s, 28140 s, 29340 s, and 30540 s, will be presented (refer section 5.1.1 for the experimental results).

Figures 5.9(a)-(b) show good agreements (with ≤ 8 % error) between the numerical results and the experimental data for the first two debinding times. For the third

debinding time, the errors are relatively high. The error in region (1,2) is 37 % while the other are between 15 % and 25 % (Fig. 5.9(c)). Figure 5.9(d) shows that the numerical results agree well with the experimental data for the last debinding time with errors ranging between 5 % and 9 %.

The numerical results show faster binder removal (especially at the last two debinding times) compared to the experimental data. This might be due to the experimental uncertainties or the higher thermal degradation rate predicted by the empirical correlations.

5.2.4.2 Binder Removal

Figure 5.10 shows the residual binder curve. For ease of discussion, this curve is divided into seven time zones. Table 5.1 shows details of these time zones. The table entries are the debinding time, the surface temperature, the residual binder, and the debinding rate. Figures 5.11 and 5.12 show the maximum vapor and total gas pressures versus the debinding time.

Figure 5.10 shows that only 0.5 % of the binder has been removed after 20400 s. The binder begins to degrade after the degradation temperature (approximately 638 K) has been reached at 24000 s. After this, the debinding rate increases within the time zones 3-6 (see Table 5.1). As shown in Eq. (5-2), the degradation rate of liquid HMW component increases as temperature increases. Meanwhile, the evaporation rate of liquid volatile fragments also increases as temperature increases. As a result, the binder removal rate increases. The vapor and total gas pressures increase as the binder removal rate increases (see Figs. 5.11 and 5.12). The maximum vapor and total gas

pressures increase significantly after 26010 s. This debinding time is within the time zone 5, in which the debinding rate increases to the peak region (Table 5.1). After 27450 s, the maximum vapor and total gas pressures begin to decrease. When more than 80 % of the binder has been removed (Fig. 5.10), more pores are created in the compact. Therefore, the vapor binder can escape faster from the compact. As a result, the buildup of vapor pressure decreases.

The debinding rate decreases after approximately 90 % of the binder has been removed at 27720 s. The thermal degradation rate decreases as liquid saturation of HMW component decreases (Eq. 5-2). As a result, the debinding rate decreases when less binder remains inside the PIM compact. As less than 10 % binder remains in the compact, the irreducible liquid saturation is reached. At this time the pendular state is considered reached. The binder removal is solely due to the gas phase transport. After 8 hours, thermal debinding in the PIM compact is normally considered complete (< 5 % residual binder) and the remaining binder will be removed via sintering at higher temperatures (Hwang and Tsou, 1992).

Table 5.1 HMW component: Debinding points of residual binder curve

Point	Debinding Time (s)	Temperature (K)	Residual Binder	Debinding Rate (1/s)
1	20400	576.70	0.995	2.9×10^{-7}
2	24000	637.83	0.95	1.2×10^{-5}
3	25200	659.04	0.88	5.8×10^{-5}
4	25920	672.16	0.72	2.2×10^{-4}
5	27270	697.82	0.26	3.4×10^{-4}
6	27720	706.76	0.10	3.6×10^{-4}
7	27990	712.23	0.05	1.9×10^{-4}

5.2.4.3 Binder Distribution

The distributions of the temperature, the liquid saturations of HMW component and volatile fragments, the total liquid saturation, the vapor pressure, and the total gas pressure were analyzed.

Due to the slow heating rate, the temperature differences (for any given time) over the thin PIM compact are small as shown in Figs. 5.13(a)-(b). The maximum temperature difference is approximately 2 K. As a result, the liquid HMW component begins to degrade throughout the whole compact at 22200 s (see Fig. 5.14(a)). The maximum difference in the liquid saturation of HMW component is 0.3 % at this time. As shown in Figs. 5.13(a)-(b), the temperatures are relatively high at the outer surfaces throughout the debinding process. This results in faster evaporation rate of the liquid volatile fragments at the outer surfaces as compared to the internal region (see Fig. 5.14(b)). As a result, the total liquid saturation is higher in the internal region (see Fig. 5.14(c)). Figure 5.14(d) shows that vapor pressure is higher in the internal region as compared to the outer surfaces. The lower vapor pressure at the outer surfaces indicates that the concentration of the vapor volatile fragments is lower there. This shows that the vapor volatile fragments at the outer surfaces can escape faster from the compact.

At 25200 s, liquid HMW component degrades faster at the corners of the compact as shown in Fig. 5.15(a). The liquid volatile fragments remain lower at the outer surfaces (see Fig. 5.15(b)). As a result, the total liquid saturation is lower at the outer surfaces as shown in Fig. 5.15(c). The liquid saturation of volatile fragments decreases as compared to that of 22200 s (Fig. 5.14(b)). This indicates that the evaporation of liquid

volatile fragments increases as temperature increases. Therefore, higher vapor pressure (compared to that of 22200 s) is observed (see Figs. 5.14(d) and 5.15(d)).

At 26040 s, the liquid saturations of HMW component and volatile fragments, and the total liquid saturation decreases towards the outer surfaces (see Figs. 5.16(a)-(c)). The degradation rate of liquid HMW component at the outer surfaces becomes faster as compared to that of internal region. The decrease in liquid saturation of volatile fragments (compared to that of 25200 s) indicates that the evaporation rate continues to increase. This results in the increases in the vapor and total gas pressures (see Figs. 5.16(d) and (e)).

As shown in Fig. 5.18, the viscosity of liquid HMW component decreases as temperature increases. At 27240 s, the viscosity ($\approx 10^{-3}$ Pa s) decreases by half as compared to that of 26040 s. At the same time, the total gas pressure gradient increases by an order of magnitude compared to that of 26040 s. This pressure gradient tends to push the less viscous liquid HMW component towards the outer surfaces. As shown in Fig. 5.17(a), the outward migration rate of liquid HMW component has increased as compared to that of 26040 s. The concentration of the liquid volatile fragments remains low ($10^{-4} - 10^{-3}$) (see Fig. 5.17(b)). As a result, the total liquid binder accumulates at the outer surfaces (see Fig. 5.17(c)). As compared to that of 26040 s, the liquid saturation of volatile fragments increases. This implies that the evaporation rate is slower compared to the degradation rate. The vapor and total gas pressures increase as the generation of volatile fragments increases (see Figs. 5.17(d)-(e)).

Overall, the binder degrades and evaporates quite evenly due to the small temperature differences in the compact (for any given time). As a result, the total binder distributes quite evenly throughout the compact. The degradation and evaporation rates increase as temperature increases. These lead to the increases in vapor and total gas pressures. The buildup of the vapor pressure is one of the main factors in causing defects to PIM products (Evans et al., 1991, Matar et al., 1993, Matar et al., 1995, Shaw and Ediringhe, 1995a, Song et al., 1996)

The distributions of the total liquid saturation at these four debinding times agree qualitatively with the binder distributions of the experimental data (discussed in section 5.1.1). In the first three debinding times, the residual binder is lower at the outer surfaces (Figs. 5.1(a)-(c) and 5.2(a)-(f)). At the last debinding time, the binder accumulation is observed (Figs. 5.1(d) and 5.2(g)-(h)). Ying et al. (2001, 2002a) predicted higher binder accumulation at the outer surfaces. This is because Ying's model did not account for highly viscous liquid polymer, which slows down the migration of the binder towards the outer surfaces.

5.2.4.4 Mass Transfers

The mass transfers of liquid and gas phases were studied. The factors that result in the mass transfers are the capillary driven action, the binary diffusion in solution, and the pressure driven action. These mass transfers are calculated based on Eqs. (2-41), (2-47), and (2-57). Sequentially, the mass transfers of liquid HMW component due to the capillary driven action (the gradients of liquid saturation and surface tension), the binary diffusion in solution, and the pressure driven action are

$$(-\langle \rho_{l,p} \rangle^{l,p} \psi_{l,p} \frac{\partial \langle P_{c,p} \rangle}{\partial S_{l,p}}) \nabla S_{l,p} + \Gamma_{sp}^{T} \nabla \langle T \rangle \qquad (5\text{-}17)$$

$$\langle \rho_{l,p} \rangle^{l,p} D_{l,p-j} \left(\frac{\theta_{l,j}}{S_{l,p} + S_{l,j}} \right) \nabla S_{l,p} + \Gamma_{sp}^{sf} \nabla S_{l,f} \tag{5-18}$$

$$\Gamma_{sp}^{p} \nabla \langle P_{g,t} \rangle^{g} \tag{5-19}$$

Similarly, the mass transfers of volatile fragments are

$$\left(-\langle \rho_{l,f} \rangle^{l,f} \psi_{l,f} \frac{\partial \langle P_{c,f} \rangle}{\partial S_{l,f}} \right) \nabla S_{l,f} + \Gamma_{sf}^{T} \nabla \langle T \rangle \tag{5-20}$$

$$\left(\langle \rho_{l,f} \rangle^{l,f} D_{l,p-f} \left(\frac{1-\theta_{l,f}}{S_{l,p} + S_{l,f}} \right) \right) \nabla S_{l,f} + \Gamma_{sf}^{sp} \nabla S_{l,p} \tag{5-21}$$

$$\Gamma_{sf}^{P} \nabla \langle P_{g,t} \rangle^{g} + \Gamma_{sf}^{pv} \nabla \langle p_{g,f} \rangle^{g} \tag{5-22}$$

The mass transfer of gas phase is

$$\Gamma_{p} \nabla \langle P_{g,t} \rangle^{g} + \Gamma_{P}^{sa} \nabla \langle p_{g,sa} \rangle^{g} \tag{5-23}$$

HMW component: The mass transfer due to the capillary driven action is the orders of 10^{-6}-10^{-5} kg/m^2 s. The mass transfer due to the binary diffusion in solution is the orders of 10^{-12}-10^{-9} kg/m^2 s. The mass transfer due to the pressure driven action is the order of 10^{-5} kg/m^2 s. Both the capillary driven action and the pressure driven action are essential for the transport of liquid HMW component. However, after 27240 s, the mass transfer due to the capillary driven action decreases to the order of 10^{-6} kg/m^2 s. This implies that the transport of liquid HMW component at higher debinding temperatures ($T > 697$ K) is mainly due to the pressure driven action.

Volatile fragments: The mass transfer due to the capillary driven action is the orders of 10^{-9}-10^{-3} kg/m^2 s. The mass transfer due to the binary diffusion in solution is the orders of 10^{-10}-10^{-9} kg/m^2 s. The mass transfer due to the pressure driven action is the orders of 10^{-4}-10^{-3} kg/m^2 s. The comparison of orders of magnitude shows that the

mass transfer of volatile fragments due to the binary diffusion in solution is negligible. The mass transfer due to the capillary driven action decreases to 10^{-9} kg/m^2 s after 27240 s. Meanwhile, the mass transfer due to the pressure driven action is the order of 10^{-3} kg/m^2 s after 27240 s. This indicates that the pressure driven action dominates the mass transfer of volatile fragments at higher debinding temperatures ($T > 674$ K).

Gas phase: The mass transfer due to the pressure gradients is the orders of 10^{-7}-10^{-4} kg/m^2 s. The mass transfer increases to the order of 10^{-4} kg/m^2 s after 27240 s. The comparison of orders of magnitude indicates that both the gas and the liquid phases transports play an important role in the mass transfers during the thermal debinding of HMW component. The liquid phase transport dominates at the beginning stage ($T <$ 674 K) and the gas phase transport dominates at the later stage when less liquid HMW component remains inside the PIM compact.

The binder removal mechanisms were also analyzed. At the outer surfaces, the HMW component degrades and evaporates into vapor volatile fragments. The vapor volatile fragments are then removed by inserting gas flow. In the internal region, the liquid HMW component migrates outwards via capillary driven and pressure driven actions. At the same time, the liquid HMW component degrades into liquid volatile fragments. As degradation occurs, the total liquid binder becomes a solution of liquid HMW component and liquid volatile fragments. The liquid volatile fragments migrate towards the outer surface due to the capillary driven and pressure driven actions. Meanwhile, the liquid volatile fragments evaporate into vapor volatile fragments. As there are open pores (> 30 vol%) inside the compact, the vapor volatile fragments diffuse in the pores towards the outer surfaces. After 27240 s, when there is less than

30 % of residual binder inside the compact, gas phase transport plays a dominant role in mass transfer.

5.2.5 Concluding Remarks

A limiting case was deduced from the mathematical model and solved numerically to simulate the thermal debinding of HMW component. The numerical model has been validated by the experimental data. The physical trends of binder removal were discussed. The mass transfer mechanisms during thermal debinding were analyzed. The capillary driven and the pressure driven actions are the dominant mechanisms in the transports of liquid HMW component and liquid volatile fragments. Both transports of the liquid and the gas phases are essential in the thermal debinding of HMW component.

5.3 Simulation on the Thermal Debinding of LMW Component

In this section, another limiting case for the thermal debinding of LMW component, which covers the temperature range from T_0 to T_4 (see Fig. 2.2), is presented. The removal of the HMW component is neglected. Thus, it is assumed that the HMW component does not degrade during the removal of LMW component. Assumptions (i) to (v) given in section 2.2.1 are used.

5.3.1 Computational Domain

The computation domain is shown in Fig. 5.19. OA is the symmetry axis and OB is an impermeable and adiabatic wall. AC is the outer surface that exchanges heat and mass with the surroundings. The PIM compact resided inside an aluminum container when the experiments were conducted. As a result, BC is modeled as an impermeable surface that exchanges heat with the surroundings.

5.3.2 Governing Equations

Three variables are solved. These are the liquid saturation of LMW component $S_{l,sa}$ (Eq. 2-31), the total gas pressure $\langle P_{g,t}\rangle^g$ (Eq. 2-57), and the local temperature $\langle T\rangle$ (Eq. 2-27). As the removal of HMW component is neglected, the second term on the right side of Eq. (2-31) vanishes. There are no volatile fragments in the solution. Thus, Eq. (2-40) is rewritten as

$$S_l = S_{l,p} + S_{l,sa} \tag{5-24}$$

As there are no volatile fragments in the total gas phase, the third and the sixth terms on the right side of Eq. (2-57) vanish. Equation (2-66) is rewritten as

$$\langle p_{g,i}\rangle^g = \langle P_{g,t}\rangle^g - \langle p_{g,sa}\rangle^g \tag{5-25}$$

Equation (2-27) is rewritten as

$$(\rho C_p)_{eff}\frac{\partial\langle T\rangle}{\partial t}+[\varepsilon S_{l,p}\langle\rho_{l,p}\rangle^{l,p}(C_{p,l})_p\langle\vec{v}_{l,p}\rangle+\varepsilon S_{l,sa}\langle\rho_{l,sa}\rangle^{l,sa}(C_{p,l})_{sa}\langle\vec{v}_{l,sa}\rangle$$
$$+\varepsilon S_g\langle\rho_g\rangle^g C_{p,g}\langle\vec{v}_g\rangle]\cdot\nabla\langle T\rangle=\nabla\cdot(k_{eff}\nabla\langle T\rangle)-\Delta H_{vap,f}\langle\dot{m}_{v,sa}\rangle \quad (5\text{-}26)$$

where,

$$(\rho C_p)_{eff}=(1-\varepsilon)\rho_s C_{p,s}+\varepsilon[S_{l,p}\langle\rho_{l,p}\rangle^{l,p}(C_{p,l})_p+S_{l,sa}\langle\rho_{l,sa}\rangle^{l,sa}(C_{p,l})_{sa}]$$
$$+\varepsilon S_g[\langle\rho_{g,sa}\rangle^g(C_{p,g})_{sa}+\langle\rho_{g,i}\rangle^g(C_{p,g})_i] \quad (5\text{-}27)$$

5.3.3 Initial and Boundary Conditions

The initial temperature and the initial total gas pressure are 300 K and 100 kPa. The initial liquid saturations of the LMW component and the HMW component are 0.4 and 0.6, respectively. Initial pores of 0.4 vol% are assumed.

At OA (symmetry axis) and OB (impermeable and adiabatic wall), the gradient normal to the surfaces of the liquid saturation of LMW component, the total gas pressure, and the temperature are set to zero. At AC (top surface), the surface mass flux boundary condition is used for the liquid saturation of LMW component. This is

$$(J_{l,sa}+J_{g,sa})_{surface}=[h_m(\rho_{g,sa})_{surface}] \quad (5\text{-}28)$$

where $(J_{l,sa})_{surface}$ and $(J_{g,sa})_{surface}$ are the mass fluxes of the liquid and the vapor LMW component and h_m is the mean mass transfer coefficient. It is estimated as (Incropera and Dewitt, 2002)

$$h_m=0.664\left(\frac{D_{g,i-sa}}{l}\right)\left(\frac{v_\infty\rho_{g,i}L}{\mu_{g,i}}\right)^{1/2}\left(\frac{\mu_{g,i}}{\rho_{g,i}D_{g,i-sa}}\right)^{1/3} \quad (5\text{-}29)$$

where $D_{g,i-sa}$ is the diffusion coefficient of total gas system, l is the distance in z-axis, v_∞ is the average free stream velocity above the compact, L is the total length of the

PIM compact. The average free stream velocity v_∞ is estimated as 1.4×10^{-3} m/s. It is based on a nitrogen volumetric flowrate of 4 liter/min and the furnace chamber cross-section area (above the compact) of 0.22×0.215 m^2. Equation (5-28) is expanded as

$$-\Gamma_{sa}\frac{\partial S_{l,sa}}{\partial x_k}=\Gamma_{sa}^{T}\frac{\partial\langle T\rangle}{\partial x_k}+\Gamma_{sa}^{P}\frac{\partial\langle P_{g,t}\rangle^{g}}{\partial x_k}+\Gamma_{sa}^{pv}\frac{\partial\langle p_{g,sa}\rangle^{g}}{\partial x_k}+[h_m\frac{(p_{g,sa})_{surface}M_{sa}}{R\langle T\rangle}] \tag{5-30}$$

Equation (5-30) is the boundary condition for the liquid saturation of LMW component at AC. As there is no convective mass transfer at BC (vertical surface) the last term of Eq. (5-28) is set to zero at the vertical surface. Note that x_k is the coordinate normal to the boundary of interest.

At AC and BC, the boundary condition for the total gas pressure is given by Eq. (5-14). The temperature at the outer surfaces is calculated based on the measured temperatures (see Fig. 5.20) for the temperature range from 300 K to 519 K. This is

$$(T)_{surface}=-6.0326\times10^{-16}t^4+4.2957\times10^{-11}t^3-1.3047\times10^{-6}t^2 +2.3920\times10^{-2}t+299.51 \tag{5-31}$$

The experimental investigations were conducted within the temperature range of 300 K and 519 K. To investigate the whole removal process of the LMW component, the heating schedule from Table 5.2 is used after 519 K. As shown in Table 5.2, a multi-segment heating schedule, which is a common practice for the thermal debinding of LMW component in industry, is used. To facilitate comparisons with the experimental data, the binder removal during the cooling period is included in the model. The temperature at the outer surfaces during the cooling period is calculated using Eq. (5-16) with a measured cooling rate of -0.4 K/min.

Table 5.2 LMW component: Heating schedule for thermal debinding

No	Temperature range (K)	Heating ramp (K/min)	Holding time (min)
1	519-523	1	30
2	523-573	1	60
3	573-583	1	60
4	583-593	1	60
5	593-603	1	120

5.3.4 Results and Discussions

Figure 5.21 shows the flow chart of the thermal debinding of LMW component. Once the evaporation temperature is reached ($\langle T \rangle \geq T_2$; Fig. 2.2), liquid LMW component $S_{l,sa}$ evaporates into vapor LMW component. This results in the buildup of vapor pressure $\langle p_{g,sa} \rangle^g$ and thus the increase in the total gas pressure $\langle P_{g,t} \rangle^g$.

A grid independence study was performed using 6×4, 18×12 and 36×24 control volumes. The maximum binder liquid saturation difference between the last two meshes is less than 5 % over the whole debinding period. Thus, the 18×12 control volumes were used. The time step of 10/64 s is sufficient to achieve time independence.

5.3.4.1 Comparisons with Experimental Results

To check the accuracy of the numerical method, six regions of the brown part are used (see Fig. 4.9). These consist of four internal regions, which are (1,2), (2,3), (3,1) and (5,2), and two outer regions, which are (1,4) and (4,4). Region (5,2) is considered as an internal region because there is no mass transfer across the vertical surface of the PIM

compact. The results at four debinding times namely, 17250 s, 25290 s, 25275 s, and 29025 s will be presented and discussed (refer section 5.1.2 for the experimental results).

Figure 5.22(a) shows good agreements (with ≤ 6 % error) between the numerical results and the experimental data for the first debinding time. For the second debinding time, the errors range between 1 % and 11 % for the four internal regions. The errors in the outer regions range between 18 % and 29 % (see Fig. 5.22(b)). For the third debinding point, the errors in the internal regions range between 6 % and 18 %. The errors are about 40 % in the outer regions (see Fig. 5.22(c)). Figure 5.22(d) show that the numerical results agree well with the experimental data for the last debinding time with errors ranging between 2 % and 12 % for the internal regions and 25 % for the outer regions. Larger errors are observed at the outer regions. This might due to the experimental uncertainties or the estimation of the average free stream velocity above the compact is lower as compared to that of the actual case.

5.3.4.2 Binder Removal

For ease of discussion, the residual binder curve is divided into 8 time zones as shown in Fig. 5.23. Table 5.3 shows the details of the typical debinding points within these time zones. The table entries are the debinding time, the surface temperature, the residual binder, the debinding rate, and the heating rate. Figure 5.24 shows the maximum vapor pressure versus the debinding time. There are two typical periods for the maximum vapor pressure. These are the increasing and decreasing periods. The increasing period of vapor pressure occurs when the temperature increases. The

decreasing period of vapor pressure occurs when the temperature is maintained at a constant value.

After 14180 s, the liquid LMW component begins to evaporate (see Fig. 5.23). Within time zones 2-3, the debinding rate increases as temperature increases. As the evaporation rate of liquid LMW component increases, the maximum vapor pressure increases (see Fig. 5.24). However, the binder removal rate decreases during the first holding period where the temperature was maintained at 523 K (Time zone 4). During this holding period, the maximum vapor pressure remains almost constant. During the heating from 523 K to 573 K, the debinding rate increases (Time zone 5) and results in significant increase in the maximum vapor pressure. This indicates that the evaporation rate of liquid LMW component increases significantly at high temperatures ($T \geq 523$ K). The debinding rate increases to the maximum during the isothermal heating at 573 K (Time zone 6). This shows that holding the temperatures would not retard the binder removal. As shown in Fig. 5.24, the maximum vapor pressure decreases during each holding period. This implies that the holding period could avoid the buildup of excessive vapor pressure inside the compact.

In time zone 8, the debinding rate begins to decrease even though the debinding temperatures increase (see Fig. 5.23). In this period, less LMW component (< 30 %) remains in the compact and thus the evaporation rate decreases. Figure 5.24 shows that the maximum vapor pressure decreases as the debinding rate decreases. After 14.2 hours, the early stage of thermal debinding is completed.

Table 5.3 LMW component: Debinding points of residual binder curve

Point	Time (s)	Temperature (K)	Residual Binder	Debinding Rate (1/s)	Heating Rate
1	14180	474.5	0.974	1.8×10^{-6}	Experimental
2	21160	507.5	0.90	1.2×10^{-5}	Experimental
3	26325	519	0.775	2.5×10^{-5}	Experimental
4	26565	523	0.77	2.1×10^{-5}	1 K/min
5	28360	523	0.74	1.6×10^{-5}	Isothermal
6	31360	573	0.65	3.1×10^{-5}	1 K/min
7	34960	573	0.33	8.8×10^{-5}	Isothermal
8	35560	583	0.28	8.6×10^{-5}	1 K/min
9	39160	583	0.11	4.8×10^{-5}	Isothermal
10	39760	593	0.09	3.1×10^{-5}	1 K/min
11	43360	593	0.03	1.7×10^{-5}	Isothermal
12	43960	603	0.02	1.5×10^{-5}	1 K/min
13	51160	603	0.002	2.9×10^{-6}	Isothermal

5.3.4.3 Binder Distribution

During this debinding stage, the total gas pressure always equals the atmospheric pressure. Thus the discussions are focused on the distributions of the temperature, the liquid saturation of LMW component, and the vapor pressure. For ease of discussion, the region of the compact that is close to the symmetry axis ($x = 0 - 7.5\times10^{-3}$ m) is defined as Region A and the region of the compact that is close to the vertical surface ($x = 7.5\times10^{-3} - 1.5\times10^{-2}$ m) is defined as Region B (see Fig. 5.25).

The mass fluxes of LMW component at the top surface (Eq. (5-30)) will be discussed extensively. The left side of Eq. (5-30) is the mass flux due to the gradient of liquid

saturation of LMW component. On the right side, sequentially, these terms are the mass fluxes due to the surface tension gradient, the pressure driven action, and the convective mass transfer, respectively. Mass fluxes due to the pressure driven action are one to three orders of magnitude smaller than the other mass fluxes. Thus, only the mass fluxes due to the gradients of the liquid saturation and the surface tension, and the convective mass transfer are discussed. Table 5.4 shows these mass fluxes at Regions A and B for three debinding times.

At any given time, the temperature differences over the PIM compact are small (see Figs. 5.27(a)-(b)). Due to this small temperature differences, the liquid LMW component evaporates throughout the whole compacts at 9000 s (see Figs. 5.28(a)-(b)). The liquid LMW component near the outer surfaces begins to migrate outwards due to higher temperatures at that region (see Fig. 5.28(c)). At this time, the convective mass transfer (right side of the Eq.(5-28)) is two orders of magnitude smaller than the total mass flux of LMW component at the outer surface (left side of the Eq.(5-28)). As a result, the LMW component accumulates at the outer surfaces (see Fig. 5.28(a)).

Due to the increase in temperature, the convective mass transfer increases by two orders of magnitude at 19800 s. As a result, the liquid LMW component evaporates and is removed faster at the top surface (see Figs. 5.29(a)-(b)). Though there is no mass transfer across the vertical surface, the concentration of LMW component near the vertical surface is low as compared to that of internal region. This is due to the higher temperatures at the vertical surface which result in higher evaporation rate of liquid LMW component. At this time, the liquid LMW component over the whole compact begins to migrate towards the top surface (see Fig. 5.29(c)). The mobility of

the liquid LMW component increases as its viscosity decreases (10^{-4} Pa s) at 502 K (see Fig. 5.26).

At 26325 s, the removals of liquid and vapor LMW component maintain at higher rates at the outer surfaces (see Figs. 5.30(a)-(b)). However, the removal rate of liquid LMW component at the top surface of Region A is higher compared to that of Region B. This can be seen from Table 5.4, the mass flux due to the liquid saturation gradient at the top surface of Region A (1.17×10^{-4} kg/m^2 s) is 27 % higher than that of Region B. As temperature increases, the migration rate of liquid LMW component towards the top surface increases (see Fig. 5.30(c)). The average magnitude of the velocity of liquid LMW component increases 2 times as compared to that of 19800 s.

At 30165 s, the liquid LMW component still decreases towards the top surface. However, the concentration of liquid LMW component is higher at the top surface of Region B as compared to that of Region A (see Fig. 5.31(a)). From Table 5.4, there is a slightly higher (< 1 %) convective mass flux at the top surface of Region B. However, the mass flux due to the surface tension gradient at the top surface of Region A is 67 % higher than that of Region B. As a result, the mass flux due to the liquid saturation gradient at the top surface of Region A (1.78×10^{-4} kg/m^2 s) is 21 % higher than that of Region B. This results in higher removal rate of liquid LMW component from the Region A. The presence of the gradient of liquid LMW component draws the liquid LMW component from the Region B towards the top surface of Region A (see Fig. 5.31(c)). Figure 5.31(b) shows that the vapor pressure is higher at the outer surfaces. At this time, the removal rate of the vapor LMW component is lower compared to the evaporation rate.

At 31365 s, the removal rate of liquid LMW component in Region A is higher compared to that of Region B (see Fig. 5.32(a)). The concentration of liquid LMW component near the vertical surface is higher. As a result, the gradient of liquid LMW component (between Regions A and B) increases which increases the migration rate of liquid HMW component from Region B towards the top surface of Region A (see Fig. 5.32(c)). As shown in Fig. 5.32(b), the higher concentration of liquid LMW component and temperatures in Region B have increased evaporation rate at that region.

At 34965 s, the liquid LMW component exhibits a similar trend to that of 31365 s (see Fig. 5.33(a)). However, the convective mass flux (1.13×10^{-4} kg/m s) in region B becomes 3 % higher than that of Region A. The convective mass flux is three orders of magnitude greater than the mass flux due to the surface tension gradient. As a result, the mass flux due to the liquid saturation gradient at the top surface of Region B (1.10×10^{-4} kg/m s) becomes 4 % higher than that of Region A. Due to this faster removal of liquid LMW component, the liquid LMW component (at the Region B) tends to migrate towards the top surface of Region B (see Fig. 5.33(c)). Concurrently, the vapor pressure decreases (compared to that of 31365 s) during this isothermal heating (see Fig. 5.33(b)). The vapor LMW component at the top surface escapes faster from the compact.

The binder distributions of the liquid LMW component agree qualitatively with the binder distributions of the experimental data. In the first debinding time, binder accumulation at the outer surfaces is observed (see Fig. 5.4(a) and 5.5(a)-(b)). In the

last three debinding times, the residual binder decreases towards the top surface and increases towards the vertical surface (see Figs. 5.4(b)-(d) and 5.5(c)-(h)).

Table 5.4 Mass fluxes at outer surface

Time (s)	Region	Mass flux due to gradient of liquid saturation (kg/m^2 s)	Mass flux due to gradient of surface tension (kg/m^2 s)	Mass flux due to convective mass transfer (kg/m^2 s)
26325	A	1.17×10^{-4}	6.28×10^{-5}	3.798×10^{-5}
	B	8.59×10^{-5}	3.59×10^{-5}	3.799×10^{-5}
30165	A	1.78×10^{-4}	6.95×10^{-5}	1.010×10^{-4}
	B	1.47×10^{-4}	4.16×10^{-5}	1.012×10^{-4}
34965	A	1.06×10^{-4}	9.11×10^{-7}	1.098×10^{-4}
	B	1.10×10^{-4}	8.85×10^{-7}	1.133×10^{-4}

5.3.4.4 Mass Transfers

The mass transfers of the liquid and gas phases have been analyzed. The factors which cause mass transfers are the capillary driven action, the binary diffusion in solution, and the pressure driven action. The mass transfers of the liquid and the gas phases are calculated based on Eqs. (2-31) and (2-57), respectively. The mass transfer of LMW component due to the capillary driven action (the gradients of liquid saturation and surface tension) is

$$(-\langle\rho_{l,sa}\rangle^{l,sa}\psi_{l,sa}\frac{\partial\langle P_{c,sa}\rangle}{\partial S_{l,sa}})\nabla S_{l,sa}+\Gamma_{sa}^{T}\nabla\langle T\rangle \tag{5-32}$$

The mass transfer of LMW component due to the binary diffusion in solution is

$$(\langle\rho_{l,sa}\rangle^{l,sa}D_{l,p-sa}(\frac{1-\theta_{l,sa}}{S_{l,sa}+S_{l,p}})\nabla S_{l,sa}+\Gamma_{sa}^{sp}\nabla S_{l,p} \tag{5-33}$$

The mass transfer of LMW component due to the pressure driven action is

$$\Gamma_{sa}^{P}\nabla\langle P_{g,t}\rangle^{g} + \Gamma_{sa}^{pv}\nabla\langle p_{g,sa}\rangle^{g} \tag{5-34}$$

The mass flux of gas phase is

$$\Gamma_{p}\nabla\langle P_{g,t}\rangle^{g} + \Gamma_{P}^{sa}\nabla\langle p_{g,sa}\rangle^{g} \tag{5-35}$$

LMW component: The mass transfer due to the capillary driven action is of the orders of 10^{-8}-10^{-5} kg/m^2 s. The mass transfer due to the binary diffusion in solution is the orders of 10^{-9}-10^{-5} kg/m^2 s. The mass transfer due to the pressure driven action is the orders of 10^{-16}-10^{-10} kg/m^2 s. The mass transfers due to the capillary driven action and the binary diffusion in solution are two to five orders of magnitude larger than the pressure driven action. Thus the contribution of the pressure driven action to the mass transfer of LMW component is negligible during the early stage of thermal debinding.

Gas phase: The mass transfer due to the pressure gradients is of the orders of 10^{-16}-10^{-7} kg/m^2 s. The mass transfer of the gas phase is at least two orders of magnitude lower than the mass transfer of the liquid phase. This indicates that the liquid phase transport plays a dominant role in mass transfers during the early stage of thermal debinding.

Based on the results of section 5.3.4.3 and this section, the binder removal mechanisms are now discussed. At the outer surface, liquid LMW component evaporates and is removed by convective mass transfer. The liquid LMW component in the internal region either evaporates into vapor phase and diffuses outwards or migrates outwards before it evaporates at the outer surface. Due to the fewer pores initially inside the compact, the total gas pressure always equals to the atmospheric pressure. The mass

transfers due to pressure driven action are found to be negligible during this early stage of thermal debinding. The liquid LMW component tends to be driven towards the outer surface by the capillary driven action and the binary diffusion in the solution. Subsequently, the liquid LMW component evaporates and is removed by convective mass transfer at the outer surface.

5.3.5 Concluding Remarks

A limiting case is deduced from the mathematical model to simulate the thermal debinding of LMW component. This model is solved numerically and is validated by the experimental data. The physical trends of binder removal are presented and discussed. The mass transfer mechanisms during the thermal debinding are analyzed. The results show the liquid LMW component tends to migrate outwards and then is removed at the outer surface. The liquid phase transport is dominant over the gas phase transport during the early stage of thermal debinding.

5.4 Simulation on the Thermal Debinding of Two-Component Binder System

In this section, the simulation of the thermal debinding of two-component binder system is presented and discussed. This involves two stages, which are the early and the final stages (see Figs. 2.2 and 2.4).

5.4.1 Computational Domain

The computational domain is similar to that in section 5.2.1 (see Fig. 5.6).

5.4.2 Governing Equations

For the early stage of thermal debinding, which involves the temperature range between T_0 and T_4 (see Fig. 2.2), five variables are solved. These are the liquid saturation of LMW component $S_{l,sa}$ (Eq. 2-31), the liquid saturation of HMW component $S_{l,p}$ (Eq. 2-41), the liquid saturation of volatile fragments $S_{l,f}$ (Eq. 2-47), the total gas pressure $\langle P_{g,t} \rangle^g$ (Eq. 2-57), and the local temperature $\langle T \rangle$ (Eq. 2-27). For the final stage of thermal debinding that covers the temperatures from T_4 to T_5, four variables are solved. These are the liquid saturation of HMW component $S_{l,p}$ (Eq. 2-41), the liquid saturation of volatile fragments $S_{l,f}$ (Eq. 2-47), the total gas pressure $\langle P_{g,t} \rangle^g$ (Eq. 2-57), and the local temperature $\langle T \rangle$ (Eq. 2-27).

5.4.3 Initial and Boundary Conditions

The initial conditions of the temperature and the total gas pressure are 300 K and 100 KPa, respectively. The initial liquid saturations are 0.4 and 0.6 for the LMW

component and the HMW component, respectively. There is no volatile fragment initially. In this simulation, 0.8 vol% of initial pores is assumed in the compact.

At OA (symmetry axis) and OB (impermeable and adiabatic wall), the gradient normal to the surfaces of the liquid saturation of LMW component, the liquid saturation of HMW component, the liquid saturation of volatile fragments, the total gas pressure, and the temperature are set to zero. At AC and BC (outer surfaces), the flux boundary conditions are used for the liquid saturation of LMW component (Eq. 5-30) and the liquid saturation of HMW component (Eq. 5-12). The boundary values are given for the liquid saturation of volatile fragments (Eq. 5-13) and the total gas pressure (Eq. 5-14). The temperature at the outer surfaces is calculated using

$$(T)_{surface} = T_{in} + \frac{dT}{dt}t \tag{5-36}$$

where T_{in} is the initial temperature. For the early stage, a multi-segment heating schedule shown in Table 5.5 is used. A constant heating rate of 1 K/min is used for the final stage of thermal debinding.

Table 5.5 Heating Schedule for early stage of thermal debinding

No	Temperature (K)	Heating Rate (K/min)	Holding time (min)
1	300-473	1	30
2	473-523	1	30
3	523-573	1	30
4	523-573	1	90
5	573-583	1	90
6	583-593	1	90
7	593-603	1	90

5.4.4 Results and Discussions

The removal of two-component binder system, the phase changes of the binders, the buildups of the vapor and total gas pressures, and the binder distributions are discussed.

Grid independence study was performed using 6x4, 18x12 and 36x24 control volumes. The maximum binder liquid saturation difference between last two meshes is less than 6 % over the whole debinding period. Thus, 18x12 control volumes are used. The time step of 30/32 s is sufficient to achieve time independence.

5.4.4.1 Binder Removal and Distributions

Figures 5.34-5.36 show the removal of the two-component binder system, the LMW component, and the HMW component, respectively. As shown in Fig. 5.34, there are two distinct regions of binder removal, namely the early and the final stages.

For the early stage, the phase change rates, the surface mass fluxes, and the vapor pressures are discussed. Table 5.6 shows the orders of magnitude of the phase change rates and the surface mass fluxes. The phase changes are the evaporation of liquid LMW component, the thermal degradation of liquid HMW component, and the evaporation of liquid volatile fragments. The surface mass fluxes are the surface mass flux of liquid LMW component and the convective mass flux in the X- and Y-directions of the compact. Figure 5.37 shows the maximum vapor pressures of the LMW component and the volatile fragments. The distributions of the liquid saturations

of LMW and HMW components, and the vapor pressure of LMW component are presented (Figs. 5.40-5.43).

For the final stage, the thermal degradation of liquid HMW component, the evaporation of liquid volatile fragments, and the vapor and total gas pressures are discussed. Figure 5.38 shows the maximum values of the thermal degradation rate of liquid HMW component and the evaporation rate of liquid volatile fragments. Figure 5.38 shows the maximum vapor and total gas pressures. The distributions of the liquid saturation of HMW component, the liquid saturation of volatile fragments, the total liquid saturation, and the vapor pressure are also presented (Figs. 5.44-5.47).

The evaporation rates and the vapor pressures exhibit increasing and decreasing trends during the early stage. As temperature increases, the evaporation rates and the vapor pressures increase. The evaporation rates and the vapor pressures decrease when the temperature is maintained at a constant value (holding period). The binder distributions during the thermal debinding of two-component binder system are similar as those discussed in the previous sections for the thermal debinding of the LMW component (section 5.3.4.3) and the HMW component (sections 5.2.4.3). The detailed discussions of the binder distributions can be found in above-mentioned sections.

During the early stage, almost 40 % of binder is removed and the removed binder is mainly LMW component (see Figs. 5.33-5.35). As shown in Table 5.6, the thermal degradation rate of HMW component into volatile fragments is low ($< 10^{-2}$ kg/m^3 s) at low temperatures. As a result, the removal of the HMW component is insignificant (< 5 %) at this stage (see Figs. 5.36 and 5.40(b)-5.43(b)).

For the period of $t \leq 9000$ s, the removal of the LMW component is small (< 1%) as shown in Fig. 5.35. This is because of the evaporation rate (< 10^{-4} kg/m^3 s) and the surface mass fluxes ($\leq 10^{-3}$ kg/m^3 s) are low as the temperature is low ($T \leq 450$ K) (see Table 5.6). Due to the low surface mass fluxes and the outward migration of the LMW component (discussed in section 5.3.4.3), the accumulation of the liquid LMW component is observed at 7980 s (see Fig 5.40(a)). At this time, the buildups of the vapor pressures of the LMW component and the volatile fragments are also low due to the low evaporation rates (see Figs. 5.37 and 5.40(c)).

During the period of 10000 s $\leq t <$ 19000 s, the surface mass fluxes (10^{-2} to 10^{-1} kg/m^2 s) increase as temperature increases (from 467 K to 557 K) (see Table 5.6). The evaporation rate of liquid LMW component decreases to 10^{-10} kg/m^3 s during the first holding period (10380 s to 12180 s) and then increases to 10^{-5} kg/m^3 s. These result in the significant removal of LMW component. More than 50 % of the LMW component is removed (see Fig. 5.35). The surface mass fluxes are at least three orders of magnitude higher than the evaporation rate of the liquid LMW component. This indicates that the liquid LMW component tends to migrate outwards to the outer surfaces rather than evaporates internally. This is because there are less pores inside the compact during the early stage. As shown in Figs. 5.41(a)-5.42(a), the removal rate of liquid LMW component is higher at the outer surfaces. The higher vapor pressure of LMW component in the internal region (compared to outer surfaces) indicates that the vapor LMW component escape faster at the outer surfaces (see Figs. 5.41(c)-5.42(c)). During this period, the maximum vapor pressures increase as evaporation rates increase (see Fig. 5.37). However, the maximum vapor pressure of the volatile

fragments is higher compared to the maximum vapor pressure of the LMW component. This is because the degradation and the evaporation rates of the HMW component are higher compared to the evaporation rate of LMW component during this period. As shown in Table 5.6, the thermal degradation rate of HMW component is at least an order of magnitude higher than the evaporation rate of LMW component during this period. The higher thermal degradation rate at this period is due to the existence of weak points in the HMW component. The lower activation energy is required to break these weak points (Chan and Balke, 1997). As a result, these weak points of the HMW component degrade easier at low temperatures.

During the period of 19000 s $\leq t <$ 22200 s, the surface mass fluxes maintain in order of 10^{-1} kg/m^2 s (see Table 5.6). After more than 50 % of LMW component is removed, more pores are created. Moreover, the temperature increases from 557 K to 573 K. As a result, the evaporation rate increases. As shown in Table 5.6, the evaporation rate begins to increase significantly from 10^{-5} to 10^{-2} kg/m^3 s. The surface mass fluxes remain an order of magnitude higher than the evaporation rate of LMW component. Thus, the removal rate of the liquid LMW component at the outer surface remains higher at 19980 s (see Fig. 5.43(a)). The vapor pressure also increases compared to that of 18780 s due to the increase in evaporation rate (see Figs. 5.42(c) and 5.43(c)).

For the period of 22200 s $\leq t <$ 33460 s, the binder removal rate of liquid LMW component decreases after less than 25 % of LMW component remains in the compact (see Figs. 5.35). This is due to the decrease (by half) in evaporation rate of LMW component. During this period, the mass transfer due to the convective mass transfer is at least an order of magnitude higher than the surface liquid mass flux of LMW

component (see Table 5.6). This indicates that the liquid LMW component tends to evaporate into vapor LMW component before migrating towards the outer surfaces at high temperatures ($T > 573$ K).

Overall, the LMW component tends to be removed faster at the outer surfaces ($t > 9000$ s) (see Figs. 5.41(a)-5.43(a)). The maximum orders of magnitude for the migration/diffusion mass fluxes (discussed in section 5.3.4.4), the surface mass fluxes, and the evaporation rate of LMW component are 10^{-5} kg/m^2 s, 10^{-1} kg/m^2 s and 10^{-2} kg/m^3 s, respectively. The surface mass fluxes are at least an order of magnitude higher than the other two mechanisms. These indicate that the early stage of thermal debinding is dominated by a surface controlled reaction.

During the final stage, 60 % of binder (HMW component) is removed (see Figs. 5.34-5.36). For the period of $t < 35130$ s, the thermal degradation rate of liquid HMW component and the evaporation rate of liquid volatile fragments are low (< 10^{-2} kg/m^3 s) (see Table 5.6 and Fig. 5.38). As a result, the removal rate of binder and the buildups of pressures are low (see Figs. 5.36 and 5.39).

During the period of 35130 s $\leq t <$ 37305 s, the thermal degradation rate increases to the order of 10^{-2} kg/m^3 s as temperature increases (from 604 K to 667 K) (see Fig. 5.38). This results in the increase in binder removal rate, more than 15 % of the HMW component is removed within this period (see Fig. 5.36). The evaporation rate of liquid volatile fragments remains in the order of 10^{-3} kg/m^3 s. As a result, the buildups of vapor and total gas pressures remain low (see Fig. 5.39). As shown in Fig. 5.44(a), the liquid HMW component degrades throughout the compact at 36180 s. The liquid and

vapor volatile fragments escape faster at the outer surfaces. Due to this, the liquid volatile fragments, the total liquid saturation, and the vapor pressure decrease towards the outer surfaces (see Figs. 5.44(b)-(d)).

During the period of 37305 s $\leq t <$ 38310 s, the thermal degradation rate and the evaporation rate increases to 10^{-1} and 10^{-2} kg/m^3 s, respectively, as temperature increases (from 667 K to 684 K) (see Fig. 5.38). More than 50 % binder is removed during this period as shown in Fig. 5.36. The increase in evaporation rate results in the increases in vapor and total gas pressures (see Fig. 5.39). As shown in Fig. 5.45(a), liquid HMW component degrades faster at the corners of the compact at 37380 s. The removal rates of liquid and vapor volatile fragments remain higher at the outer surfaces (see Fig. 5.45(b) and (d)). As a result, the concentration of total liquid binder remains lower at the outer surfaces (see Fig. 5.45(c)).

During the period of 38310 s $\leq t <$ 39270 s, the thermal degradation rate and the evaporation rate are of the same order (10^{-1} kg/m^3 s) and reach the maximum at almost the same time (see Fig. 5.38). The thermal degradation of liquid HMW component is no longer dominant over the evaporation rate of liquid volatile fragments as temperature continues to increase ($T >$ 684 K). This indicates that the liquid volatile fragments evaporate into vapor volatile fragments instantly after the degradation at high temperatures. As the evaporation rate increases, the vapor and total gas pressures increase to the maximum during this period (see Fig. 5.39). As shown in Figs. 5.46(a)-(d), the distributions of the liquid HMW component, the liquid volatile fragments, the total liquid binder, and the vapor pressure decrease towards the outer surfaces at 38580 s.

For the period of $t \geq 39270$ s, the thermal degradation rate and the evaporation rate remain in same order of magnitude (10^{-1} kg/m^3 s) (see Fig. 5.38). However, the thermal degradation and the evaporation rates begin to decrease after less than 25 % residual binder inside the compact (see Figs. 5.36 and 5.38). As the evaporation rate decreases, the vapor and total gas pressures decrease during this period (see Fig. 5.39). At 39270 s, slightly higher total liquid binder is observed at the outer surfaces (see Fig. 5.47(c)). The vapor pressure increases as compared to that of 38580 s (see Fig. 5.47(d)).

During the final stage of thermal debinding, the liquid binder distributes quite evenly throughout the compact (see Figs. 5.44(c)-5.47(c)). The maximum orders of magnitude for the migration/diffusion mass fluxes (discussed in section 5.2.4.4), the thermal degradation rate, and the evaporation rate are 10^{-3} kg/m^2 s, 10^{-1} kg/m^3 s and 10^{-1} kg/m^3 s, respectively. These indicate that the final stage of thermal debinding is dominated by the volumetric reactions. The thermal degradation dominates the binder removal during the period of $t < 38310$ s. After this, both of the thermal degradation and evaporation dominate the binder removal.

Table 5.6 Phase change rates and surface mass fluxes during early stage

Time (s)	Evaporation rate of LMW component (kg/m^3 s)	Degradation rate of HMW component (kg/m^3 s)	Evaporation rate of volatile fragments (kg/m^3 s)	Surface liquid mass flux of LMW component (kg/m^2 s)	Convective mass flux (kg/m^2 s)
$t \leq 9000$ s	10^{-8} to 10^{-5}	10^{-6} to 10^{-4}	10^{-10} to 10^{-5}	$\leq 10^{-3}$	10^{-8} to 10^{-4}
10000 s $\leq t <$ 19000 s	10^{-10} to 10^{-5}	10^{-4}	10^{-7} to 10^{-5}	10^{-2} to 10^{-1}	10^{-4} to 10^{-2}
19000 s $\leq t <$ 22200 s	10^{-5} to 10^{-2}	10^{-3}	10^{-4} to 10^{-3}	10^{-1}	10^{-2}
22200 s $\leq t <$ 33460 s	10^{-2}	10^{-3}	10^{-4} to 10^{-3}	10^{-5} to 10^{-3}	10^{-4} to 10^{-1}

5.4.5 Concluding Remarks

A mathematical model to simulate the thermal debinding of two-component binder system from the PIM compact has been established and solved numerically. The simulation results show two distinct stages of the binder removal. These are the early and final stages. The LMW component is removed during the early stage; meanwhile, the HMW component is removed during the final stage. For these two stages of thermal debinding, the phase changes, the buildups of the vapor and total gas pressures, the distributions of the binders and the pressures are discussed. The results indicate that the early stage of thermal debinding is dominated by a surface controlled reaction. The final stage of thermal debinding is dominated by volumetric reactions, which are the thermal degradation and the evaporation.

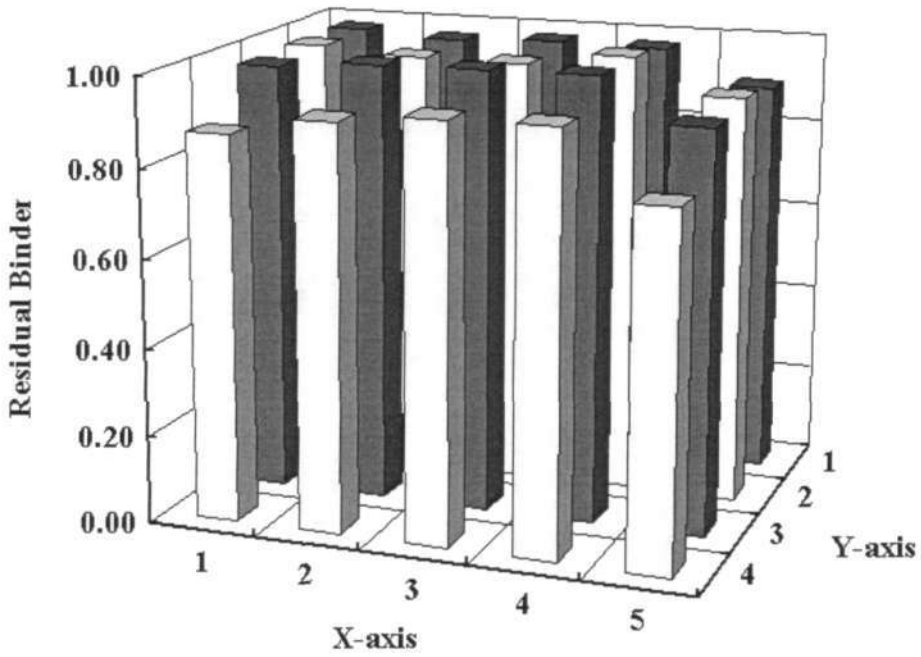

Figure 5.1(a) HMW component: Binder distribution at 26940 s

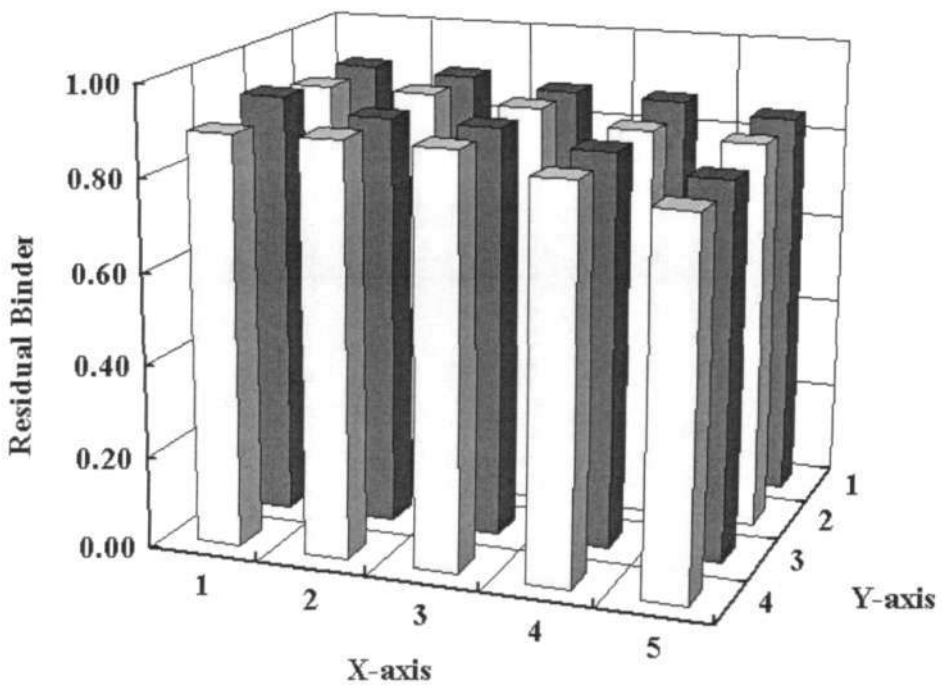

Figure 5.1(b) HMW component: Binder distribution at 28140 s

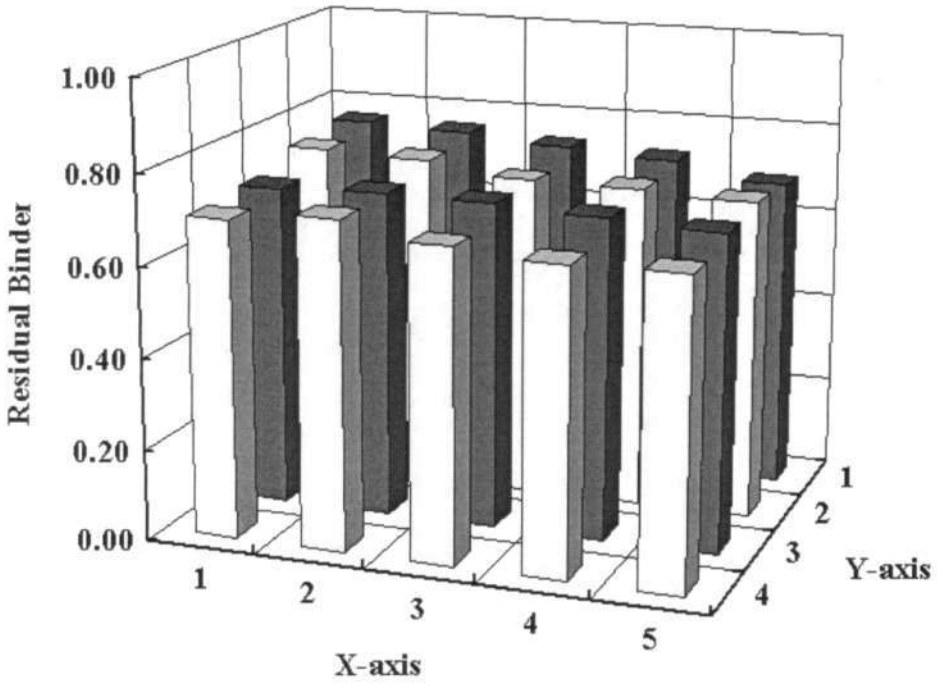

Figure 5.1(c) HMW component: Binder distribution at 29340 s

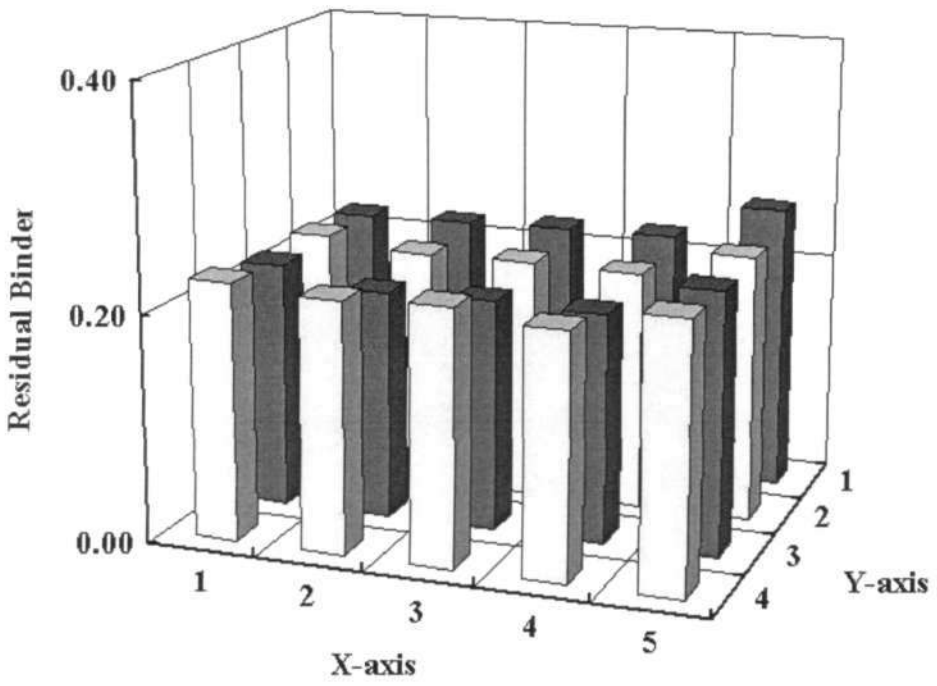

Figure 5.1(d) HMW component: Binder distribution at 30540 s

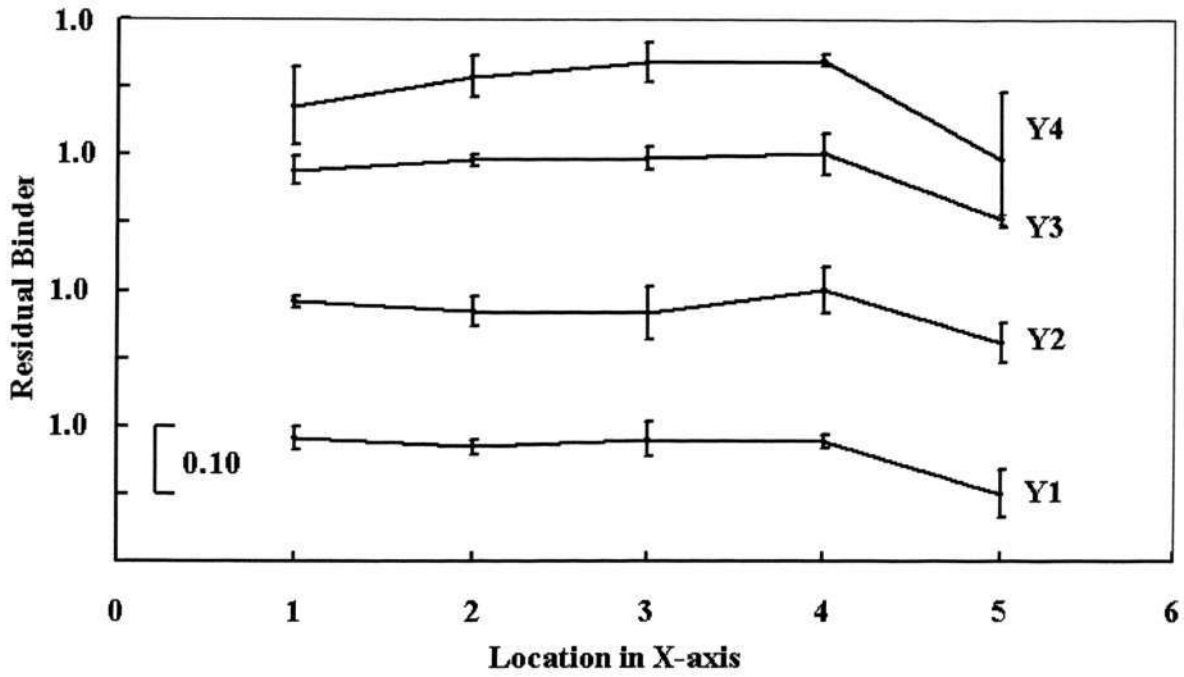

Figure 5.2(a) HMW component: Binder distribution in X-direction at 26940 s

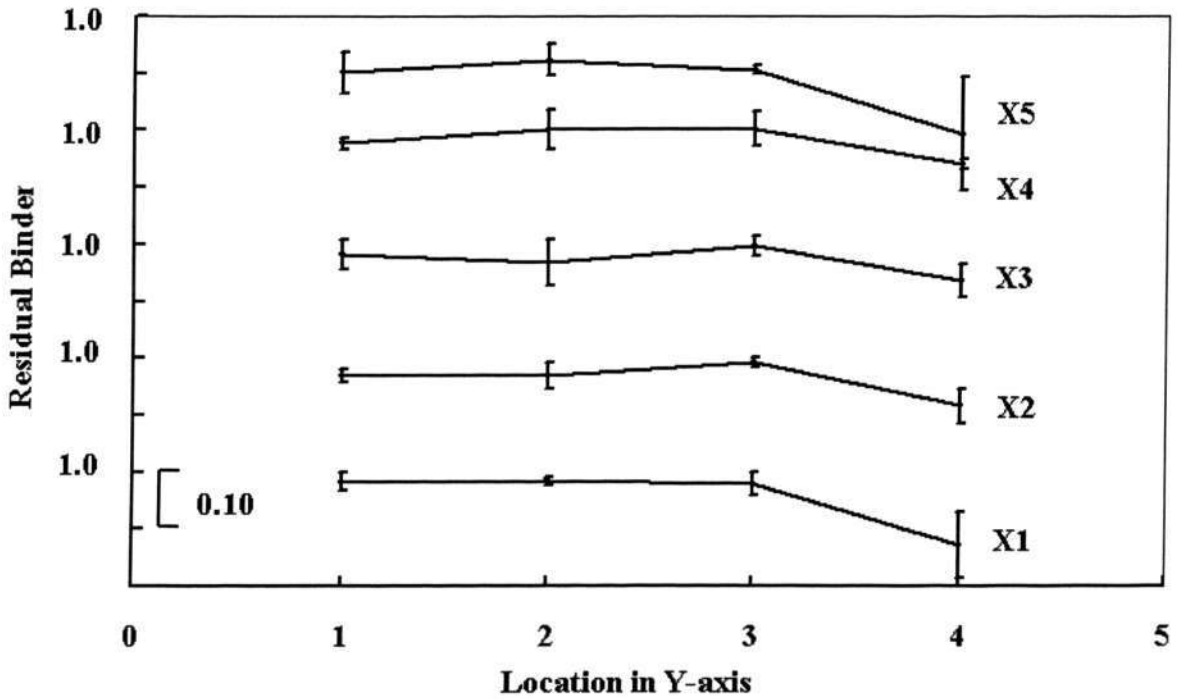

Figure 5.2(b) HMW component: Binder distribution in Y-direction at 26940 s

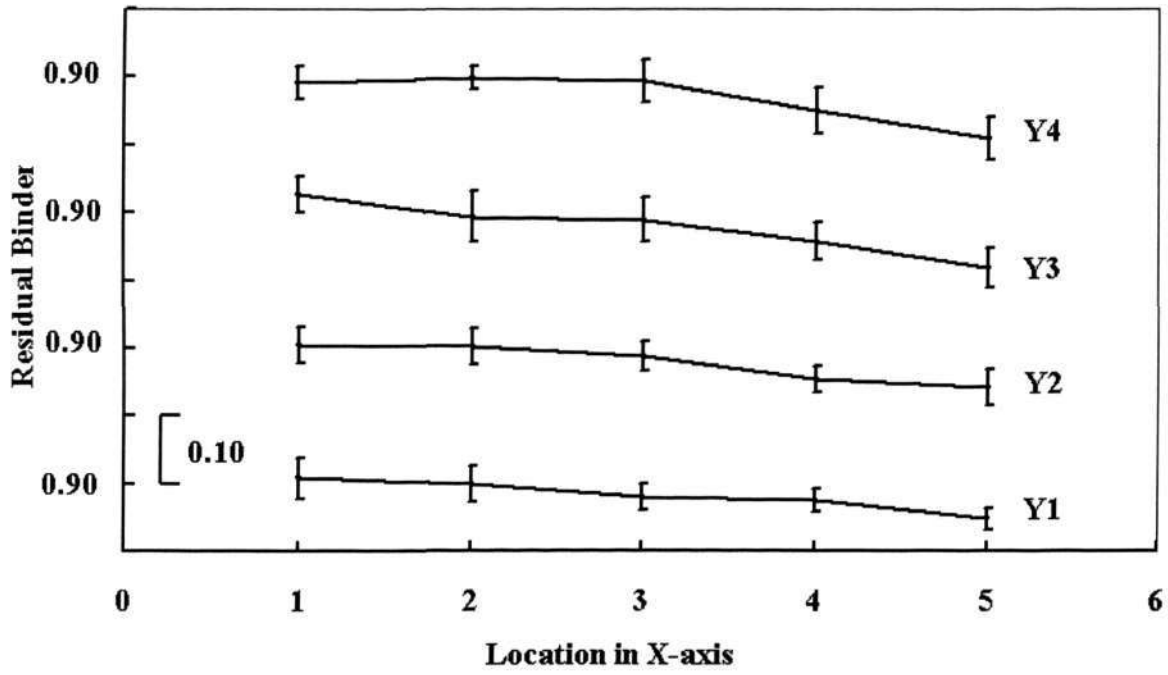

Figure 5.2(c) HMW component: Binder distribution in X-direction at 28140 s

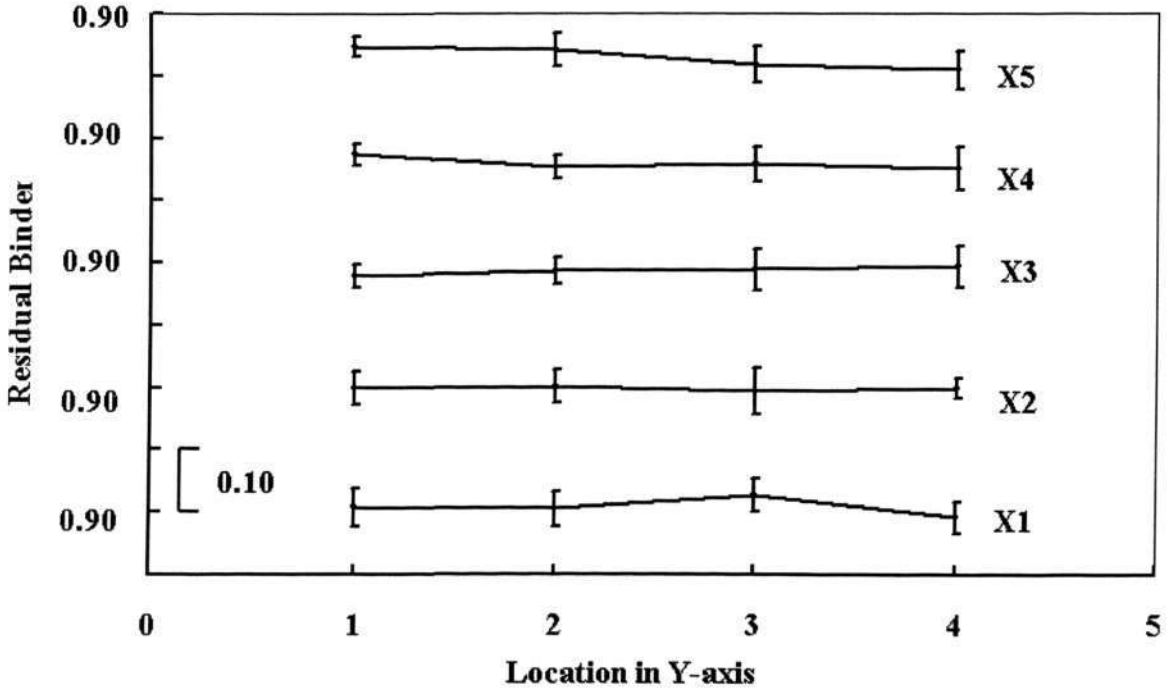

Figure 5.2(d) HMW component: Binder distribution in Y-direction at 28140 s

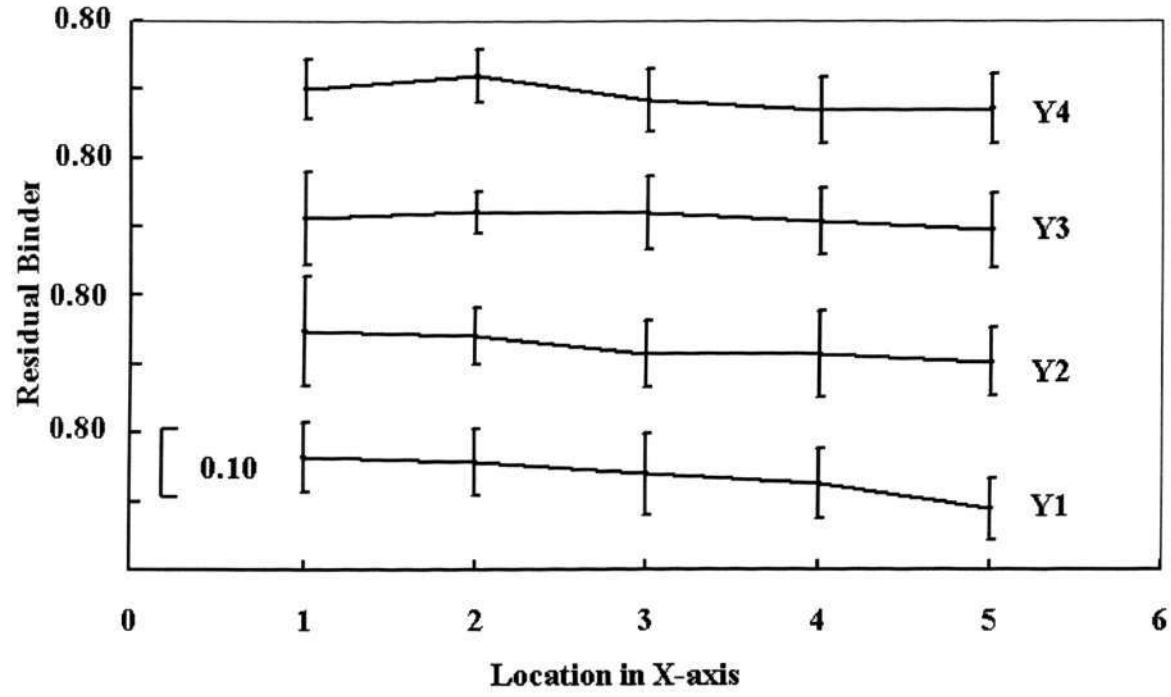

Figure 5.2(e) HMW component: Binder distribution in X-direction at 29340 s

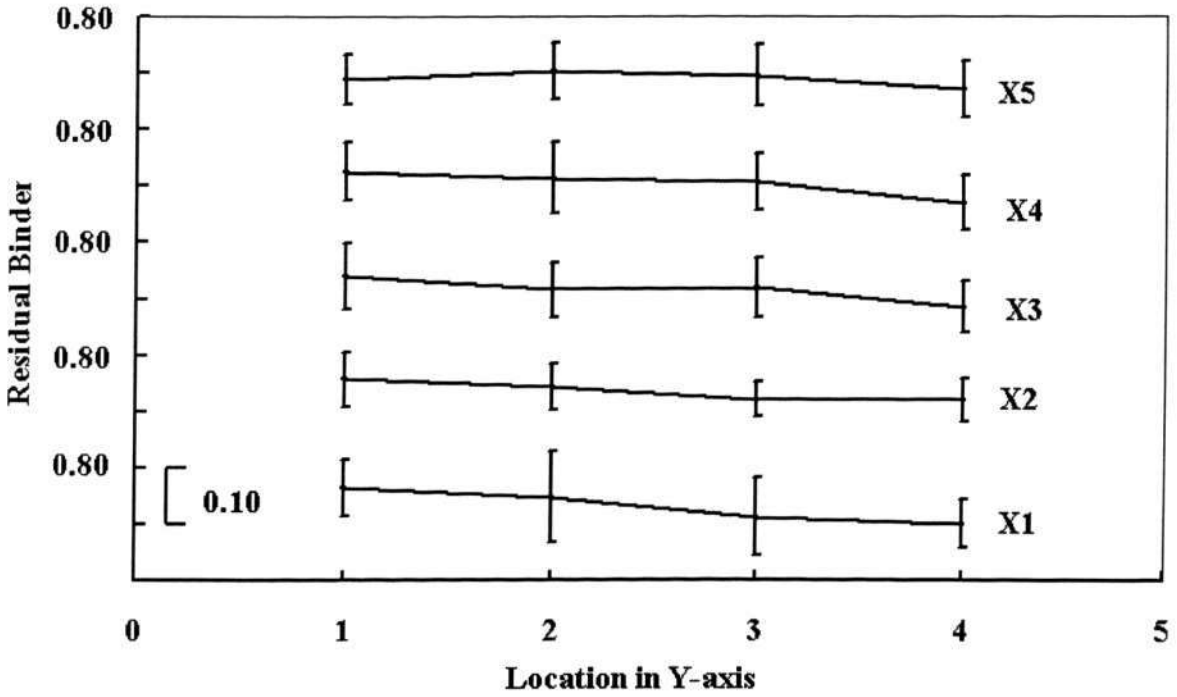

Figure 5.2(f) HMW component: Binder distribution in Y-direction at 29340 s

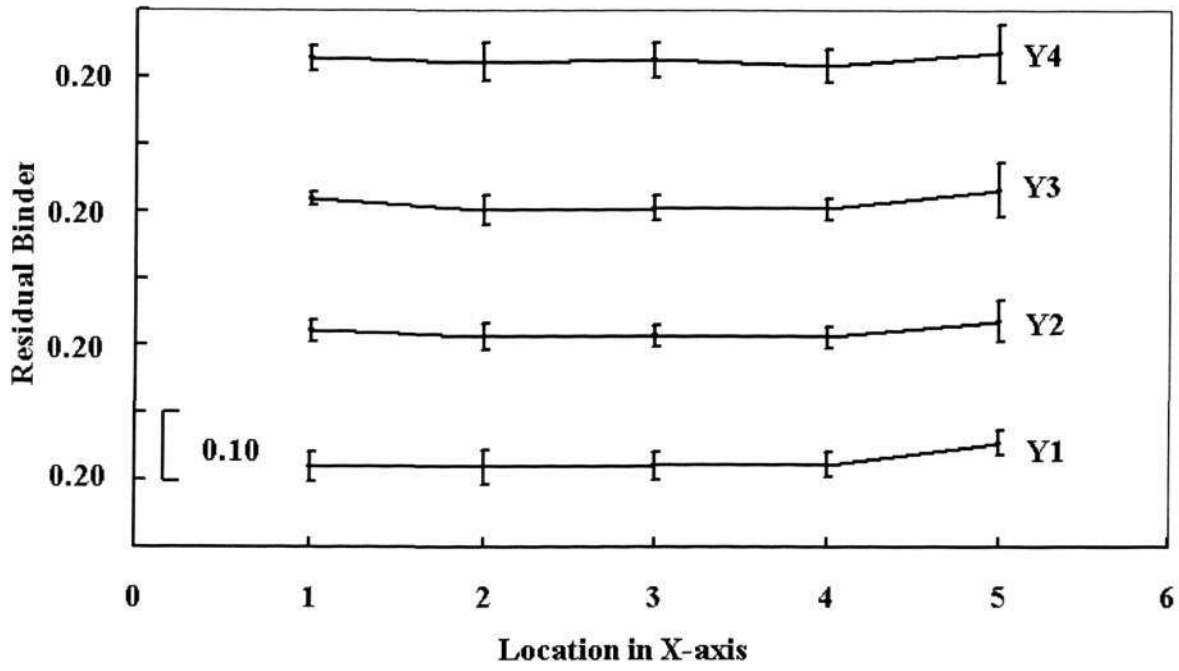

Figure 5.2(g) HMW component: Binder distribution in X-direction at 30540 s

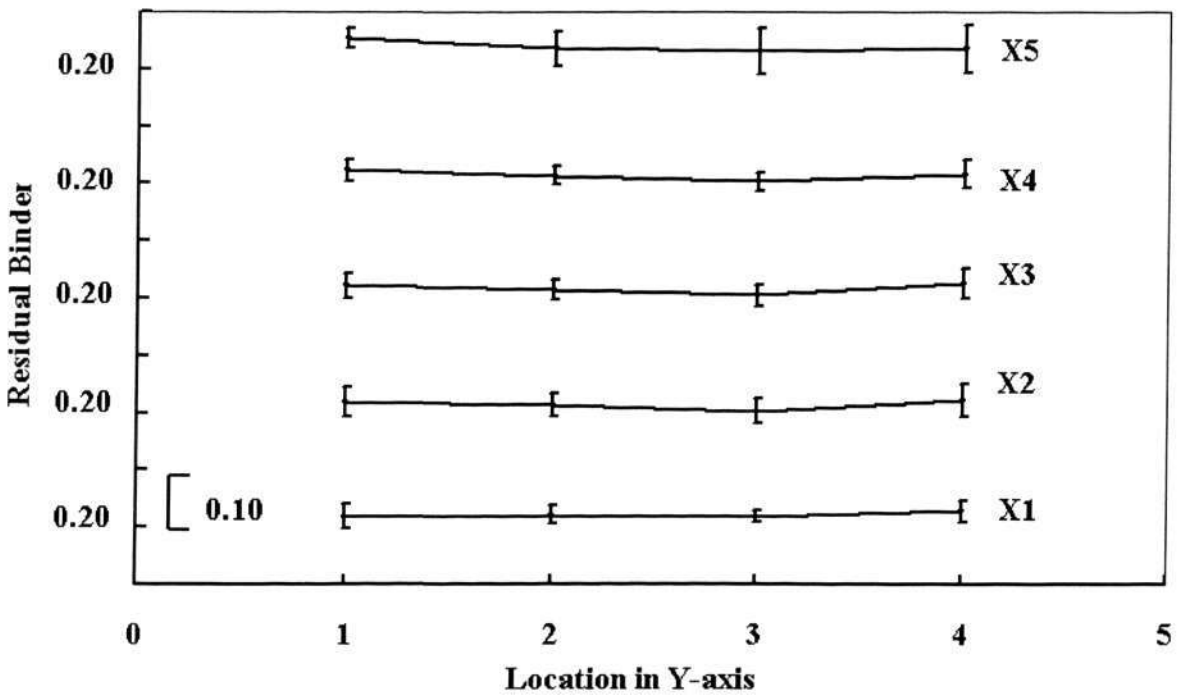

Figure 5.2(h) HMW component: Binder distribution in Y-direction at 30540 s

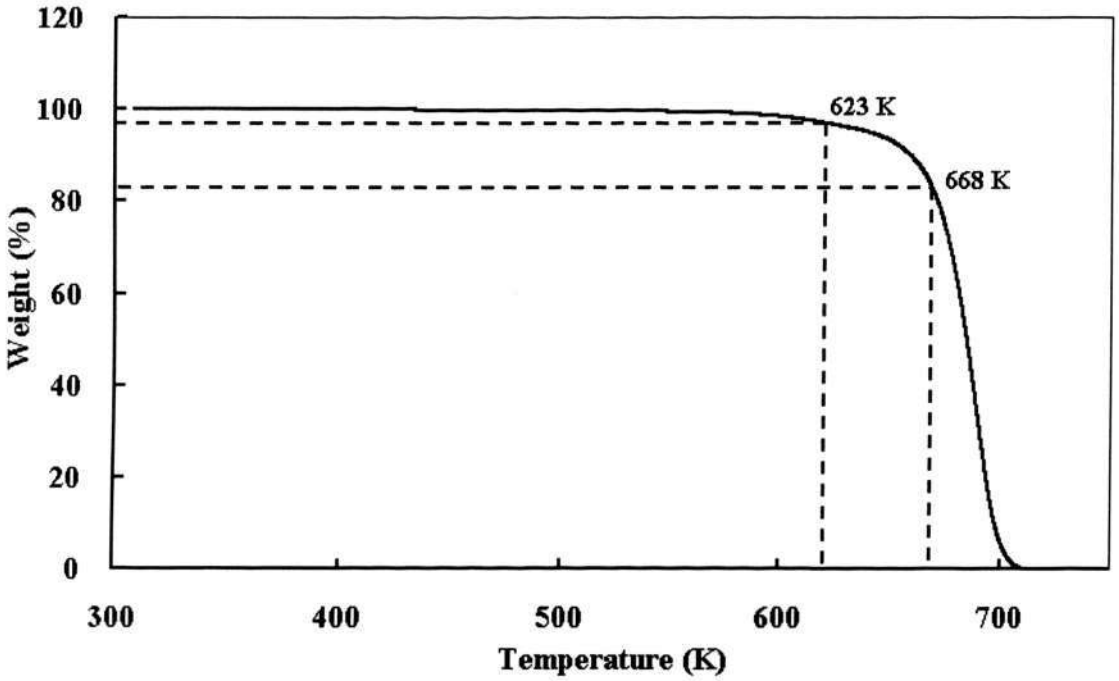

Figure 5.3 TGA behavior of PP with heating rate of 1 °C/min

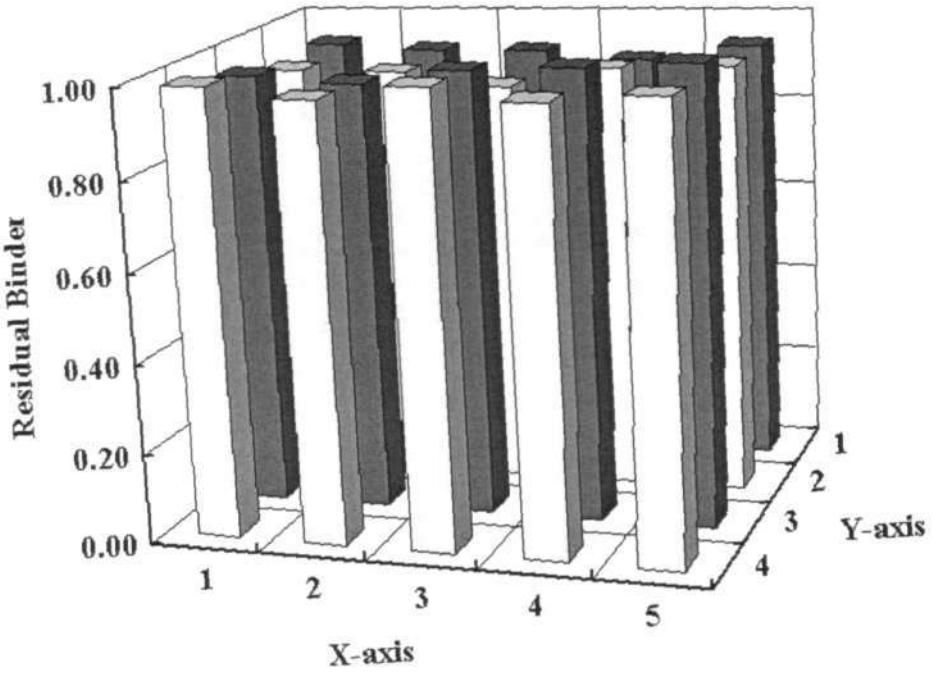

Figure 5.4(a) LMW component: Binder distribution at 17250 s

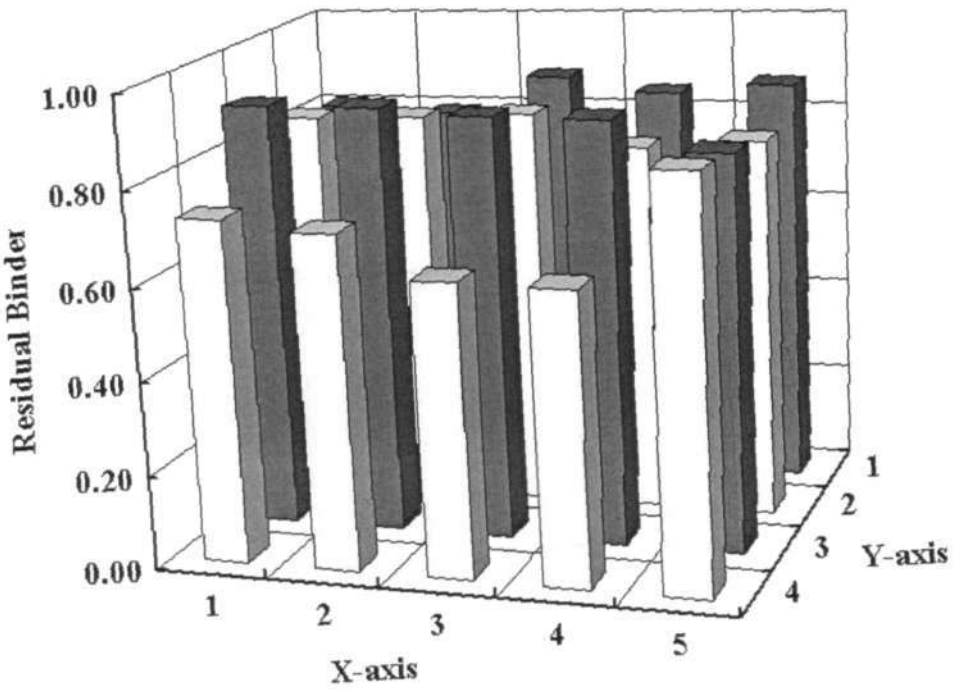

Figure 5.4(b) LMW component: Binder distribution at 25290 s

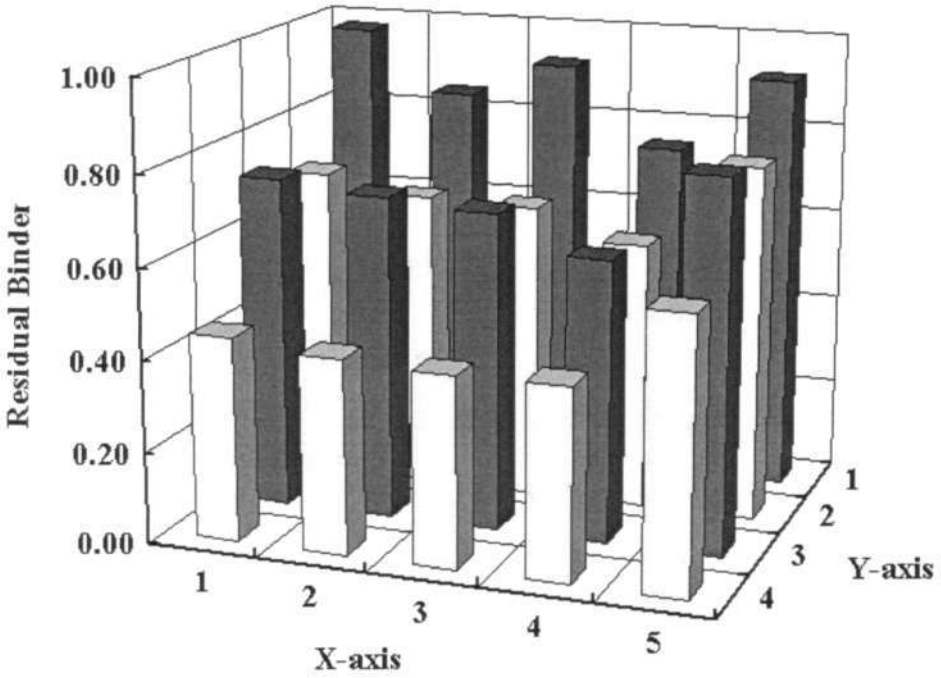

Figure 5.4(c) LMW component: Binder distribution at 25275 s

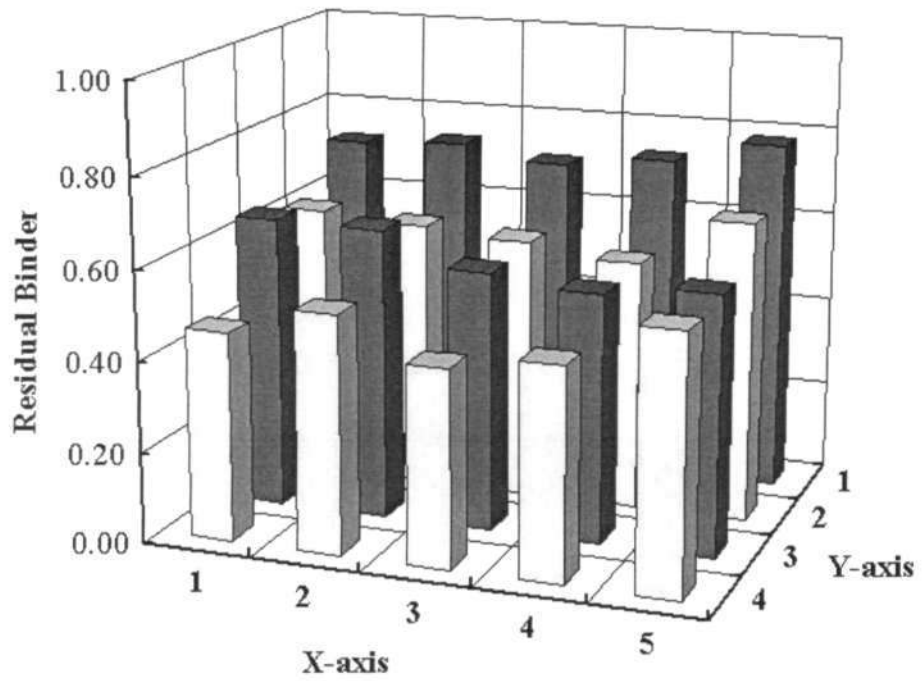

Figure 5.4(d) LMW component: Binder distribution at 29025 s

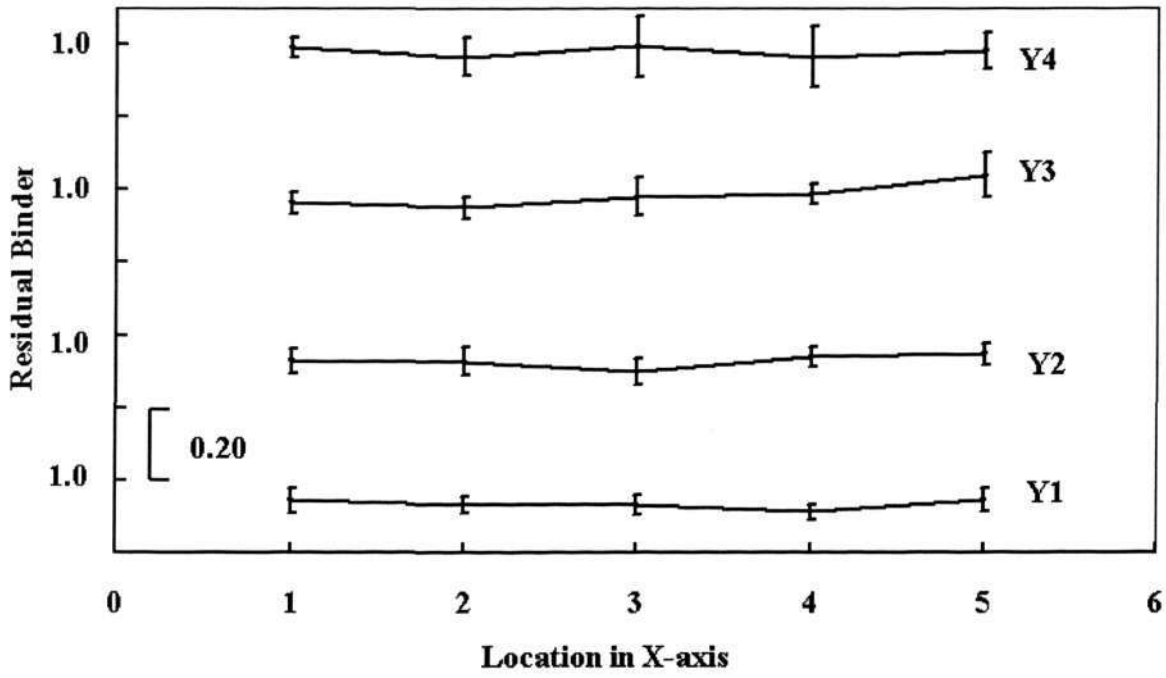

Figure 5.5(a) LMW component: Binder distribution in X-direction at 17250 s

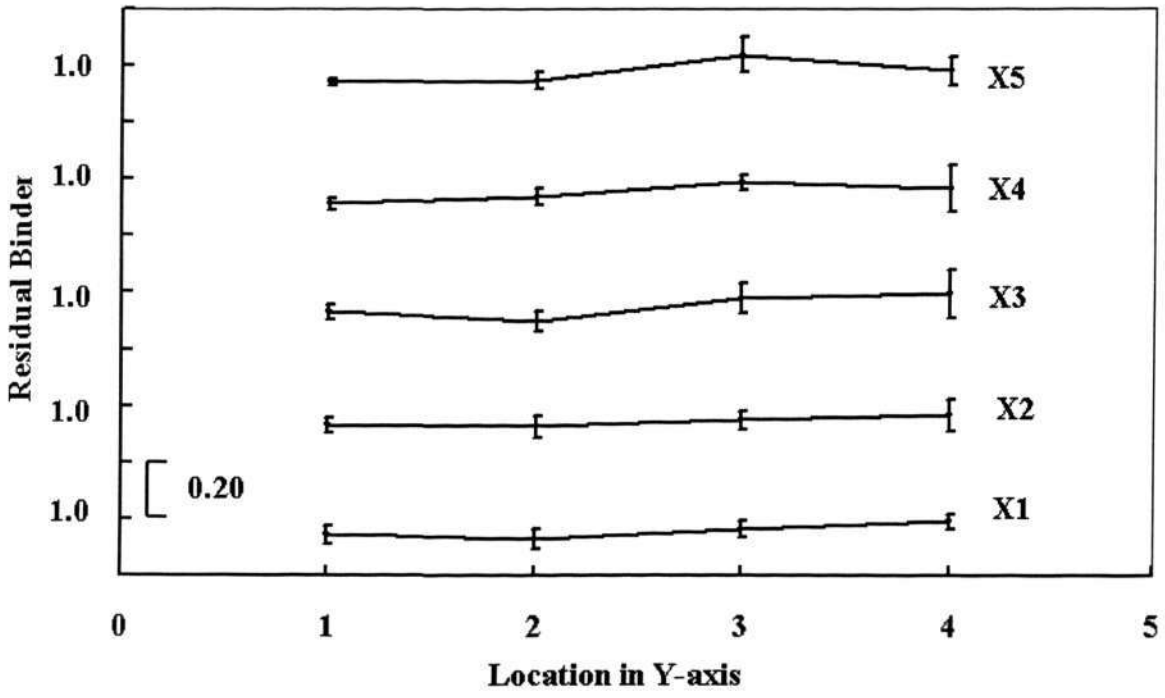

Figure 5.5(b) LMW component: Binder distribution in Y-direction at 17250 s

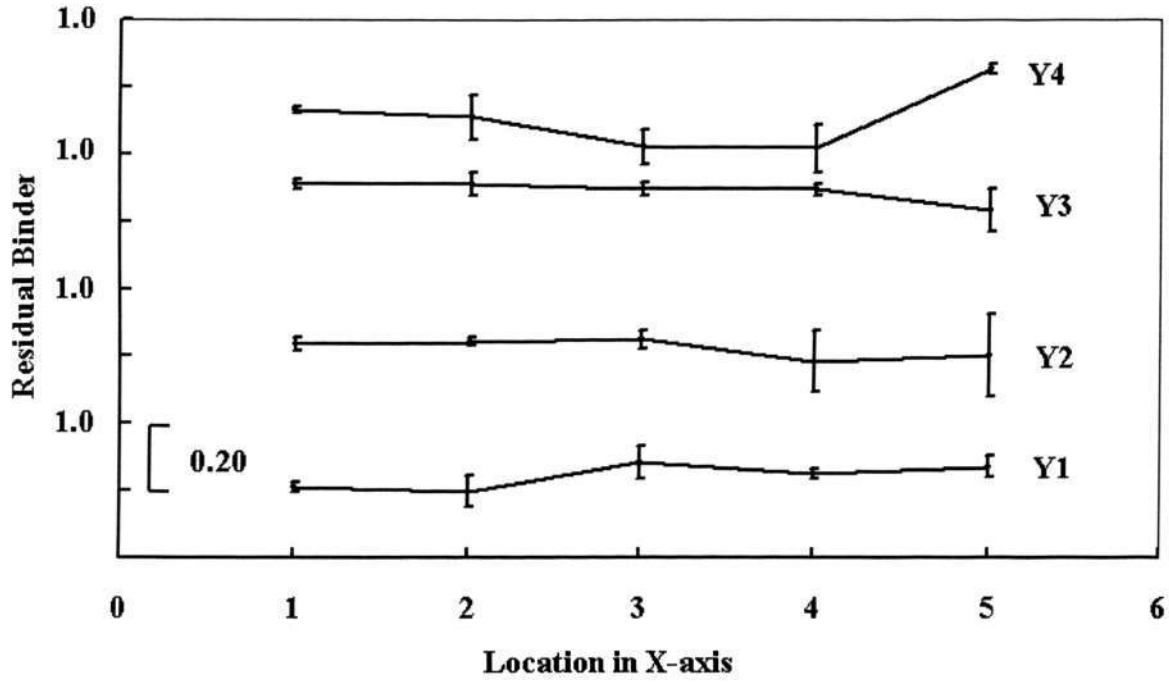

Figure 5.5(c) LMW component: Binder distribution in X-direction at 25290 s

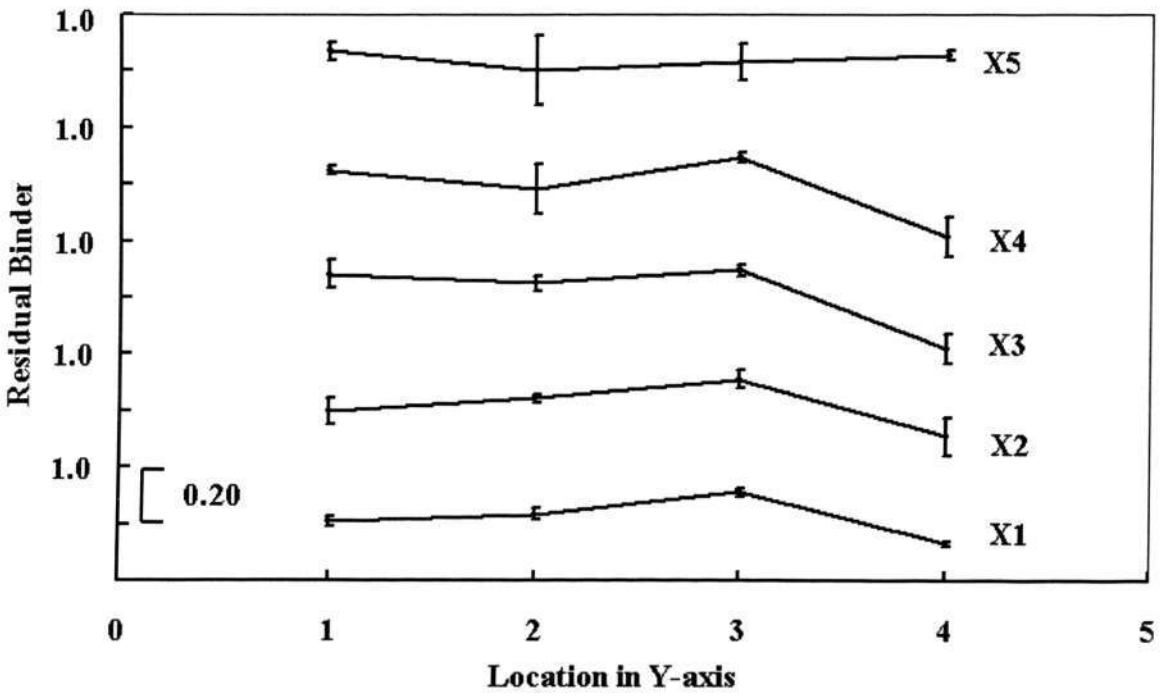

Figure 5.5(d) LMW component: Binder distribution in Y-direction at 25290 s

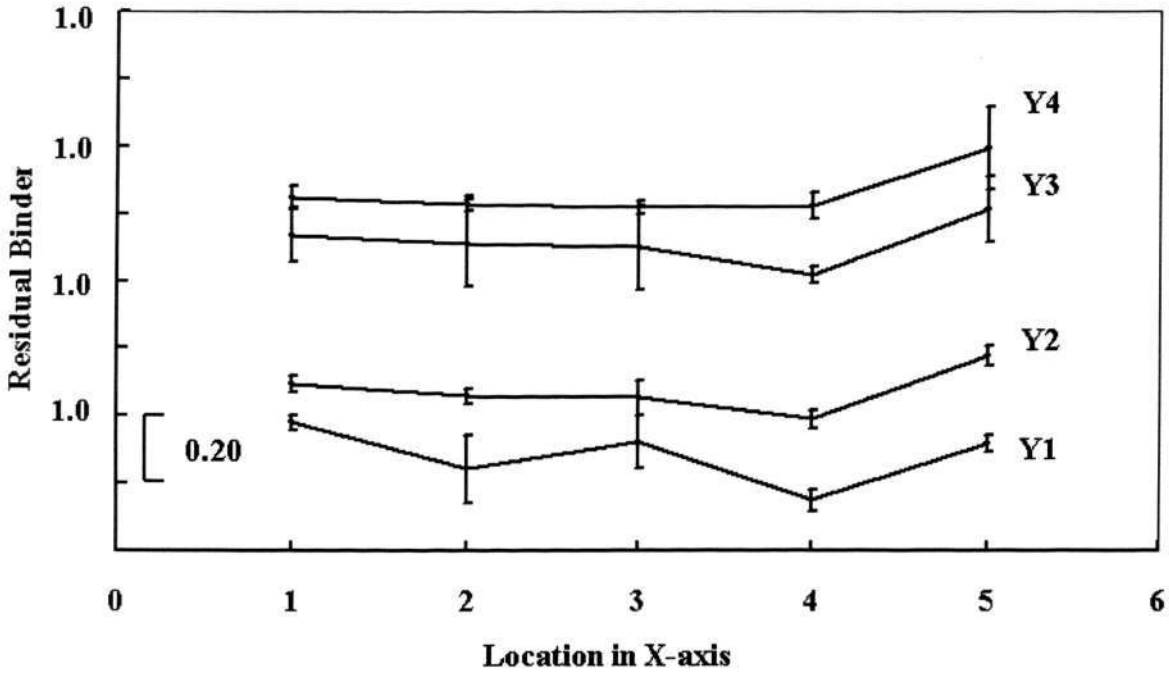

Figure 5.5(e) LMW component: Binder distribution in X-direction at 25275 s

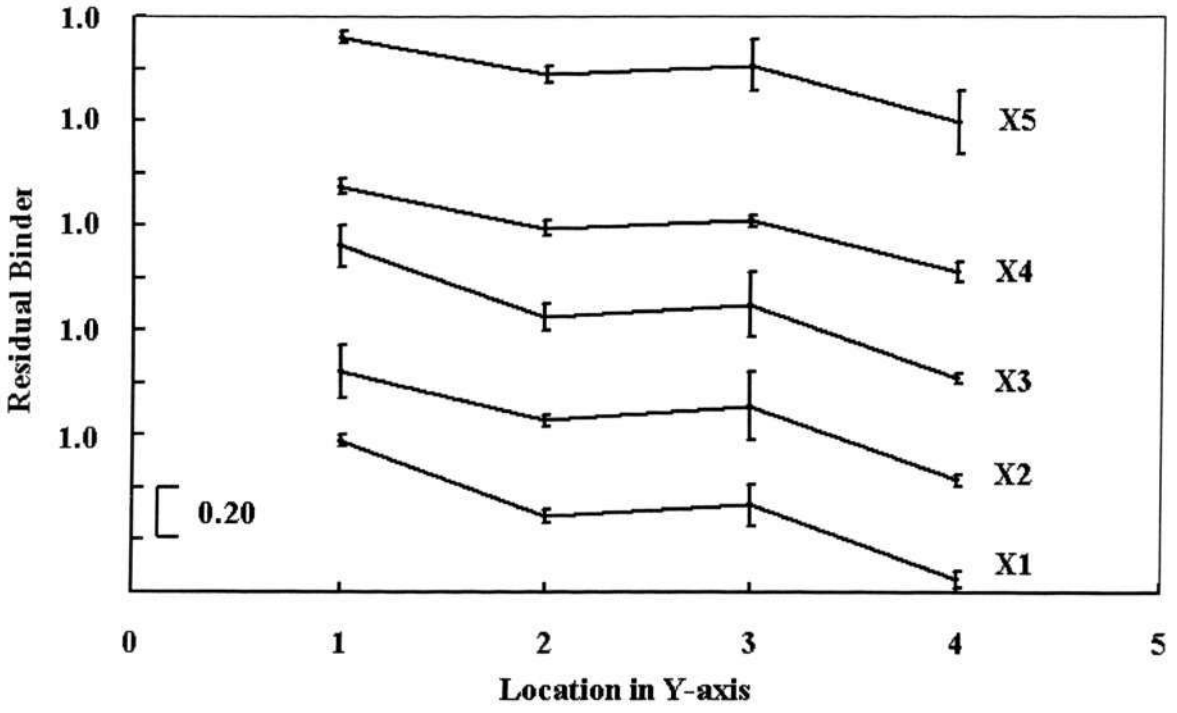

Figure 5.5(f) LMW component: Binder distribution in Y-direction at 25275 s

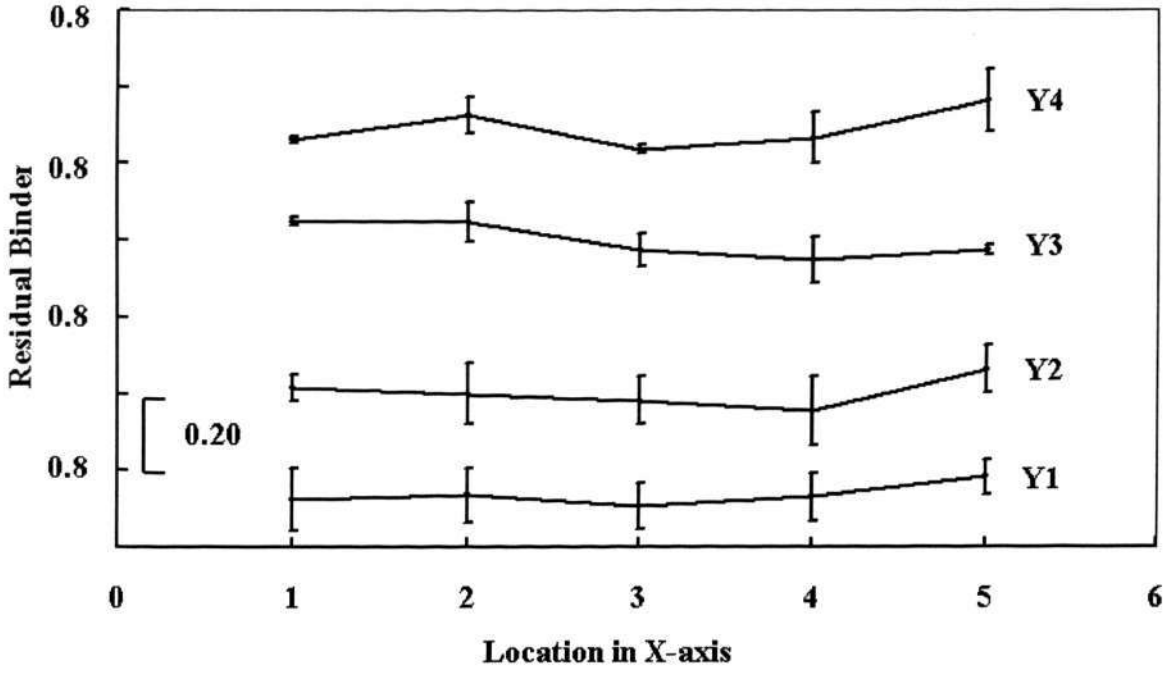

Figure 5.5(g) LMW component: Binder distribution in X-direction at 29025 s

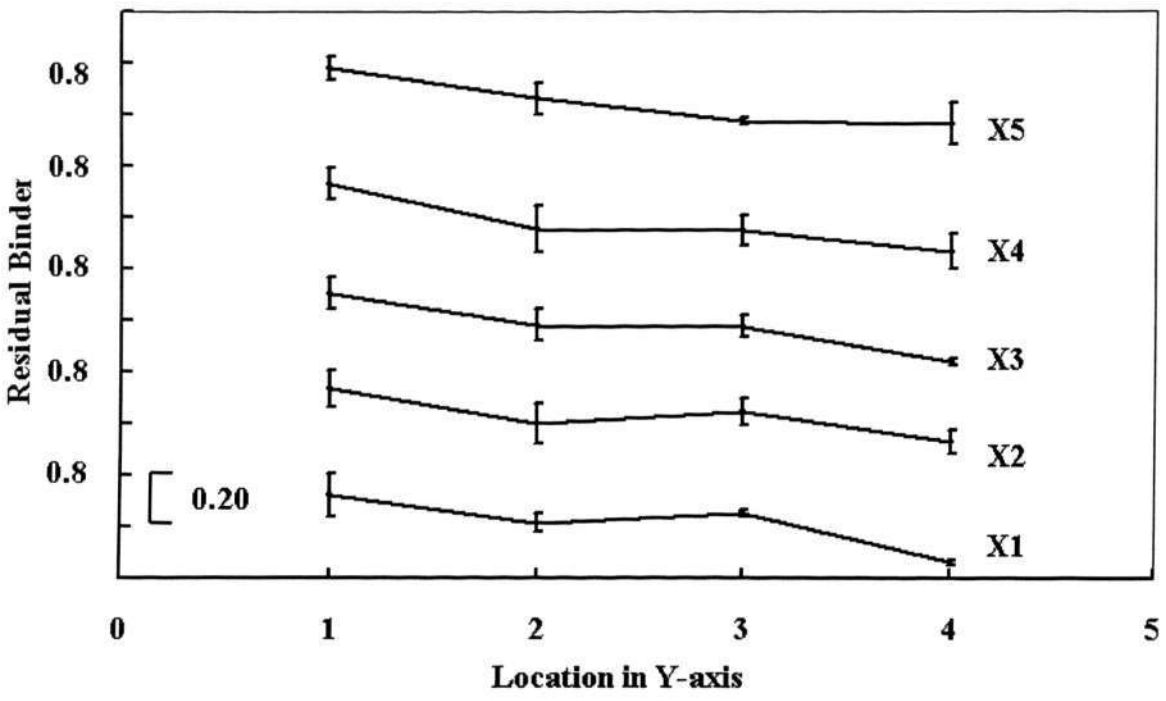

Figure 5.5(h) LMW component: Binder distribution in Y-direction at 29025 s

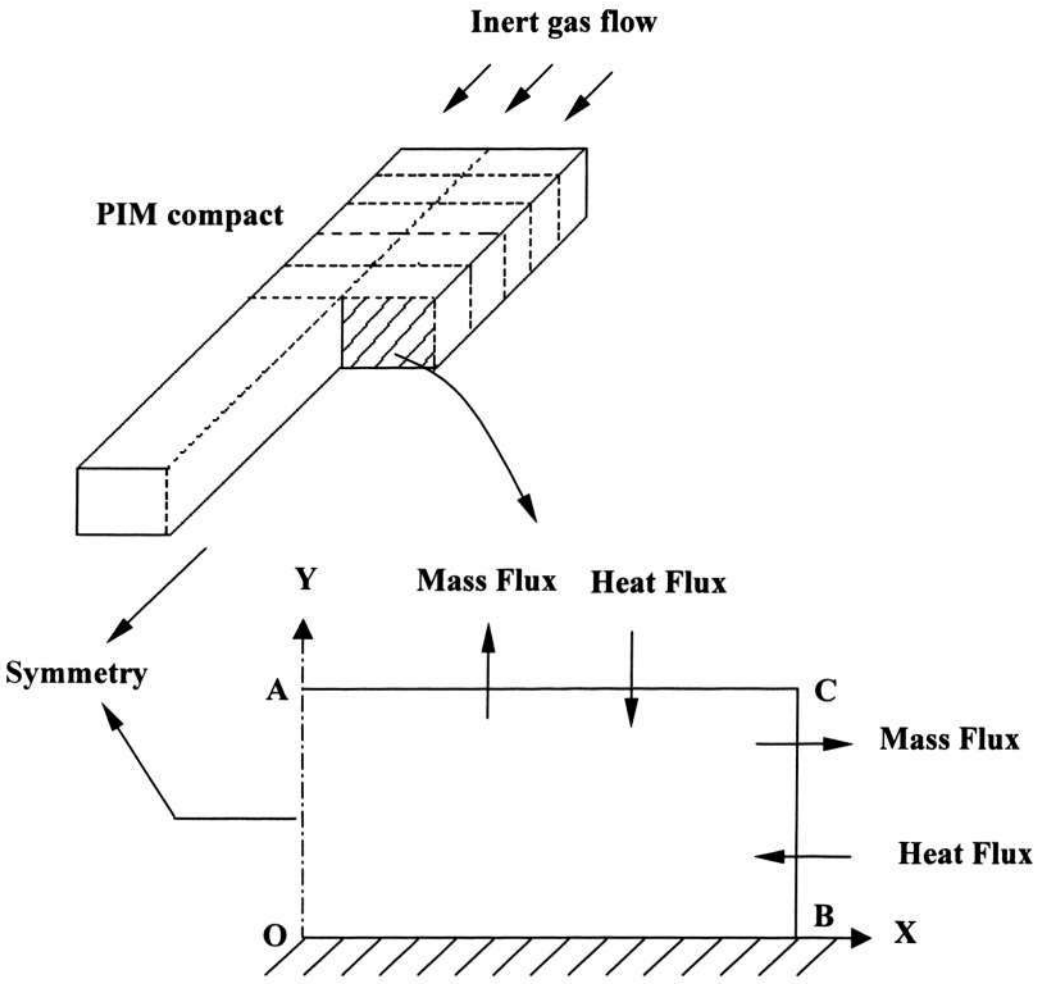

Figure 5.6 HMW component: Computation domain

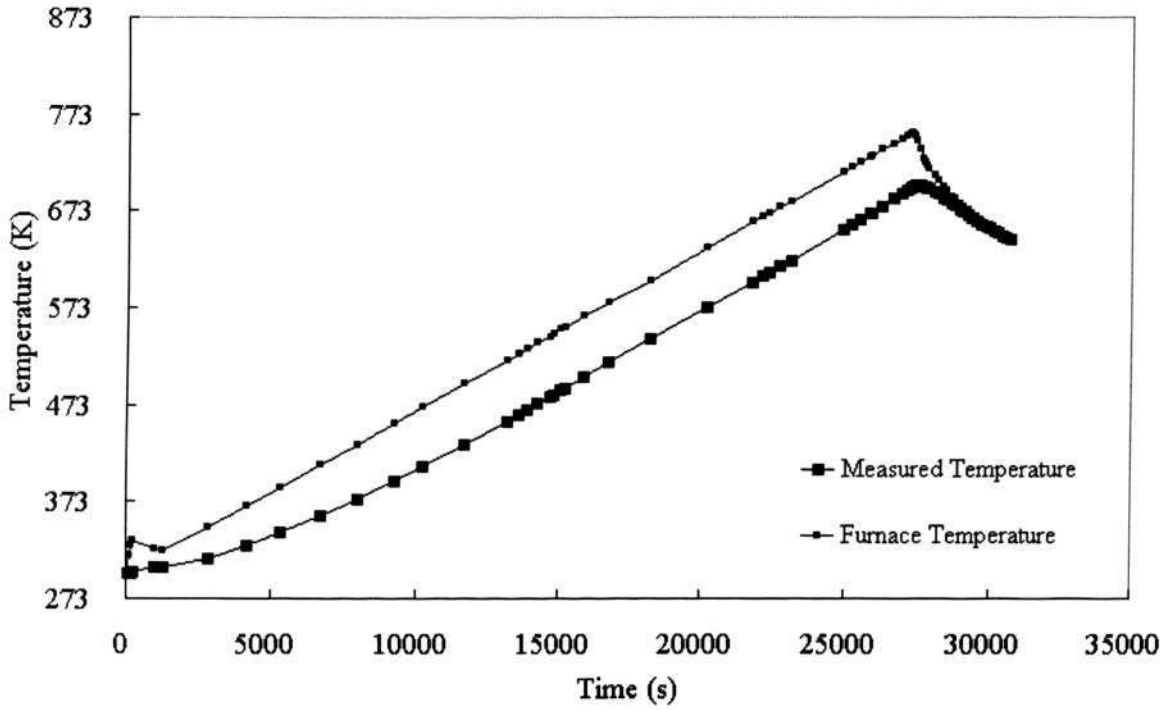

Figure 5.7 HMW component: Heating schedule of thermal debinding

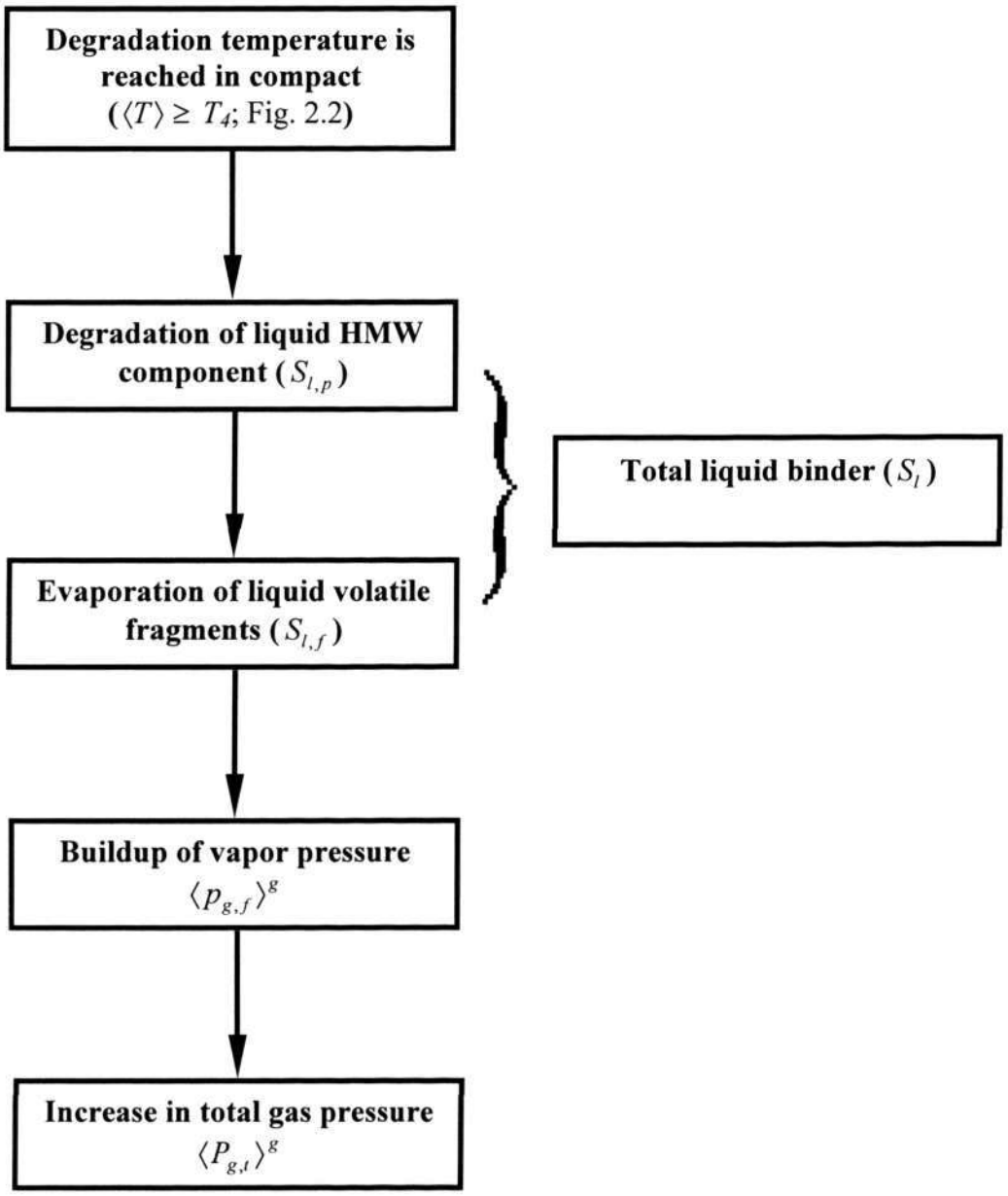

Figure 5.8 HMW component: Flow chart of thermal debinding process

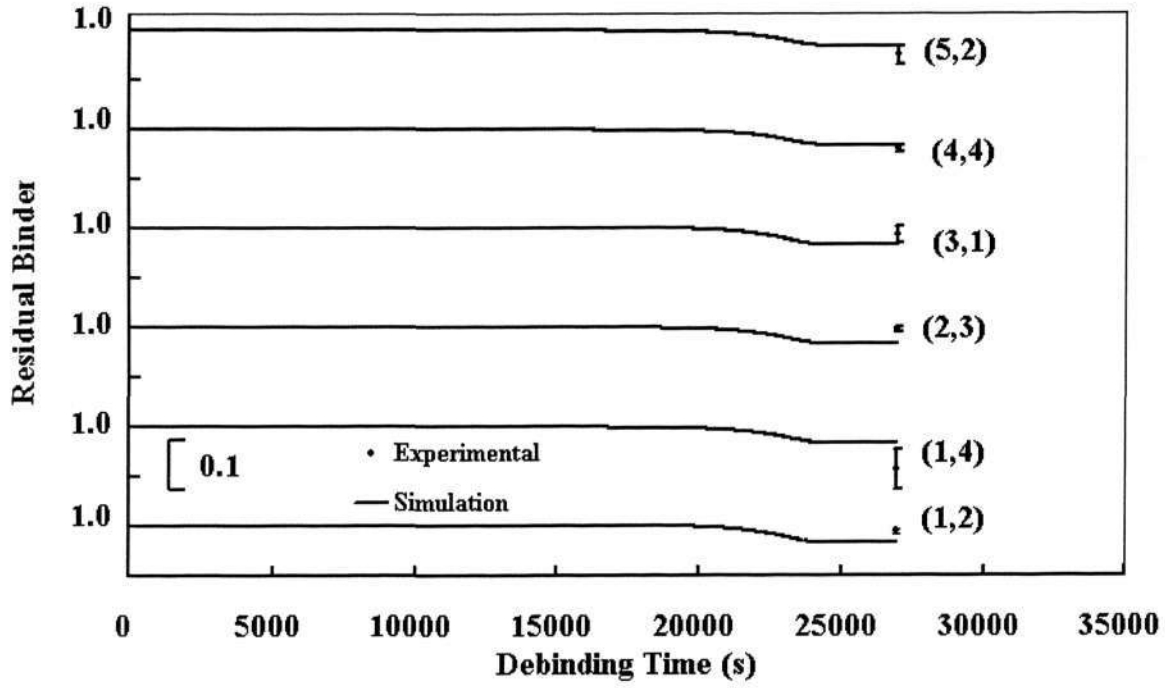

Figure 5.9(a) HMW component: Result comparisons at first debinding time

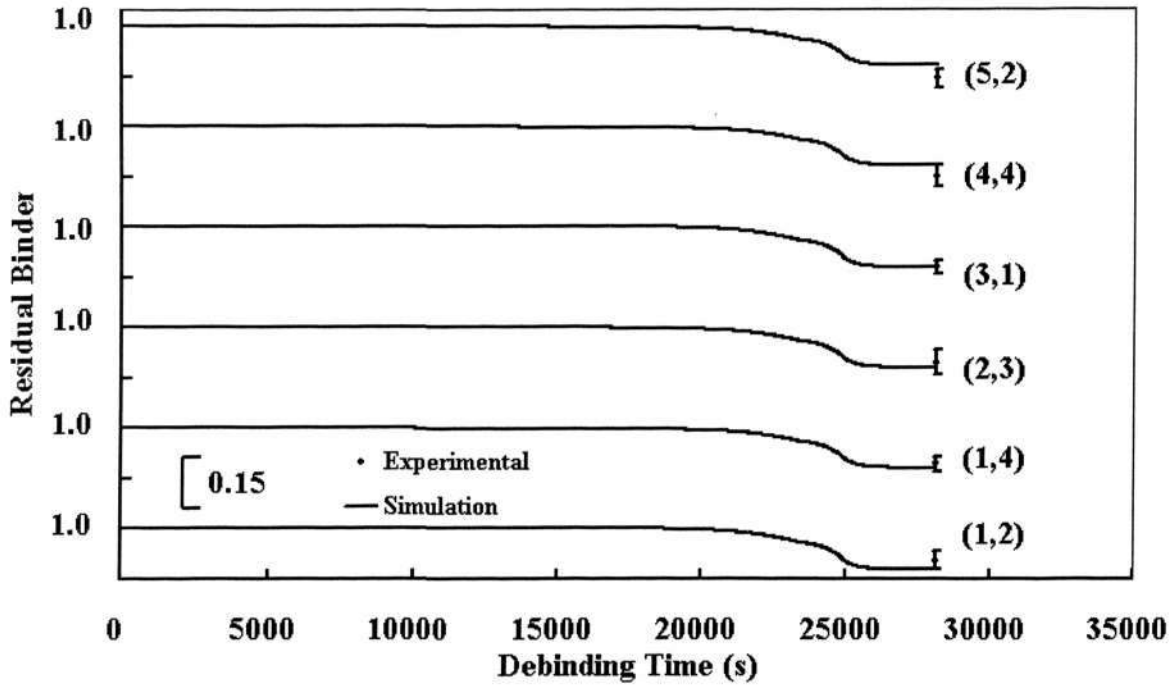

Figure 5.9(b) HMW component: Result comparisons at second debinding time

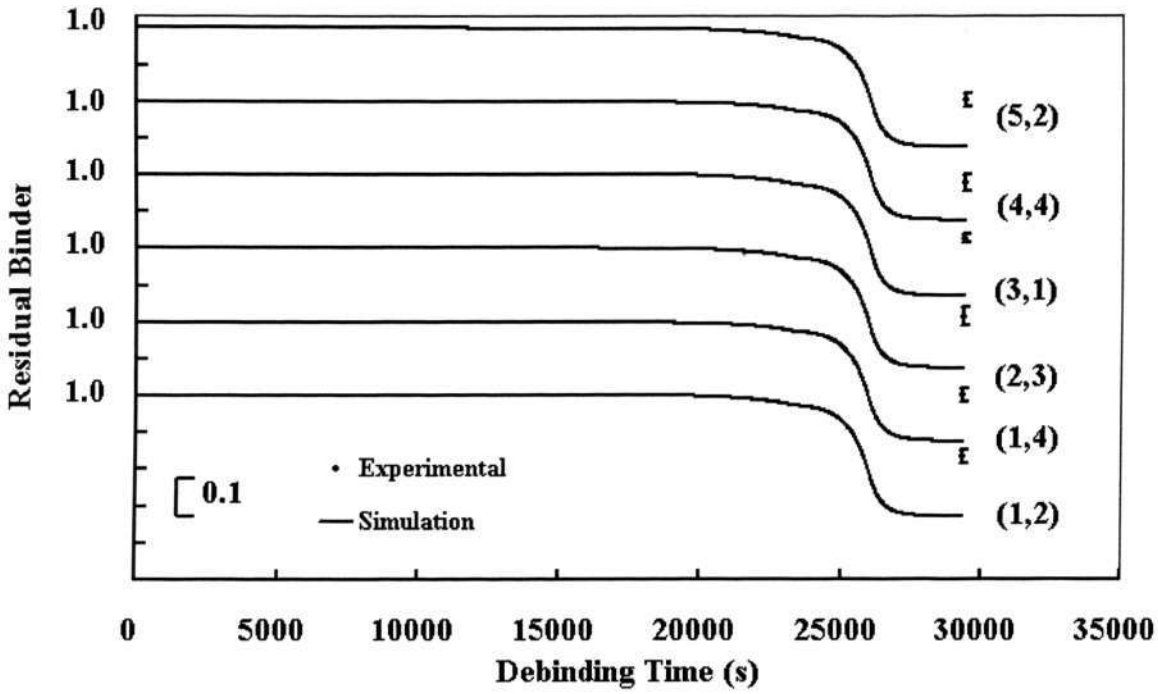

Figure 5.9(c) HMW component: Result comparisons at third debinding time

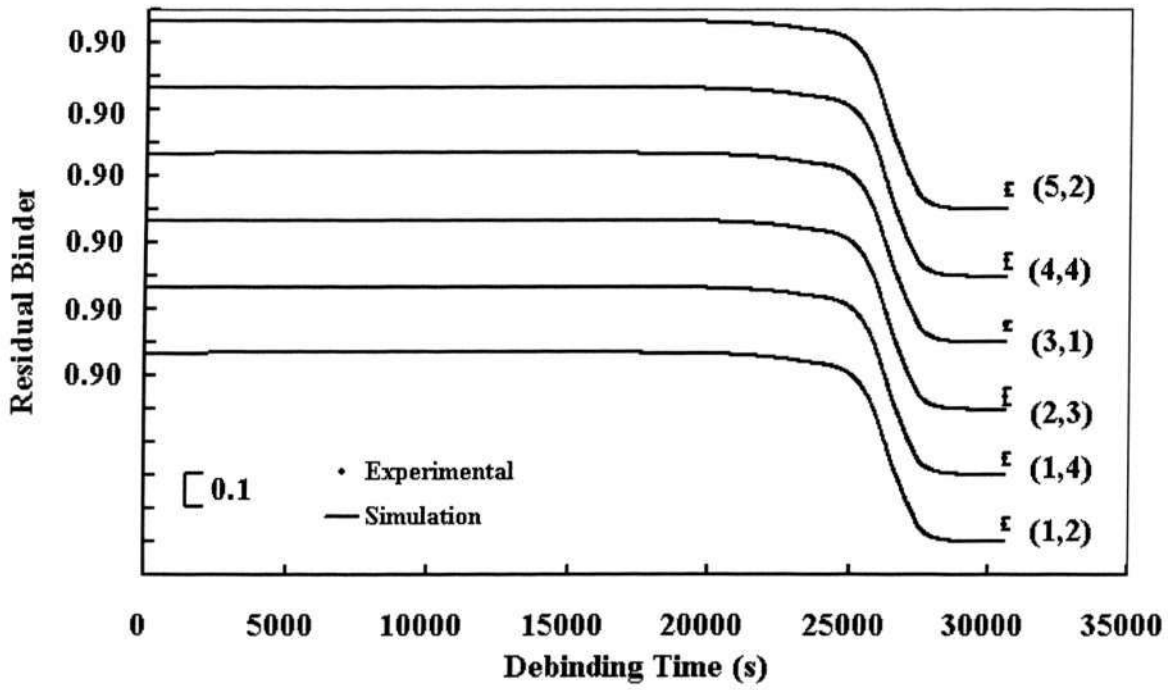

Figure 5.9(d) HMW component: Result comparisons at fourth debinding time

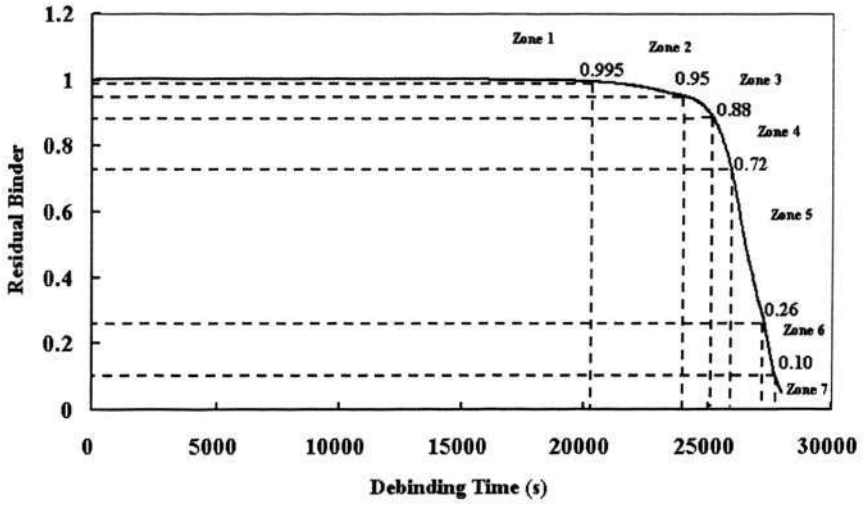

Figure 5.10 HMW component: Residual binder versus debinding time

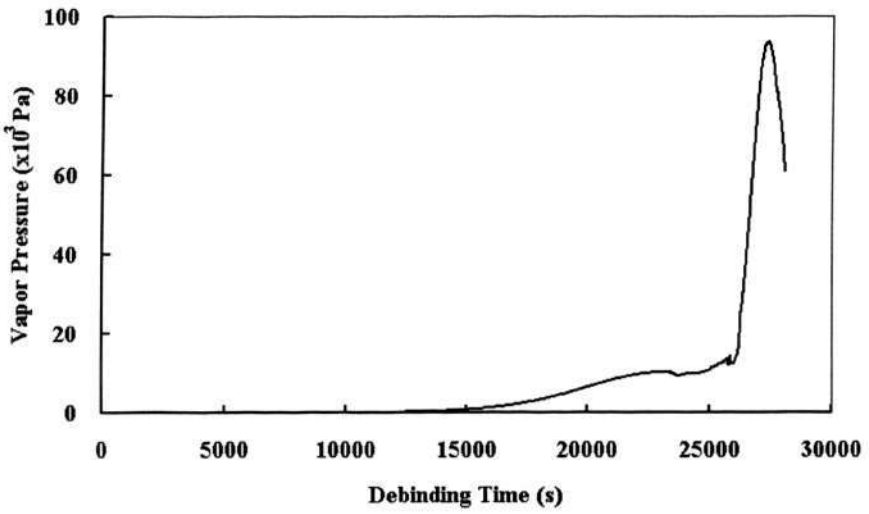

Figure 5.11 HMW component: Vapor pressure versus debinding time

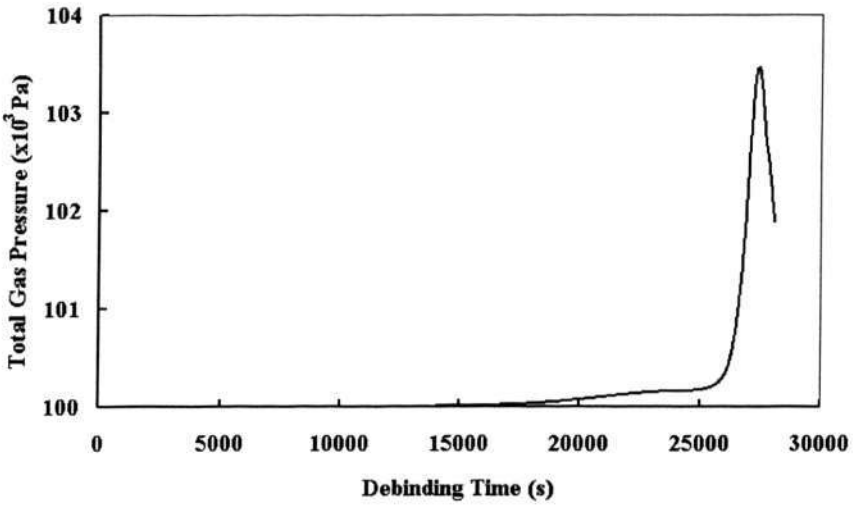

Figure 5.12 HMW component: Total gas pressure versus debinding time

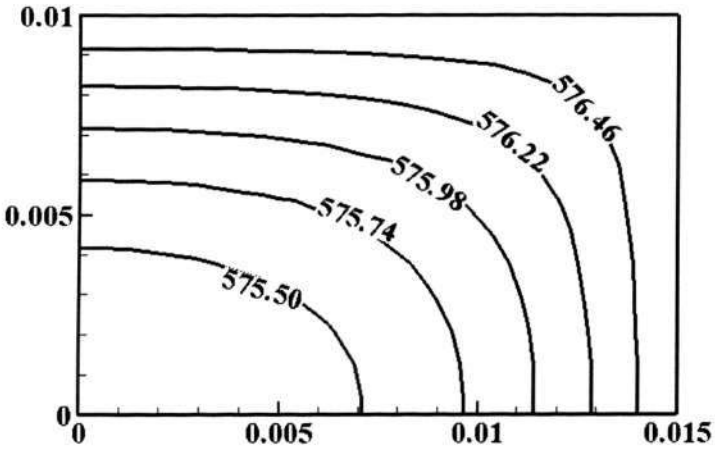

(a)

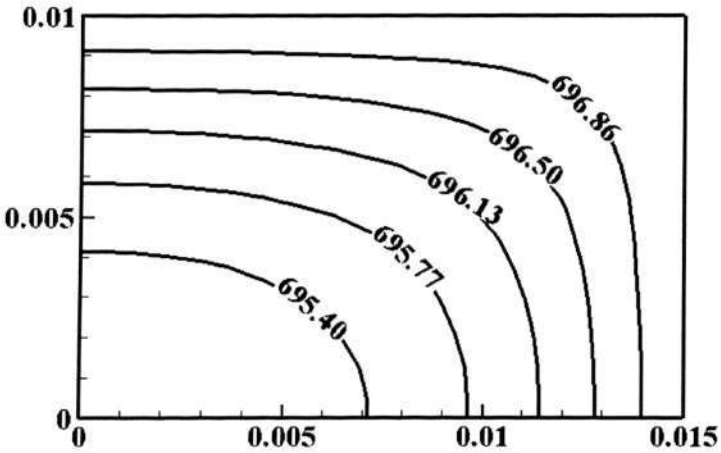

(b)

Figure 5.13 Temperature distributions at debinding times of (a)20400 s ($T_{surface}$ = 576.70 K) and (b)27240 s ($T_{surface}$ = 697 K)

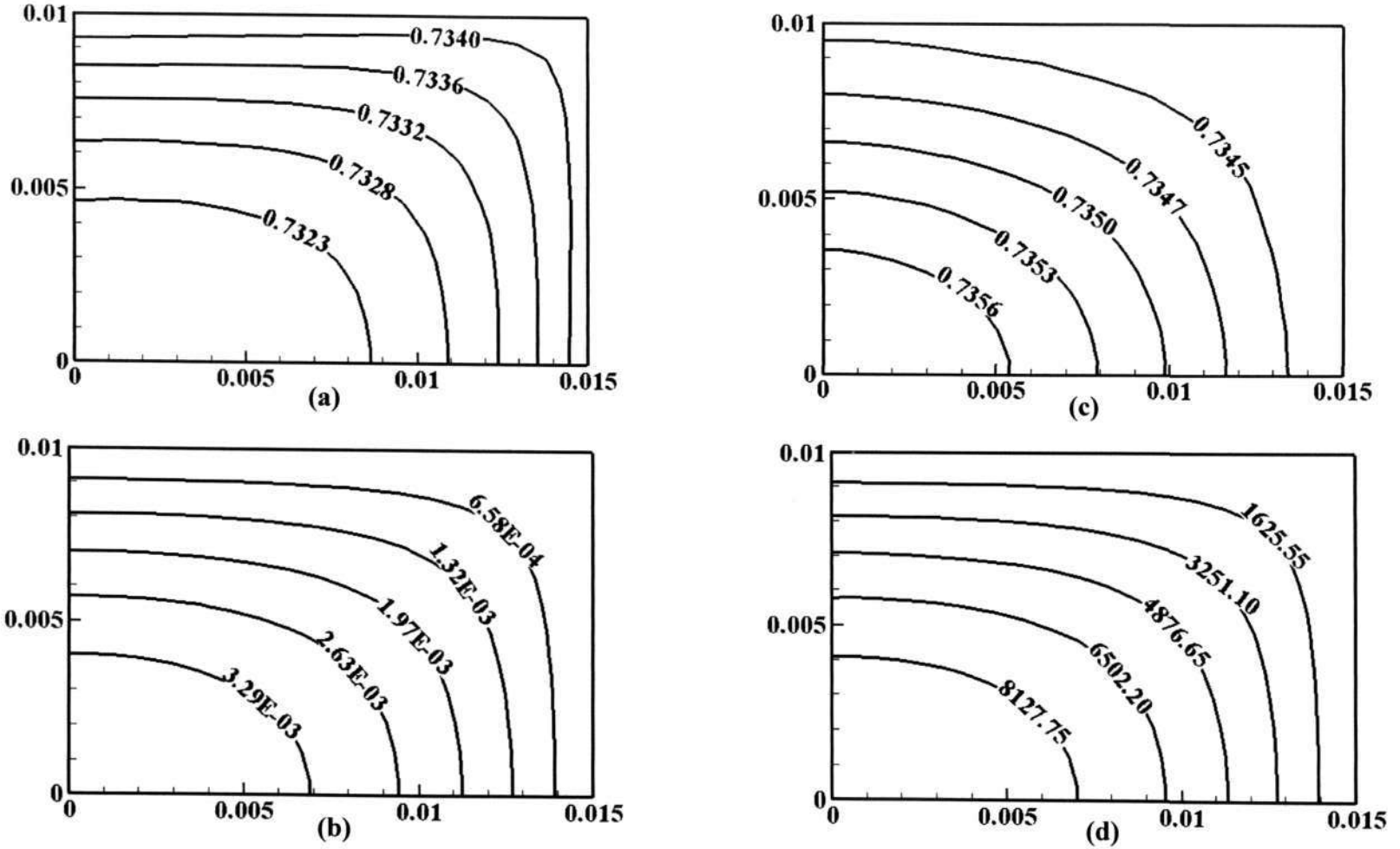

Figure 5.14 Distributions of (a) liquid saturation of HMW component, (b) liquid saturation of volatile fragments, (c) total liquid saturation, and (d) vapor pressure at 22200 s ($T_{surface}$ = 606.98 K)

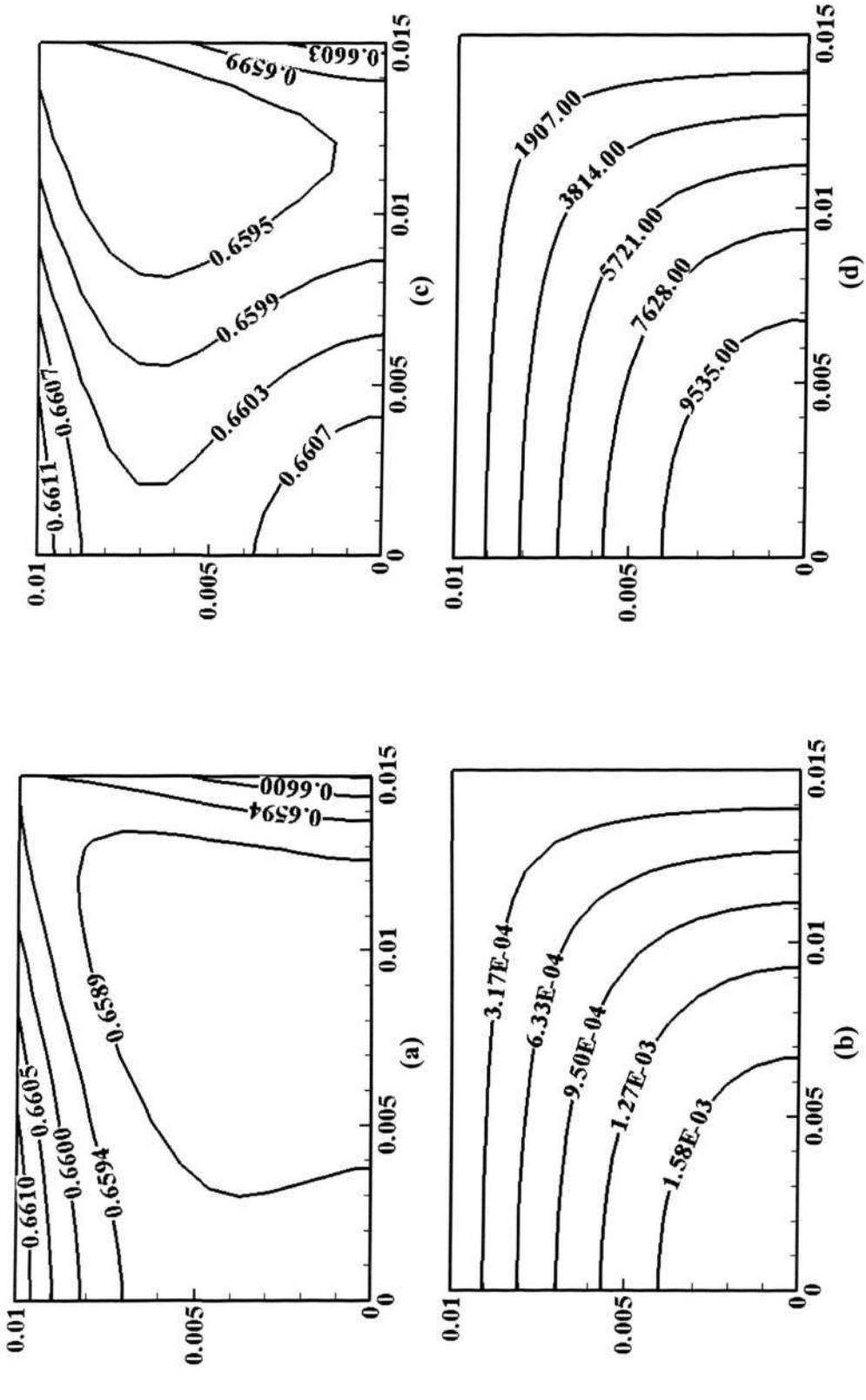

Figure 5.15 Distributions of (a) liquid saturation of HMW component, (b) liquid saturation of volatile fragments, (c) total liquid saturation, and (d) vapor pressure at 25200 s ($T_{surface}$ = 659.05 K)

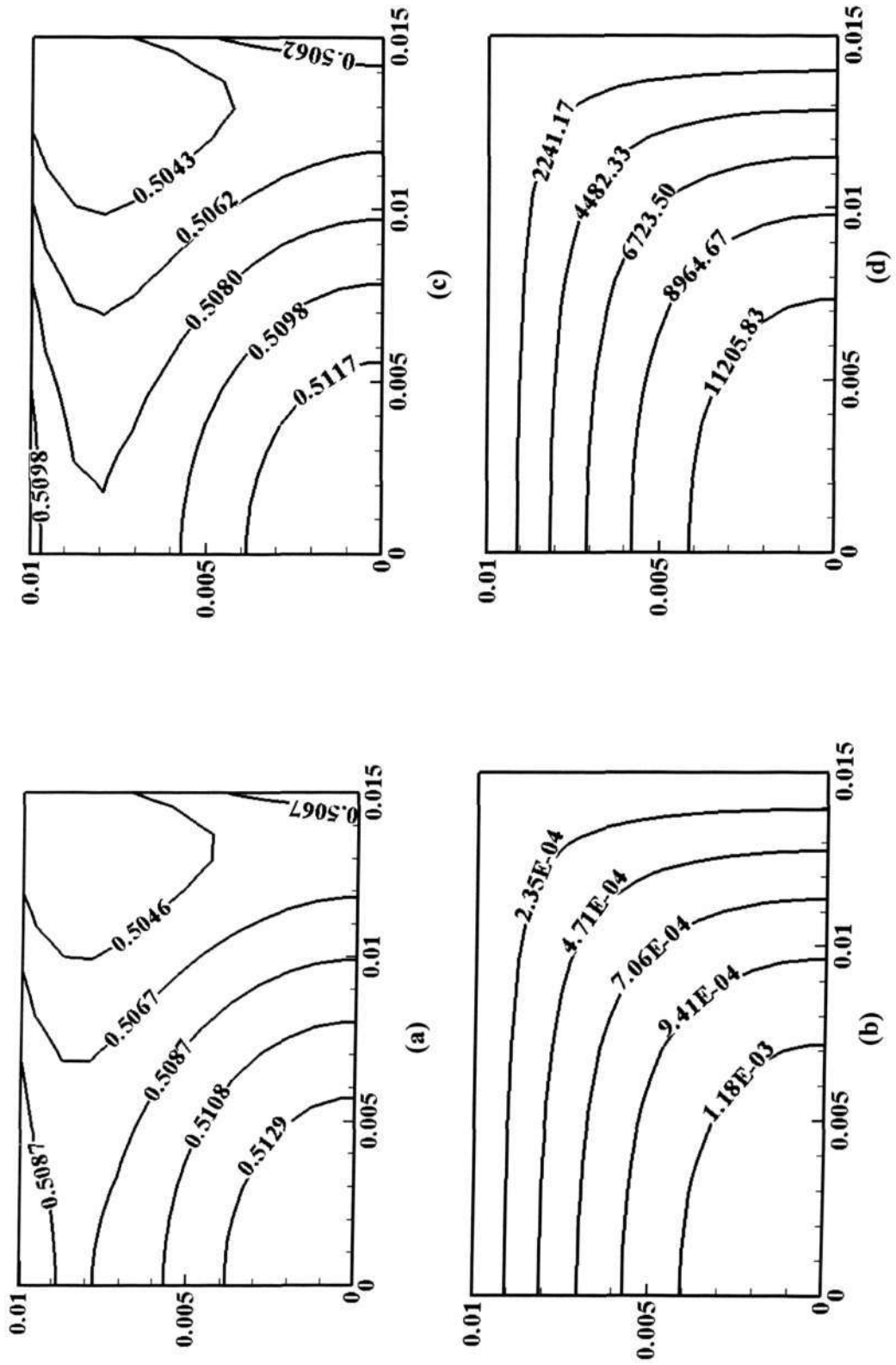

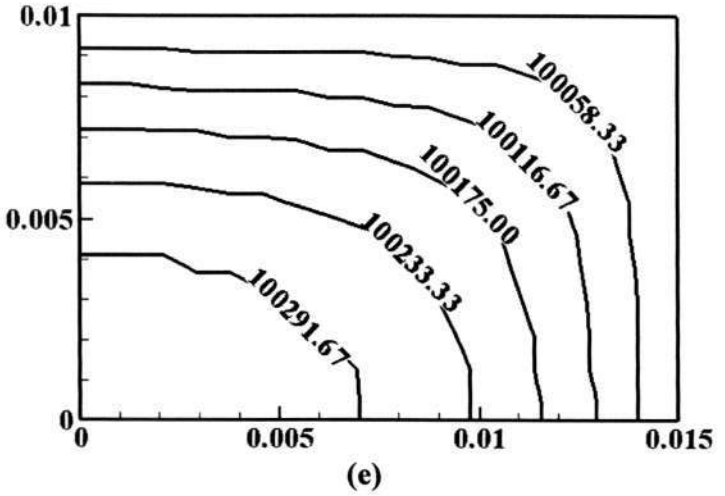

Figure 5.16 Distributions of (a) liquid saturation of HMW component, (b) liquid saturation of volatile fragments, (c) total liquid saturation, and (e) total gas pressure at 26040 s ($T_{surface}$ = 674 K)

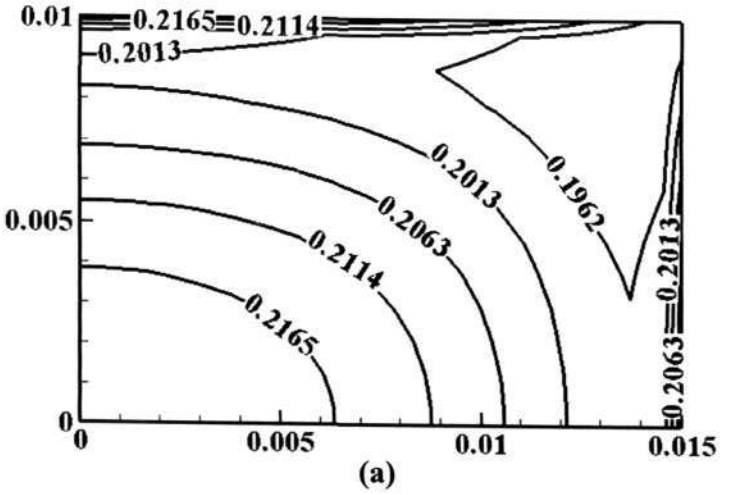

(a)

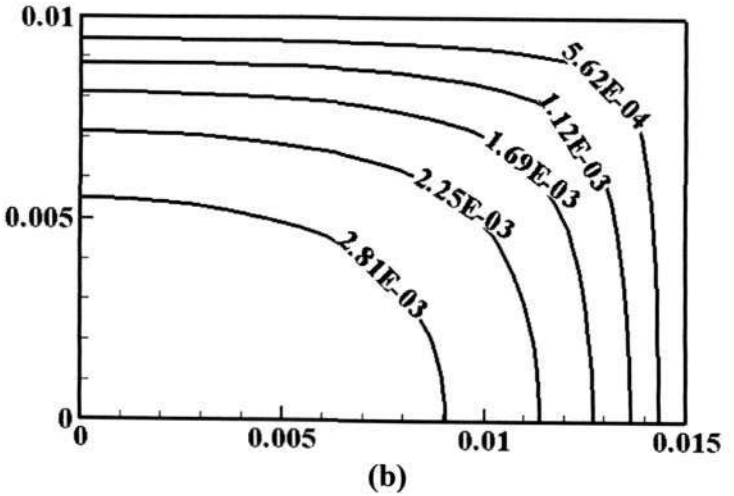

(b)

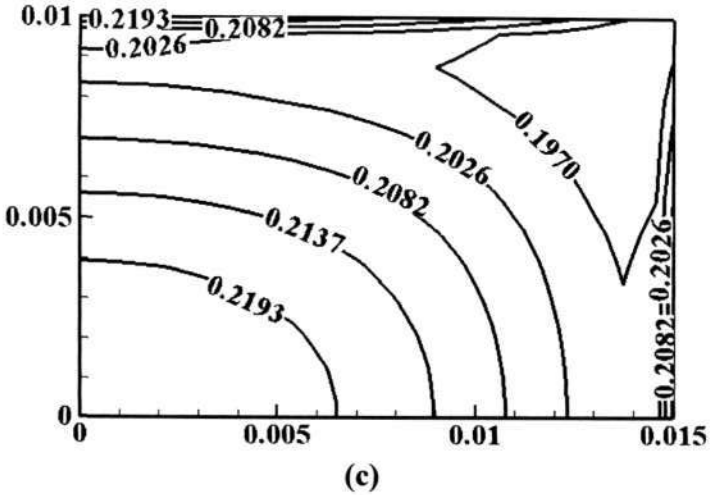

(c)

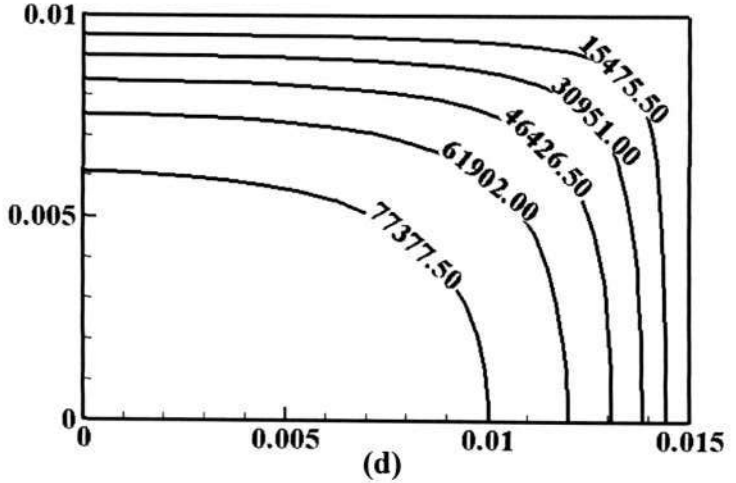

(d)

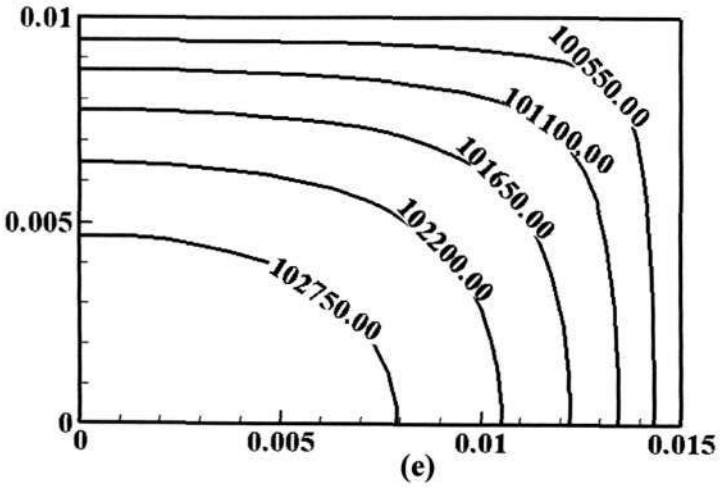

Figure 5.17 Distributions of (a) liquid saturation of HMW component, (b) liquid saturation of volatile fragments, (c) total liquid saturation, (d) vapor pressure, and (e) total gas pressure at 27240 s ($T_{surface}$ = 697 K)

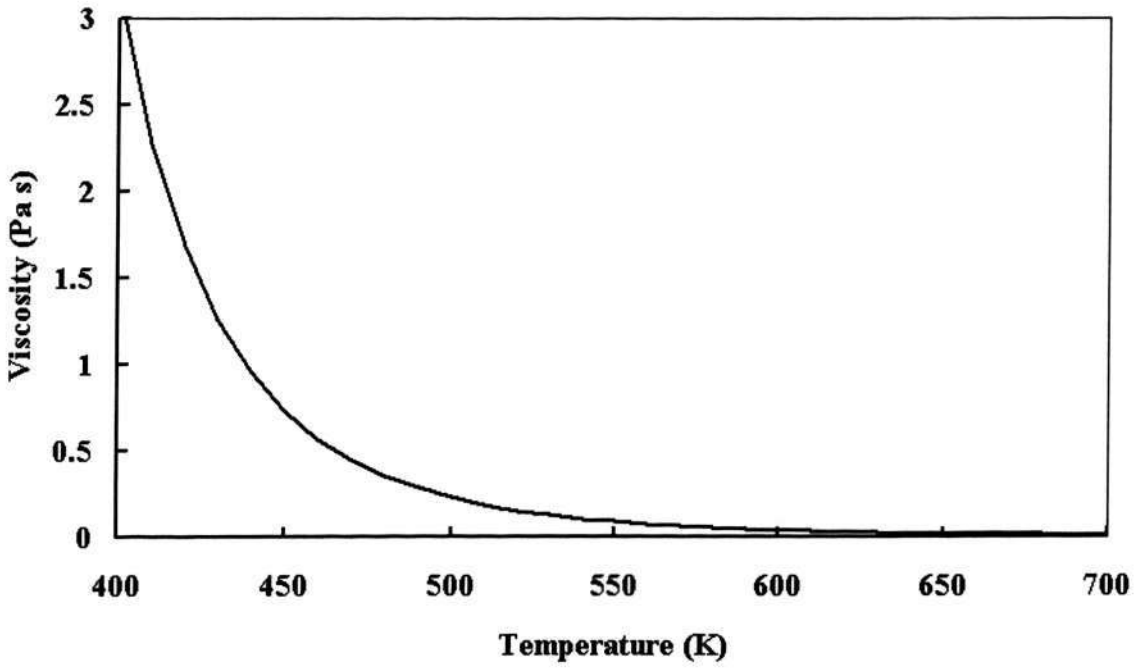

Figure 5.18 Viscosity of HMW component

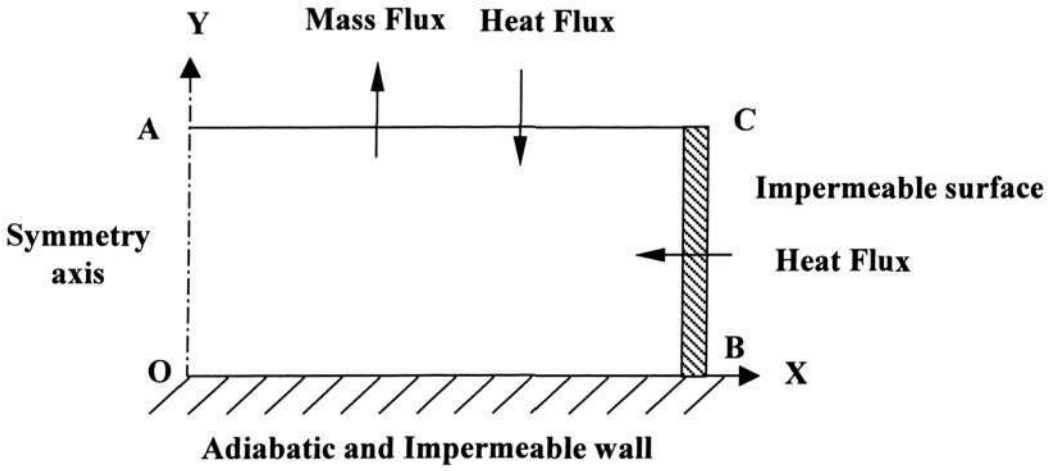

Figure 5.19 LMW component: Computation domain

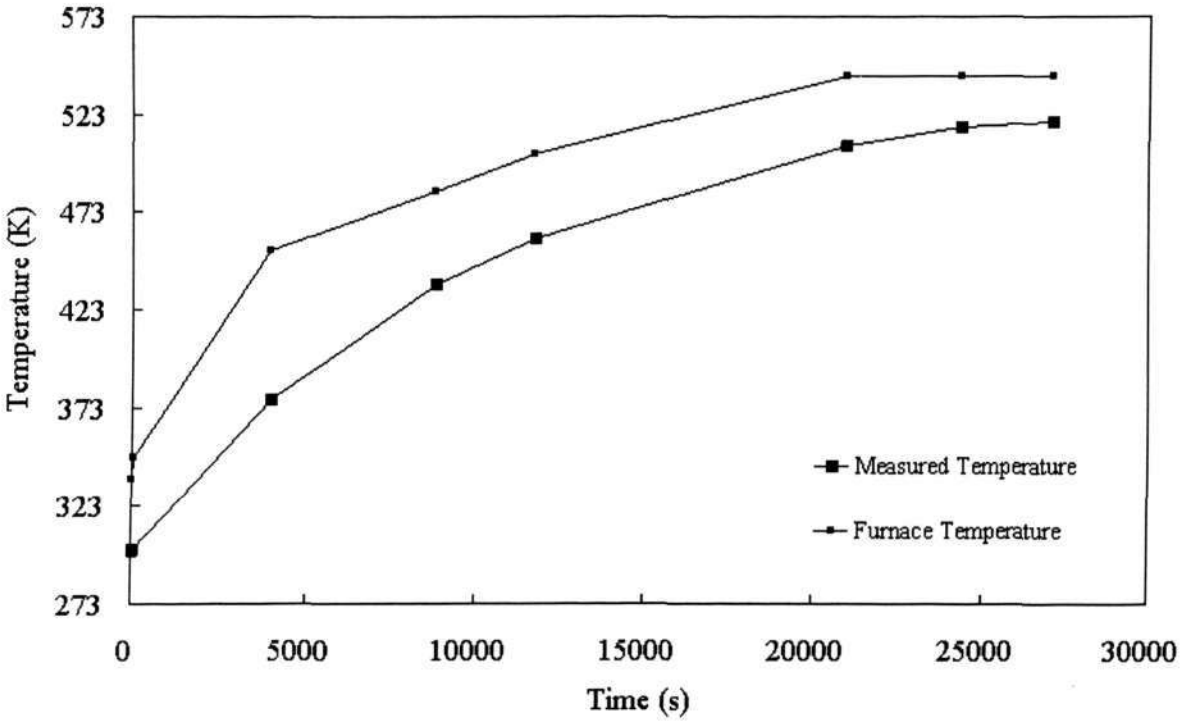

Figure 5.20 LMW component: Heating schedule of thermal debinding

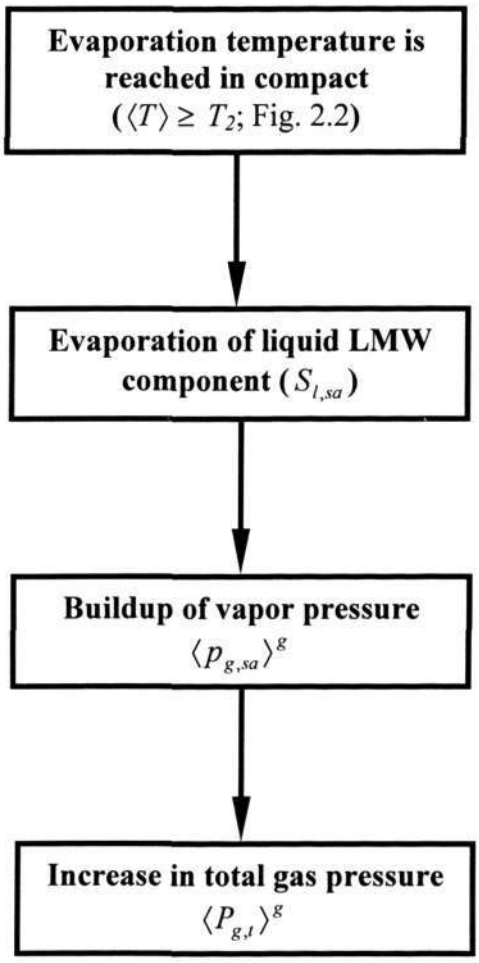

Figure 5.21 LMW component: Flow chart of thermal debinding process

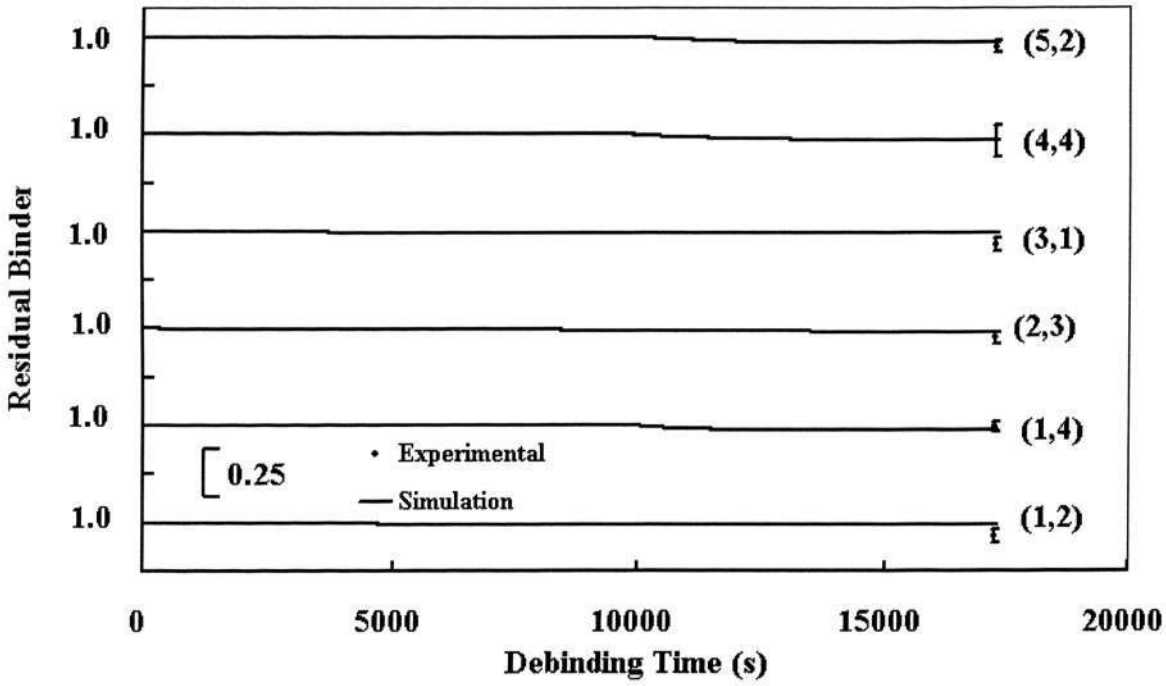

Figure 5.22(a) LMW component: Result comparisons at first debinding time

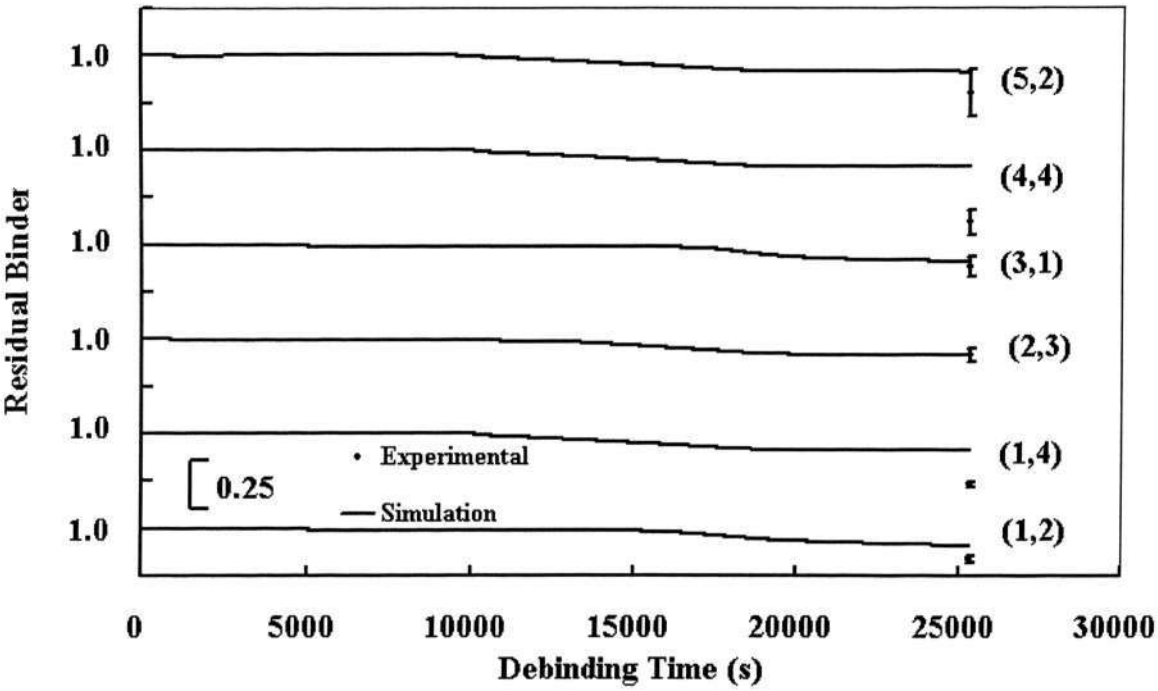

Figure 5.22(b) LMW component: Result comparisons at second debinding time

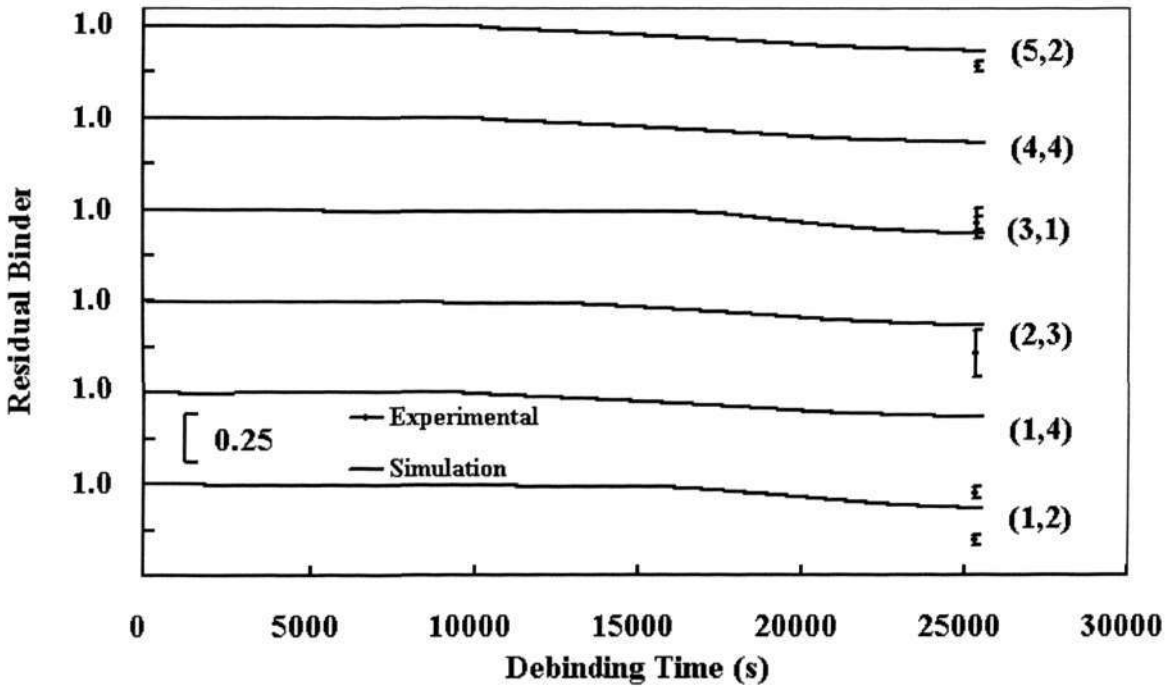

Figure 5.22(c) LMW component: Result comparisons at third debinding time

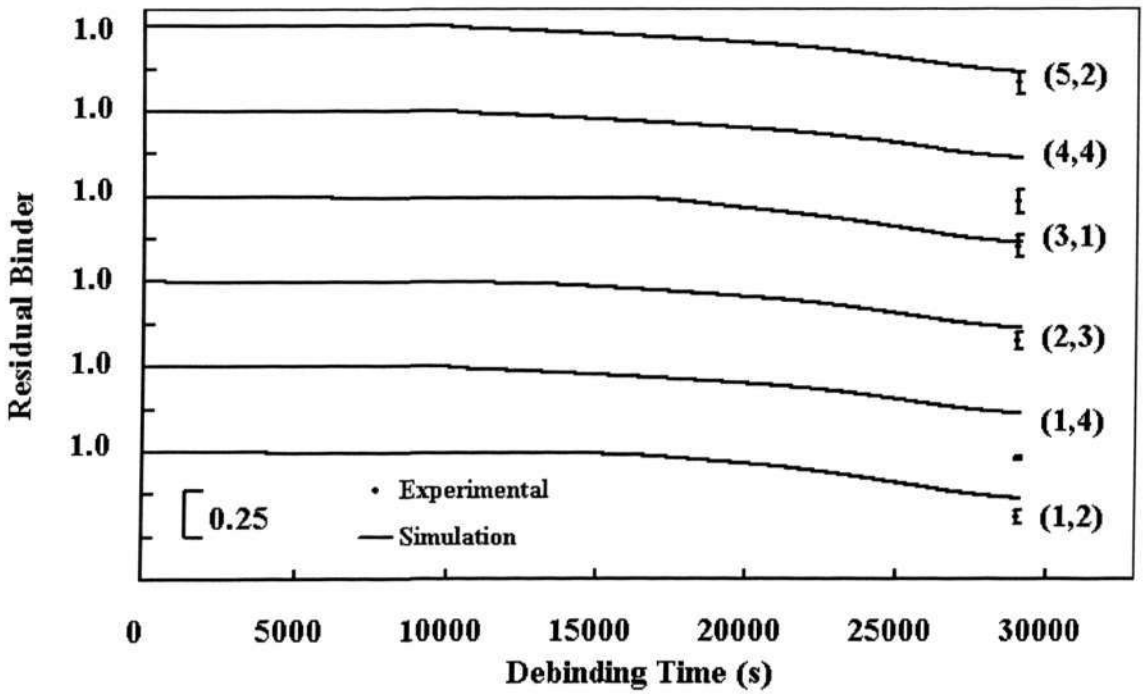

Figure 5.22(d) LMW component: Result comparisons at fourth debinding time

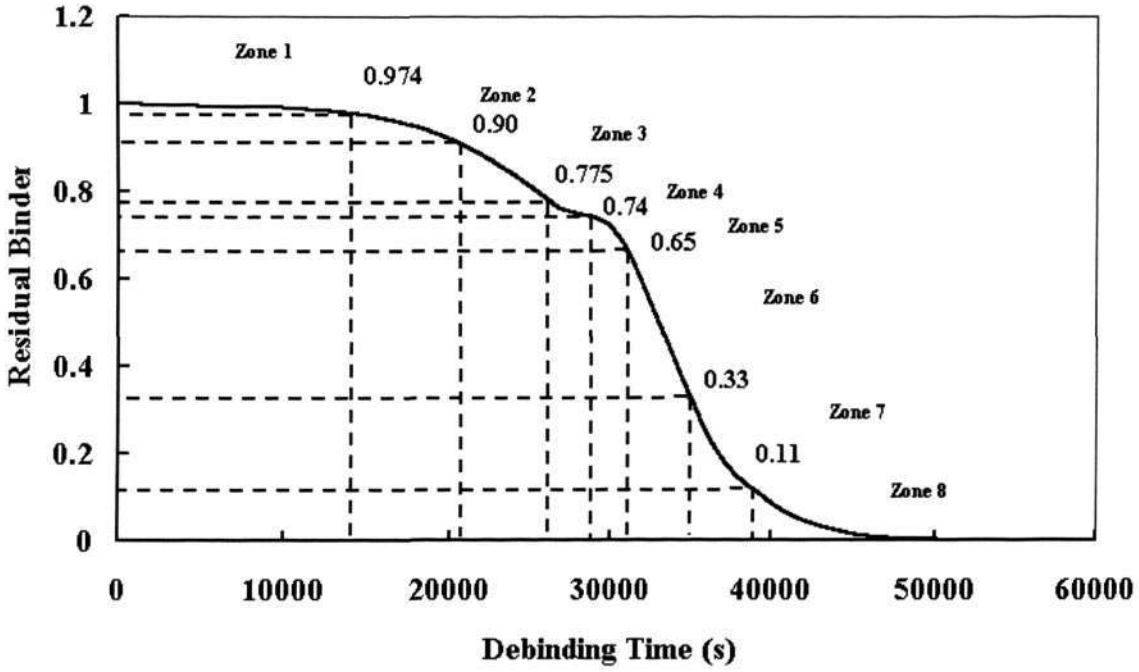

Figure 5.23 LMW component: Residual binder versus debinding time

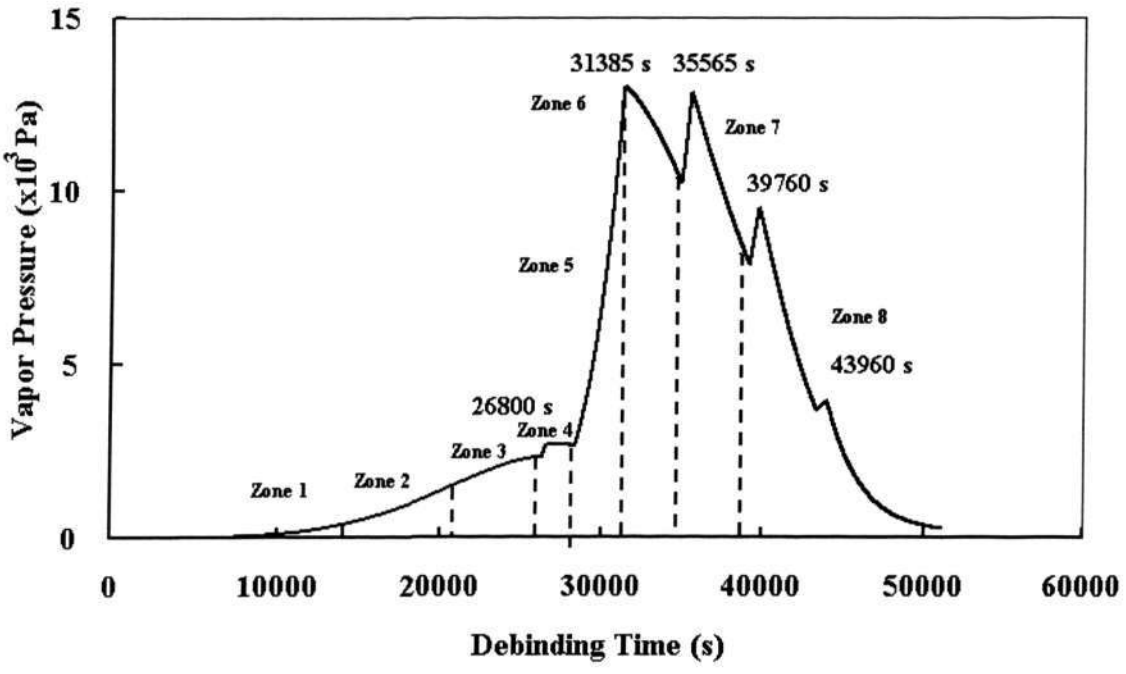

Figure 5.24 LMW component: Vapor pressure versus debinding time

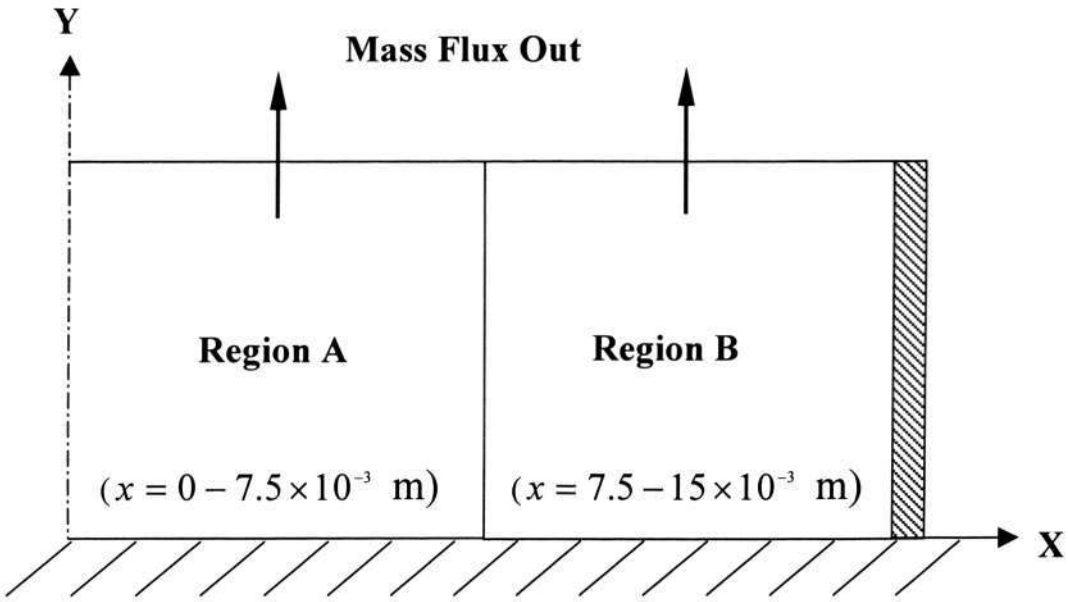

Figure 5.25 Mass transfer at the outer surface

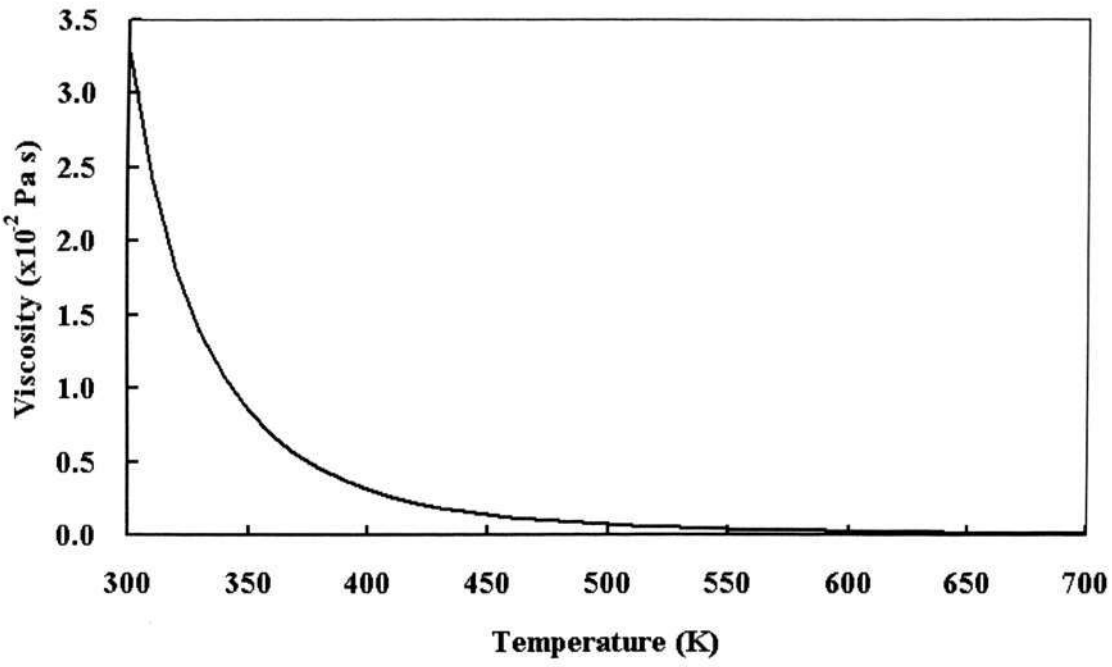

Figure 5.26 Viscosity of LMW component

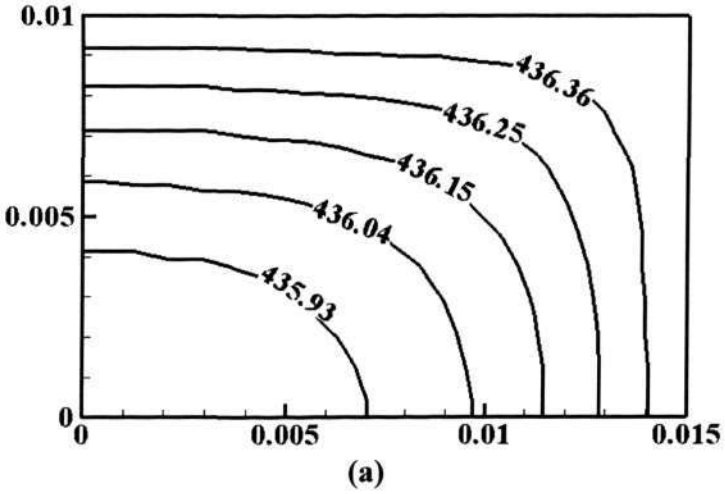

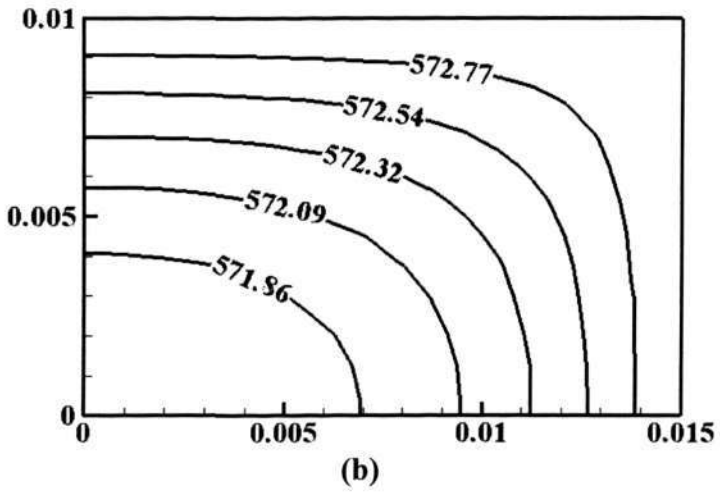

Figure 5.27 Temperature distributions at debinding times of (a)9000 s ($T_{surface}$ = 436.47 K) and (b)31365 s ($T_{surface}$ = 573 K)

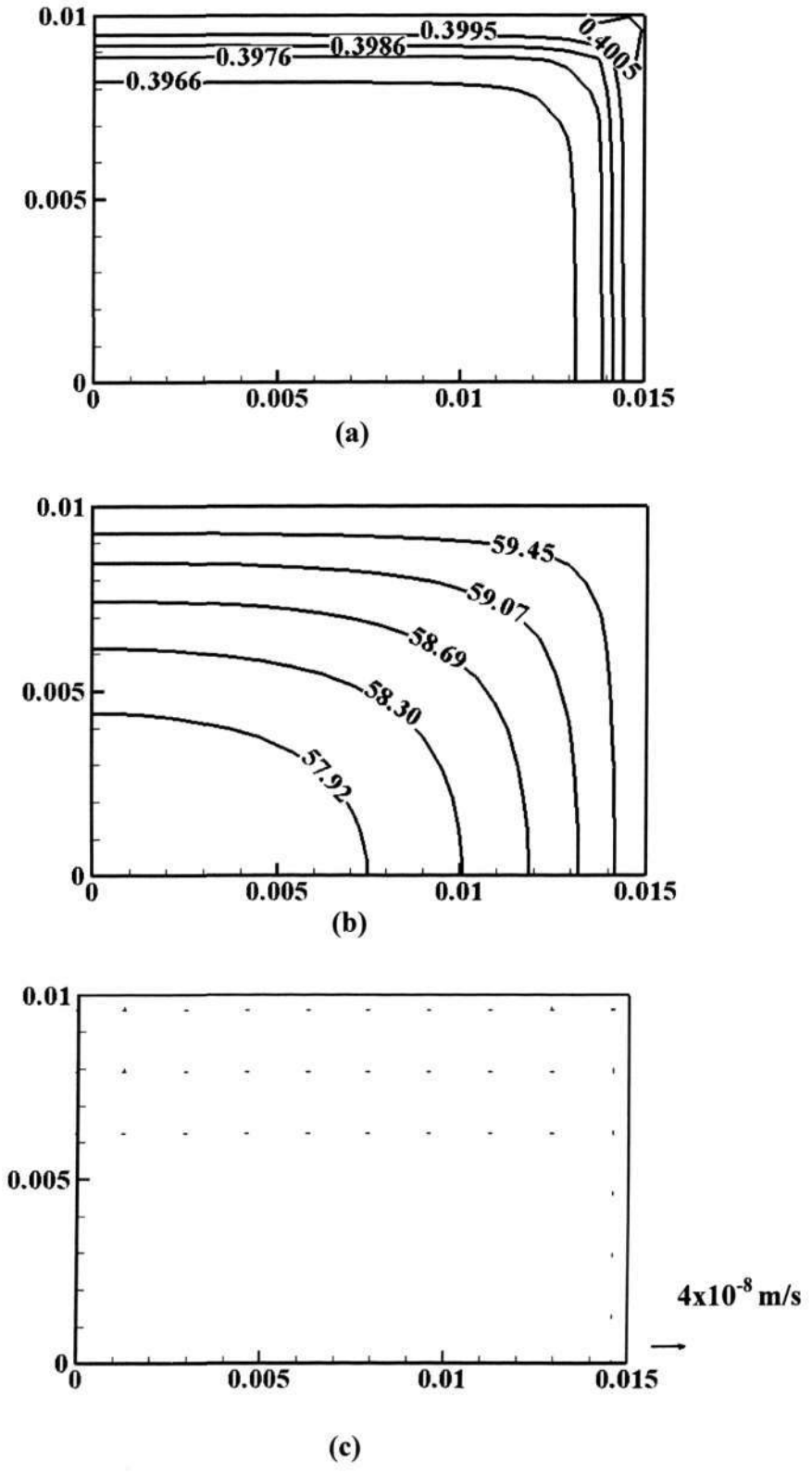

Figure 5.28 Distributions of (a) liquid saturation, (b) vapor pressure, and (c) liquid velocity of LMW component at 9000 s ($T_{surface}$ = 436.47 K)

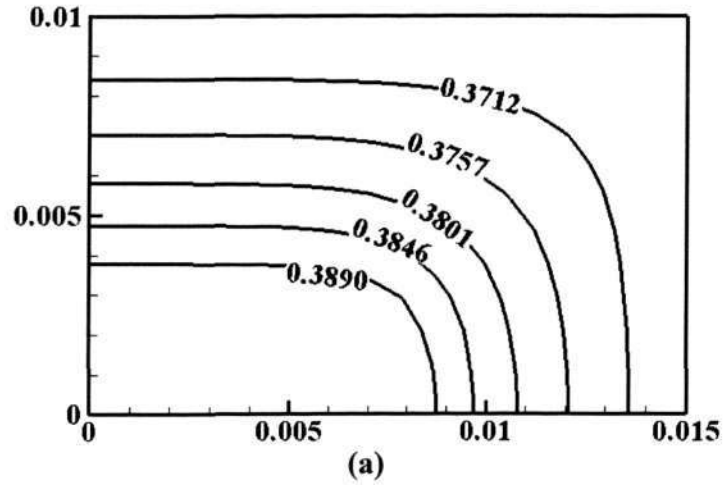

(a)

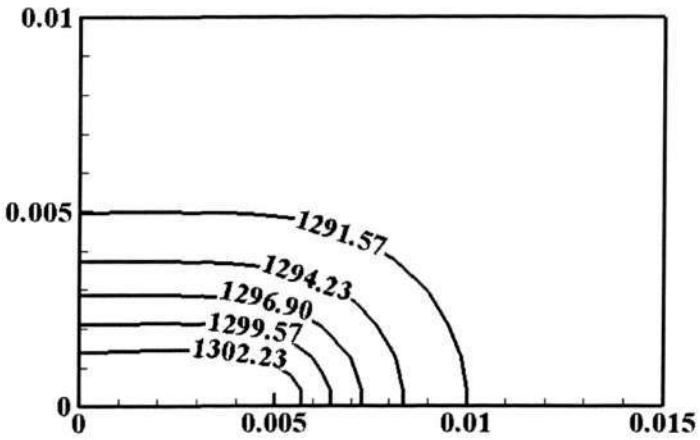

(b)

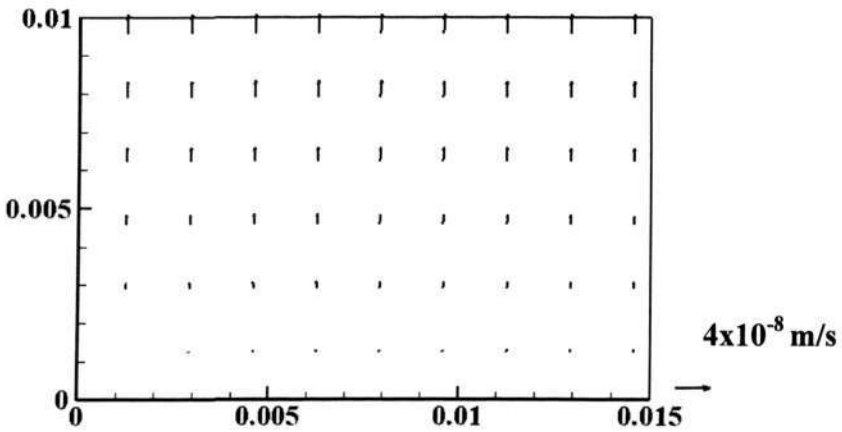

(c)

Figure 5.29 Distributions of (a) liquid saturation, (b) vapor pressure, and (c) liquid velocity of LMW component at 19800 s ($T_{surface}$ = 502.36 K)

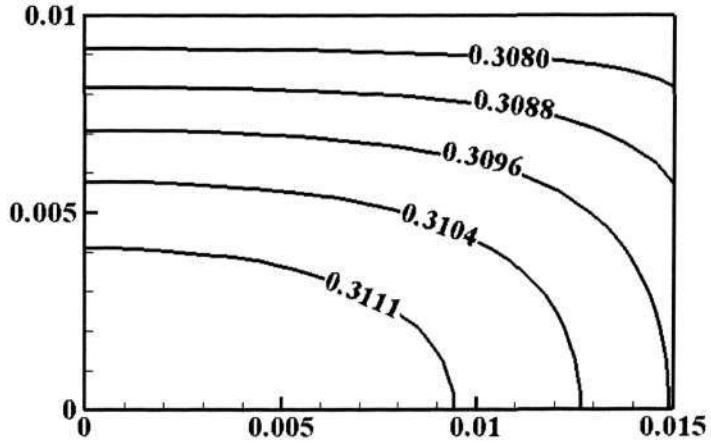

(a)

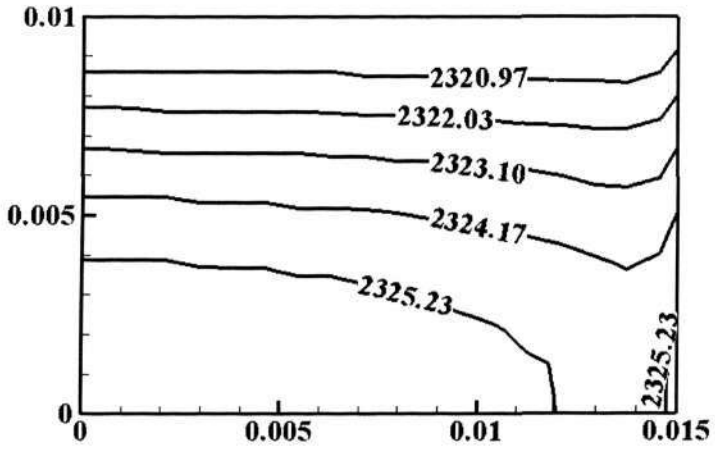

(b)

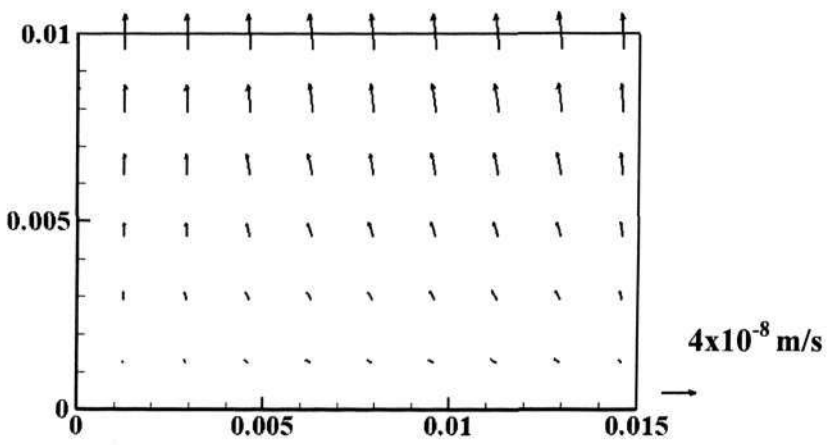

(c)

Figure 5.30 Distributions of (a) liquid saturation, (b) vapor pressure, and (c) liquid velocity of LMW component at 26325 s ($T_{surface}$ = 519 K)

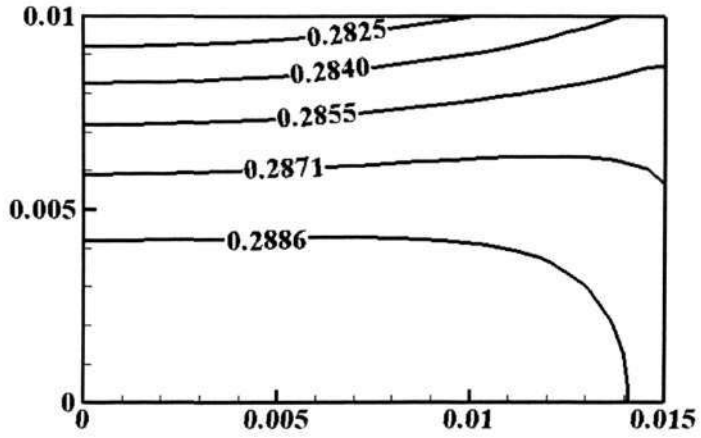

(a)

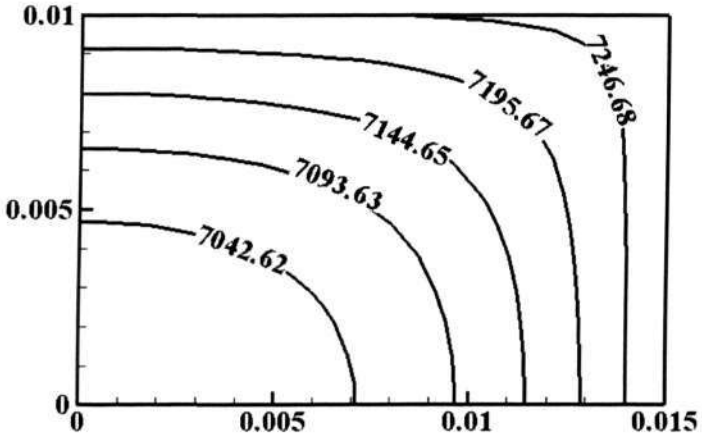

(b)

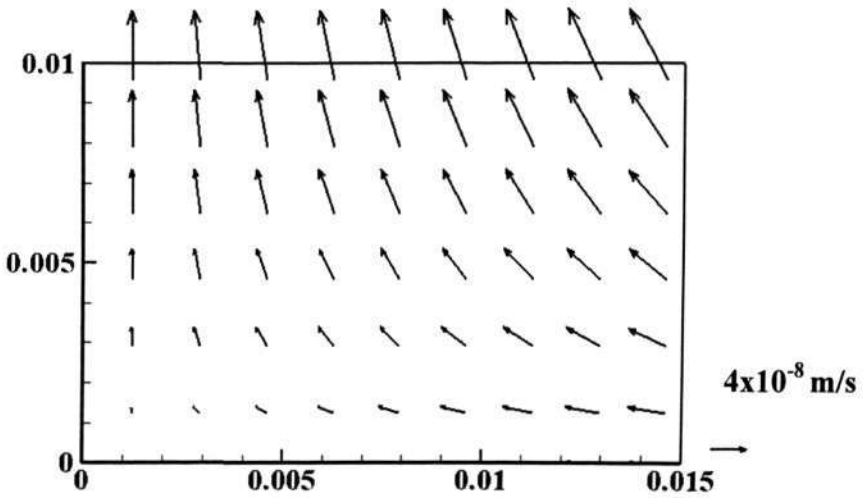

(c)

Figure 5.31 Distributions of (a) liquid saturation, (b) vapor pressure, and (c) liquid velocity of LMW component at 30165 s ($T_{surface}$ =553 K)

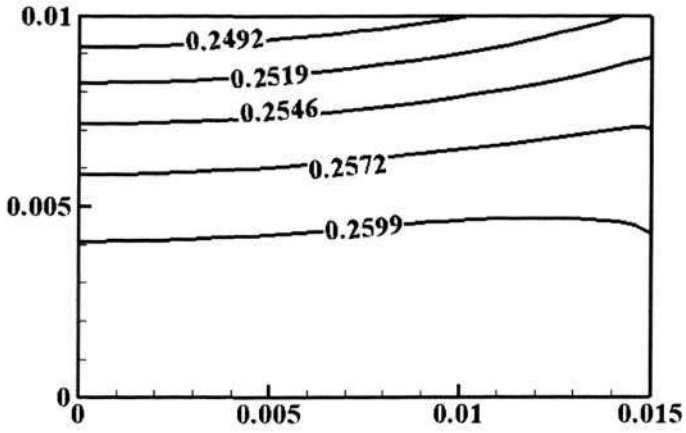

(a)

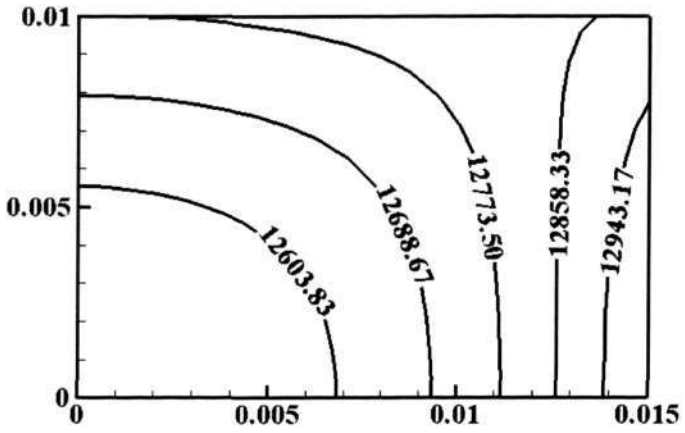

(b)

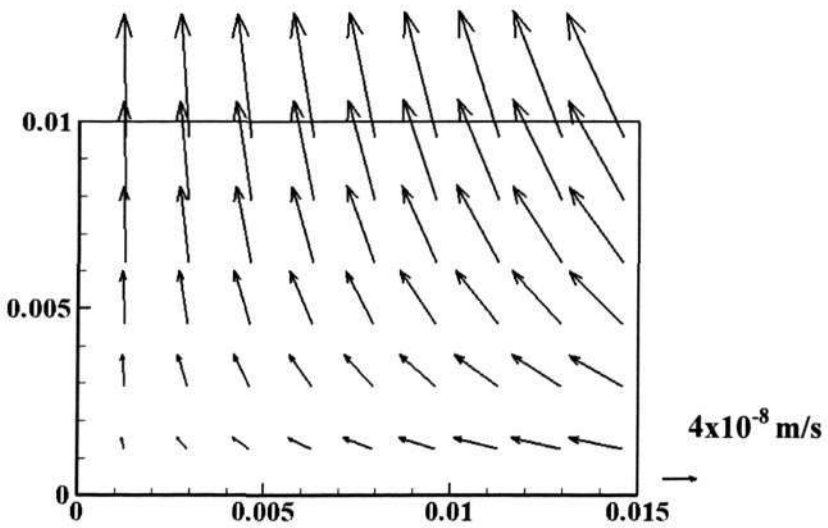

(c)

Figure 5.32 Distributions of (a) liquid saturation, (b) vapor pressure, and (c) liquid velocity of LMW component at 31365 s ($T_{surface}$ = 573 K)

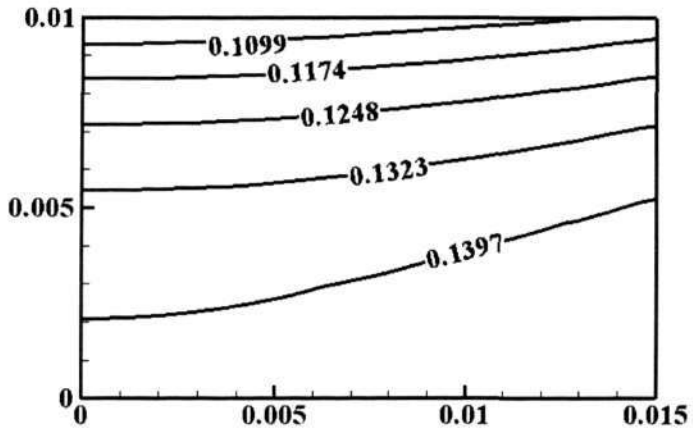

(a)

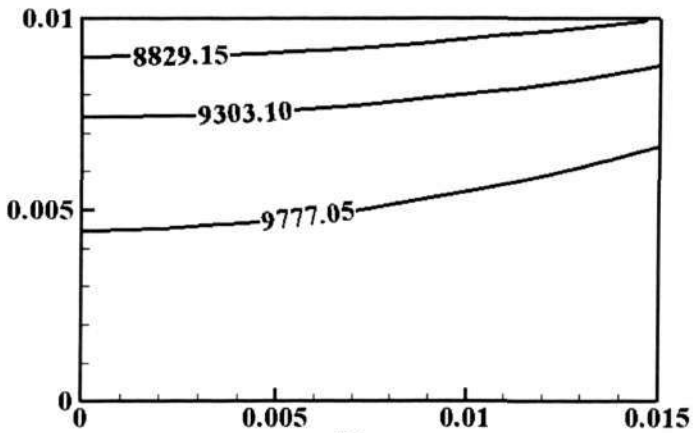

(b)

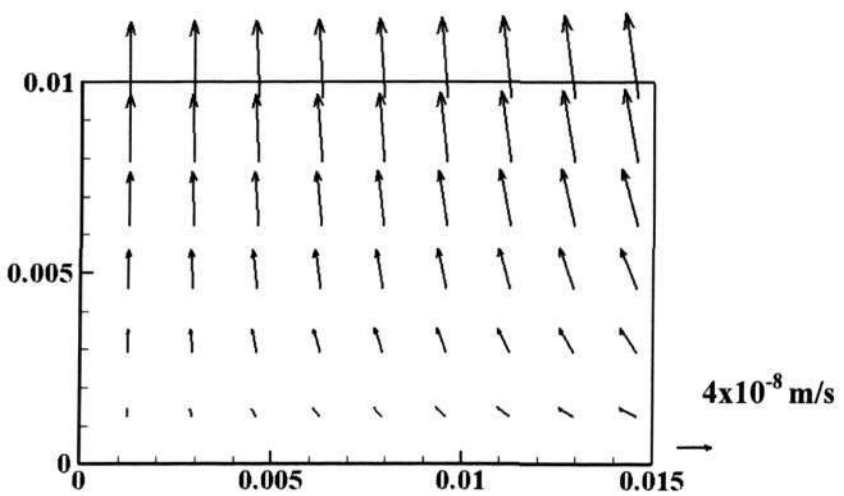

(c)

Figure 5.33 Distributions of (a) liquid saturation, (b) vapor pressure, and (c) liquid velocity of LMW component at 34965 s ($T_{surface}$ = 573 K)

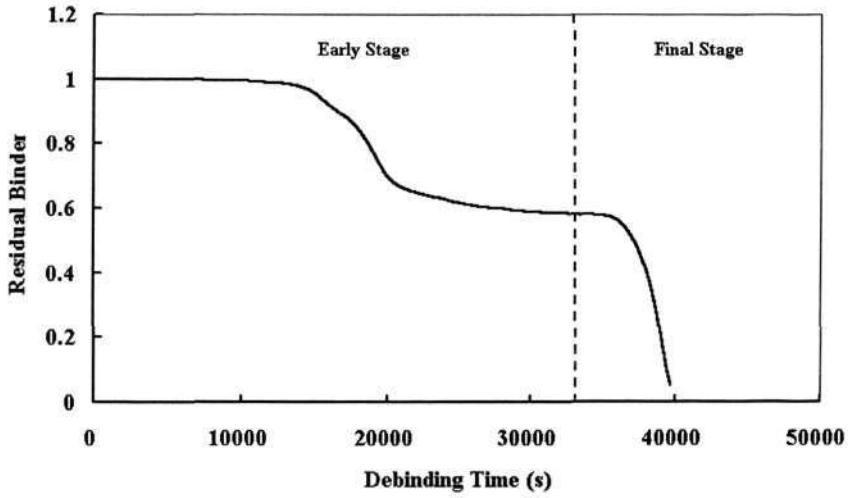

Figure 5.34 Two-component: Residual binder versus debinding time

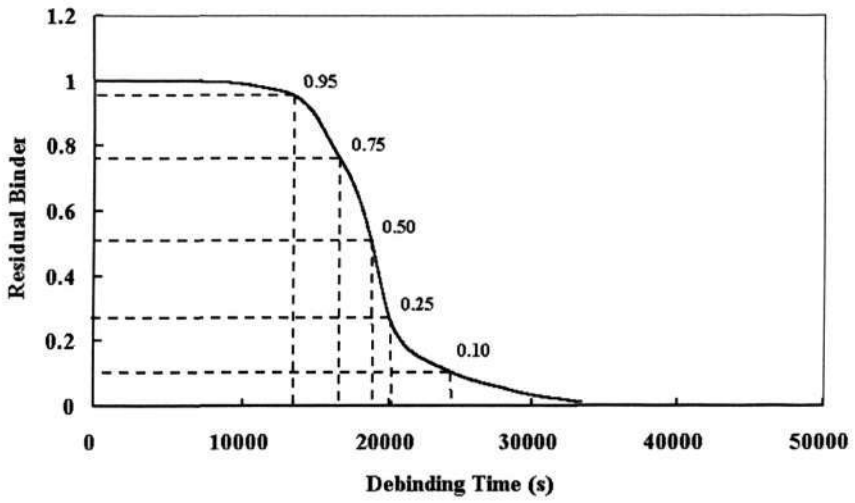

Figure 5.35 Two-component: Residual LMW component versus debinding time

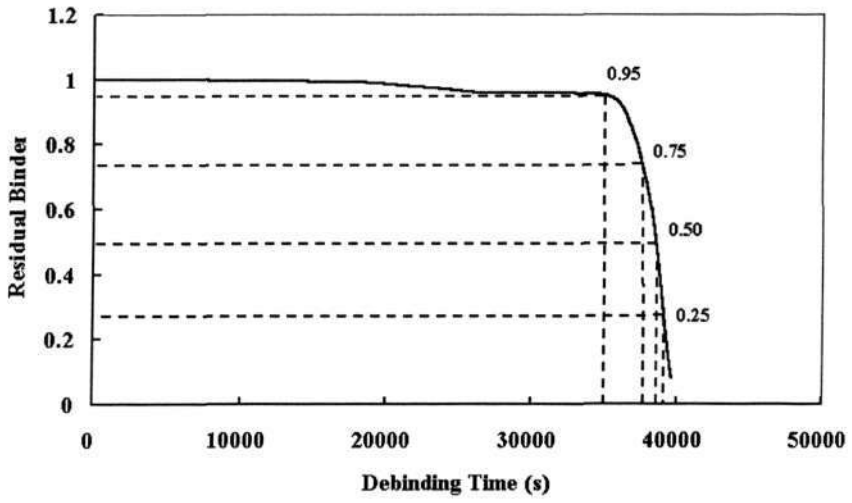

Figure 5.36 Two-component: Residual HMW component versus debinding time

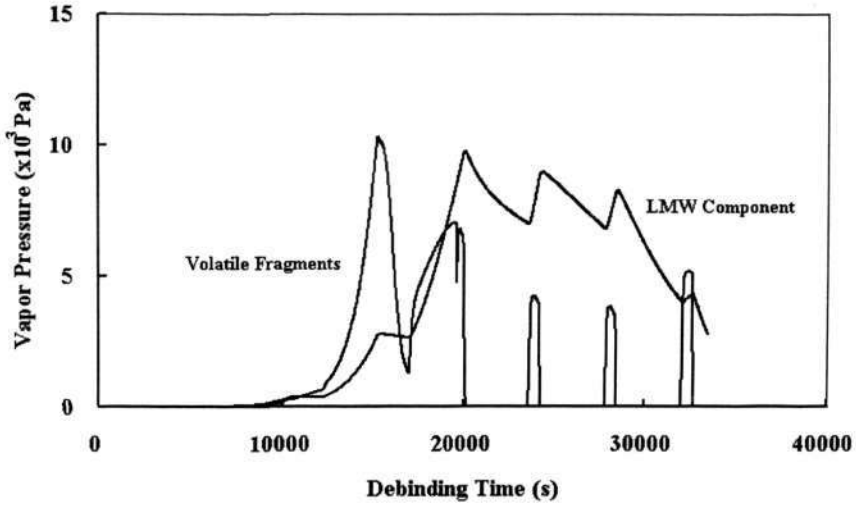

Figure 5.37 Vapor pressures during early stage of thermal debinding

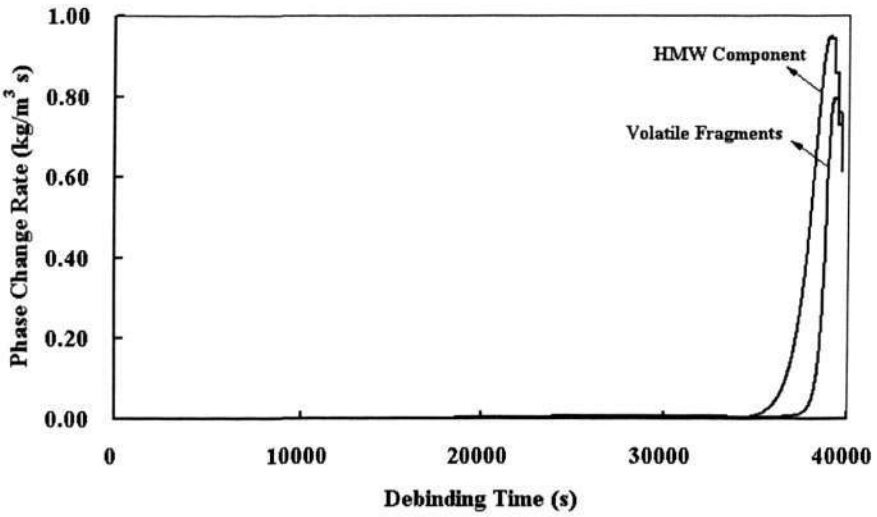

Figure 5.38 Phase changes during final stage of thermal debinding

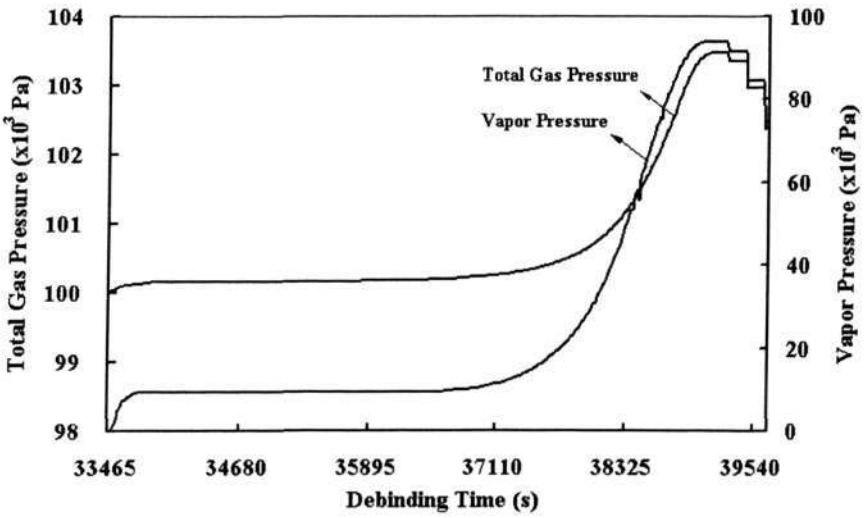

Figure 5.39 Pressures during final stage of thermal debinding

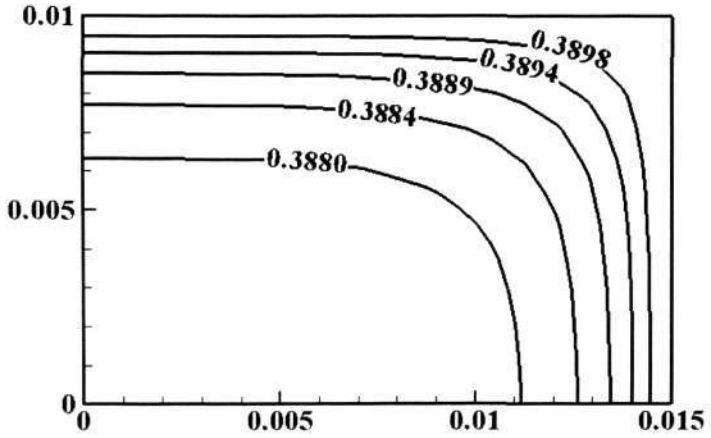

(a)

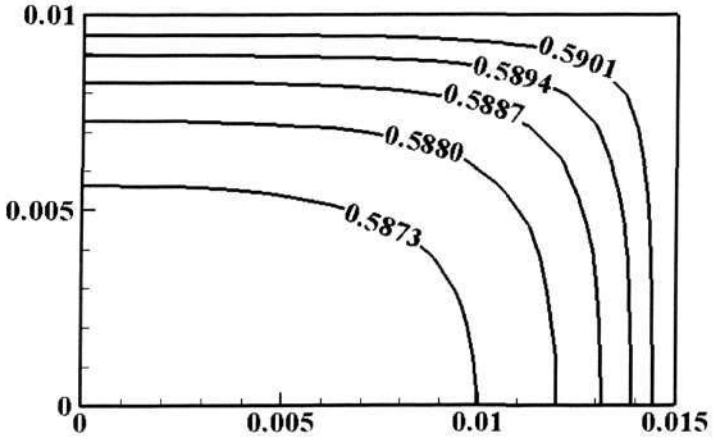

(b)

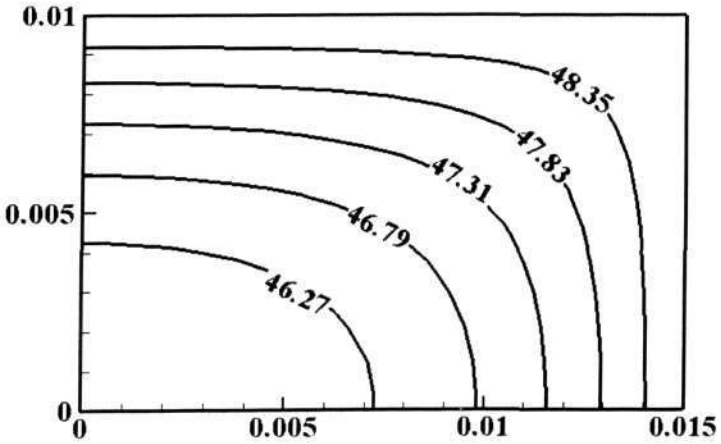

(c)

Figure 5.40 Distributions of (a) liquid saturation of LMW component, (b) liquid saturation of HMW component, and (c) vapor pressure at 7980 s ($T_{surface}$ = 433 K)

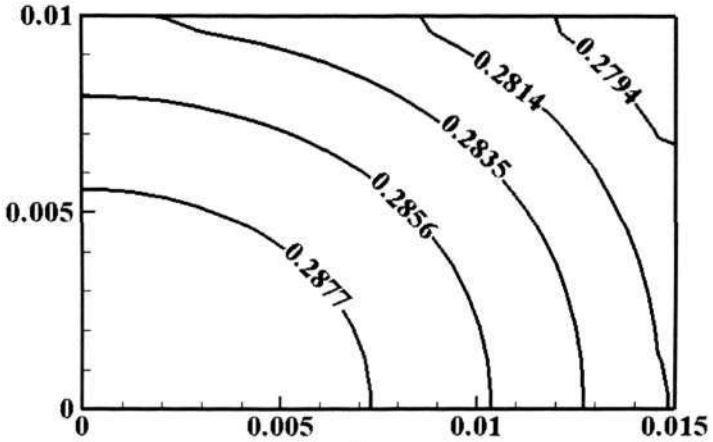

(a)

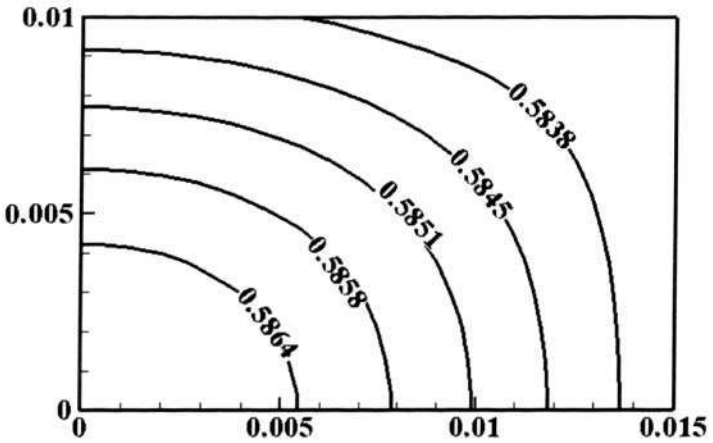

(b)

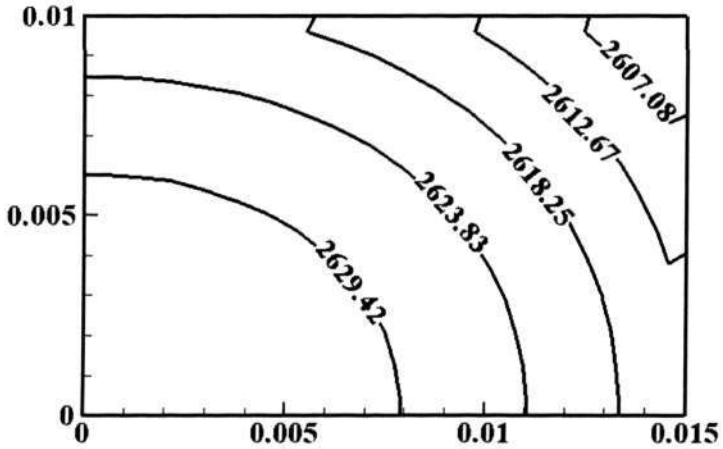

(c)

Figure 5.41 Distributions of (a) liquid saturation of LMW component, (b) liquid saturation of HMW component, and (c) vapor pressure at 16980 s ($T_{surface}$ = 523 K)

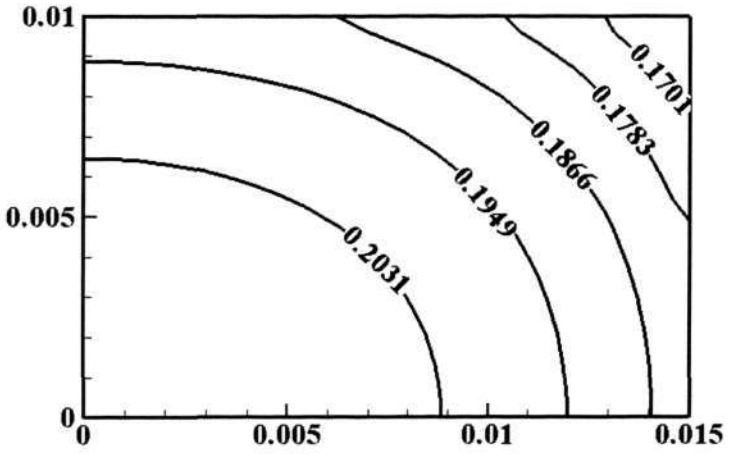

(a)

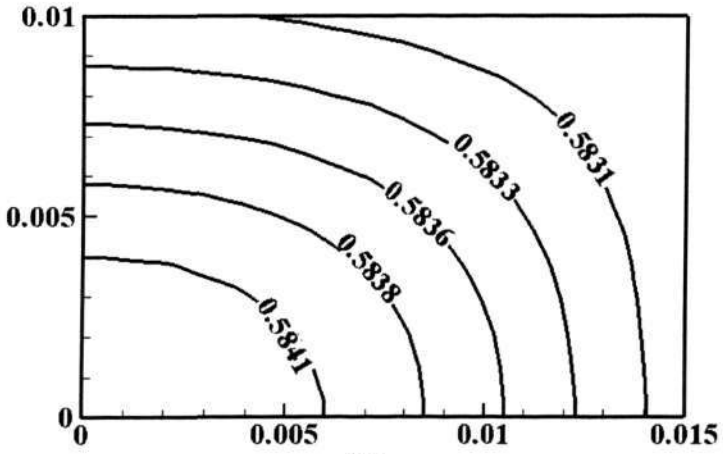

(b)

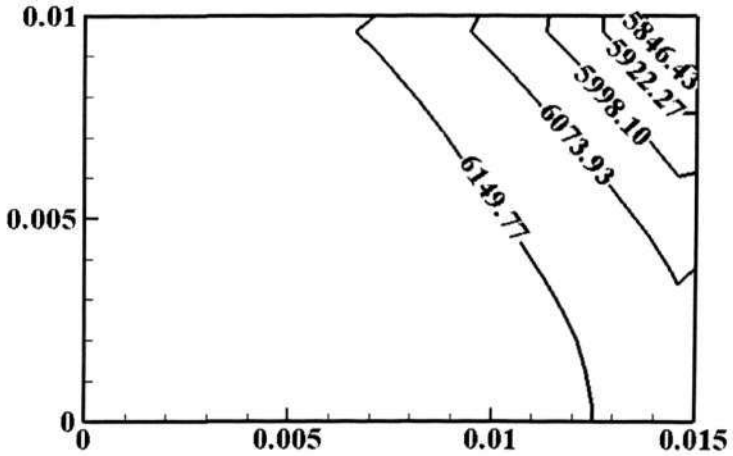

(c)

Figure 5.42 Distributions of (a) liquid saturation of LMW component, (b) liquid saturation of HMW component, and (c) vapor pressure at 18780 s ($T_{surface}$ = 553 K)

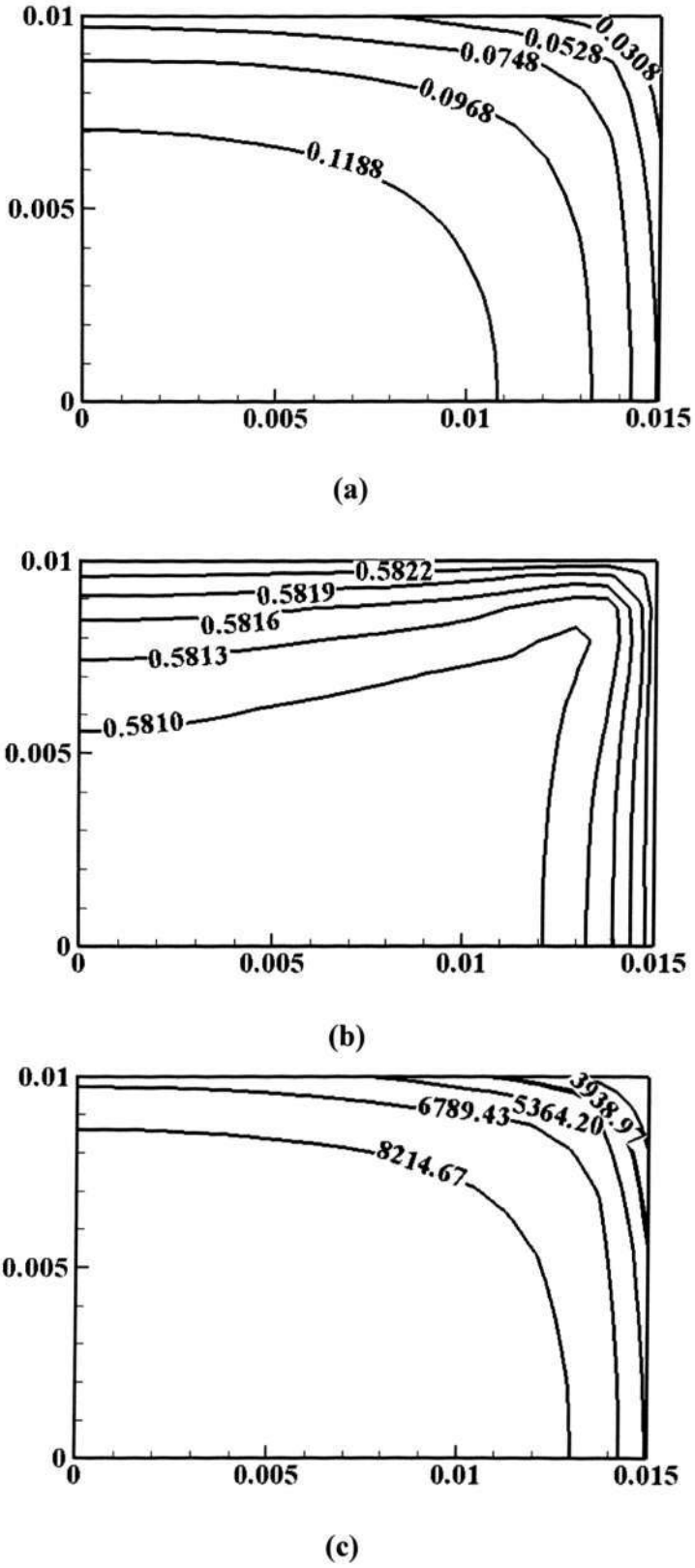

Figure 5.43 Distributions of (a) liquid saturation of LMW component, (b) liquid saturation of HMW component, and (c) vapor pressure at 19980 s ($T_{surface}$ = 573 K)

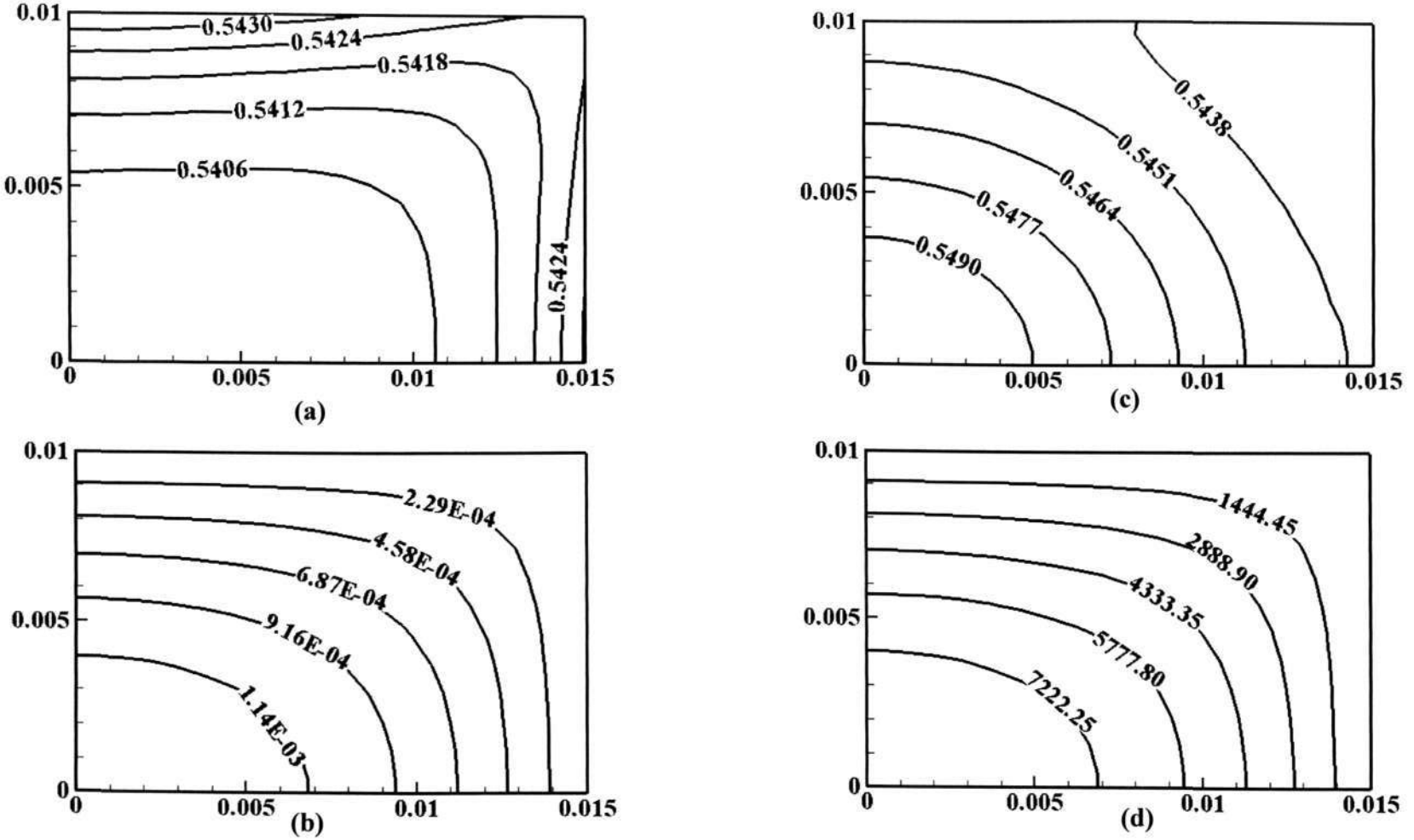

Figure 5.44 Distributions of (a) liquid saturation of HMW component, (b) liquid saturation of volatile fragments, (c) total liquid saturation, and (d) vapor pressure at 36180 s ($T_{surface}$ = 648 K)

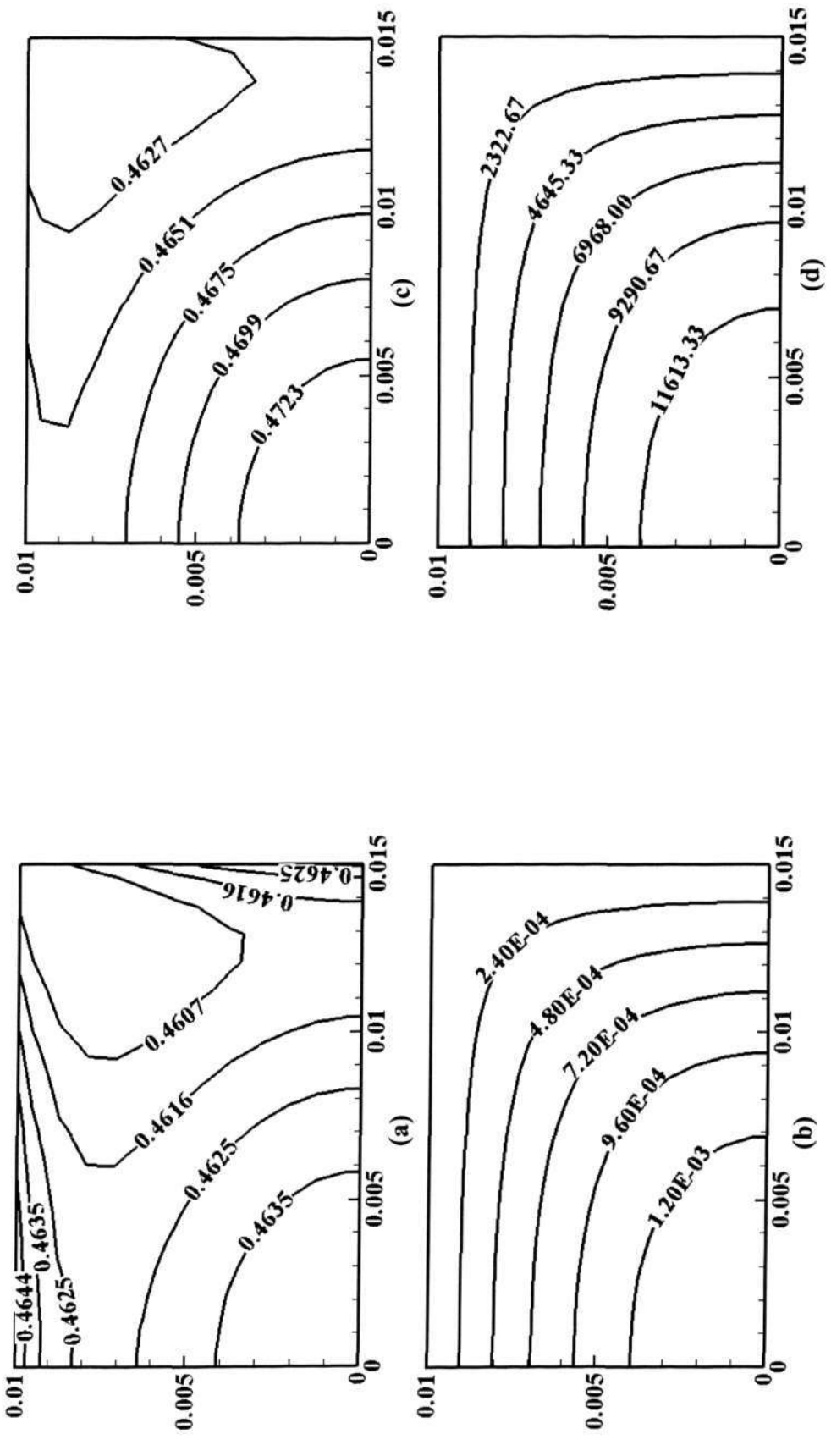

Figure 5.45 Distributions of (a) liquid saturation of HMW component, (b) liquid saturation of volatile fragments, (c) total liquid saturation, and (d) vapor pressure at 37380 s ($T_{surface}$ = 668 K)

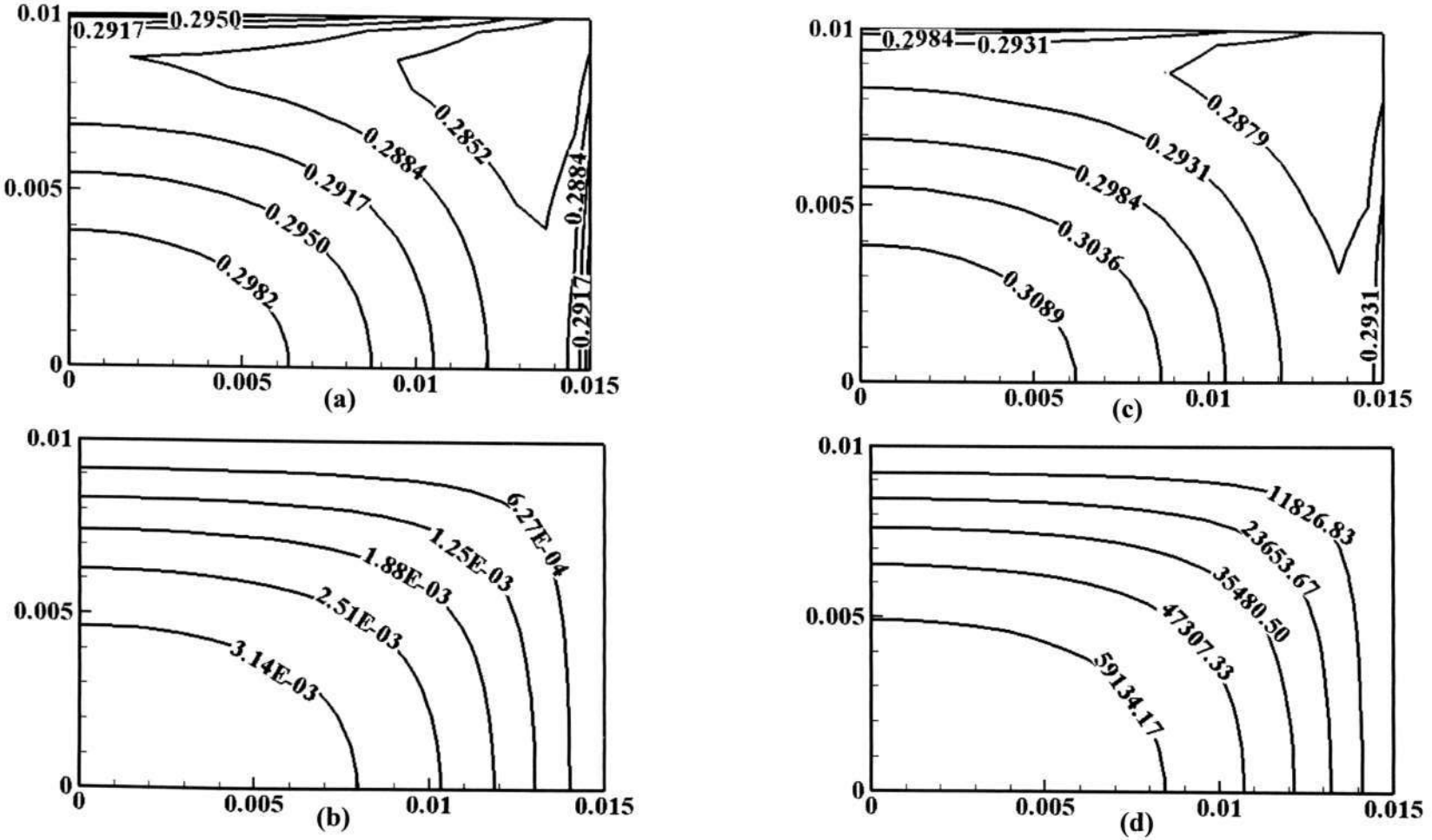

Figure 5.46 Distributions of (a) liquid saturation of HMW component, (b) liquid saturation of volatile fragments, (c) total liquid saturation, and (d) vapor pressure at 38580 s ($T_{surface}$ = 688 K)

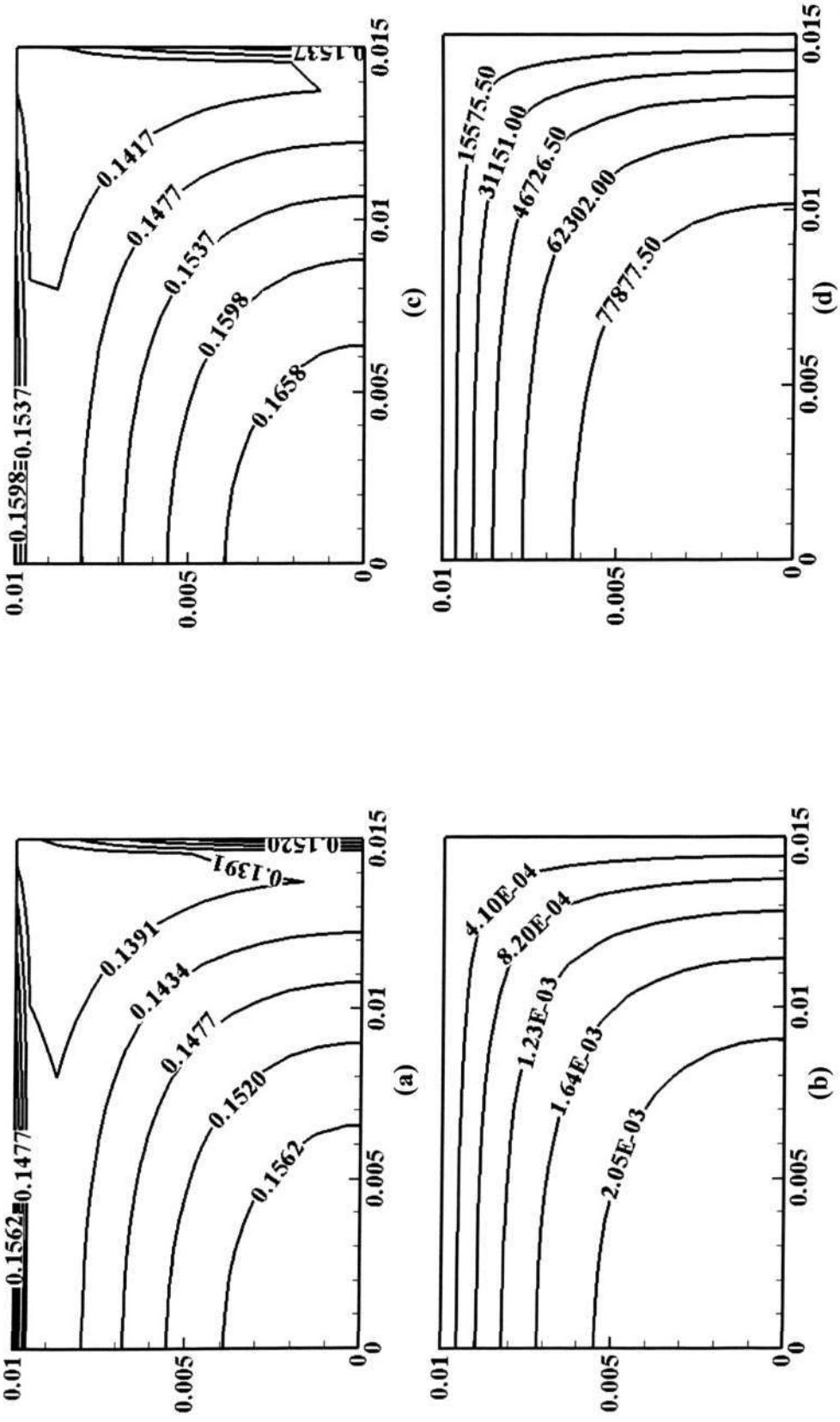

Figure 5.47 Distributions of (a) liquid saturation of HMW component, (b) liquid saturation of volatile fragments, (c) total liquid saturation, and (d) vapor pressure at 39180 s ($T_{surface}$ = 698 K)

CHAPTER 6

CONCLUSIONS AND RECOMMENDATIONS

6.1 Conclusions

As mentioned earlier, the thermal debinding process was investigated numerically and experimentally. A theoretical model was developed to simulate the thermal debinding of a two-component binder system (PP and SA) from a PIM compact. The model describes the physical phenomena of thermal debinding that involve simultaneous heat and mass transfers and phase changes in a porous medium. This is the first attempt to model the thermal debinding process of a two-component binder system that involves early and final stages. During the early stage, the LMW component is first removed and followed by the removal of the HMW component at the final stage.

To validate the theoretical model, two limiting cases were deduced from the model and solved numerically, respectively, for the early and the final stages. Experimental works were conducted to investigate the binder distributions during the thermal debinding of the LMW component and the HMW component. The numerical results are then compared with the experimental data for both stages of the thermal debinding. The numerical models successfully predict quantitatively the residual binder and the binder distributions during these two stages of thermal debinding. After the validations, the numerical models were integrated to simulate the thermal debinding of a two-component binder system from a PIM compact.

Based on the numerical results, the binder removals, the phase changes, the vapor and total gas pressures, the mass transfers, the distributions of the binders, and the binder removal mechanisms were studied.

Binder removal: During the early stage, the LMW component is removed at low temperatures (greater than evaporation temperature). The HMW component is only removed significantly at high temperatures (greater than degradation temperature) during the final stage. For both stages, the binder removal rate increases as temperature increases.

Phase changes: During the early stage, the evaporation rate of liquid LMW component reaches the order of 10^{-2} kg/m^3 s. The thermal degradation rate of liquid HMW component and evaporation rate of liquid volatile fragments are low (< 10^{-2} kg/m^3 s). During the final stage, the thermal degradation rate of liquid HMW component and the evaporation rate of liquid volatile fragments reach the order of 10^{-1} kg/m^3 s. However, the thermal degradation of liquid HMW component dominates over (an order of magnitude greater than) the evaporation of liquid volatile fragments before the later period of final stage ($t < 38310$ s). For both stages, the evaporation rates and the thermal degradation rate increase as temperature increases.

Vapor and total gas pressures: Because there are less pores inside the compact and the temperature is low, the buildups of vapor pressures (LMW component and volatile fragments) are insignificant (< 15 KPa) during the early stage. As a result, the total gas pressure is approximately equivalent to the atmospheric pressure. As more pores are created and the temperature increases, the buildup of the vapor pressure (volatile

fragment) becomes significant (> 90 KPa). This results in the increase in total gas pressure during the final stage. The vapor and total gas pressures decrease towards the outer surface indicating that the vapor phase escapes faster at the outer surfaces. For both stages, the vapor pressures increase as the evaporation rates increase.

Mass transfers: The mass transfers of LMW component are mainly due to the capillary driven action and the binary diffusion in solution of liquid LMW and HMW components. The pressure driven action and the gas phase transport are insignificant during the early stage. During the final stage, the mass transfers of the HMW component and the volatile fragments are mainly due to the capillary driven and pressure driven actions. Both of the liquid phase and gas phase transports are essential in mass transfers during the final stage. The gas phase transport dominates the mass transfers at the later period when less liquid phase remains inside the compact.

Distributions of binders: During the thermal debinding process, the temperature differences throughout the whole compact are small (for any given time). As a result, the thermal degradation and evaporation occur throughout the compact. For the early stage, the accumulation of liquid LMW component is observed during the beginning period. This is due to the outward migration of liquid LMW component and the low surface mass transfers. As temperature increases, the liquid and vapor LMW component at the outer surfaces always are removed faster than that in the internal region. This is because the surface mass transfers are high compared to the internal evaporation of liquid LMW component. During the final stage, the distributions of total liquid binder (liquid HMW component and volatile fragments) decrease towards the outer surfaces at the beginning period of final stage. As temperature increases, the

increased gradient of total gas pressure tends to drive the less viscous liquid HMW component towards the outer surfaces. This results in the accumulation of total liquid binder at the outer surfaces.

Binder removal mechanisms: During the early stage, there are less pores inside the compact. Instead of evaporating internally, the liquid LMW component is preferable to migrate outwards and is then removed at the outer surfaces. The comparison of orders of magnitude shows that the surface mass transfers dominate over the evaporation of liquid LMW component and the migration/diffusion mass transfers. These results indicate that the early stage of thermal debinding is dominated by a surface controlled reaction. Overall, the total liquid binder (liquid HMW component and liquid volatile fragments) distributes quite evenly throughout the compact. The comparison of orders of magnitude shows that the thermal degradation of liquid HMW component and the evaporation of liquid volatile fragments dominate over the migration/diffusion mass transfers. These results indicate that the final stage of thermal debinding is dominated by the volumetric reactions.

6.2 Recommendations

The numerical model is capable of describing the physical mechanisms involved in the thermal debinding process. However, quite a number of transport equations and empirical equations are used in the model. Thus, this is a highly nonlinear problem that required underrelaxation extensively in the numerical solution. To evaluate the robustness of the model, sensitivity analyses could be conducted on the involved parameters.

It is suggested that the numerical model be extended to three-dimensional for more practical applications. The experimental works could be further advanced to three-dimensional to investigate the binder distributions and to compare with the numerical results.

Studies on the criteria of the defect formation inside the PIM compact during thermal debinding could be done. Considering the criteria in the model, the optimization of the thermal debinding process could be conducted.

REFERENCES

Angermann, H. H., Yang, F. K. and Van Der Biest, O., 1992, Removal of low molecular weight components during thermal debinding of powder compacts, *J. Mater. Sci., Vol. 27, pp. 2534-2538*

Angermann, H. H. and Van Der Biest, O., 1993, Low temperature debinding kinetics of two-component model systems, *Int. J. Powder Metall. Vol. 29, pp. 239-250*

Barone, M. R. and Ulicny, J. C., 1990, Liquid-Phase Tansport During Removal of Organic Binders in Injection-Molded Ceramics, *J. Am. Ceram. Soc., Vol. 73 No. 11, pp. 3323-3333*

Barone, M. R., Ulicny, J. C., Hengst, R. R. and Pollinger, J. P., 1988, Removal of organic binder in ceramic powder compacts, Messing, C. L., Fuller, E. R., Hausner, H. Jr. (eds.), *Ceramic Transactions, Ceramic Powder Science II, American Ceramic Society, Westerville, OH, Vol. 1, pp. 575-583*

Baver, L. D. and Gardner, W. H., 1972, Soil Physics, 4^{th} *ed. Wiley, New York*

Bicerano, J., 1993, Prediction of polymer properties, *Marcel Dekker, New York*

Bockhorn, H., Hornung, A., Hornung, U. and Schawaller, D., 1999, Kinetic study on the thermal degradation of polypropylene and polyethylene, *J. Anal. Appl. Pyrol., Vol. 48, pp. 93-109*

Calvert, P. and Cima, M., 1990, Theoretical models for binder burnout, *J. Am. Ceram. Soc., Vol. 73 No. 3, pp. 575-579*

Chan, J. H. and Balke, S. T., 1997, The thermal degradation kinetics of polypropylene: Part II. Thermogravimetric analyses, *Polym. Degrad. Stabil., Vol. 57, pp. 135-149*

Cima, M. J., Lewis, J. A. and Devoe, A. D., 1989, Binder distribution in ceramic greenware during thermolysis, *J. Am. Ceram. Soc., Vol. 72, No. 7, pp. 1192-1199*

Chung, K. H., Wu, C. S. and Malawer, E. G., 1989, Thermomagnetometry and thermogravimetric analysis of carbonyl iron powder, *Thermochim. Acta, Vol. 154, No. 2, pp. 195-204*

Dullien, F. A. L., 1992, Porous media: Fluid transport and pore structure, *2nd ed., Academic Press, San Diego*

Evans, J. R. G., Edirisinghe, M. J., Wright, J. K. and Crank, J., 1991, On the removal of organic vehicle from moulded ceramic bodies, *Proc. R. Soc. Lond. A, Vol. 432, pp. 321-340*

Feng, Z. C., He, B. and Lombardo, S. J., 2002, Stress distribution in porous ceramic bodies during binder burnout, *J. Appl. Mech., Vol. 69, pp. 497-501*

Feng, K. and Lombardo, S. J., 2003a, Modeling of the pressure distribution in three-dimensional porous green bodies during binder removal, *J. Am. Ceram. Soc., Vol. 86, No. 2, pp. 234-240*

Feng, Z. C. and Lombardo, S. J., 2003b, Analytical method for the minimum time for binder removal from three-dimensional porous green bodies, *J. Mater. Res., Vol. 18, No. 11, pp. 2717-2723*

Flory, P. J., 1953, Principles of Polymer Chemistry, *Cornell University Press, Ithaca*

German, R. M., 1981, Porosity and particle size effects on the gas flow characteristics of porous metals, *Powder Technol., Vol. 30, pp. 81-86*

German, R. M., 1987, Theory of thermal debinding, *Int. J. Powder Metall., Vol. 23, pp. 237-245*

German, R. M., 1990, Powder Injection Molding, *Metal Powder Industries Federation*

German, R. M. and Bose, A., 1997, Injection Molding of Metals and Ceramics, *Metal Powder Industries Federation*

Hong S. U., 1995, Prediction of polymer/solvent diffusion behavior using free-volume theory, *Ind. Eng. Chem. Res., Vol. 34, pp. 2536-2544*

Hrdina, K. E., Halloran, J. W., Oliveira, A. and Kaviany, M., 1998, Chemistry of removal of ethylene vinyl acetate binders, *J. Mater. Sci., Vol. 33, pp. 2795-2803*

Hsu, C. T., Cheng, P. and Wong, K. W., 1995, A lumped-parameter model for stagnant thermal conductivity of spatially periodic porous media, *ASME J. Heat Trans., Vol. 117, pp. 264-269*

Hwang, K. S. and Tsou, T. H., 1992, Thermal debinding of powder injection molded parts: observations and mechanisms, *Metall. Mater. Trans. A, Vol. 23A, pp. 2775-2782*

Incropera, F. P. and Dewitt, D. P., 2002, Fundamentals of Heat and Mass Transfer, *5th ed., John Wiley & Sons, New York*

Jacob, B. and Bachmat, Y., 1991, Introduction to Modeling of Transport Phenomena in Porous Media, *Kluwer Academic Publishers, Dordrecht, Boston*

Japka, J. E., 1988, Microstructure and properties of carbonyl iron powder, *Journal of Metals, Vol. 40, No. 8, pp. 18-21*

Kaviany, M., 1991, Principles of Heat Transfer in Porous Media, *Springer-Verlag, New York*

Lam, Y. C., Ying S. J., YU, S. C. M. and Tam, K. C., 2000, Simulation of polymer removal from a powder injection molding compact by thermal debinding, *Metall. Mater. Trans. A, Vol. 31A, pp. 2597-2606*

Lam, Y. C., Ying, S. J., Lam, K. H., Ma, J., YU, S. C. M. and Tam, K. C., 2002, Numerical and experimental investigation of thermal debinding, *Powder Metall., Vol.45, No. 3, pp. 233-236*

Langer, I. and Lehnert, W., 1998, Optimization of thermal debinding by using drying theory, *Proceedings of the 1998 Powder Metallurgy World Congress & Exhibition, European Powder Metallurgy Association, pp. 45-50*

Lewis, J. A. and Cima, M. J., 1990, Direct Observation of Binder Distribution Processes in 2-D Porous Networks During Thermolysis, Messing, G. L., Hirano, S., Hausner, Jr. H. (eds.), *Ceramic Transactions, Ceramic Powder Science III, American Ceramic Society, Westerville, OH, Vol. 12, pp. 583-590*

Lewis, J. A., Cima, M. J. and Bentz, D. P., 1996, Computer Simulations of Binder Removal from 2-D and 3-D Model Particulate Bodies, *J. Am. Ceram. Soc., Vol. 79, No. 5, pp. 1377-1388*

Li, Y. M., Liu, S. J., Qu, X. H. and Huang, B. Y., 2003, Thermal debinding processing of 316L stainless steel powder injection molding compacts, *J. Mater. Process. Tech., Vol. 6487, pp. 1-5*

Lin, S. T. and German, R. M., 1990, Mechanical properties of fully densified injection-molded carbonyl iron powder, *Metall. Mater. Trans. A, Vol. 21A, pp. 2531-2539*

Liu, D-M and Tseng, W. J., 1997, Porosity development in ceramic injection moulduings via different strategies, *J. Mater. Sci. Lett., Vol. 16, pp. 482-484*

Liu, D-M and Tseng, W. J., 1999, Binder removal from injection moulded zirconia ceramics, *Ceram. Int., Vol. 25, pp. 529-534*

Lombardo, S. J. and Feng, Z. C., 2002, Pressure distribution during binder burnout 3-dimensional porous ceramic bodies with anisotropic permeability, *J. Mater. Res., Vol. 17, pp. 1434-1440*

Lu, P. K. and Lannutti, J. J., 2000, Effect of density on dimensional tolerance during binder removal, *J. Am. Ceram. Soc., Vol. 83, No. 10, pp. 2536-2542*

Matar, S. A., Edirisinghe, M. J., Evans, J. R. G. and Twizell, E. H., 1993, The effect of porosity development on the removal of organic vehicle from ceramic or metal moldings, *J. Mater. Res., Vol. 8, No. 3, pp. 617-625*

Matar, S. A., Edirisinghe, M. J., Evans, J. R. G. and Twizell, E. H., 1995, Modeling the removal of organic vehicle from ceramic or metal mouldings: the effect of gas permeation on the incidence of defects, *J. Mater. Res. Vol. 30, pp. 3805-3810*

Matar, S. A., Edirisinghe, M. J., Evans, J. R. G. and Twizell, E. H., 1996, Diffusion of degradation products in ceramic moldings during pyrolysis: Effect of geometry, *J. Am. Ceram. Soc., Vol. 79, No. 3, pp. 749-755*

Maximenko, A. and Van Der Biest, O., 1998, Finite element modeling of binder removal from ceramic mouldings, *J. Eur. Ceram. Soc., Vol. 79, pp. 1001-1009*

Oliveira, A. A. M., Kaviany, M., Hrdina, K. E. and Halloran, J. W., 1999, Mass diffusion-controlled bubbling and optimum schedule of thermal degradation of polymeric binders in molded powders, *Int. J. Heat Mass Trans., 42, pp. 3307-3329*

Patankar, Suhas V., 1980, Numerical Heat Transfer and Fluid Flow, *Hemisphere Publishing Corporation*

Reich, L. and Stivala, S. S., 1971, Element of Polymer Degradation, *McGraw-Hill, New York*

Reid, R. C., Prausnitz, J. M. and Poling, B. E., 1987, The Properties of Gases and Liquids, *4th ed., McGraw-Hill, New York*

Shaw, H. M., Hutton, T. J. and Edirisinghe, M. J., 1992, On the formation of porosity during removal of organic vehicle from injection-moulded ceramic bodies, *J. Mater. Sci. Lett., Vol. 11, pp. 1075-1077*

Shaw, H. M., Edirisinghe, M. J. and Holding, S., 1993, Binder degradation and redistribution during pyrolysis of ceramic injection mouldings, *J. Mater. Sci. Lett., Vol. 12, pp. 1227-1230*

Shaw, H. M. and Ediringhe, M. J., 1995a, A model for the diffusion of organic additives during thermolysis of ceramic body, *Philos. Mag. A, Vol. 72, No. 1, pp. 267-280*

Shaw, H. M. and Ediringhe, M. J., 1995b, Shrinkage and particle packing during removal of organic vehicle from ceramic injection mouldings, *J. Eur. Ceram. Soc., Vol. 15, pp. 109-116*

Shi, Z., Guo, Z. X. and Song, J. H., 2002, A diffusion-controlled kinetic model for binder burnout in a powder compact, *Acta Mater., 50, pp. 1937-1950*

Shi, Z. and Guo, Z. X., 2003, Modelling of binder removal from a (fibre+powder) composite pre-form, *Acta Mater., 51, pp. 899-909*

Shi, Z. and Guo, Z. X., 2004, Kinetic modeling of binder removal in powder-based, *Mat. Sci. Eng. A, Vol. 365, pp. 129-135*

Song, J. H., Ediringshe, M. J. and Evans, J. R. G., 1996, Modeling the effect of gas transport on the formation of defects during thermolysis of powder moldings, *J. Mater. Res., Vol. 11, No. 4, pp. 830-839*

Sproson, D. W. and Messing, G. L., 1988, Organic removal process in closed pore powder-binder systems, Messing, C. L., Euller, E. R., Hausner, Jr. H. (eds.), *Ceramic Transactions, Ceramic Powder Science II, American Ceramic Society, Westerville, OH, Vol. 1, pp. 528-537*

Stangle, G. C. and Aksay, I. A., 1990, Simultaneous momentum, heat and mass transfer with chemical reaction in a disordered porous medium: application to binder removal from a ceramic green body, *Chem. Eng. Sci., Vol.45, No. 7, pp. 1719-1731*

Sundback, C. A. and Costantini, M. A., Robbins, W. H., 1989, Part distortion during binder removal, V. J. Tennery (eds.), *Ceramic Materials and Components for Engines, Proc. Of 3rd Int. Symp., American Ceramic Society, Westerville, OH, pp. 191-200*

Taylor, J. R., 1997, An Introduction to Error Analysis, *2nd ed., University Science Books, California*

Trunec, M. and Cihlar, J., 2002, Thermal removal of multi-component binder from ceramic injection molding, *J. Eur. Ceram. Soc., Vol. 22, pp. 2231-2241*

Tsai, D.-S., 1991, Pressure buildup and internal stresses during binder burnout: Numerical Analysis, *AIChE J., Vol.37, No. 4, pp. 547-554*

Udell, K. S., 1985, Heat transfer in porous media considering phase change and capillarity – the heat pipe effect, *Int. J. Heat Mass Trans., Vol. 28, No. 2, pp. 485 – 495*

Van Krevelen, D. W., 1990, Properties of polymers: Their correlation with chemical structure; their numerical estimation and prediction from addictive group contributions, 3rd ed., Elsevier Science Publishers, Oxford

Vrentas, J. S. and Vrentas, C. M., 1994, Solvent self-diffusion in rubbery polymer-solvent system, *Macromolecules, Vol. 27, pp. 4684 – 4690*

West, A. C. and Lombardo, S. J., 1998, The role of thermal and transport properties on the binder burnout of injection-molded ceramic composites, *Chem. Eng. J., Vol. 71, pp. 243-252*

Whitaker, S., 1977, Simultaneous heat, mass, and momentum transfer in porous media: A theory of drying, *Hartnett, J. P., and Irvine, T. F., Ir (eds.), Advances in Heat Transfer, Vol. 13, Academic Press*

Yaws, C. L., 1999, Chemical properties handbook, *McGraw-Hill*

Yaws, C. L., 2003, Yaw's handbook of thermodynamic and physical properties of chemical compounds, *Knovel*

Ying, S. J., Lam, Y. C., Yu, S. C. M. and Tam, K. C., 2001, Two-dimensional simulation of mass transportion polymer removal from a powder injection molding compact by thermal debinding, *J. Mater. Res., Vol. 16, No. 87, pp. 2436-2451*

Ying, S. J., Lam, Y. C., Yu, S. C. M. and Tam, K. C., 2002a, Thermal debinding modeling of mass transport and deformation in powder injection molding compact, *Metall. Mater. Trans. B, Vol. 33B, No. 3, pp. 477-488*

Ying, S. J., Lam, Y. C., Yu, S. C. M. and Tam, K. C., 2002b, Thermo-mechanical simulation of PIM thermal debinding, *Int. J. Powder Metall., Vol. 38, No. 8, pp. 41-55*

Ying, S. J., Lam, Y. C. and Chai, J. C., 2004a, Evolution of liquid-bond strength in powder injection moulding compact during thermal debinding: numerical simulation, *Model. Simul. Mater. Sc., Vol. 12, pp. 311-323*

Ying, S. J., Lam, Y. C. and Chai, J. C., 2004b, Simulation of thermal debinding: effects of mass transport on equivalent stress, *Comp. Mater. Sci., Vol. 30, pp. 496-503*

Yoshikawa, K. and Ohmori, H., 2001, Outstanding features of powder injection molding for micro parts manufacturing, *RIKEN Review, No. 34, pp. 13-18*

APPENDIX A: Constitutive equations

The constitutive equations in the thesis are presented. These equations govern the thermal degradation rate, the vapor pressure, and the capillary pressure.

A) Thermal degradation rate

In the model, PP serves as the HMW component. This polymer degrades into volatile fragments via random chain scission during thermal degradation. The thermal degradation rate can be expressed as (Reich and Stivala, 1971)

$$\langle \dot{m}_d \rangle = \varepsilon \langle \rho_{l,p} \rangle^{l,p} \left(\frac{S_{l,p}}{S_{l,initial}}\right)^r C_o \exp\left(\frac{-E_{dg}}{R\langle T \rangle}\right) \quad \text{(A-1)}$$

where $S_{l,initial}$ is the initial liquid saturation of the polymer, r is the reaction order, C_o is the rate constant, and E_{dg} is the activation energy. PP encounters three regions of degradation mechanisms during the thermal degradation (Chan and Balke, 1997). The Region I is when the degradation of polymer with 'weak links' occurs and the Region II is when the high degrees of chain scission occur at higher temperatures. Region III is the transitional region between these regions. Assuming the reaction to be first order, the thermal degradation parameters for these three regions are estimated using TGA (heating rate of 1 °C/min) following analysis of Chan and Balke (1997). These degradation parameters are shown in Table A1.

Table A1 Thermal degradation parameters

Regions	Remaining PP (%)	E (KJ/mol)	C_o (1/s)
Region I	≤ 99.4	44.7	2.18×10^{-2}
Region III	≤ 95.8	101.6	5.57×10^{3}
Region II	> 95.8	321.1	3.33×10^{21}

B) Vapor pressure

In order to estimate the vapor pressure of solution during thermal debinding, the solution is assumed to be in local chemical and phase equilibria. Therefore, the volume averaged vapor pressure is

$$\langle p_{g,j} \rangle^g = a_j \langle p^o_{g,j} \rangle^g \tag{A-2}$$

where the activity of species liquid phase in the solution a_j. It can be estimated using the Flory-Huggins relation (Flory, 1953) as

$$a_j = \frac{S_{l,j}}{S_{l,p-j}} \exp[(1 - \frac{S_{l,j}}{S_{l,p-j}}) + \chi_j (1 - \frac{S_{l,j}}{S_{l,p-j}})^2] \tag{A-3}$$

In Eqs. (A-2) and (A-3), $\langle p^o_{g,j} \rangle^g$ is the vapor pressure of pure species liquid phase and χ_j is the interaction parameter of the solution.

C) Capillary pressure

Capillary pressure plays an important role in liquid phase transport, especially in porous media with small pore size. The experimental and theoretical studies on capillary pressure were reviewed by Dullien (1992) and Kaviany (1991). It can be defined as the pressure difference across the liquid-vapor phase interface,

$$\langle P_{c,j} \rangle = \langle P_{g,t} \rangle^g - \langle P_{l,j} \rangle^{l,j} \tag{A-4}$$

In the estimation of the capillary pressure of liquid phase, the following expression is used

$$\langle P_{c,j} \rangle = 2\sigma_j \langle H_j \rangle \tag{A-5}$$

where $\langle H_j \rangle$ is the volume averaged mean meniscus curvature that depends on the liquid saturation. In present, the available models to estimate $\langle H_j \rangle$ are the capillary, network, and empirical models. The empirical correlation, which is generally used in

modeling multiphase flow in porous media, is used. For an empirical model, the capillary pressure can be expressed in Leverett reduced function, which is (Kaviany, 1991)

$$J(S_j) = \frac{\langle P_{c,j} \rangle}{\sigma_j} \left(\frac{K}{\varepsilon}\right)^{1/2} \tag{A-6}$$

where the $\frac{\langle P_{c,j} \rangle}{\sigma_j}$ represents the mean interfacial curvature and $\left(\frac{K}{\varepsilon}\right)^{1/2}$ is the pore-level length scale. The functional form of J is (Udell, 1985)

$$J(S_j) = 1.714(1 - S_j) - 2.120(1 - S_j)^2 + 1.263(1 - S_j)^3 \tag{A-7}$$

where,

$$S_j = \frac{S_{l,j} - S_{l,ir}}{1 - S_{l,ir} - S_{g,ir}} \tag{A-8}$$

In Eq. (A-8), $S_{l,ir}$ and $S_{g,ir}$ are the irreducible liquid saturation and the irreducible gas saturation respectively. Since carbonyl iron metal powder is close to spherical shape, the values $S_{l,ir} = 0.09$ and $S_{g,ir} = 0.05$ are used (Kaviany, 1991). The surface tension σ_j is expected to be a function of temperature. Therefore, the average capillary pressure also can be expressed as

$$\langle P_{c,j} \rangle = f(\langle T \rangle, S_{l,j}) \tag{A-9}$$

Assuming that the porous media is homogeneous, the gradient of $\langle P_{c,j} \rangle$ can be written as

$$\nabla \langle P_{c,j} \rangle = \frac{\partial \langle P_{c,j} \rangle}{\partial S_{l,j}} \nabla S_{l,j} + \frac{\partial \langle P_{c,j} \rangle}{\partial \langle T \rangle} \nabla \langle T \rangle \tag{A-10}$$

APPENDIX B: Transport Coefficients

In this section, the transport coefficients are presented. These coefficients include the effective thermal conductivity, the permeability, the relative permeability, the binary diffusion coefficient of solution, and the effective diffusion coefficient of gas phase in porous media.

A) Effective thermal conductivity

Lumped parameter model of Hsu et. al. (1995) is used to estimate the effective thermal conductivity of the PIM compact. The effective thermal conductivity is expressed as

$$\frac{k_{eff}}{k_{fd}} = \gamma_a \gamma_c \frac{k_s}{k_{fd}} + \frac{\gamma_a (1-\gamma_c)\frac{k_s}{k_{fd}}}{(1-\gamma_a)\frac{k_s}{k_{fd}} + \gamma_a} + \frac{(1-\gamma_a)\frac{k_s}{k_{fd}}}{(1-\gamma_a\gamma_c)\frac{k_s}{k_{fd}} + \gamma_a\gamma_c} \tag{B-1}$$

The thermal conductivity of fluid is estimated by considering the contribution of liquid and gas phases according to their volume fractions,

$$k_{fd} = \varepsilon k_l + \varepsilon S_g k_g \tag{B-2}$$

The thermal conductivity of liquid phase is

$$k_l = S_{l,p} k_{l,p} + S_{l,sa} k_{l,sa} + S_{l,f} k_{l,f} \tag{B-3}$$

The thermal conductivity of total gas phase is

$$k_g = \langle \rho_{g,sa} \rangle^g k_{g,sa} + \langle \rho_{g,f} \rangle^g k_{g,f} + \langle \rho_{g,i} \rangle^g k_{g,i} \tag{B-4}$$

The structure of porous media is considered as an array of in-line cubes with smaller connecting bars (see Fig. B1). The volume fraction of the solid phase is

$$1-\varepsilon = \gamma_a^{\,2} + 2\gamma_c\gamma_a(1-\gamma_a) \tag{B-5}$$

$$\gamma_a = \frac{a}{l} \tag{B-6}$$

$$\gamma_c = \frac{c}{a} \tag{B-7}$$

Using contact parameter $\gamma_c = 0.03$ and porosity $\varepsilon = 0.4$, γ_a can be calculated with Eq. (B-5).

B) Permeability

According to the Darcy law, the permeability is the measure of the flow conductance of porous media. The permeability of metal powder porous media is estimated as (German, 1981)

$$K = 4.8 \times 10^{-13} (d^{1.3})(\varepsilon^{4.8}) \tag{B-8}$$

C) Relative Permeability

The relative permeability is used to account for the phase distributions. It serves as an estimation of the effective permeability of the phases for the multiphase flow in porous media. A general empirical correlation is used (Udell, 1985)

$$K_{rl} = S_l^3 \tag{B-9}$$

$$K_{rg} = (1 - S_l)^3 \tag{B-10}$$

D) Binary diffusion coefficient of the solutions

Free volume theory of diffusion is used in the estimation of the binary diffusion coefficient for the solutions. The binary diffusion coefficient $D_{l,p-j}$ can be expressed as (Vrentas and Vrentas, 1994, Hong, 1995)

$$D_{l,p-j} = D_1 (1 - \theta_{l,j})^2 (1 - 2\chi_j \theta_{l,j}) \tag{B-11}$$

$$D_1 = D_{01}\exp\{-(\frac{W_j V_j(0) + \xi W_p V_p(0)}{W_j(\frac{k_{11}}{\eta})[k_{21} - T_{g,j} + \langle T\rangle] + W_p(\frac{k_{12}}{\eta})[k_{12} - T_{g,p} + \langle T\rangle]})\} \quad \text{(B-12)}$$

$$D_{01} = D_0\exp(-\frac{E_{dif}}{RT}) \quad \text{(B-13)}$$

$$W_j = \frac{\langle\rho_{l,j}\rangle^{l,j}\theta_{l,j}}{\langle\rho_{l,j}\rangle^{l,j}\theta_{l,j} + \langle\rho_{l,p}\rangle^{l,p}(1-\theta_{l,j})} \quad \text{(B-14)}$$

$$W_p = \frac{\langle\rho_{l,p}\rangle^{l,p}(1-\theta_{l,j})}{\langle\rho_{l,j}\rangle^{l,j}\theta_{l,j} + \langle\rho_{l,p}\rangle^{l,p}(1-\theta_{l,j})} \quad \text{(B-15)}$$

$$\xi = \frac{V_{l,j}(0)}{0.0925T_{g,p} + 69.47} \quad \text{(B-16)}$$

where D_{01} is the pre-exponential factor for diffusion in Eq. (B-12), D_0 is the pre-exponential factor for diffusion in Eq. (B-13), $\theta_{l,j}$ is the volume fraction of species in the solution, W_j is the mass fraction of species, W_p is the mass fraction of polymer, $V_j(0)$ is the specific volume at 0 K, ξ is the ratio of critical molar volume of hopping units of species and polymer, η is the overlap factor for free volume, κ_{11} and κ_{12} are the free volume parameters, κ_{21} and κ_{22} are the William-Landel-Ferry (WLF) constants, $T_{g,j}$ is the glass transition temperature of species, $T_{g,p}$ is the glass transition temperature of polymer, and E_{dif} is the activation energy for diffusion. The required parameters are estimated following the analysis of Hong (1995) and are shown in Table B1.

Table B1 Parameters for estimating the binary diffusion coefficient

Parameter	Solution of PP and Volatile fragment	Solution of PP and SA	Unit
$V_{l,j}(0)$	1.0744	0.9990	cm^3/g
$V_{l,p}(0)$	1.005	1.005	cm^3/g
D_0	1.94×10^{-3}	2.87×10^{-2}	cm^2/s
E_{dif}	1740.79	2180.54	J/mol
$\frac{\kappa_{11}}{\eta}$	7.60×10^{-4}	2.63×10^{-4}	$cm^3/g\,K$
$\frac{\kappa_{12}}{\eta}$	5.04×10^{-4}	5.02×10^{-4}	$cm^3/g\,K$
$\kappa_{21}-T_{g,j}$	-24.13	59.82	K
$\kappa_{22}-T_{g,p}$	-205.4	-205.4	K

F) Effective diffusion coefficient of gas phase in porous media

In the model, the total gas phase is assumed as a binary gas system that consists of inert gas and species gas (either vapor LMW component or vapor volatile fragments). The diffusion coefficient of binary gas system is estimated using the empirical correction of Wilke and Lee (Reid et al., 1987) as

$$D_{g,i-j}=\frac{(3.03-0.98/M_{i-j}^{1/2})(10^{-3})\langle T\rangle^{3/2}}{\langle P_{g,t}\rangle^{g} M_{i-j}^{1/2}\alpha_{eff}^{2}\Pi_D} \tag{B-17}$$

where the subscripts i and j denotes the inert gas and the species gas respectively.

The effective molecular weight is

$$M_{i-j}=\frac{2M_jM_i}{M_j+M_i} \tag{B-18}$$

The effective characteristic length of molecular is

$$\alpha_{eff}=\frac{\alpha_j+\alpha_i}{2} \tag{B-19}$$

The characteristic length for species is

$$\alpha_j = 1.18 V_{b,j}^{1/3} \tag{B-20}$$

where $V_{b,j}$ is the molar volume at normal boiling temperature.

The $V_{b,j}$ can be related with critical volume $V_{cri,j}$ as (Reid et al., 1987)

$$V_{b,j} = 0.285 V_{cri,j}^{1.048} \tag{B-21}$$

The dimensionless diffusion collision integral is

$$\Pi_D = \frac{A_d}{(T^*)^{B_d}} + \frac{C_d}{\exp(D_d T^*)} + \frac{E_d}{\exp(F_d T^*)} + \frac{G_d}{\exp(H_d T^*)} \tag{B-22}$$

where,

$A_d = 1.06036$, $B_d = 0.1560$, $C_d = 0.19300$, $D_d = 0.47635$, $E_d = 1.03587$, $F_d = 1.52996$, $G_d = 1.76474$, $H_d = 3.89411$

The dimensionless temperature is

$$T^* = \frac{\langle T \rangle}{1.15 (T_{b,j} T_{b,i})^{1/2}} \tag{B-23}$$

The effective diffusion coefficient of total gas phase in the porous structure of a PIM compact is estimated as (Baver and Gardner, 1972)

$$D_{geff,i-j} = D_{g,i-j} (1 - S_l)^{10/3} \varepsilon^{4/3} \tag{B-24}$$

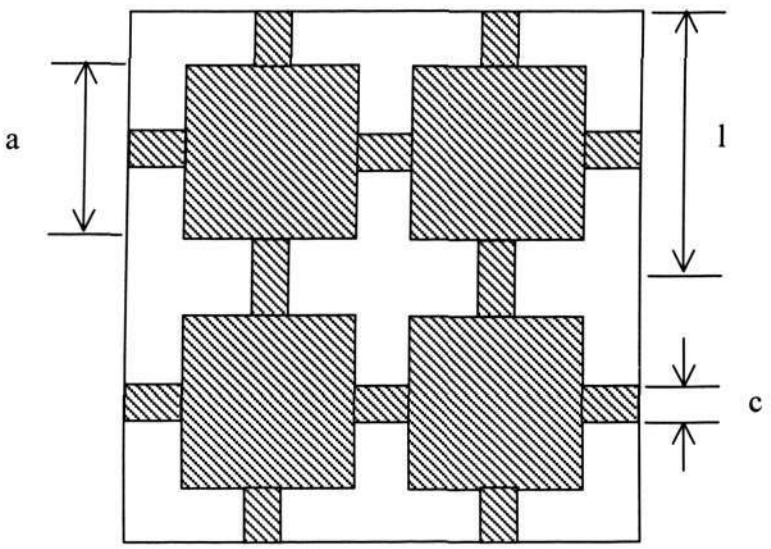

Figure B1 Effective thermal conductivity of porous media

APPENDIX C: Material Properties

The material properties of the HMW component and its volatile fragments, the LMW component, and the inert gas are presented. These materials are polypropylene (PP), 1-tetradecene, stearic acid (SA), and nitrogen, respectively.

The monomer of PP is propylene (C_3H_6). However, PP degrades via random chain scission, in which variety of volatile fragments are produced. To simplify the model, PP is assumed to degrade into one type of volatile fragment exclusively. The composition of the volatile fragments for PP is dienes (7.6%), alkanes (7.6%), and alkenes (84.8 %). The alkene of C_{14} is the most preferable volatile fragment (Bockhorn et al., 1999). Therefore, 1-tetradecene ($C_{14}H_{28}$) is assumed to be the only volatile fragment during the thermal degradation of PP. The metal powder is iron carbonyl. Normally, iron carbonyl contains more than 90% of iron element besides compounds of carbon, oxygen, and nitrogen (Japka, 1988). Therefore, the properties of this metal powder are estimated based on the properties of iron.

The required material properties include the pure component constants and chemical structures, the volumetric properties, the viscosity of liquid phase, the viscosity of gas phase, the surface tension, the vapor pressure, the enthalpy of vaporization, the solubility and interaction parameter, the specific heat capacity, and the thermal conductivity.

A) Pure component constants and chemical structures

The pure component constants of the materials, which are stearic acid ($C_{18}H_{36}O_2$), 1-tetradecene ($C_{14}H_{28}$) and polypropylene $(C_3H_6)_n$ are shown in Table C1. The chemical structures of the organic components are shown in Fig. C1.

Table C1 Pure component constants

Constants	Stearic Acid	1-Tetradecene	Polypropylene
Molecular Weight M (g/mol)	284.483 (Yaws, 2003)	196.376 (Yaws, 2003)	-
Average Molecular Weight M_w (g/mol)	-	-	8000
Boiling Temperature T_b (K)	648.35 (Yaws, 2003)	524.25 (Yaws, 2003)	-
Critical Temperature T_{cri} (K)	799.0 (Yaws, 2003)	692.0 (Yaws, 2003)	-
Glass Transition Temperature T_g (K)	-	-	235.0 (Bicerano, 1993)
Critical Pressure P_{cri} (Bar)	13.60 (Yaws, 2003)	16.60 (Yaws, 2003)	-
Critical Volume V_{cri} (cm^3/mol)	1020.0 (Yaws, 2003)	817.0 (Yaws, 2003)	-

B) Volumetric properties: molar volume and density

i) LMW component and volatile fragments

The empirical correction of Yaw (2003) is used to estimate the density (in unit of g/cm^3). It is

$$\langle \rho_{l,j} \rangle^{l,j} = A_\rho \times B_\rho^{-(1-\frac{\langle T \rangle}{T_{cri}})^{n_\rho}} \qquad \text{(C-1)}$$

For 1-tetradecene, $A_\rho = 0.2404$, $B_\rho = 0.252$, and $n_\rho = 0.3045$.

For SA, $A_\rho = 0.2798$, $B_\rho = 0.2686$, and $n_\rho = 0.3025$.

ii) HMW component

The molar volume of PP are estimated (in unit of cm^3/mol) as (Bicerano, 1993)

$$V_{l,p} \approx V_{l,p}(298K)[1+\omega(298K)(\langle T\rangle - 298)] \tag{C-2}$$

where the thermal expansion coefficient is

$$\omega(298K) \approx \frac{1}{(298+4.23T_{g,p})} \tag{C-3}$$

For PP, the molar volume at room temperature $V_{l,p}(298K)$ is 49 cm^3/mol.

The density of PP $\langle \rho_{l,p} \rangle^{l,p}$ is estimated (in unit of g/cm^3) as

$$\langle \rho_{l,p} \rangle^{l,p} = \frac{M_{monomer}}{V_{l,p}} \tag{C-4}$$

where $M_{monomer}$ is the molar weight of monomer for PP with value of 42.081 g/mol (Reid et al. 1987).

C) Viscosity of liquid phase

i) LMW component and volatile fragments

The viscosity of liquid phase is estimated (in unit of cP) using an empirical correlation as (Yaw, 2003)

$$\log_{10} \mu_{l,j} = A_{\mu l} + \frac{B_{\mu l}}{\langle T\rangle} + C_{\mu l}\langle T\rangle + D_{\mu l}\langle T\rangle^2 \tag{C-5}$$

For 1-tetradecene, $A_{\mu l} = -6.731$, $B_{\mu l} = 1.2666\times10^3$, $C_{\mu l} = 0.0124$,

$D_{\mu l} = -1.0611\times10^{-5}$

For SA, $A_{\mu l} = -3.5929$, $B_{\mu l} = 1.3465\times10^3$, $C_{\mu l} = 0.0029$, $D_{\mu l} = -2.7617\times10^{-6}$

ii) HMW component

The Newtonian viscosity of PP is a function of the temperature $\langle T \rangle$ and the average molecular weight M_w. It is estimated (in unit of Pa s) as (Bicerano, 1993)

$$\mu_{l,p} \approx \mu_{l,p}^{cr} \times (\frac{M_w}{M_{cr}}) \tag{C-6}$$

Eq. (C-6) is only applicable for the case of $M_w \leq M_{cr}$. In the simulation, M_w with value of 8000 g/mol is used. The correlation for critical average molecular weight of the Newtonian viscosity is (Van Krevelen, 1990)

$$M_{cr} \approx 169(\frac{M_{monomer}}{K_{stiff}})^4 \tag{C-7}$$

where K_{stiff} is the molar stiffness function. For PP, K_{stiff} is 15.70 $g^{0.25}cm^{1.5}/mol^{0.75}$. Normally, an amorphous polymer is in a rubbery form between temperatures $T_{g,p}$ to $1.2T_{g,p}$ and becomes molten as viscous flow at the temperature of $T > 1.2T_{g,p}$. The critical zero-shear viscosity for $T > 1.2T_{g,p}$ can be expressed as (Bicerano, 1993)

$$\log_{10}[\frac{\mu_{l,p}^{cr}(\langle T \rangle)}{\mu_{l,p}^{cr}(1.2T_{g,p})}] \approx \frac{(T_g - \langle T \rangle)E_\mu}{2.3R\langle T \rangle T_{g,p}} \tag{C-8}$$

The critical zero-shear viscosity at temperature $1.2T_g$ can be estimated (in unit of Pa s) as

$$\log_{10}[\mu_{l,p}^{cr}(1.2T_{g,p})] \approx \frac{E_\mu(0.052 - 8.5\times10^{-5}T_{g,p})}{T_{g,p}} - 1.4 \tag{C-9}$$

The activation energy for viscous flow is

$$E_\mu = (\frac{H_\mu}{M_{monomer}})^3 \tag{C-10}$$

where H_μ is the molar viscosity-temperature function. For PP, H_μ is estimated as 1480 $gJ^{1/3}mol^{-4/3}$ using group contribution method.

D) Viscosity of gas phase

i) LMW component and volatile fragments

Viscosity of vapor phase is estimated (in unit of μP) using an empirical correlation as (Yaws, 2003)

$$\mu_{g,j} = A_{\mu g} + B_{\mu g}\langle T\rangle + C_{\mu g}\langle T\rangle^2 \tag{C-11}$$

For 1-tetradecne, $A_{\mu g} = -1.547$, $B_{\mu g} = 0.1568$, $C_{\mu g} = -8.2620\times10^{-6}$

For SA, $A_{\mu g} = -17.287$, $B_{\mu g} = 0.216$, $C_{\mu g} = -3.8707\times10^{-5}$

ii) Inert gas

Viscosity of nitrogen is estimated (in unit of μP) using an empirical correlation (Yaws, 1999). It is

$$\mu_{g,i} = A_{\mu,i} + B_{\mu,i}\langle T\rangle + C_{\mu,i}\langle T\rangle^2 \tag{C-12}$$

where $A_{\mu,i} = 42.606$, $B_{\mu,i} = 4.7500\times10^{-1}$, $C_{\mu,i} = -9.8800\times10^{-5}$

iii) Total gas phase

In the model, the total gas phase is assumed as a binary gas system. The dynamic viscosity of total gas phase is considered as the combination of two gases as (Reid et al., 1987)

$$\mu_g = \sum_{A=1}^{2} \frac{\Lambda_A \mu_{g,A}}{\sum_{B=1}^{2} \Lambda_B Z_{AB}} \tag{C-13}$$

Where Λ is the molar fraction of the pure gas components and Z_{AB} is the mixing coefficient. The subscript A and B represent the types of gases. Setting j as species vapor phase and i as inert gas phase, the viscosity of total gas phase can be written as

$$\mu_g = \frac{\Lambda_j \mu_{g,j}}{\Lambda_j Z_{jj} + \Lambda_i Z_{ji}} + \frac{\Lambda_i \mu_{g,i}}{\Lambda_i Z_{ii} + \Lambda_j Z_{ij}} \tag{C-14}$$

The molar fraction of species gas phases in the mixture of gases is

$$\Lambda_j = \frac{\langle p_{g,j} \rangle^g}{\langle P_{g,t} \rangle^g} \tag{C-15}$$

The mixing coefficient is

$$Z_{ij} = \frac{[1 + (\frac{\mu_{g,j}}{\mu_{g,i}})^{1/2} (\frac{M_i}{M_j})^{1/4}]^2}{[8(1 + \frac{M_j}{M_i})]^{1/2}} \tag{C-16}$$

where,

$$Z_{ij} = Z_{ji} (\frac{\mu_{g,j}}{\mu_{g,i}})(\frac{M_j}{M_i}) \tag{C-17}$$

$$Z_{jj} = Z_{ii} = 1.0 \tag{C-18}$$

E) Surface tension

i) LMW component and volatile fragments

The surface tension is calculated (in unit of dyn/cm) as (Yaws, 2003)

$$\sigma_j = A_\sigma (1 - \frac{\langle T \rangle}{T_{cri}})^{n_\sigma} \tag{C-19}$$

For 1-tetradecene, $A_\sigma = 56.297$ and $n_\sigma = 1.3469$

For SA, $A_\sigma = 53.650$ and $n_\sigma = 1.1470$

ii) HMW component

The surface tension of polymer is estimated (in unit of dyn/cm) as (Bicerano, 1993)

$$\sigma_p \approx (\frac{P_s}{V_{l,p}})^4 \tag{C-20}$$

where P_s is the molar parachor and $V_{l,p}$ is the molar volume. For PP, P_s is 118.2 $(cm^3/mol)(dyn/cm)^{1/4}$.

F) Vapor pressure

The vapor pressure of pure liquid phase is estimated (in unit of mmHg) using an empirical relationship (Yaws, 2003). It is

$$\log_{10}(p^o_{g,j}) = A_{pv} + \frac{B_{pv}}{\langle T\rangle} + C_{pv}\log_{10}(\langle T\rangle) + D_{pv}\langle T\rangle + E_{pv}\langle T\rangle^2 \qquad \text{(C-21)}$$

For 1-tetradecne, $A_{pv} = 100.11, B_{pv} = -7040.3, C_{pv} = -33.05, D_{pv} = 1.1591\times10^{-2}$, and $E_{pv} = -1.3156\times10^{-14}$

For SA, $A_{pv} = -40.364$, $B_{pv} = -4772.4$, $C_{pv} = 24.502$, $D_{pv} = -3.7665\times10^{-2}$, and $E_{pv} = 1.4595\times10^{-5}$

G) Enthalpy of vaporization

An empirical correction is used to estimate the enthalpy of evaporation (in unit of kJ/mol) as (Yaws, 2003)

$$\Delta H_{vap} = A_{hvap}\left(1 - \frac{\langle T\rangle}{T_{cri}}\right)^{n_{hvap}} \qquad \text{(C-22)}$$

For 1-tetradecene, $A_{hvap} = 87.014$ and $n_{hvap} = 0.418$

For SA, $A_{hvap} = 131.71$ and $n_{hvap} = 0.417$

H) Solubility and interaction parameter

A semi-empirical equation is used to estimate the interaction parameter of the solution (Hong, 1995)

$$\chi_j = 0.35 + \frac{V_{l,j}}{RT}(\delta_j - \delta_p)^2 \quad \text{(C-23)}$$

The solubility parameter of the volatile fragments or LMW component is estimated (in unit of $(J/cm^3)^{0.5}$) as (Yaws, 2003)

$$\delta_j = [\frac{(H_{vap} - R\langle T\rangle)}{V_{l,j}}]^{0.5} \quad \text{(C-24)}$$

where $V_{l,j}$ is the molar volume of the volatile fragments or LMW component.

The solubility parameter of the polymer is estimated (in unit of $(J/cm^3)^{0.5}$) as (Bacerano, 1993)

$$\delta_p = \sqrt{\frac{E_{coh}}{V_{l,p}}} \quad \text{(C-25)}$$

where E_{coh} is the cohesive energy of polymer and $V_{l,p}$ is the molar volume of the polymer. For PP, E_{coh} is 12646 J/mol. In the simulation, the interaction parameter of solution of HMW component and volatile fragments at room temperature is estimated using Eqs. (C-23) to (C-25) and it is assumed constant throughout the thermal debinding.

I) Specific heat capacity

i) LMW component and volatile fragments

The heat capacity of liquid phase is calculated (in unit of J/mol K) with an empirical correlation as (Yaws, 2003)

$$(C_p)_{l,j} = A_{cpl} + B_{cpl}\langle T\rangle + C_{cpl}\langle T\rangle^2 + D_{cpl}\langle T\rangle^3 \quad \text{(C-26)}$$

For 1-tetradecne, $A_{cpl} = 135.178$, $B_{cpl} = 2.0938$, $C_{cpl} = -5.0407\times10^{-3}$, $D_{cpl} = 5.0893\times10^{-6}$

For SA, $A_{cpl} = 99.012$, $B_{cpl} = 3.5874$, $C_{cpl} = -7.2484 \times 10^{-3}$, $D_{cpl} = 5.9035 \times 10^{-6}$

The estimation of heat capacity of gas phase (in unit of J/mol K) is based on an empirical correlation (Yaws, 2003). It is

$$(C_p)_{g,j} = A_{cpg} + B_{cpg}\langle T\rangle + C_{cpg}\langle T\rangle^2 + D_{cpg}\langle T\rangle^3 + E_{cpg}\langle T\rangle^4 \qquad \text{(C-27)}$$

For 1- tetradecene, $A_{cpg} = 1.6790 \times 10^2$, $B_{cpg} = 3.1544 \times 10^{-1}$, $C_{cpg} = 1.0739 \times 10^{-3}$, $D_{cpg} = -1.200 \times 10^{-6}$, $E_{cpg} = 3.6046 \times 10^{-10}$

For SA, $A_{cpg} = 7.5150$, $B_{cpg} = 1.6996$, $C_{cpg} = -9.2847 \times 10^{-4}$, $D_{cpg} = 1.756 \times 10^{-7}$, $E_{cpg} = 3.6437 \times 10^{-12}$

ii) HMW component

The heat capacity of polymer liquid phase is estimated (in unit of J/mol K) as (Bicerano, 1993)

$$(C_p)_{l,p} = (C_p)_{l,p}(298K)(0.613 + 1.3 \times 10^{-3}\langle T\rangle) \qquad \text{(C-28)}$$

The heat capacity of liquid phase of PP at room temperature is $(C_p)_{l,p}(298K) = 94.0$ J/mol K (Bicerano, 1993).

iii) Inert gas

The heat capacity of nitrogen is estimated (in unit of J/mol K) using an empirical correlation (Yaws, 1999). It is

$$(C_p)_{g,i} = A_{cgi} + B_{cgi}\langle T\rangle + C_{cgi}\langle T\rangle^2 + D_{cgi}\langle T\rangle^3 + E_{cgi}\langle T\rangle^4 \qquad \text{(C-29)}$$

where $A_{cgi} = 29.342$, $B_{cgi} = -3.5395 \times 10^{-3}$, $C_{cgi} = 1.0076 \times 10^{-5}$, $D_{cgi} = -4.3116 \times 10^{-9}$, $E_{cgi} = 2.5935 \times 10^{-13}$

iv) Metal powder

The heat capacity of iron (in unit of J/mol K) is estimated using an empirical correlation (Yaws, 1999). It is

$$(C_p)_s = A_{cs} + B_{cs}\langle T\rangle + C_{cs}\langle T\rangle^2 \qquad \text{(C-30)}$$

where $A_{cs} = 26.748$, $B_{cs} = -1.5339\times10^{-2}$, $C_{cs} = 3.8405\times10^{-5}$

J) Thermal conductivity

i) LMW component and volatile fragments

The thermal conductivity of liquid phase is estimated (in unit of W/m K) using an empirical correlation as (Yaws, 2003)

$$k_{l,j} = A_{kl} + B_{kl}\langle T\rangle + C_{kl}\langle T\rangle^2 \qquad \text{(C-31)}$$

For 1-tetradecene, $A_{kl} = 0.188$, $B_{kl} = -1.6810\times10^{-4}$, $C_{kl} = -2.5162\times10^{-8}$

For SA, $A_{kl} = 0.2423$, $B_{kl} = -1.7143\times10^{-4}$, $C_{kl} = -8.9286\times10^{-8}$

The thermal conductivity of vapor phase is estimated (in unit of W/m K) using an empirical correlation as (Yaws, 2003)

$$k_{g,j} = A_{kg} + B_{kg}\langle T\rangle + C_{kg}\langle T\rangle^2 \qquad \text{(C-32)}$$

For 1-tetradecene, $A_{kg} = 1.8155\times10^{-3}$, $B_{kg} = 3.3595\times10^{-5}$, $C_{kg} = 3.0581\times10^{-8}$

For SA, $A_{kg} = -1.04878\times10^{-2}$, $B_{kg} = 5.9499\times10^{-5}$, $C_{kg} = 2.0774\times10^{-8}$

ii) HMW component

The thermal conductivity of PP is estimated (in unit of W/m K) as (Bicerano, 1993)

$$k_{l,p} \approx k_{l,p}(T_{g,p})\left(\frac{\langle T\rangle}{T_{g,p}}\right)^{0.22} \qquad \text{(C-33)}$$

The thermal conductivity of polymer at glass transition temperature $k_{l,p}(T_{g,p})$ can be related with the thermal conductivity of polymer at room temperature $k_{l,p}(298\,\mathrm{K})$ as

$$k_{l,p}(T_{g,p}) \approx \frac{k_{l,p}(298K)}{(\frac{298}{T_{g,p}})^{0.22}} \tag{C-34}$$

For PP, $k_{l,p}(298\,\mathrm{K})$ is 0.143 W/m K (Bicerano 1993).

iii) Inert gas

The thermal conductivity of nitrogen is estimated (in unit of W/m K) using an empirical correlation as (Yaws, 1999)

$$k_{g,i} = A_{kgi} + B_{kgi}\langle T\rangle + C_{kgi}\langle T\rangle^2 \tag{C-35}$$

where $A_{kgi} = 0.00309$, $B_{kgi} = 7.5930\times10^{-5}$, $C_{kgi} = -1.1014\times10^{-8}$

iv) Metal powder

The thermal conductivity of iron is estimated (in unit of W/m K) as (Yaws, 1999)

$$k_s = A_{ks} + B_{ks}\langle T\rangle + C_{ks}\langle T\rangle^2 \tag{C-36}$$

where $A_{ks} = 117.3180$, $B_{ks} = -1.3759\times10^{-1}$, $C_{ks} = 5.4170\times10^{-5}$

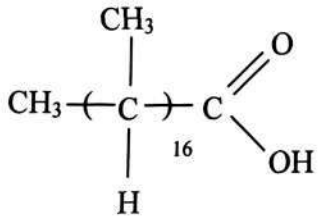

Stearic Acid

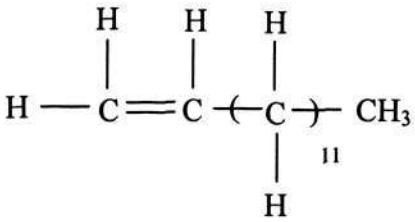

1-Tetradecene

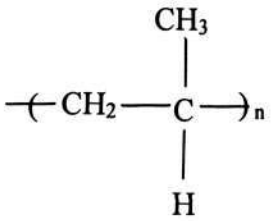

Polypropylene

Figure C1 Chemical structures of stearic acid, 1-tetradecene and polypropylene